

André F. Martins

MULTIMODAL IMAGING PROBES FOR THE DIAGNOSTICS OF ALZHEIMER'S DISEASE

Ph.D. Thesis

2013



UNIVERSIDADE DE COIMBRA



UNIVERSITÉ D'ORLÉANS

André F. Martins

Multimodal Imaging Probes for the Diagnostics of Alzheimer's Disease

Ph.D. Thesis

Supervisors: Prof. Carlos F.G.C. GERALDES
Dr. Eva JAKAB TOTH

Dissertation presented to obtain a Ph.D. degree in Biochemistry, speciality of Molecular Biophysics, at the Faculty of Sciences and Technology of the University of Coimbra

International work developed in a joint-institutional supervision



FCTUC FACULDADE DE CIÊNCIAS
E TECNOLOGIA
UNIVERSIDADE DE COIMBRA

+



The scientific work presented in this manuscript is the result of collaboration between the Centre de Biophysique Moléculaire, CNRS, Orléans, France and the Center for Neuroscience and Cell Biology, University of Coimbra, Portugal. The synthesis of the ligands, the physical-chemical and relaxometric characterization of the probes, the binding and the *in vitro* aggregation studies were performed at the CBM-CNRS, while the NMR studies and self-assembly structural studies were done in Coimbra. Several other collaborations have also contributed to this work. The *ex vivo* data on human brain slices have been obtained in Centre de Recherche de l'Institut du Cerveau et de la Moelle, CNRS UMR7225, INSERM, UMR975 and UPMC, Hôpital de la Pitié-Salpêtrière and the *in vivo* studies were carried out at the Inserm U930; Université François Rabelais and CHRU de Tours, France, the advanced 2D NMR studies were performed at the Instituto de Química Física "Rocasolano", C.S.I.C-Madrid, Spain. The scientific work had the financial support from FCT-Fundação para a Ciência e a Tecnologia that granted a scholarship to the doctoral candidate (SFRH/BD/46370/2008) and from the CNRS-Orléans.



+



In memory of my grandfather

João Rosa

To my family

To act, that is true intelligence. I will be whatever I want. But I have to want it. Success is in succeeding, and not in being able to succeed. Any large landplot can host a palace, but where will the palace be if it is not built there?

Fernando Pessoa

Publications

Part of the contents of this thesis have been published in:

1. André F. Martins, Jean-François Morfin, Anna Kubíčková, Vojtěch Kubíček, Frédéric Buron, Franck Suzenet, Milena Salerno, Adina N. Lazar, Charles Duyckaerts, Nicolas Arlicot, Denis Guilloteau, Carlos F. G. C. Geraldés, and Éva Tóth “PiB-Conjugated, Metal-Based Imaging Probes: Multimodal Approaches for the Visualization of β -Amyloid Plaques”, *ACS Med. Chem. Lett.*, **2013**, 436-440.

Other publications:

2. S. Silvério, S. Torres, J. A. Martins, J. P. André, L. Helm, A. F. Martins, M. Isabel M. Prata, A. C. Santos and C. F.G.C. Geraldés, " Lanthanide Chelates of (bis)-Hidroxymethyl-substituted DTTA with Potential Application as Contrast Agents in Magnetic Resonance Imaging", *Dalton Trans.*, **2009**, 4656–4670.

3. Miguel F. Ferreira, André F. Martins, José A. Martins, Paula M. Ferreira, Éva Tóth and Carlos F.G.C. Geraldés, “Gd(DO3A-N- α -aminopropionate): a versatile and easily available synthon with optimized water exchange for the synthesis of high relaxivity, targeted MRI contrast agents”, *Chem. Commun.*, **2009**, 6475–6477.

4. Silvia Chaves, Ana C. Mendonça, Sérgio M. Marques, Maria I.M. Prata, Ana C. Santos, André F. Martins, Carlos F.G.C. Geraldés, M. Amélia Santos, “A Gallium Complex with a New Tripodal Tris-Hydroxypyridinone for Potential Nuclear Diagnostic Imaging: Solution and in vivo Studies of ^{67}Ga -Labeled Species”, *Journal of Inorganic Biochemistry*, **2010**, 31–38.

5. João P. Monteiro, André F. Martins, Marlene Lúcio, Salette Reis, Carlos F. G. C. Geraldés, Paulo J. Oliveira, Amália S. Jurado, “Interaction of carbonylcyanide p-trifluoromethoxyphenylhydrazone (FCCP) with lipid membrane systems: a biophysical approach with relevance to mitochondrial uncoupling”, *J. Bioenerg. Biomembr.*, **2011**, 287–298.

6. João P. Monteiro, André F. Martins, Marlene Lúcio, Salette Reis, Teresa J.T. Pinheiro, Carlos F. G. C. Geraldés, Paulo J. Oliveira, Amália S. Jurado, “Nimesulide interaction with membrane model systems: Are membrane physical effects involved in nimesulide mitochondrial toxicity?”, *Toxicology in Vitro*, **2011**, 1215–23.

7. Luís M. P. Lima, Rita Delgado, Petr Hermann, Radek Sevik, Premysl Lubal, Henrique F. Carvalho, André F. Martins, Éva Tóth, Carlos F. G. C. Geraldes, “Tris(phosphonomethyl)cyclen derivatives: Thermodynamic stability, kinetics, solution structure, and relaxivity of Ln^{3+} complexes”, *Eur. J. Inorg. Chem.*, **2012**, 2548–2559
8. Miguel F. Ferreira, André F. Martins, Catarina I.O. Martins, Paula M. Ferreira, Éva Tóth, Tiago B. Rodrigues, Daniel Calle, Sebastian Cerdan, Pilar López-Larrubia, José A. Martins, Carlos F.G.C. Geraldes, “Amide conjugates of the DO3A-N-(α -amino) propionate ligand: leads for stable, high relaxivity contrast agents for MRI?”, *Contrast Media Mol Imaging*, **2013**, 40–9.
9. M Amelia Santos, André F. Martins, Andrea Melchior, Sérgio Marques, Sílvia Chaves, Pier Luigi Zanonato, Marilena Tolazzi, Plinio Di Bernardo, Carlos F.G.C. Geraldes “New Tris-3, 4-HOPO lanthanide complexes as potential imaging probes: complex stability and magnetic properties”, *Dalton Transactions*, **2013**, 6046-6057.
10. André F. Martins, M. I. M. Prata, S. P. J. Rodrigues, Carlos F. G. C. Geraldes, P. J. Riss, A. Amor-Coarasa, C. Burchardt, C. Kroll, F. Roesch “Spectroscopic, radiochemical, and theoretical studies of the Ga^{3+} -N-2-hydroxyethyl piperazine-N'-2-ethanesulfonic acid (HEPES buffer) system: evidence for the formation of Ga^{3+} -HEPES complexes in ^{68}Ga labeling reactions”, *Contrast Media Mol. Imaging*, **2013**, 265–273.
11. João P. Monteiro, André F. Martins, Cláudia Nunes, Catarina M. Morais, Marlene Lúcio, Salette Reis, Teresa J.T. Pinheiro, Carlos F.G.C. Geraldes, Paulo J. Oliveira, Amália S. Jurado “A biophysical approach to menadione membrane interactions: Relevance for menadione-induced mitochondria dysfunction and related deleterious/therapeutic effects”, *BBA. Biomembranes*, **2013**, 1899–1908.

Acknowledgements

Here comes the big moment in this long journey of four years, which seemed to me to last only 4 days. The end of a great beginning in my life, living through better and worse times, I can just remember the lovely people, the exciting science, the big personalities, the good environment, much learning, the sun that sometimes (not so often...) shone in the sky with all its energy ... they all made the difference. I feel like I can finally thank to all the people that I met and helped me write this thesis. I am indebted to many people for making the time spent working on my Ph.D. an unforgettable experience.

First and foremost, I would like to thank my promoter and supervisor Prof. Carlos Geraldes for his trust, support, advising, and friendship and constant scientific stimulus to proceed further and better. Not only our discussions often led to key insights, but also you were always present in the right moments. I consider you as a father in the science. Thank you for everything!

At the same time, I would like to acknowledge my external supervisor and co-promoter Dr. Eva Tòth for welcoming me in her spectacular team. You have oriented and supported me with promptness and care. Your ability to select and to approach compelling research problems, your high scientific standards and your hard work are my example to follow. I admire your ability to balance research interests and personal pursuits. Above all, you, together with your splendid family, made me feel as a friend, which I appreciate from the bottom of my heart.

Furthermore, I am very grateful to my Organic Chemistry tutor, work colleague and friend, Jean-François Morfin, for the insightful comments both in my work and in this thesis, for his support, and for many motivating discussions. Life was always easier when you were there supporting me. My work was not possible without your help, scientific decisions, and motivation to do better things. I learned a lot from you, even in the more stressful moments. I hope I never disappoint you when applying your precious transmitted knowledge.

I have also very big thank you to transmit to Dr. Douglas Laurents for his active collaboration, friendship, support and insightful discussions. Also to Prof. Marta Bruix and Prof. Manuel Rico for having received me in their lab so warmly. The picture of us all, sitting on the stool where once the Marie Curie also sat, is in

my office as a key memory.

I am indebted also to Prof. Denis Guiloteau, Dr. Nicolas Arlicot, Prof. Charles Duyckaerts, Dr. Milena Salerno, David Dias, Dr. Adina Lazar, Dr. Frank Suzenet and Dr. Vojtěch Kubíček for their very important collaboration and trust, as well to Dr. Anna Kubíčková that initiated the project.

My team colleagues - Célia, Sarah, Agnés, Fátima - also deserve my sincerest thanks, their friendship and assistance has meant more to me than I could ever express. I will never forget your invaluable friendly assistance.

I also thank my friends in CBM and Orléans that are so many to list here (you know who you are!) for providing support and friendship that I needed. The “Orleanaise mafia”!

Special thanks also to João Teixeira, Paulo Gameiro, Rui Costa, Luís Nobre, João Duarte and João Rodrigues. You are really precious to me. My team 7!

I would also like to heartfelt thank to my mother, father, and sisters for always believing in me and encouraging me to follow my dreams. You were and are my anchor.

Finally, I would like to thank to the most precious little thing I have found lost in the world. Le joli renard qui m'a apprivoisé. My beloved sweet Inês... a minha paixão!

CONTENTS

ABREVIATIONS	15
SUMMARY	19
RESUME	23
RESUMO	27
CHAPTER 1 " <i>Introduction to Neuroimaging, Contrast Agents and Alzheimer's Disease</i> "	31
1.1. Introduction to Medical Imaging	32
1.2. Neuroimaging techniques	33
1.2.1. PET and SPECT	33
1.2.2. Magnetoencephalography	36
1.2.3. Computed Axial Tomography	37
1.2.4. Magnetic Resonance Imaging	37
1.3. MRI Contrast Agents	40
1.3.1. Positive Contrast Agents (T1)	40
1.3.2. New generation, positive Contrast Agents	46
1.3.3. Negative Contrast Agents	47
1.4. Multimodality agents	49
1.5. Imaging of Alzheimer's disease	50
1.5.2. Amyloid cascade hypothesis	54
1.5.3. The Blood Brain Barrier enigma	56
1.5.3. Molecular Imaging probes for Alzheimer's Disease	59
1.5.3.1. Nuclear imaging	59
1.5.3.2. MRI	63
1.6. Outline of the Thesis	64
CHAPTER 2 " <i>Objectives of the Thesis and Probe Design</i> "	65
CHAPTER 3 " <i>Organic Synthesis of the Ligands</i> "	72
3.1. Synthesis of the DO3A-BTA derivatives	73
3.2. Synthesis of the BTA moiety, 4-(6-methoxybenzol[d]thiazol-2-yl)aniline .	74
3.2.1. Synthesis of the BTA <i>chloroacetamide</i> reaction intermediates	75
3.2.2. Synthesis of DO3A-BTA derivatives, L ₁ , L ₂ , L ₃	77
3.3. Synthesis of the DOTAGA-BTA derivative.	78
3.3.1. Synthesis of the DOTAGA-BTA derivative, L ₄	79
3.4. Synthesis of the bis-Trityl-MAMA-BTA derivative, L ₅	81
3.5. Experimental	83
3.5.1. Materials and methods	83
3.5.2. Synthesis of the Benzothiazol moiety	84
3.5.3. Synthesis of L ₁	86
3.5.4. Synthesis of L ₂	88

3.5.5. Synthesis of L ₃	91
3.5.6. Synthesis of L ₄	95
3.5.7. Synthesis of L ₅	100
CHAPTER 4 "Physical-Chemical Characterization of Gd-D03A-PiB Derivatives"	103
4.1.Introduction	104
4.2.Experimental	105
4.2.1. Sample Preparation	105
4.2.2. Determination of the Octanol-Water Partition Coefficient	106
4.2.3. ¹ H NMRD measurements.....	106
4.2.4. ¹⁷ O NMR experiments.....	107
4.2.5. HSA affinity constants determination for GdL _{1,3}	107
4.3.Results and discussion.....	108
4.3.1. Lipophilicity determined by the partition coefficient.....	108
4.3.2. Relaxometric measurements	109
4.3.2.1. Micellar aggregation	109
4.3.3. ¹⁷ O NMR and NMRD measurements.....	112
4.3.3.1. Water exchange rate	120
4.3.3.2. Rotational dynamics.....	120
4.3.4. Relaxometric assessment of the interaction of the complexes with Human Serum Albumin (HSA) and Ab ₁₋₄₀ peptide.....	123
4.4.Conclusion.....	126
CHAPTER 5 " In Vitro Interactions and Beta-Amyloid Self-Assembly with Ln-D03A-PiB Derivatives "	127
5.1.Introduction	128
5.2.Experimental	130
5.2.1. Materials and sample preparation	130
5.2.2. Surface Plasmon Resonance.....	130
5.2.3. Nuclear Magnetic Resonance.....	131
5.2.4. Circular Dichroism.....	134
5.2.5. Aggregation assays using ThT Fluorescence	135
5.2.6. Dynamic Light Scattering	135
5.2.7. Transmission Electron Microscopy.....	135
5.3.Results and Discussion.....	136
5.3.1. Binding of LnL ₁ and LnL ₃ to Aβ ₁₋₄₀	136
5.3.2. Effect of binding of Ln ³⁺ complexes on the secondary structure of Ab ₁₋₄₀	150
5.3.3. Studies of the aggregation of Aβ ₁₋₄₀ by Thioflavin T fluorescence, dynamic light scattering and transmission electron microscopy.....	155

CONTENTS

5.4. Conclusions	159
CHAPTER 6 " <i>In Vivo Studies of M³⁺-D03A-PiB Derivatives</i> "	164
6.1. Introduction	165
6.2. Experimental.....	166
6.2.1. <i>Ex vivo</i> human immunostaining studies	166
6.2.1.1. Cases.....	166
6.2.2. Diagnosis	167
6.2.3. Samples for staining	167
6.2.4. Senile plaques staining	167
6.2.5. Immunofluorescent labeling of senile plaques ²⁵⁰	168
6.2.6. Animal studies	168
6.2.7. <i>In vitro</i> autoradiography	169
6.2.8. Radiolabeling.....	169
6.2.9. <i>In vivo</i> biodistribution in mice.....	169
6.3. Results and Discussion	170
<i>Conclusions and Perspectives</i>	176
APPENDIX 1: Analysis of NMRD and ¹⁷ O NMR data.....	180
APPENDIX 2: Saturation Transfer Difference (STD) NMR	187
APPENDIX 3 : Competitive Binding Data	190
REFERENCES.....	192

ABBREVIATIONS

$(A_{\text{STD}})_0$	zero saturation time extrapolation STD amplification factor
A/\tilde{z}	hyperfine or scalar coupling constant
AAZTA	6-[bis(hydroxycarbonylmethyl)amino]-1,4-bis(hydroxycarbonylmethyl)-6-methylperhydro-1,4-diazepine
AD	Alzheimer's disease
ΔH^\ddagger	activation enthalpy for the water exchange
ApoE	apolipoprotein E
APP	amyloid precursor protein
ΔS^\ddagger	activation entropy
A_{STD}	STD amplification factor
BBB	blood-brain barrier
BTA	benzothiazol
BZM	S-(-)-N-[(1-ethyl-2-pyrrolidinyl)methyl]-2-hydroxy-3-iodo-6-methoxybenzamide)
CA	contrast agents
CAT	computed axial tomography
CDCl_3	chloroform deuterated
CH_2Cl_2	dichloromethane
CLIO	cross-linked iron-oxide
CR	Congo red
CT	computed tomography
D_2O	deuterium oxide
D_{GdH}	diffusion coefficient
DLS	dynamic light scattering
DMA	dimethylacetamide
DO3A	1,4,7,10-tetraazacyclododecane-1,4,7-triacetate
DOTA	1,4,7,10-tetraazacyclododecane-1,4,7,10-tetraacetic acid
DOTAGA	4-(4,7,10-tris(2-(tert-butoxy)-2-oxoethyl)-

	1,4,7,10-tetraazacyclododecan-1-yl)pentanoic acid)
DPFGSE	double pulse field gradient spin echo
DSS	4,4-dimethyl-4-silapentane-1-sulfonic acid
DTPA	diethylene triamine pentaacetic acid
ECD	ethyl cysteinate dimer
EDC	1-ethyl-3-(3-dimethylaminopropyl)carbodiimide)
EDTA	ethylenediaminetetraacetic acid
EEC	electroencephalography
E_v	activation energy for the modulation of the ZFS
g	gram (s)
HBS-EP	HEPES buffered saline buffer
HCl	hydrochloric acid
HMPAO	hexamethylpropyleneamine oxime
HOBt	hydroxybenzotriazole
HOPO	hydroxypyridinonate
HRMS-ESI	high Resolution Mass Spectrometry
Hz	hertz
IMPY	2-(4'-dimethylamino-)phenyl-imidazo[1,2-a]pyridine)
J	coupling constant (NMR)
K_2CO_3	potassium carbonate
k_{ex}	water exchange rate
$LiAlH_4$	lithium aluminium hydride
LiOH	lithium hydroxide
Ln	lanthanide
MAMA	monoamine-monoamide
Me	methyl
MEG	magnetoencephalography
MeOD	methanol-deuterated
MeOH	methanol
mg	milligram
MION	monocrystalline iron-oxide
mL	milliliter (s)
mM	millimole.L ⁻¹
mmol	millimole
MOFS	metal-organic frameworks

Na ₂ CO ₃	sodium carbonate
Na ₂ SO ₄	sodium sulphate
NaHCO ₃	sodium bicarbonate
NaOH	sodium hydroxide
NFT	neurofibrillary tangles
NHS	<i>N</i> -hydroxysuccinimide
NMR	nuclear magnetic resonance
NMRD	nuclear magnetic resonance dispersion
NSF	nephrogenic systemic fibrosis
PET	positron emission tomography
PFG	pulse field gradient
PSEN1	presenilin 1
PSEN2	presenilin 2
<i>q</i>	hydration number
q	quartet
R_1	longitudinal relaxation rate = $1/T_1$
r_1	longitudinal proton relaxivity
r_{GdO}	mean Gd(III) coordinated water oxygen distance
SPECT	single-photon emission computed tomography
SPIO	superparamagnetic iron-oxide
SPR	surface plasmon resonance
STD	saturation transfer difference
T_{1e}	(electronic) longitudinal relaxation time
T_{2e}	(electronic) transverse relaxation time
TBTA	tert-butyl-trichloroacetimidate
t-Bu or tert-Bu	tert-butyl
TEM	transmission electron microscopy
TFA	trifluoroacetic acid
THF	tetrahydrofuran
ThT	thioflavin-T
USPIO	ultra small superparamagnetic iron-oxide
UV	ultra-violet

“Multimodal Imaging Probes for the Diagnostics of Alzheimer’s Disease”

SUMMARY

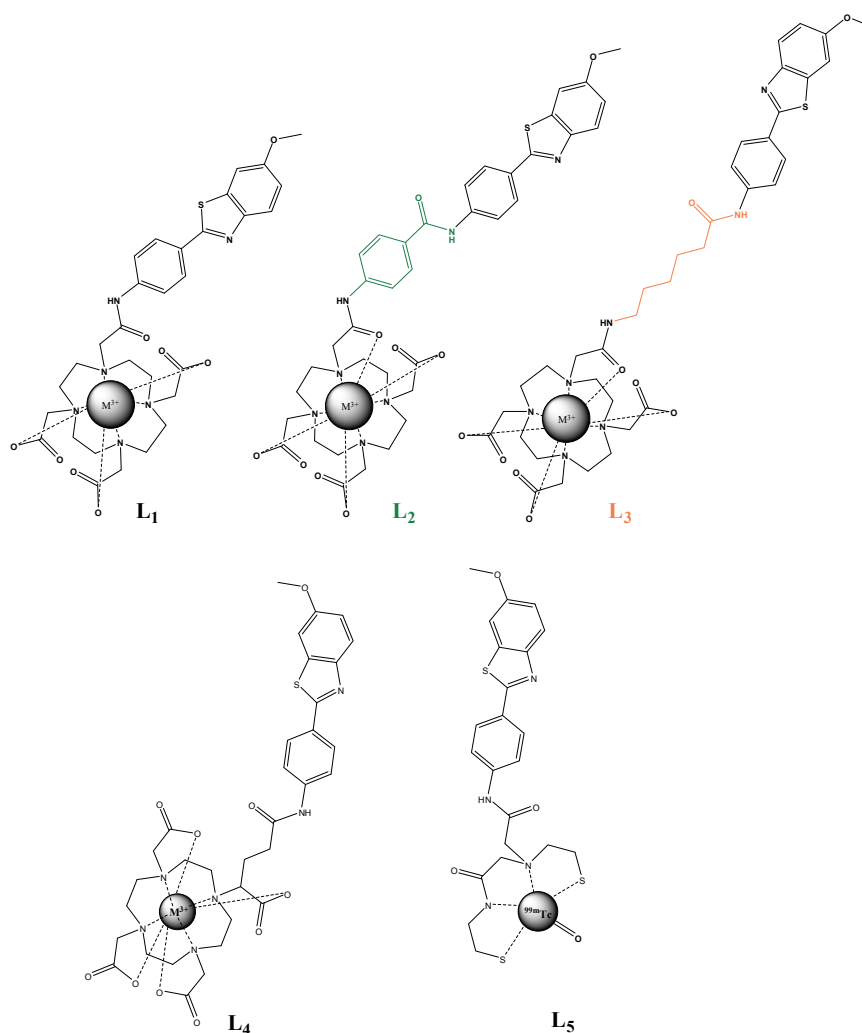
Alzheimer’s disease (AD) is a chronic neurodegenerative disorder that leads to progressive decline of cognitive functions that usually begins with memory loss and impairment, and is followed by loss of judgement, decision-making, orientation and language.

The exploration of novel imaging solutions based on the design of innovative imaging probes that visualize amyloid plaques is highly important as it could largely contribute to the early identification of the disease allowing for: 1) early intervention to slow down the disease process—even without definitive cure available today—and 2) delineating novel therapies.

In this thesis we report the design, synthesis, *in vitro* and *in vivo* validation of multimodal imaging probes based on metal complexes for the detection of amyloid plaques.

We have used a modular approach to create these probes where a targeting unit (PiB), capable of selective binding to the amyloid plaques is linked to a metal chelator (DO3A, DOTA, MAMA) which acts as an imaging reporter. The major advantage of this approach is that it allows the use of a large number of metal ions as imaging probes for a variety of modalities. By a simple choice of the appropriate metal in the imaging probe, we can create a platform of imaging agents for various modalities by using the same chelator and targeting unit: e.g. Gd^{3+} for MRI, $^{111}In^{3+}$ or $^{67}Ga^{3+}$ for SPECT and $^{68}Ga^{3+}$ for PET detection. According to their chelating structures, these ligands include DO3A derivatives (L_1 , L_2 , L_3), one DOTA derivative (L_4), and a MAMA derivative (L_5). Indeed, DO3A and DOTA derivatives are well known to form very stable complexes with lanthanide (Ln^{3+}) and other trivalent metal ions (M^{3+}), while MAMA derivatives are commonly used for complexation of the reduction products of $^{99m}TcO_4^-$ in Nuclear Medicine for application in SPECT brain imaging (**Scheme 1**).

SUMMARY



Scheme 1

The Gd³⁺-complexes have been evaluated with respect to their potential use as contrast agents in T₁-weighted MRI (Chapter 4). This included the assessment of their logP_{oct/water} coefficient (logP_{oct/water} = -0.15-0.32), their critical micellar concentration (cmc) by relaxometry, as well as their relaxometric properties in the absence and in the presence of Aβ₁₋₄₀ and Human Serum Albumin (HSA). A combined ¹⁷O NMR and ¹H NMRD study has been carried out on GdL₃. The affinity constants characterizing HSA binding were also determined by paramagnetic relaxation enhancement (PRE) measurements (K_{A,GdL1} = 709 ± 89 M⁻¹; K_{A,GdL3} = 250 ± 18 M⁻¹). These *in vitro* studies suggest that our Gd³⁺-complexes show promising characteristics to be used as MRI contrast agents for Aβ amyloid detection in AD.

We have also investigated the *in vitro* interaction of the Ln³⁺ complexes

with A β ₁₋₄₀ in solution using different experimental techniques, such as Surface Plasmon Resonance (SPR), Saturation Transfer Difference NMR (¹H STD NMR), Circular Dichroism, Thioflavin-T fluorescence, 2D HSQC NMR, Dynamic Light Scattering and TEM images (Chapter 5). The neutral Ln³⁺ complexes of the two DO3A-PiB derivatives, L₁ and L₃, interact with aggregated A β ₁₋₄₀ in aqueous solution. A modification of the L₁ ligand by introduction of an aliphatic C₅ chain spacer between the chelating DO3A macrocycle and the targeting PiB moiety changes the strength of the interaction (as measured by the dissociation constants, K_D), as well as the stability of the aggregated structures. We also found that the most hydrophobic monomer, GdL₃, stabilizes the α -helical peptide structure and has the better protective effect against peptide aggregation.

Our results also suggest that LaL₃ and probably LaL₁ will not interact with monomeric A β at normal, physiologically relevant concentrations of the peptide. This is important since it preserves the bacteriostatic effect of A β ₁₋₄₀ in the brain at low (μ M) concentrations, which is therefore not diminished by a possible interference with our probes. The absence of interaction also reduces the non-specific background, thus enhancing the signal contrast when these MRI probes bind to A β ₁₋₄₀ amyloid fibrils and plaques.

To conclude the work, we have studied the capability of our neutral complexes to bind amyloid deposits *ex vivo* and *in vivo* (Chapter 6). *Ex vivo* studies with *post-mortem* AD human brain slices confirm the selective binding of our EuL₁ complexes to human A β amyloid deposits. The *in vivo* biodistribution studies of the SPECT tracer formed by L₁ and the radioactive γ -emitter Indium³⁺ (¹¹¹InL₁) in normal Swiss mice show that it is able to permeate the Blood Brain Barrier to a small extent (0.36 and 0.11 %ID/g of the ¹¹¹InL₁ complex at 2 and 30 min post injection, respectively).

In this thesis, we have covered the entire process of imaging probe development, including the chemical synthesis and physico-chemical evaluation of the probes, the investigation of their interaction with amyloid peptides, *ex vivo* studies on AD Human brain slices and transgenic mice (APP^{swe}/PS1/dE9 mutation), as well as *in vivo* SPECT studies using ¹¹¹In labeled complexes in normal mice.

“ Sondes d'imagerie multimodales pour le diagnostic de la maladie d'Alzheimer ”

RESUME

La maladie d'Alzheimer (MA) est une maladie neurodégénérative chronique qui conduit à un déclin progressif des fonctions cognitives et qui s'accompagne habituellement de pertes de mémoire et d'un dysfonctionnement des fonctions coordinatrices. Il survient ensuite une altération du jugement, de l'expression orale et une désorientation spatiale. Cette maladie est caractérisée par la formation de plaques amyloïdes et n'est diagnostiquée le plus souvent qu'à un stade avancé, suite à des tests comportementaux.

Le développement de nouvelles sondes d'imagerie capables de visualiser ces plaques amyloïdes pourrait permettre d'améliorer le diagnostic de la maladie en le rendant beaucoup plus précoce. Ceci pourrait aboutir à: 1) ralentir de manière significative la progression de la maladie, même si aucun traitement curatif n'est encore disponible à ce jour 2) la formulation de nouvelles thérapies.

Dans cette thèse, nous avons conçu, synthétisé et étudié des nouvelles sondes d'imagerie multimodales à base de complexes métalliques pour la détection des plaques amyloïdes.

Nous avons utilisé une approche modulaire pour créer ces sondes où une unité de ciblage (PiB), capable de reconnaître sélectivement les plaques amyloïdes, est liée à un chélateur métallique (DO3A, DOTA, MAMA) qui agit comme un rapporteur d'imagerie. Le principal avantage de cette approche est qu'elle permet l'utilisation d'un grand nombre d'ions métalliques comme sondes d'imagerie pour une large variété de modalités. Par un simple choix du métal approprié dans la sonde d'imagerie, nous pouvons créer une plateforme d'agents de diagnostic pour diverses applications en utilisant le même ligand: par exemple, Gd^{3+} pour l'Imagerie de Résonance Magnétique (IRM), $^{111}In^{3+}$ ou $^{67}Ga^{3+}$ pour la Tomographie d'Emission Monophotonique (TEMP) et $^{68}Ga^{3+}$ pour la détection Tomographie par Emission de Positons (TEP).

RESUME

Nous avons synthétisé des dérivées de DO3A (L_1 , L_2 , L_3), un dérivé de DOTA (L_4), et un dérivé de MAMA (L_5). En effet, les dérivées de DO3A et les dérivés DOTA sont bien connus pour former des complexes très stables avec des lanthanides (Ln^{3+}) et d'autres ions métalliques trivalents (M^{3+}), tandis que les dérivés MAMA sont couramment utilisés pour la complexation de ^{99m}Tc en médecine nucléaire pour les applications en imagerie cérébrale par TEMP (schéma 1).

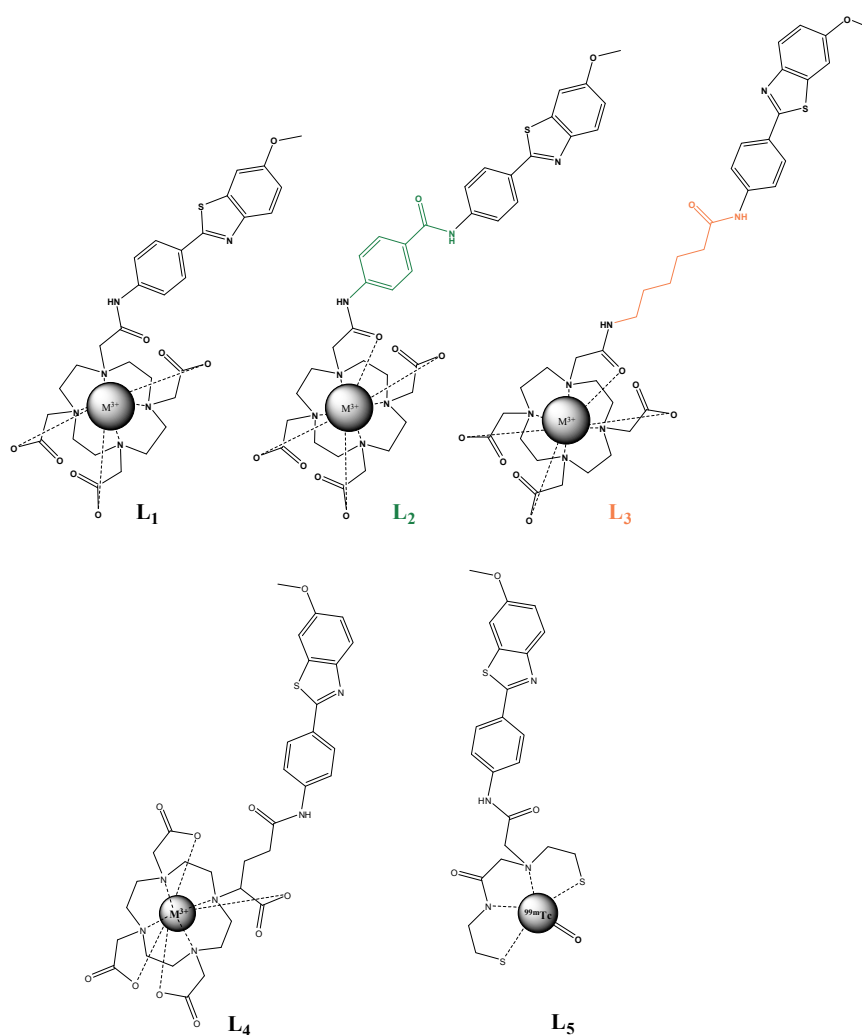


Schéma 1

Les complexes de Gd^{3+} des ligands L_1 , L_2 , L_3 ont été étudiés en vue d'une potentielle utilisation comme agents de contraste en IRM pondérée en T_1 (Chapitre 4). Cela comprend la détermination de leur coefficient de partage $\log P_{\text{oct/eau}}$, leur concentration micellaire critique (cmc) par relaxométrie, ainsi que

leurs propriétés relaxométriques en présence et en l'absence du peptide A β 1-40 humain et de l'albumine du sérum humain (ASH). Les études d' ^{17}O par Résonance Magnétique Nucléaire (RMN) et de Résonance Magnétique Nucléaire par Dispersion (RMND) ont été réalisées avec le complexe GdL $_3$. Les constantes d'affinité de certains complexes de Gd $^{3+}$ avec la ASH ont également été déterminées par des mesures d'augmentation de résonance paramagnétique (ARP) (K_A , GdL $_1$ = $709 \pm 89 \text{ M}^{-1}$; K_A , GdL $_3$ = $250 \pm 18 \text{ M}^{-1}$). Ces études *in vitro* suggèrent que nos complexes de Gd $^{3+}$ présentent des caractéristiques prometteuses pour être utilisés comme agents de contraste IRM pour la détection de l'A β amyloïde dans la MA.

Nous avons également étudié l'interaction *in vitro* des complexes des Ln $^{3+}$ avec A β $_{1-40}$ en solution en utilisant différentes techniques expérimentales comme la Résonance Plasmatique de Surface (RPS), la Différence de Transfert de Saturation par RMN ^1H (DTS RMN), le dichroïsme circulaire, la fluorescence de la thioflavine T, 2D HSQC RMN, la diffusion dynamique de la lumière (DDL) et le Microscopie Electronique à Transmission (MET) (chapitre 5). Les complexes des Ln $^{3+}$ neutres avec les ligands L $_1$ et L $_3$, interagissent avec le peptide A β $_{1-40}$ agrégé en solution aqueuse. Une modification du ligand L $_1$ par l'introduction d'une chaîne aliphatique C $_5$ entre le chélatant (un macrocycle DO3A) et la cible PiB, modifie la force de l'interaction (mesurée par les constantes de dissociation, K_D), ainsi que la stabilité des structures agrégées. Nous avons également constaté que le monomère plus hydrophobe, GdL $_3$, stabilise la structure du peptide en hélice alpha et possède le meilleur effet protecteur contre l'agrégation des peptides.

Nos résultats suggèrent également que le complexe LaL $_3$ et probablement le complexe LaL $_1$ n'interagissent pas avec le peptide A β monomérique à des concentrations physiologiquement pertinentes du peptide. Ceci est important car il préserve l'effet bactériostatique à de faibles concentrations (μM) du peptide A β $_{1-40}$ dans le cerveau, qui n'est donc pas diminuée par une possible interférence avec nos sondes. L'absence d'interaction réduit également le bruit de fond non spécifique, améliorant ainsi le contraste du signal lorsque ces sondes IRM détectent des fibrilles et des plaques amyloïdes.

Pour conclure ce travail, nous avons étudié la capacité de nos complexes neutres de détecter les dépôts amyloïdes *ex vivo* et *in vivo* (chapitre 6). Les études

RESUME

ex vivo avec des tranches de cerveau humain portant la MA, *post-mortem*, confirme la liaison sélective du complexe EuL_1 aux dépôts $\text{A}\beta$ amyloïdes humains. Les études de biodistribution in vivo par TEMP avec le traceur formé par L_1 et l'émetteur γ radioactive Indium³⁺ ($^{111}\text{InL}_1$) ont été réalisées avec des souris suisses saines. Ils montrent que le complexe $^{111}\text{InL}_1$ est capable de traverser, bien que faiblement, la barrière hémato-encéphalique (0,36 et 0,11% ID / g à 2 et 30min après injection, respectivement).

Dans cette thèse, nous avons exploré l'ensemble du processus de développement d'une sonde d'imagerie : la synthèse chimique et l'évaluation physico-chimique des ces sondes, leur interaction avec des peptides amyloïdes, des études ex vivo sur des tranches de cerveau humain et de souris transgéniques (APP^{swe} / PS1/dE9 mutation) porteurs de la MA, ainsi que les études in vivo à l'aide de l'imagerie TEMP avec des complexes marqués à ^{111}In et chez la souris saines.

“Sondas de imagem multimodal para o Diagnóstico da Doença de Alzheimer”

RESUMO

A doença de Alzheimer (DA) é uma doença neurodegenerativa crónica que conduz a uma diminuição progressiva de funções cognitivas e é geralmente acompanhada pela perda de memória e disfunção na coordenação de movimentos. Em seguida, ocorre um desequilíbrio na tomada de decisões, na comunicação oral e uma desorientação espacial. Esta doença é caracterizada pela formação de placas amiloides e é frequentemente diagnosticada numa fase já bastante tardia, após uma avaliação por testes comportamentais. O desenvolvimento de novas sondas capazes de visualizar estas placas amiloides pode melhorar o diagnóstico da doença, podendo detecta-la em fases bastante precoces do seu desenvolvimento. Isto poderá levar a: 1) uma redução significativa da progressão da doença, mesmo que a cura ainda não seja possível 2) um melhor desenvolvimento de novas terapias.

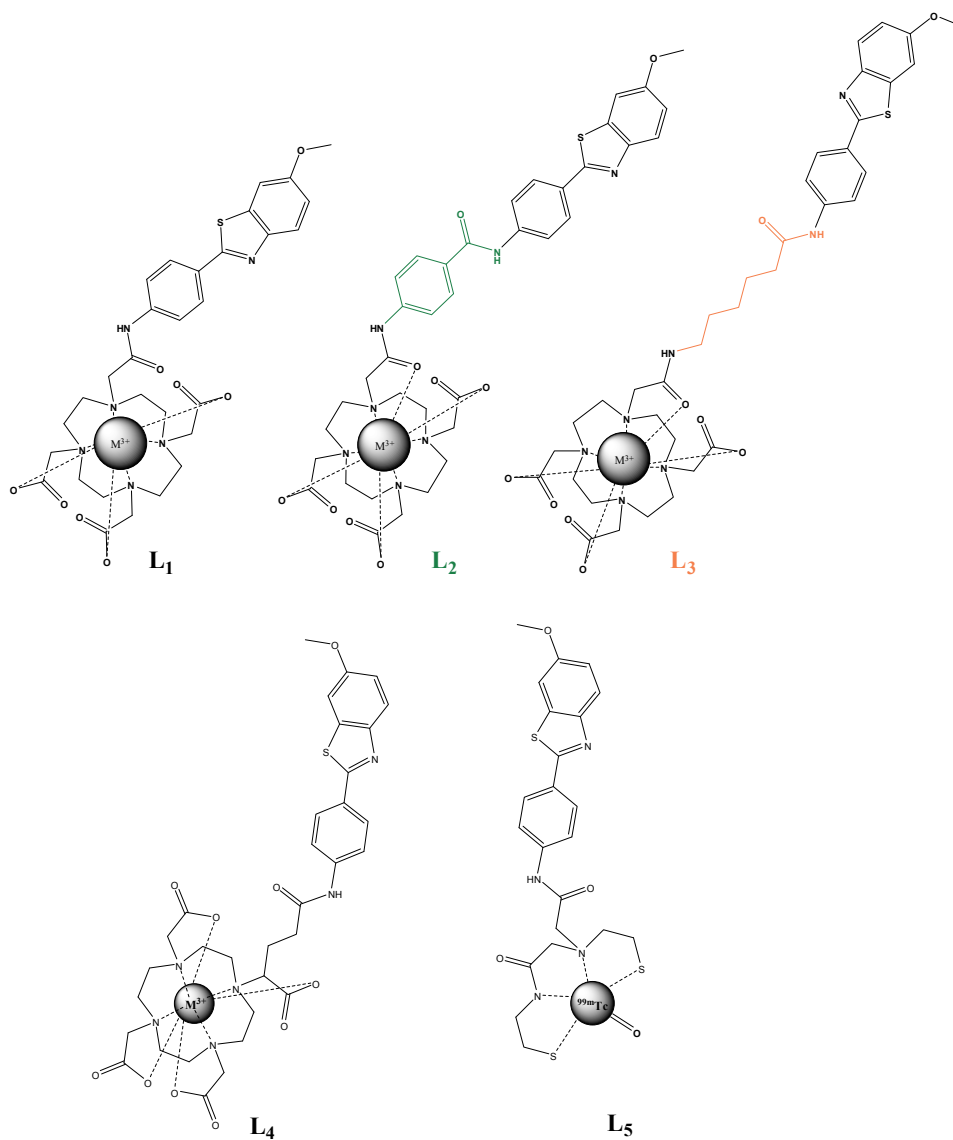
Nesta tese, desenvolvemos algumas estratégias para a síntese química de novas sondas de imagens multimodais e estudamos as propriedades físico-químicas dos seus complexos metálicos de coordenação para a detecção de placas amiloides.

Usamos uma abordagem modular de síntese, onde a unidade de reconhecimento alvo (o PiB), capaz de reconhecer seletivamente as placas amiloides, vai estar ligada a um quelante de metais (DO3A, DOTA, MAMA) funcionando como um repórter de imagem. A principal vantagem desta abordagem é que ela permite a utilização de um vasto número de iões metálicos que podem ser explorados em várias modalidades. Escolhendo o metal apropriado na sonda de imagem, podemos utiliza-la depois em várias aplicações, usando o mesmo ligando, como por exemplo, o Gd^{3+} para Imagem Ressonância Magnética (IRM), ou $^{111}In^{3+}$ e $^{67}Ga^{3+}$ para Tomografia Computadorizada por Emissão de Fóton Simples (TCEFS) e $^{68}Ga^{3+}$ para a detecção por Tomografia por Emissão de Positrões

RESUMO

(TEP).

Sintetizamos portanto vários derivados de DO3A (L_1 , L_2 , L_3), um derivado de DOTA (L_4), e um derivado de MAMA (L_5). Os derivados de DO3A e DOTA são bem conhecidos por formar complexos muito estáveis com vários lantanídeos (Ln^{3+}) e outros íons metálicos trivalentes (M^{3+}). Os derivados MAMA são comumente usados para a complexação do ^{99m}Tc em medicina nuclear para o cérebro com o TCEFS (Esquema 1).



Esquema 1

Os complexos de Gd^{3+} foram estudados em relação ao seu uso potencial como agentes de contraste em IRM com ponderação em T1 (Capítulo 4). A este estudo foi incluída também a avaliação do seu coeficiente de partição ($\log P_{\text{oct/água}}$), a sua concentração micelar crítica (CMC), por relaxometria, bem como as suas propriedades relaxométricas na ausência e na presença de péptidos $A\beta_{1-40}$ e albumina do soro humano (ASH). Os estudos de RMN de ^{17}O e 1H RMND foram realizados para o complexo GdL_3 . As constantes de afinidade com a ASH foram determinadas através de medidas de aumento da relaxação paramagnética (ARP) ($K_A, GdL_1 = 709 \pm 89 M^{-1}$; $K_A, GdL_3 = 250 \pm 18 M^{-1}$), estes estudos *in vitro* sugerem que os complexos Gd^{3+} apresentam características promissoras para serem usadas como agentes de contraste em IRM para a detecção da β -amiloide na DA.

Investigamos também a interação *in vitro* dos complexos Ln^{3+} com os $A\beta_{1-40}$ em solução aquosa utilizando diferentes técnicas experimentais, tais como ressonância plasmática de superfície (RPS), Diferença de Transferência de Saturação por RMN (1H DTS-RMN), dicroísmo circular, fluorescência da tioflavina T, 2D HSQC RMN, difusão dinâmica da luz (DDL) e imagens de Microscopia Electrónica de Transmissão (MET) (Capítulo 5). Os complexos neutros de Ln^{3+} dos dois derivados de DO3A-PIB, L_1 e L_3 , interagem com os $A\beta_{1-40}$ em solução aquosa na sua forma agregada. Uma simples modificação do ligando L_1 pela introdução de uma cadeia hidrocarbonada C_5 que funciona como espaçador entre o quelante macrocíclico DO3A e a unidade de reconhecimento alvo PiB, consegue alterar a força de interação (medida pelas constantes de dissociação, K_D), bem como a estabilidade das estruturas agregadas de $A\beta_{1-40}$. Descobrimos também que o complexo mais hidrofóbico, GdL_3 , estabiliza a estrutura do peptídeo em hélice α e tem um efeito protetor contra a agregação dos péptidos.

Os nossos resultados sugerem também que LaL_3 e provavelmente LaL_1 não interagem com a forma monomérica dos péptidos $A\beta$ em concentrações fisiologicamente relevantes do péptido. Isto é importante uma vez que se preserva o efeito bacteriostático que os $A\beta_{1-40}$ têm no cérebro a baixas concentrações (μM), que não é, por conseguinte, diminuído devido a uma possível interferência com as nossas sondas. A ausência de interação reduz também o ruído de fundo não

RESUMO

específico, aumentando assim o contraste do sinal de ressonância magnética quando estas sondas se ligam às fibrilas de $A\beta_{1-40}$ e às placas amiloides.

Para concluir, estudamos ainda a capacidade de nossos complexos neutros para detectar os depósitos amiloides *ex vivo* e *in vivo* (Capítulo 6). Os estudos *ex vivo* foram efectuados com fatias de cérebro humano *post-mortem* de pacientes com DA para confirmar a ligação seletiva dos nossos complexos EuL_1 aos depósitos de amiloides $A\beta$ humanos. Os estudos de biodistribuição *in vivo* por TCEFS foram realizados com os complexos formados por L_1 e o emissor γ radioativo de Indium³⁺ ($^{111}\text{In}L_1$) em ratinhos suíços normais e mostraram que o complexo $^{111}\text{In}L_1$ é capaz de penetrar a barreira hematoencefálica ainda que fracamente (0,36 e 0,11% ID/g com o complexo $^{111}\text{In}L_1$ a 2 e 30 min após a injeção, respectivamente).

Nesta tese, exploramos todo o processo de desenvolvimento de sondas imagiológicas, incluindo a síntese química e avaliação físico-química das sondas, a investigação da sua interação com peptídeos amilóides $A\beta_{1-40}$, estudos *ex vivo* em fatias de cérebro de humanos de pacientes com doença de Alzheimer e ratinhos transgênicos (mutação APP^{swe} / PS1/dE9), e ainda os estudos *in vivo*, usando os complexos marcados com $^{111}\text{In}^{3+}$ para TCEFS em ratinhos normais.

CHAPTER 1

*“Introduction to
Neuroimaging,
Contrast Agents and
Alzheimer’s Disease”*

1.1. Introduction to Medical Imaging

Medical imaging is defined as the set of processes and techniques used to image the human body for clinical purposes or medical science. Although imaging of removed organs and tissues can be performed for medical reasons, such procedures are not usually referred to as medical imaging, but rather are a part of pathology.

Medical sciences have undergone a huge progress in the last few decades and most of the advances are due to the developments in biomedical engineering and new imaging technologies. For a long time, medical examination of human organs and tissues was not easily accessible and in most of the cases it was very invasive due to the traditional protocols used. The introduction of modern imaging technologies has created a new paradigm for clinicians to examine the human body by combining information from anatomy, physiology, cellular/tissue morphology, molecular events, etc.¹

In the last decade, medical imaging has become possible at the level of molecular events and gave rise to a new field known as Molecular Imaging, which involves non-invasive *in vivo* assessment of biological events at the cellular and molecular level, either in normal or in pathological situations.

The advances in Molecular Imaging prompted the elaboration of new chemical strategies to create new drugs, called molecular imaging probes, able to visualize biological events at the molecular level. Drug design is the research field responsible for the development of new compounds capable of earlier detection of abnormal events and preventing and treating diseases. In molecular imaging, the cooperation of many different disciplines such as chemistry, physics, biology, medicine and computer sciences is required, making this field one of most multidisciplinary ones.

Many novel imaging systems and applications have been discovered lately. This is nicely reflected in the drastic increase of review publications in the field and the constant introduction of new enigmas to explore. In the field of probe design, the major goal is the optimization of the inherent imaging probe properties

regarding the technique used. The understanding of all the limitations is a key step in the discovery of highly optimized systems.

Recently, the combination of more than one biomedical imaging modalities, to acquire the maximum information, by using a single imaging probe, opened new avenues. This requires the development of novel multimodal probes that can be used in different imaging techniques at the same time.

In this introductory chapter, we present a short overview of the different techniques used in neuroimaging and we introduce the main concepts and the strategies reported in the literature to design multimodal imaging probes for early diagnostics of Alzheimer's disease.

1.2. Neuroimaging techniques

1.2.1. PET and SPECT

In the field of nuclear imaging, most praise must be given to Henri Becquerel and Marie Curie for the discovery of natural radionuclides, largely used later in nuclear medicine.^{2,3}

Nuclear medicine appeared almost 50 years after the first discoveries on radionuclides, but it was soon implemented as one of the most successful diagnostic approaches. In 1946, when radioactive iodine (I-131) was first injected for the treatment of thyroid cancer, a whole new era has begun.

PET (Positron Emission Tomography) and SPECT (Single Photon Emission Computerized Tomography) are non-invasive nuclear imaging techniques used to obtain 3D image reconstructions from the body distributions of injected radiopharmaceuticals. Since these techniques are very sensitive, small doses of radiopharmaceuticals are injected to obtain accurate imaging probe distributions.⁴⁻⁶

The differences between these techniques relate to their physical properties resulting in different sensitivity, spatial resolution, examination time and specificity.

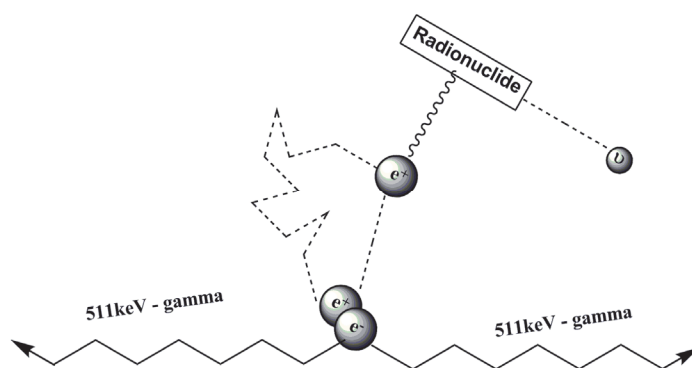


Figure 1.1. Schematic representation of positron emission by a radionuclide and subsequent annihilation with two-photon emission.

PET imaging implies the use of a short-living positron-emitting radionuclide. Initially, a proton decays to a neutron in the nucleus resulting in the emission of a positron and a neutrino (β^+ decay). The positron collides with an electron in its path and they mutually annihilate. This phenomenon produces two opposite gamma photons with energies of 511 keV, being emitted at almost 180 degrees to each other.⁷ Hence, it is possible to localize with detectors their source along a straight line of coincidence (also called the line of response, or LOR). As represented in **Figure 1.1**, the positron range and the photon non-collinearity are the limiting factors for the spatial resolution of the images obtained. Another limiting factor of the technique relates to the short half-life of the radionuclides that requires expeditious radiochemistry to produce the radiolabelled molecules. Nevertheless, the introduction of new synthetic strategies, such as click-chemistry, simple methylations or other nucleophilic/electrophilic additions, opened a new range of applications for PET in nuclear medicine^{8–11}

SPECT is a nuclear medicine tomographic imaging technique that detects single gamma ray photons. The gamma decay observed by SPECT is of lower energy photons (93-363 keV). Like gamma cameras, it detects first the single photons for a 2D reconstruction and then, to get the 3D SPECT images, a rotation around the patient of the gamma camera is combined with computational methodologies. The projections obtained from the various angles are then reconstructed giving rise to a SPECT image of the body (Figure 1.2).

The limitations of SPECT are more related to the technical instrumentation used than to the inherent physical properties.¹² The radiochemistry implied for

SPECT is less laborious and the radiolabels produced have longer half-life times (several hours and days), enabling the imaging of several important biological processes and kinetic studies *in vivo* (**Table 1**).^{13,14}

PET and SPECT are nowadays largely used for brain imaging. For instance, in SPECT several compounds labelled with ^{99m}Tc and ¹²³I showed good brain imaging: ^{99m}Tc-HMPAO or ^{99m}Tc-ECD, both with good access to the brain and to metabolic brain pathways; ¹²³I-IMPY and ¹²³I-BZM, brain receptor agonists and Alzheimer's disease labels.¹⁵⁻¹⁹ Being PET one of the most sensitive techniques for imaging small amounts of radiotracers *in vivo*, it is not surprising that the use of this technique for neuroimaging purposes evolved impressively in the last decade, with the contribution of several radiotracers,

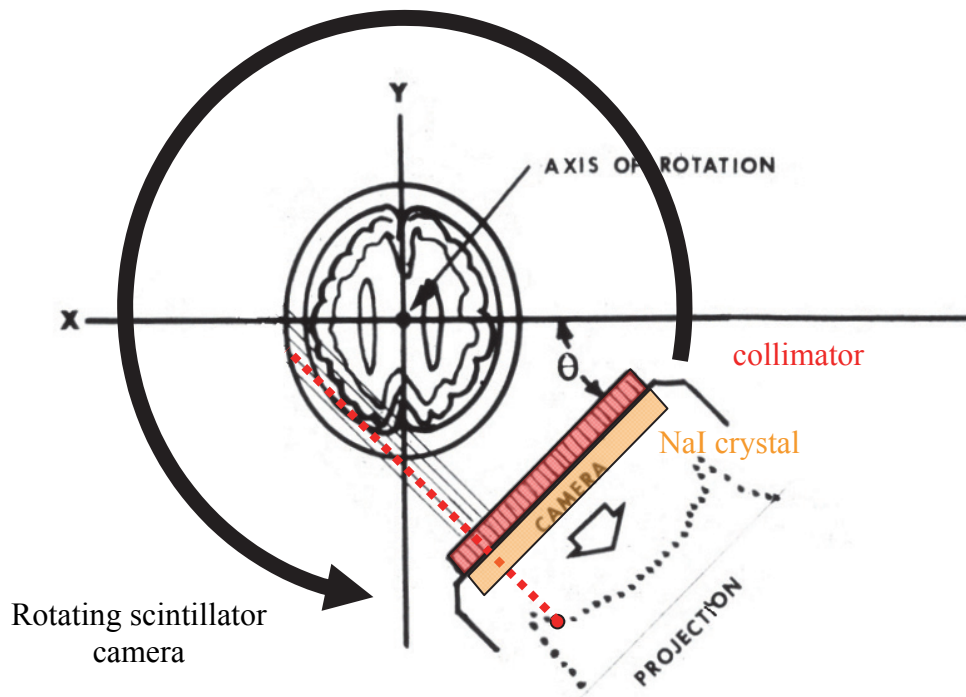


Figure 1.2. Schematic representation of SPECT imaging.

Table 1.1. Most common PET and SPECT radionuclides^{20,21}

PET									
Nucleus	¹¹ C	¹³ N	⁶⁸ Ga	⁶⁴ Cu	¹⁵ O	¹⁸ F	⁸² Rb	¹⁵² Tb	¹⁶⁶ Ho
hν/keV	511	511	511	511	511	511	511	511	511
T _{1/2}	20min	10min	68min	13h	122sec	110min	76sec	18h	27h

SPECT									
Nucleus	^{99m} Tc	¹²³ I	⁶⁷ Cu	⁶⁷ Ga	¹¹¹ In	¹⁵⁹ Gd	¹⁶⁶ Ho	¹⁷⁷ Lu	¹⁵³ Sm
hν/keV	140	159	185	93	245	363	80	208	103
T _{1/2}	6h	13h	3d	78h	3d	20h	26h	7d	47h

such as fluorodeoxyglucose (¹⁸F-FDG) for general brain metabolic activity²², and ¹¹C-specific radioligands for brain tumours,²³ Alzheimer's²⁴, Parkinson's²⁵ disease, etc.

1.2.2. Magnetoencephalography

Magnetoencephalography (MEG) is an imaging technique used to measure the magnetic fields produced by electrical activity in the brain via extremely sensitive devices. MEG measures the neural electrical activity with very high temporal resolution but relatively low spatial resolution. Neurons vary in size and shape that are intricately connected to each other. Functionally, these neurons form transient coherent networks using chemical and electrical synapses and producing changes in local electrical and chemical properties. It is possible to detect, with sensors outside the head, changes relating to either electrical activity (instantaneous reflections of neural events) or changes in metabolic consumption of nutrients and oxygen (caused by neuronal demand and mediated by blood supply). The advantage of measuring the magnetic fields produced by neural activity is that they are likely to be less distorted by surrounding tissue

(particularly the skull and scalp) compared to the electric fields measured by electroencephalography (EEG).²⁶

There are many uses for MEG, including assisting surgeons in localizing pathology, assisting researchers in determining the function of various parts of the brain, neurofeedback, and others.

1.2.3. Computed Axial Tomography

Computed tomography (CT) or Computed Axial Tomography (CAT) scanning uses a series of X-rays of the head taken from many different directions. Typically used for quickly viewing brain injuries, CT scanning uses a computer program that performs a numerical integral calculation (the inverse Radon transform) on the measured X-ray series to estimate how much of an X-ray beam is absorbed in a small volume of the brain. Typically the information is presented as cross sections of the brain.²⁷

1.2.4. Magnetic Resonance Imaging

Nuclear Magnetic Resonance (NMR) was discovered by physicists and quickly spread its influence to many scientific areas. In almost 60 years, six Nobel prizes were awarded in the field of NMR and a specific one for Magnetic Resonance Imaging (MRI) in 2003, shared by Paul Lauterbur and Peter Mansfield - Nobel Prize in Physiology or Medicine. The basic concepts that led to MRI were laid out by Bloch and Purcell in the late 1940s, by detecting the ability of some nuclei, with their nuclear spins aligned in the presence of an external magnetic field, to receive and transmit electromagnetic energy.²⁸⁻³¹ Therefore, nuclei with odd number of protons and neutrons have a magnetic moment and angular *momentum*, magnetically induced and detectable. Many different isotopes are currently used for NMR spectroscopy, such as hydrogen (¹H), fluorine (¹⁹F), sodium (²³Na), phosphorous (³¹P), carbon (¹³C), nitrogen (¹⁵N), oxygen (¹⁷O), etc. Isotopes have different abundances and sensitivities, which determine the ease of their detection. In this respect, ¹H is the most common isotope used in NMR spectroscopy.

These concepts, complemented by the use of magnetic field gradients to spatially localise the NMR signals, gave rise to the production of the first clinical MRI prototypes. From the early 1980s till today, the application of Magnetic Resonance Imaging (MRI) in radiology as a non-invasive clinical imaging technique has rapidly increased.

MRI is a very unique method to produce high resolution 2D and 3D-images of organs and soft tissues, and a non-invasive technique that does not require harmful ionizing radiation. The images obtained from a MRI scanner arise from the water protons present in the tissues that represent more than 70% of the human body weight. Since the various tissues and organs differ case by case in water compositions - fats, muscles, fibres, etc. - resolvable and accurate MR images of the body can be recorded.^{32,33}

External magnetic fields produced by the magnets in MRI scanners typically vary in the 1.5-11.7 T (Tesla) range, these values corresponding to the ^1H Larmor frequencies of 60-500 MHz. The maximum magnetic field presently allowed for human use is 9.4 T. Besides that, magnetic coils are used along different axes in order to generate gradients employed for slice selection and phase and frequency encoding. With frequency encoding, magnetic field gradients are aligned on the homogeneous magnetic field. As a result, protons positioned in different locations have different chemical shifts. The total information gathered is translated into 2D and 3D images.³⁴

Magnetic Resonance Imaging provides 3D images of different ^1H resonance intensities of the water localized in different parts of the body. Manipulation of intrinsic parameters inherent to nuclear magnetic relaxation can optimize MR images. These are the spin-lattice or longitudinal relaxation time (T_1), which determines the rate of recovery of the longitudinal magnetization (M_z) to its equilibrium value (M_0) after eg. a 90° pulse has made it zero, and the spin-spin or transverse (T_2) relaxation time, determining the rate of disappearance of the transverse magnetization (M_{xy}) created by that pulse (**Figure 1.3**).

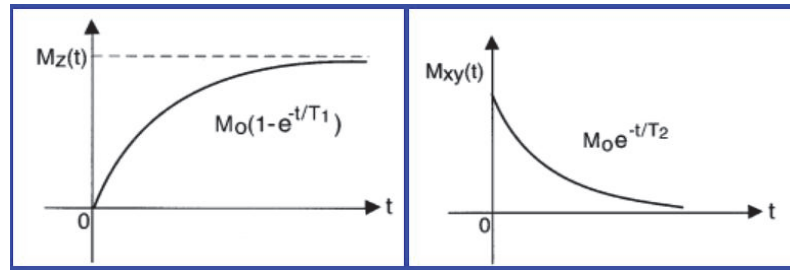


Figure 1.3. Longitudinal (T_1) and transverse relaxation curve (T_2).

The relaxation times may be used to redefine the intensity of MR images with the aid of specific pulse sequences and the settings of their specific time delays (extrinsic parameters).³⁵ T_1 - and T_2 -weighted images have been developed to produce different types of contrast in tissues. T_1 -weighted images produce a positive contrast effect and T_2 -weighted images a negative contrast (**Figure 1.4**).^{36,37}

Body tissues and organs can produce MR images without the introduction of any agent able to enhance the contrast of tissues within the body. This is because the water protons of different tissues have different T_1 and T_2 values. However, contrast media have been developed in order to record images with better contrast, needed in some clinical situations.

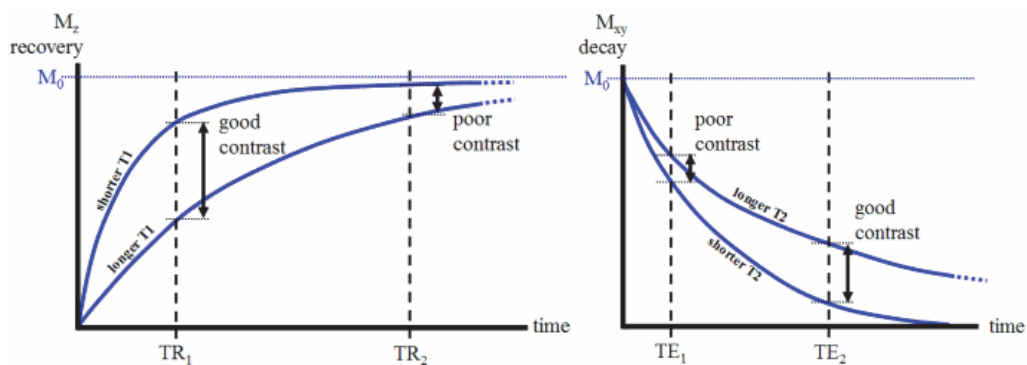


Figure 1.4. Representation of the effect in T_1 and T_2 on the time evolution of the magnetization components, M_z and M_{xy} , in a spin-echo experiment. The change in T_1 and T_2 can be due to the inherent differences of water mobility in different tissues or to the presence of contrast agents which decrease the relaxation times. The time evolution is represented by the extrinsic parameters TR (repetition time) and TE (evolution or echo time) of the pulse sequence used.

1.3.MRI Contrast Agents

MRI Contrast Agents (CA) are used to increase the contrast in MR images. This is possible because MRI CAs are paramagnetic complexes or superparamagnetic particles able to decrease the relaxation times T_1 and T_2 of tissue protons. The information perceived in anatomical MR images with contrast agents is the result of their influence in the surrounding water molecules in the organs. The surrounding water proton nuclear spins in the tissues experience the paramagnetic effect of the CAs which causes a decrease of their relaxation times.

These exogenous contrast agents affect both T_1 and T_2 . The image contrast obtained depends on the dominant effect: decreased T_1 results in positive contrast in T_1 -weighted images while decreased T_2 leads to negative contrast in T_2 -weighted images (**Figure 1.4**).

1.3.1. Positive Contrast Agents (T_1)

Positive (T_1) contrast agents are exogenous complexes containing a paramagnetic metal ion which decrease the longitudinal proton relaxation time of water protons. The gadolinium cation (Gd^{3+}) is the metal of choice for these approaches because it has a high magnetic moment ($\mu^2 = 63 \text{ BM}^2$), 7 unpaired f-electrons and long electronic spin relaxation times.^{38,39}

The Gd^{3+} metal ion is extremely toxic with very low lethal doses. The toxicity of Gd^{3+} is linked to its capability to replace Ca^{2+} and block ionic channels and enzymatic biological processes (involving eg. calmodulin, calsequestrin, calexitin).⁴⁰⁻⁴³ To suppress toxicity, Gd^{3+} must be coordinated by specific ligands, able to form thermodynamically very stable and kinetically inert complexes (**Table 2**). The stability of the Gd^{3+} complexes is a very important requirement to avoid the release of free metal ion into the body. It has been demonstrated that all the critical cases of nephrogenic systemic fibrosis (NSF), a potentially lethal disease linked to the presence of Gd^{3+} , occurred in kidney failure patients after injection of Gd^{3+} -based contrast agents which have low kinetic/thermodynamic stabilities.^{40,42,44} Thus, in safe contrast agents the transmetallation processes that

can occur in the presence of other endogenous metal ions (Zn^{2+} , Ca^{2+} , Cu^{2+} , etc.) and ligands (lactate, bicarbonate, phosphate, etc.) must be negligible.⁴⁵

The majority of the clinically approved T_1 contrast agents are gadolinium-based and formed with polyaminocarboxylate derivatives (Table 2).⁴⁶ Macrocyclic polyaminocarboxylate ligands, such as DOTA or HP-DO3A, have been shown to form Gd^{3+} complexes of high thermodynamic stability and kinetic inertness.⁴⁷ Some linear ligands, such as DTPA, were also reported to have high thermodynamic stability constants, similar to the ones measured for macrocyclic ligands. However, DTPA bis-amide derivatives have lower thermodynamic and especially kinetic stabilities (**Figure 1.5 and Table 2**).

Table 2. Thermodynamic stability constants, $\log K$, proton relaxivities and commercial names of clinical Gd-based CAs

Chemical name	Generic Name	Brand Name	r_1 ($\text{mM}^{-1}\text{s}^{-1}$)	$\log K$
GdDTPA	Gadopentetate	Magnevist	4.30^{a} ⁴⁸	22.46 ⁴⁹
GdDOTA	Gadoterate	Dotarem	4.20^{a} ⁴⁸	25.30 ⁵⁰
GdDTPA-BMA	Gadodiamide	Omniscan	4.39^{a} ⁵¹	16.85 ⁵¹
GdHP-DO3A	Gadoteridol	Prohance	3.70^{b} ⁵²	23.80 ⁵³
GdDO3A-butrol	Gadobutrol	Gadovist	3.60^{b} ⁵⁴	21.80 ⁵³
GdDTPA-BMEA	Gadoversetamide	OptiMARK	4.70^{b}	16.84 ⁵⁰

Relaxivities in water at ^a20MHz, 25°C and ^b40°C

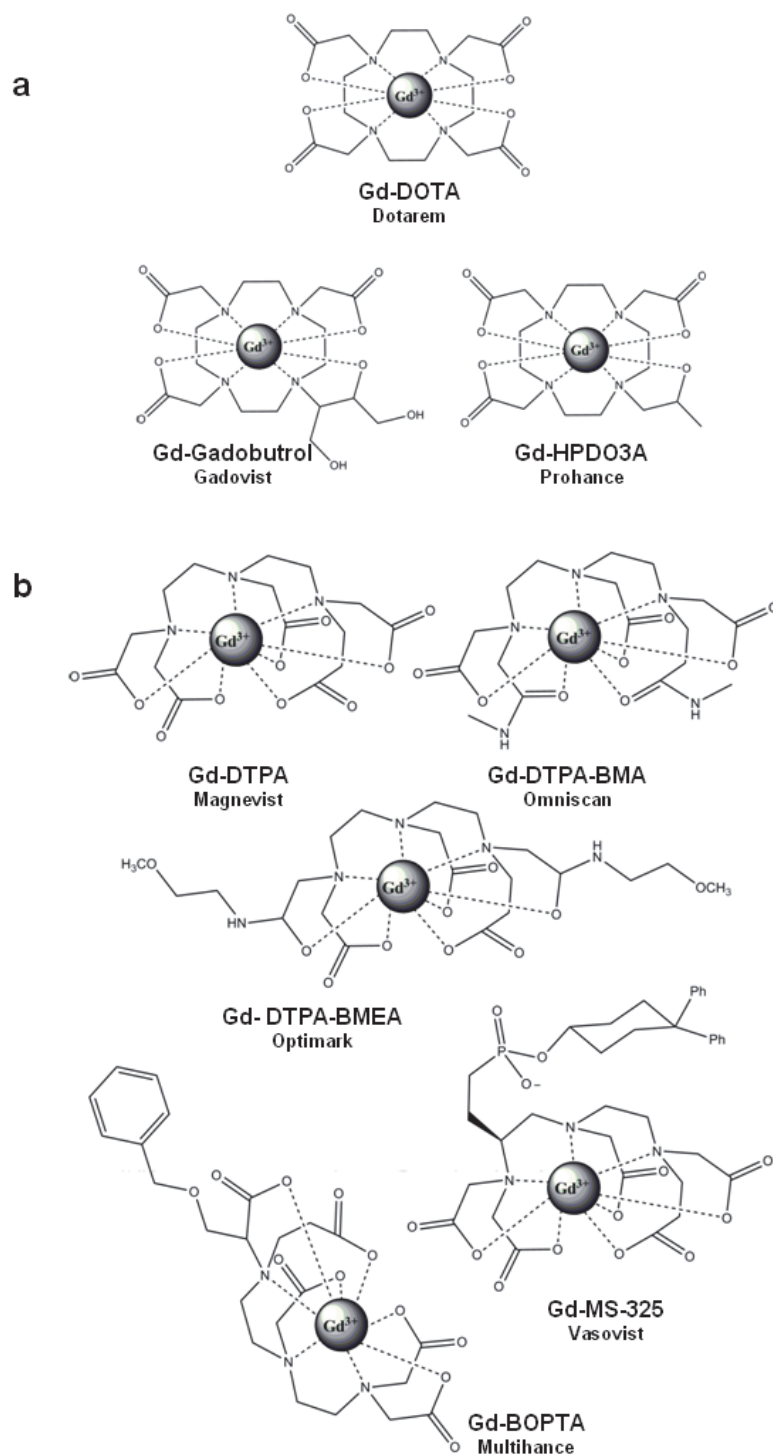


Figure 1.5. Schematic representation of commercially available and clinical Gd-based CAs: a) polyaza macrocycles, b) linear polyaminocarboxylates.

The efficiency of an MR contrast agent is defined by its relaxivity, r_1 , that is the longitudinal paramagnetic relaxation rate enhancement ($1/T_1$) observed for 1 mM of contrast media in aqueous solution. It is represented in $\text{mM}^{-1}\text{s}^{-1}$ and is dependent on the magnetic field and temperature (**Equation 2**).

$$\frac{1}{T_{1obs}} = \frac{1}{T_{1d}} + \frac{1}{T_{1p}} \quad (1)$$

$$\frac{1}{T_{1obs}} = \frac{1}{T_{1d}} + r_1[Gd] \quad (2)$$

$$r_1 = r_1^{IS} + r_1^{OS} \quad (3)$$

Here $1/T_{1obs}$ represents the observed water proton relaxation rate, $1/T_{1d}$ is the diamagnetic water proton relaxation rate contribution and $1/T_{1p}$ is the paramagnetic contribution. $1/T_{1d}$ is obtained in the same conditions as $1/T_{1obs}$ but in the absence of the paramagnetic complex (solvent contribution).

The relaxivity is composed of an inner sphere and an outer sphere term (**Equation 3**). The inner sphere term describes the relaxation effect originating from the closest hydrogen nuclei of water molecules interacting directly with the paramagnetic ion, while the outer sphere term describes the effect of the interactions between the paramagnetic ion and closely diffusing water molecules without interacting with the complex (outer sphere). In some cases, water molecules weakly interacting with the ligand might constitute a second hydration sphere, which can lead to a second sphere relaxivity term, see **Figure 1.6**). For clinical agents, approximately 60% of the relaxivity originates from inner sphere and 40% from outer sphere effects.

The inner sphere relaxivity term is linearly proportional to the hydration number (q) of the Gd^{3+} complex. All the examples shown in **Figure 1.5** are monohydrated complexes ($q = 1$), meaning that in the inner coordination sphere of the metal complex there is space for a single water molecule. Complexes with higher hydration numbers ($q = 2$ or 3), presenting high thermodynamic constants

have been also suggested as potential MRI contrast agents, such as GdHOPO derivatives or GdAAZTA.^{55,56} However, increasing the hydration number often compromises the thermodynamic stability of the complexes and makes them more vulnerable to a transmetallation or transchelation process with biogenic metal ions or anions (lactate, HCO_3^- , PO_4^{3-} , aspartate and glutamate protein residues), specially if the two water molecules are in a *cis* position in the Gd^{3+} coordination sphere.⁵⁷

In addition to the hydration number, other parameters that govern the efficiency of a given MR contrast agent can be also optimized: the Gd-H distance, r_{GdH} ; the water exchange rate, $k_{\text{ex}} = 1/\tau_{\text{M}}$, where τ_{M} is the mean lifetime of the water molecule(s) in the inner sphere of the metal ion; the rotational correlation time, τ_{R} ; the electronic spin relaxation times, T_{1e} and T_{2e} (**Figure 1.6**).

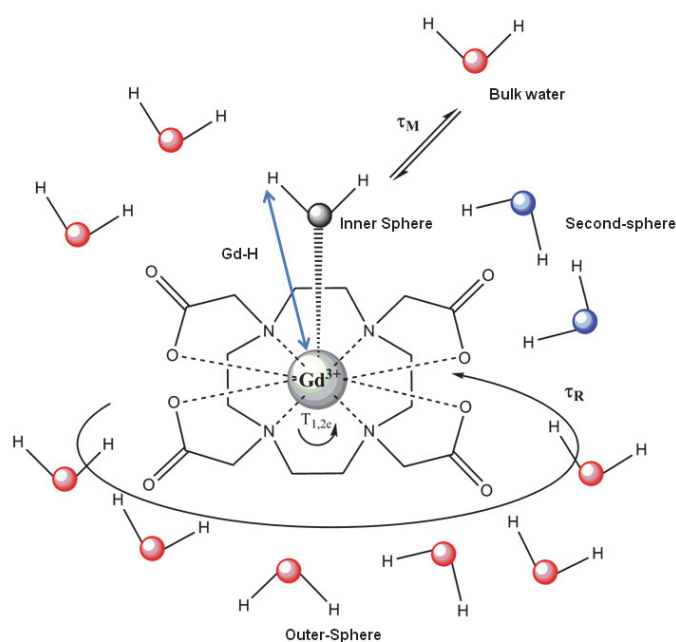


Figure 1.6. Schematic representation of a Gd^{3+} -complex (GdDOTA) with one coordinated water molecule (*inner-sphere* water, its oxygen is in black) in solution (*bulk water*, oxygens are in red). *Second-sphere* water molecules (water oxygens in blue) are close to the carboxylate groups with their hydrogens oriented towards the carboxylate oxygens. The parameters that govern the relaxivity are also represented.

The inner sphere term is represented as in **Equation 4**, where c is the molal concentration of the contrast agent, q is the number of bound water molecules per paramagnetic ion, τ_M is the mean lifetime of water molecules in the inner sphere, and $1/T_{1m}$ is the longitudinal proton relaxation rate in the bound state. $1/T_{1m}$ comprises a dipole-dipole term and a scalar term (**Equation 5**). The scalar term is negligible for Gd^{3+} complexes, $1/T_{1m}$ is essentially determined by the dipole-dipole mechanism.

The dipole-dipole term is modulated by reorientation of the nuclear spin vector with respect to the electron spin vector, by variations of the electron spin orientation, and by the water exchange rate. All this can be seen in **Equation 6**, where γ_I is the nuclear gyromagnetic ratio, g is the electron g - factor, μ_0 is the Bohr magneton, r_{GdH} is the proton distance to the electronic spins, S is the total spin quantum number of the paramagnetic ion, ω_S is the electron Larmor frequency, ω_I is nuclear Larmor frequency, and τ_{ci} are the correlation times of the dipolar interaction (**Equation 7**). Thus, τ_{ci} are influenced by the water exchange lifetime, τ_m , the rotational correlation time, τ_r , and the longitudinal/transverse electron spin relaxation times of the metal ion, T_{1e} and T_{2e} , respectively.

$$\frac{1}{T_1^{IS}} = \frac{cq}{55.55} \times \left(\frac{1}{(T_{1m}^H + \tau_m)} \right) \quad (4)$$

$$\frac{1}{\tau_{1m}} = \frac{1}{T_1^{DD}} + \frac{1}{T_1^{SC}} \quad (5)$$

$$\frac{1}{T_1^{DD}} = \frac{2}{15} \left(\frac{\mu_0}{4\pi} \right)^2 \frac{\hbar^2 \gamma_I^2 \gamma_S^2}{r_{GdH}^6} S(S+1) \times [3J(\omega_I; \tau_{c1}) + 7J(\omega_S; \tau_{c2})] \quad (6)$$

$$\frac{1}{\tau_{ci}} = \frac{1}{T_r} + \frac{1}{T_{ie}} + \frac{1}{\tau_m}, i = 1,2 \quad (7)$$

1.3.2. New generation, positive Contrast Agents

Targeted contrast agents may greatly improve diagnostic molecular imaging by increasing the sensitivity of the method, making it possible to visualize specific biological structures and selectively detect the target moieties.⁵⁸⁻⁶⁰ In order to overcome the limitations posed by the low sensitivity of MRI and the low target concentrations, targeting approaches and the efficacy of the agents should be simultaneously optimized in order to generate detectable MRI contrast at the targeted site.

Another class of contrast agents that will significantly affect the field of MRI involves responsive agents. A responsive agent is capable of reporting of a metabolic or physiological event by changing its relaxivity. The design of this new class of agents exploits the fundamental means by which a paramagnetic species affects the intensity of an image acquired by MRI. Examples of responsive MRI agents include: enzymatically activated contrast agents, probes sensitive to pH, temperature, radicals, oxygen partial pressure, or metal ion concentration (**Figure 1.7**). Responsive agents have a great promise of becoming potent diagnostic tools. However, in order to quantitatively relate the observed relaxivity change to the local change of a physiological parameter (e.g. pH), the local concentration of the contrast agent must be known independently, by using ratiometric methods for instance.^{61,62}

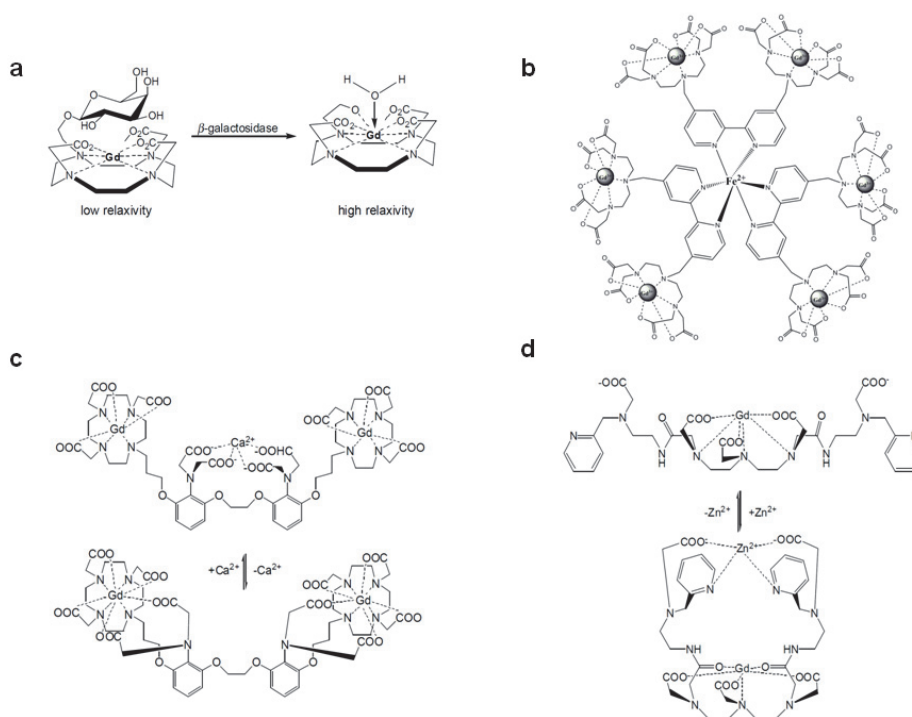


Figure 1.7. Examples of some Gd^{3+} complexes reported as responsive MRI CAs: a) enzyme responsive⁶³, b) iron responsive⁶¹, c) calcium responsive⁶⁴, d) zinc responsive⁶⁵.

1.3.3. Negative Contrast Agents

T_2 contrast agents decrease the water signal intensity by shortening the transverse relaxation times. The large magnetic susceptibility anisotropies induced by these agents are able to create local magnetic field gradients in solution, which efficiently diphas the transverse magnetization components.

Nowadays, the importance of high magnetic field MRI scanners (scientific and clinical use) is growing steadily. T_1 contrast agents become less efficient at high magnetic fields (B_0) due to the decrease of r_1 relaxivity with increasing field. On the other hand, T_2 contrast agents can be an efficient solution for high field applications since the transverse relaxivity (r_2) increases at high fields, as can be seen by the relaxation time (T_2) dependence on the square of B_0 (**Equation 8**), thus their development is growing with the technical evolution.^{66,67}

$$\frac{1}{T_2} = fq \frac{\tau_m \Delta\omega_M^2}{1 + \tau_m^2 \Delta\omega_M^2} \quad 8)$$

In **Equation 8**, f represents the complex/water concentration ratio, q is the hydration number, τ_m is the residence time of the water molecules and $\Delta\omega_M$ is the paramagnetic chemical shift of the coordinated water molecules, which is proportional to B_0 in fast chemical exchange conditions, $\tau_m \cdot \Delta\omega_M \ll 1$.

Currently, the majority of T_2 contrast agents are iron-oxide based superparamagnetic nanoparticles that can be coated with dextran, silicates or other non-immunogenic polymers. Surface coating is useful not just because it provides biocompatibility, but also because most of the coating polymers can be functionalized, allowing strategies for specific and selective targeting, multimodality and therapy applications to be explored.⁶⁸⁻⁷¹ In fact, depending on their coating and the size of iron-oxide particles, one can design SPIO (Superparamagnetic, 50-500nm), USPIO (Ultra small superparamagnetic, 4-50nm), MION (monocrystalline) and CLIO (cross-linked) nanoparticles with quite different relaxivities and biodistributions.

Recently, many novel systems, such as carbon nanotubes (iron oxide doped)⁷², zeolites (Dy^{3+} doped)⁷³ and metal-organic frameworks (MOFS) (Dy^{3+} doped)⁷⁴ have been studied as potential T_2 contrast agents, for multimodality (T_1 , T_2 , optical imaging, radioactive) techniques and for different targeting strategies (**Figure 1.8**).

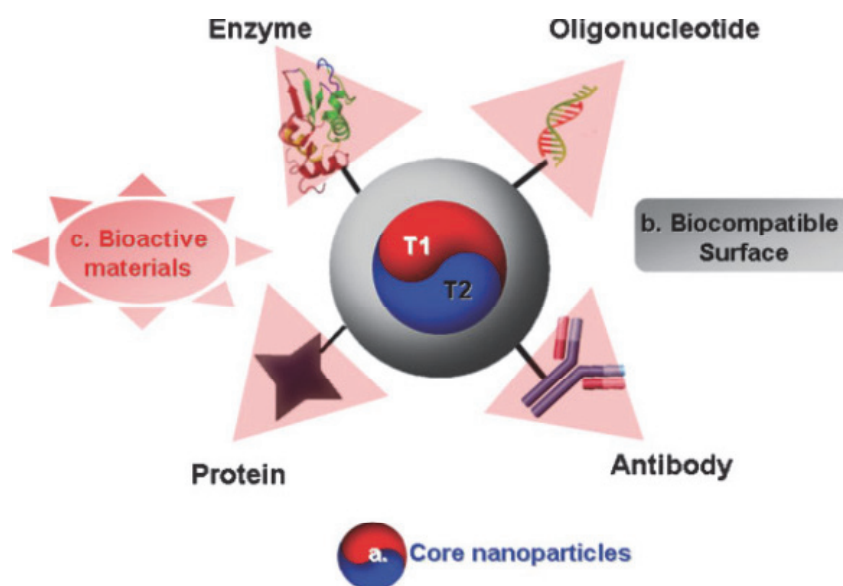


Figure 1.8. General scheme of an MRI contrast agent based on nanoparticles.⁷¹

1.4. Multimodality agents

In the recent years, multimodality imaging has emerged as a novel concept that combines simultaneously or successively two or more imaging methodologies to provide complementary information in biological studies and medical diagnostics. Magnetic Resonance Imaging (MRI) is endowed with excellent resolution, while nuclear imaging techniques offer detection of the probes with remarkable sensitivity. Optimally, in multimodal approaches the imaging probes used in the different modalities should possess identical biodistribution enabling an easy overlap of the acquired images (**Figure 1.9**).

When multimodal applications are concerned, metal-based imaging agents are particularly interesting. Indeed, metal ions may provide suitable probes for various imaging modalities (PET, SPECT, MRI, optical imaging). By the appropriate choice of a chelating agent, one can complex, with the same ligand, different metal ions that possess properties for these imaging modalities. Provided their charge is identical, these metal complexes formed with the same ligand might be expected to have similar biodistribution and are therefore interesting candidates for multimodal imaging applications. Evidently, the concentration of

the probe will have to be adapted to each imaging modality.^{75,76}

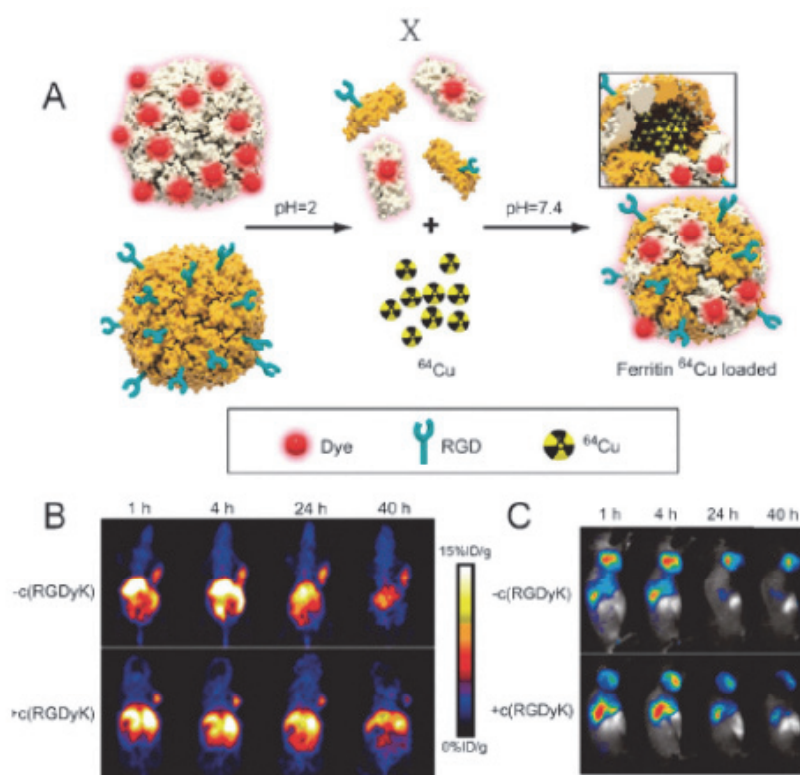


Figure 1.9. (A) Schematic representation of ferritin loaded in triplicate with (RGD peptide, dye and ^{64}Cu), resulting in ferritin nanoprobes. (B) *In vivo* PET images and (C) fluorescence images after injection of ferritin nanoprobes.⁷⁷

1.5. Imaging of Alzheimer's disease

1.5.1. Introduction to Alzheimer's disease

Alzheimer's disease (AD) is a neurodegenerative disorder that represents in the last decades the most common cause of dementia in the elderly population worldwide.⁷⁸ The latest report of the Alzheimer's Disease International (2012) states that about 30 million people are suffering from AD, and the percentage number can increase in 2040 to 90 million people due to the increasing life expectancy.⁷⁹ The incidence of AD increases with age: every five years after the age of 65 the risk of developing this devastating disease approximately doubles.⁸⁰

In addition, AD represents a major public health problem being among the most costly diseases in Europe and in the United States. The economic burden of AD is considerable. It is estimated that 36 million people worldwide are living with dementia, with numbers doubling every 20 years to 66 million by 2030, and 115 million by 2050. The worldwide costs associated (US\$604 billion in 2010) amount to more than 1% of the global GDP. If dementia care were a country, it would be the world's 18th largest economy. Alzheimer's disease is among the most significant social, health and economic crises of the 21st century.⁸¹

The first clinical manifestations of AD include memory impairment and a lack of cognitive capacities and typically, a gradual and chronic failure of memory is recognized. Other symptoms include confusion, impaired social judgment, language disturbance, agitation, withdrawal, irritability and impulsivity.

The diagnostics of AD is very subjective in the first medical approach and normally is detected from the patient history, collateral precedents from relatives, and clinical observations, based on the presence of characteristic neurological and neuropsychological disturbances. Based on cognitive tests, the diagnosis of AD becomes definitive only at later stages of the disease, when much of the brain is seriously damaged and progressive cognitive decline has occurred. The confirmation of the neuropathology is done by *post-mortem* histology and also observation of cortical atrophy, degeneration of cholinergic basal forebrain neurons, hippocampal atrophy and enlarged ventricles.^{82,83}

AD pathology is characterized by the presence of extracellular senile plaques composed of abnormal miscleaved amyloid- β ($A\beta$) peptides and intraneuronal neurofibrillary tangles caused by hyperphosphorylated tau protein and microtubules cellular dysfunction.^{84,85} Those evidences gave rise to the most scientifically accepted hypotheses: amyloid - most currently accepted – and tau. Both hypotheses consider these proteins as key players for the evolution of the disease.

The genetics seems to play also an important role, since according to twin studies, a major part of the risk for sporadic AD is genetically determined by the autosomal dominant familiar inheritance (5% of cases) and polygenic background in people having more than 65 years of age ($\geq 95\%$ of cases).^{86,87}

In addition to the genetic component, other factors affect the risk for developing AD: life style, environment, sex, traumatic injury, depression,

education, medication, etc.⁸⁸

The dominant identification of gene mutation that is implicated in biological mechanisms leading to A β accumulation and senile plaques generation is also an issue to be addressed. The amyloid precursor protein (APP) and the presenilin 1 (PSEN1) and 2 (PSEN2) genes are currently known to be implicated in the familial forms of AD (**Table 1.3**).^{88,89} In contrast with the familial AD, the causing factors of the A β accumulations and other pathological mechanisms remain mostly unclear in the sporadic form. Most A β peptides are composed of 40 (A β_{1-40}) or 42 (A β_{1-42}) amino acids, produced by proteolytic cleavage of the trans-membrane amyloid precursor protein (APP) by β - and γ - secretases. However, so far only the apolipoprotein E (ApoE) gene has been associated with the risk for AD.^{90,91}

Table 1.3. Major reported polymorphisms in AD⁹²

Gene (protein)	Chromosomal location	Mode of inheritance	N° of pathogenic mutations	Relevance to AD pathogenesis
APP (beta-amyloid precursor protein)	21q21.3	AD	31 (84)	Increase in A β (A $\beta_{1-42/40}$ ratio)
PSEN1 (presenilin1)	14q24.3	AD	175 (389)	Increase in A β (A $\beta_{1-42/40}$ ratio)
PSEN2 (presenilin2)	1q31-42	AD	14 (23)	Increase in A β (A $\beta_{1-42/40}$ ratio)
ApoE (apolipoprotein E, E4-allele)	19q13.32	Complex risk increase	n.a.	Increase in A β aggregation: lipid/cholesterol transport?

ApoE is known to be involved in lipid transport and its metabolism. Furthermore, it plays a specific role in the central nervous system, including neuronal development, regeneration and certain neurodegenerative processes. The polymorphism of the ApoE gene determines three isoforms of the ApoE protein ($\epsilon 2$, $\epsilon 3$, $\epsilon 4$) with different conformation, binding and lipid composition.^{93,94} Strong relationships were found between the number of the inherited $\epsilon 4$ alleles - ApoE $\epsilon 4$ - and the risk for developing AD and the age at onset.⁹³

Membrane cholesterol modulates the cleavage of the APP protein and in the presence of the $\epsilon 4$ isoform the balance is shifted to the production of $A\beta$.⁹⁵

The amyloid cascade hypothesis has been the predominant model of molecular mechanisms underlying the pathogenesis of AD. According to this model, the fundamental cause of AD is the accumulation and aggregation of the $A\beta$ peptide in the brain.⁸⁵ A major role for other pathogenic mechanisms includes: inflammation, oxidative stress, lipid dysfunction, signalling abnormalities and neuronal degradation (**Figure 1.10**).

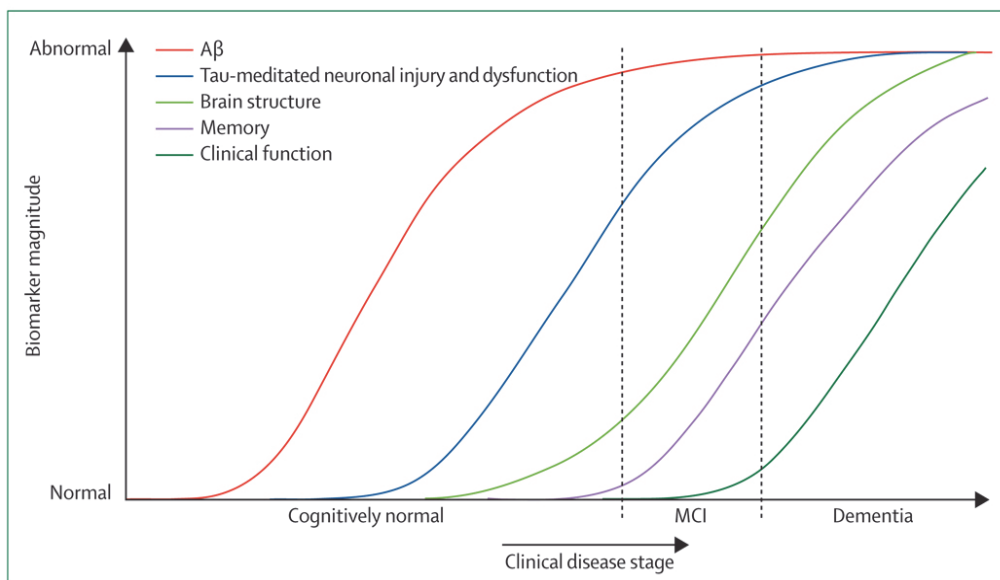


Figure 1.10. Hypothetical model of Alzheimer's disease “amyloid cascade hypothesis”.⁹⁶

1.5.2. Amyloid cascade hypothesis

It was when Alois Alzheimer first analyzed microscopically the *post-mortem* brain of a 51 year old patient, Auguste Deter, presenting strange behavioural symptoms, short-term memory loss and presence of plaques and neurofibrillary tangles (NFT) that all the scientific community started to elaborate the amyloid cascade hypothesis. This hypothesis suggests that insoluble plaques, formed due to excessive accumulation and aggregation of miscleaved A β amyloid peptides (mainly A β ₁₋₄₀ and A β ₁₋₄₂) initiate a downstream cascade that leads to AD onset: synaptic alterations, deregulation of the intracellular soluble tau protein, formation of neurofibrillary tangles and progressive neuronal loss.⁸⁵

The amyloid precursor protein (APP), a membrane-anchored receptor, is implicated in neuronal synapses and is a constituent part of neurons. The production of A β from APP is conciliated to certain protective biological functions. Normal cleaved A β is naturally degraded in cells, which have their own mechanisms.

The generation of A β peptides from ubiquitously expressed APP has been thought to have a natural biological function, as cells are known to contain enzymatic machinery necessary for the production and degradation of normal cleaved A β .⁹⁷ This non-amyloidogenic pathway is still unclear in the way that it cellular machinery acts, but it is known that the majority of the normal processes include the first approach of α -secretase cleavage of the peptide (**Figure 1.11**).

The problem persists when, at first glance, the APP is first cleaved by the β -secretase (BACE1). This proteolytic enzyme is implicated in a general physiological mechanism, regulated intramembrane proteolysis (RIP), and is a functional component of APP itself. The action of β -secretase is responsible for the release of the first amyloid ectodomain.

The remaining stub then binds to the active site of γ -secretase, which contains transmembrane domains presenilin-1 or 2. The action of γ -secretase is implicated in both non- and amyloidogenic pathways.

The cleavage by γ -secretase occurs in the transmembranar domain and results in the liberation of the amyloid β -protein (A β) and the APP intracellular domain (AICD), which possess transcriptional regulatory activity (**Figure 1.12**).⁹⁸

γ -secretase can cleave the protein at several sites after amino acids 38, 40 or 42, and therefore has the propensity to yield three different isoforms, determining the peptide's toxicity. The most common isoforms are $A\beta_{1-40}$ and $A\beta_{1-42}$, with $A\beta_{1-40}$ being the most frequently cleaved, but $A\beta_{1-42}$ is the most fibrillogenic and thus aggregates forming the amyloid plaques, related in Alzheimer's disease onset.^{84,99}

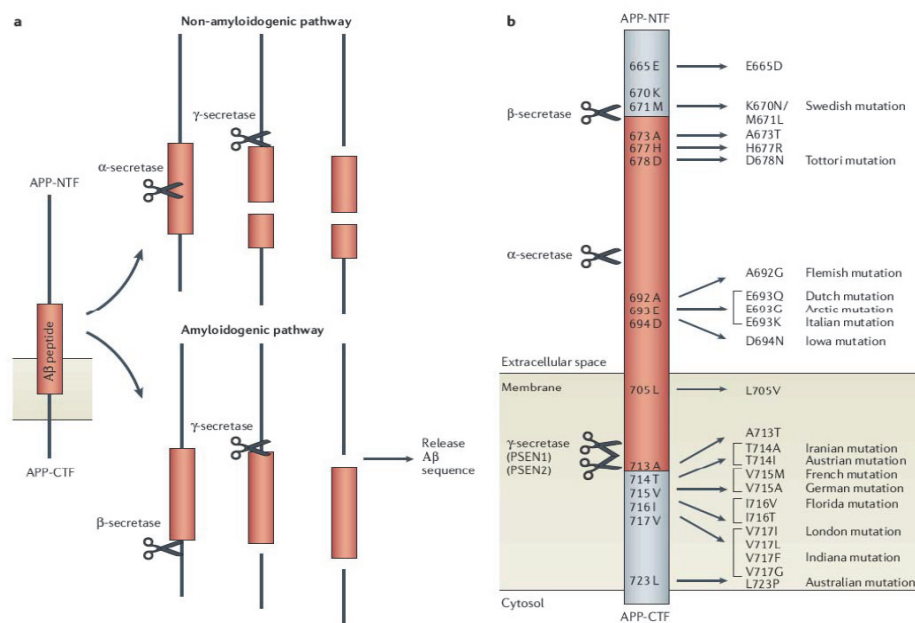


Figure 1.11. Mechanisms for the amyloidogenic pathway. a) Schematic representation of a typical non- and amyloidogenic pathway. b) Types of abnormal cleavage by secretases and typical mutations.¹⁰⁰

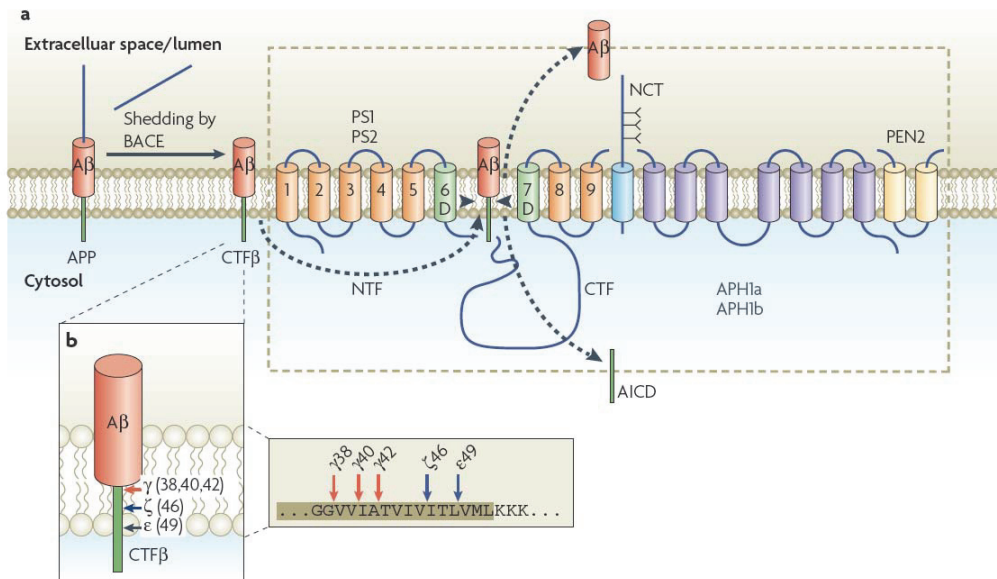


Figure 1.12. Production of amyloid- β protein from amyloid precursor protein (APP) by the amyloidogenic pathway. a) APP is cleaved by β -secretase, resulting in the secretion of the large ectodomain and the APP intracellular domain (AICD). b) γ -secretase can cleave the protein intramembranously at several sites after amino acids 38, 40 or 42.⁹⁹

1.5.3. The Blood Brain Barrier enigma

The most important factor limiting the development of new drugs for the central nervous system (CNS) is their ability to cross the blood-brain barrier (BBB). This morphological structure typically comprises four different types of cells: the endothelium, the pericyte, the astrocyte foot process and the capillary nerve ending (**Figure 1.13**). Notwithstanding, it is in the endothelial cells that the crucial effect of impermeability to certain molecules starts. The endothelium in brain capillaries is aided by tight junctions that narrow the spacing between the endothelial cells, resulting in a very selective and restrictive permeation of metabolites. Adding to that fact, there is still another intrinsic barrier for compounds able to surpass the first obstacle, the brain-to-blood efflux systems (P-glycoprotein and other multidrug resistance proteins, MRPs), enzymatic activity, plasma protein binding, and cerebral blood flow.^{101,102} It is thus very improbable that huge and hydrophilic molecules cross brain endothelial capillaries by passive diffusion.^{103,104}

The BBB is thus the structure responsible for the flow between the circulating blood to the brain extracellular fluid (BECF) and the Central Nervous System (CNS). The exchange of metabolites (and other specific molecules) and the selective mechanisms that lead to the specific restriction of large particles, hydrophilic and harmful molecules, while allowing the diffusion of certain metabolites and hydrophobic molecules (O_2 , CO_2 , water, ethanol, hormones, L-dopa, etc), is being the issue of some important studies and discussions. Electric charge, lipid solubility, and molecular weight can be used to help predict whether or not a molecule will cross the BBB.¹⁰⁴

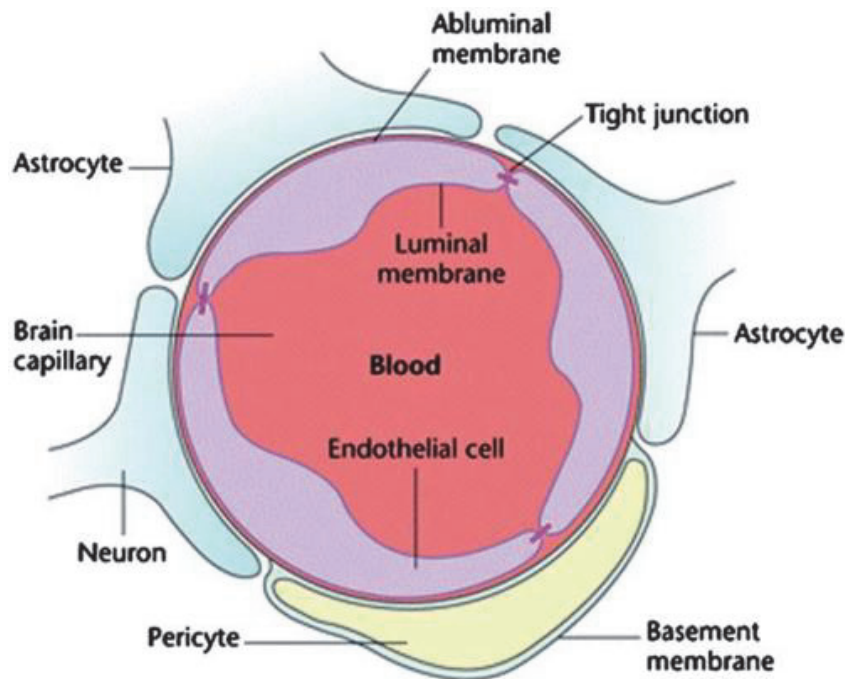


Figure 1.13. Brain microvasculature representation comprising the endothelium, the pericyte, the astrocyte foot process and the capillary nerve ending.¹⁰⁵

Brain tumors have a fenestrated BBB and diseases such as multiple sclerosis have episodes that involve temporary weakening of the BBB. Gd^{3+} -based contrast agents^{106,107} and monocrystalline (MION) particles¹⁰⁸ have been used to image these BBB breakdowns.

There are some methods used to image rat or mice brains by injecting superparamagnetic iron oxide particles directly into the brain.¹⁰⁹ Pautler et al.

reported also that Mn(II) chloride could be used to map active regions of the brain since the manganese(II) ion (biologically not harmful) participates in synaptic action potential by voltage-gated calcium channels.¹¹⁰

Disruption of the BBB can be induced by other means, using for example intra-carotid arterial infusion of hyperosmotic solutions¹¹¹, local ultrasonic irradiation^{112,113} and vasoactive compounds (mannitol)^{114,115}. However these invasive methods are not very well considered for clinical use. In this sense, the strategies required to cross the BBB, without the requirement of external disruption, imply generally the use of endogenous BBB transporters by mediated transport, and can be classified into carrier-mediated transport (CMT), active efflux transport (AET) and receptor mediated transport (RMT).¹¹⁶ Some examples can be seen in **Figure 1.14**. Whereas the CMT and AET systems are responsible for the transport of small molecules between blood and brain¹¹⁷, the RMT systems are responsible for the transport across the BBB of certain endogenous large molecules.¹¹⁸

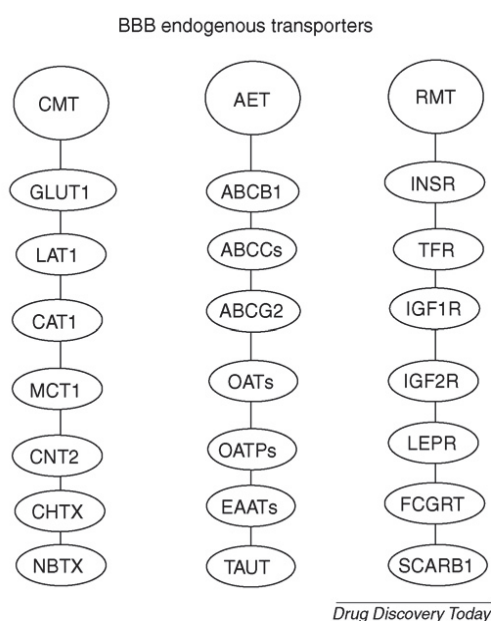


Figure 1.14. Endogenous blood–brain barrier transporters. Carrier-mediated transport (CMT), active efflux transport (AET) and receptor mediated transport (RMT). GLUT1, glucose transporter; LAT1, large neutral amino acid transporter; CAT1, cationic amino acid transporter; MCT1, monocarboxylic acid transporter; CNT2, concentrative nucleoside transporter; CHT, choline transporter; NBT,

nucleobase transporter; ABCB1, adenosine triphosphate-binding cassette (ABC) transporter; OAT, organic anion transporter; OATP, organic anion-transporting polypeptide; EAAT, glutamic acid amino acid transporter; TAUT, taurine transporter; INSR, insulin receptor; TFR, transferrin receptor; IGFR, insulin-like growth factor receptor; LEPR; leptin receptor; FCGRT, Fc fragment of IgG receptor transporter; SCARB1, scavenger receptor, class B. The X designation for the CHT and NBT transporter indicates these transporters have not yet been cloned or identified at the molecular level for the blood–brain barrier (BBB).^{103,116}

Those targets opened a full box of new ideas and formulations, with the aim to increase the permeability to the BBB by the help of specific carriers, inhibiting the efflux multidrug-resistance or using the receptors in the brain endothelial cells.^{103,119} The idea of using a “Trojan horse” by this means is being greatly explored and some reports showed that large particles and proteins usually not present in the brain are now able to cross the BBB.^{120–122}

1.5.3. Molecular Imaging probes for Alzheimer's Disease

Currently, no clinical imaging techniques are available for early detection of the disease. The development of diagnostic agents for early *in vivo* visualization of the amyloid plaques is a critical issue, which would also be highly important for monitoring new therapeutic strategies. The most significant advances have been made in the field of nuclear imaging, in particular in positron emission tomography (PET).

1.5.3.1. Nuclear imaging

Many small organic compounds have been developed to possess high binding affinities for the A β aggregates. Several structures were identified to present promising binding properties to amyloid plaques: Congo Red, Chrysamine G, Thioflavin S, bromo-styrylbenzene (BSB), and smaller styrylbenzenes (**Figure 1. 15**).¹²³

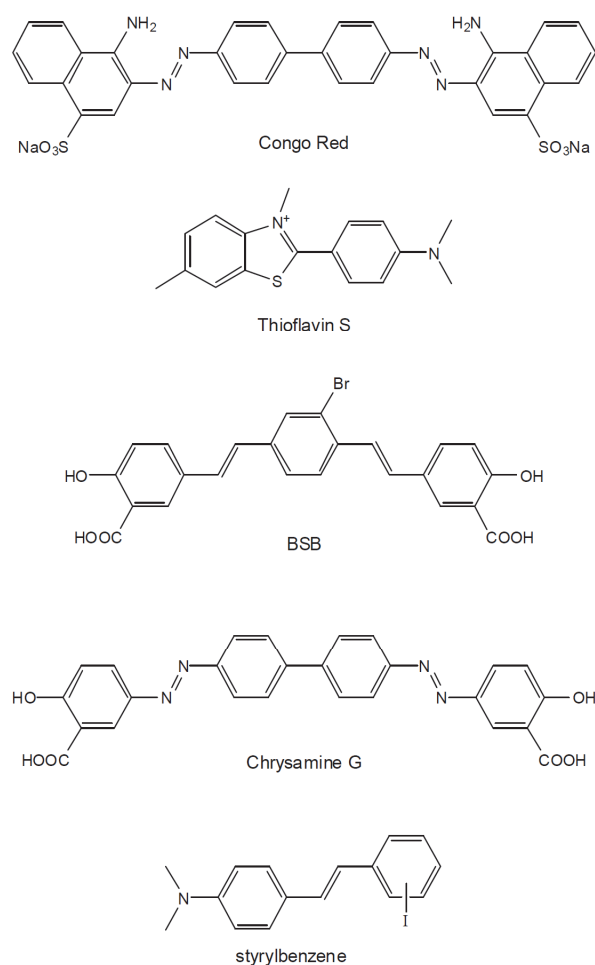


Figure 1.15. Chemical structures of compounds that bind to A β plaques: Congo Red, Chrysamine G, Thioflavin S, BSB, and styrylbenzenes.

Recently modified, non-charged stilbenes and benzothiazoles showed both to label A β aggregates very specifically and to permeate the BBB *in vivo* (**Figure 1.16**).^{124,125} Some of these molecules have fluorescent properties useful for optical detection.^{126,127} ¹¹C - and ¹⁸F-labelled derivatives of stilbene (florbetapir)¹²⁸ and the Pittsburgh compound-B (PiB)^{129,130} are among the most promising PET tracers of AD (**Table 1.4**). Certain compounds are making their way into the clinics with very exciting and promising results. The uptake mechanism across the BBB is still uncertain but passive transcellular diffusion is the most probable way of entrance.¹²⁷

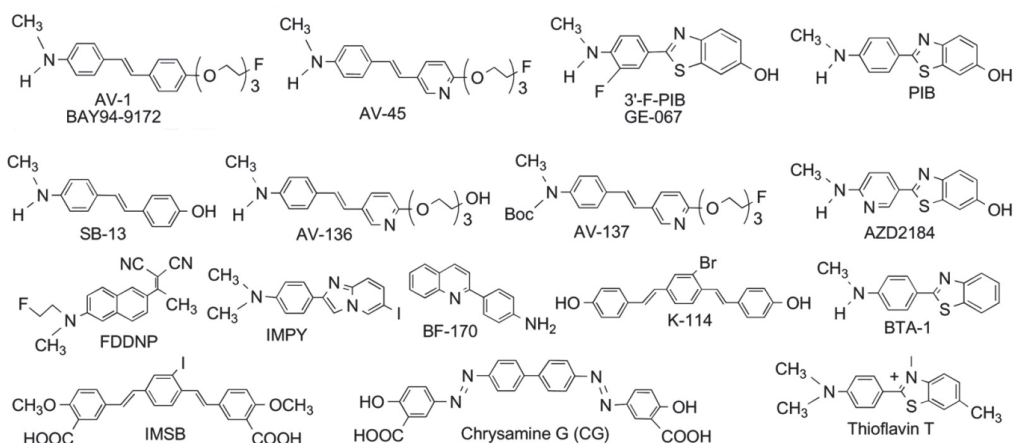


Figure 1.16. Promising benzothiazol and stilbene derivatives reported to cross the BBB and to specifically target the amyloid plaques.¹²⁵

Table 1.4. Inhibition constants (K_i , nM)^{*} of various agents against binding of ^{18}F -AV-45 to $\text{A}\beta$ plaques in postmortem AD brain homogenates.¹²⁵

Compound name	K_i (nM, $n=3$)	Compound name	K_i (nM, $n=3$)
BAY 94-9172 (AV-1)	2.22 ± 0.54	AV-45	2.87 ± 0.17
AV-136	6.37 ± 3.75	AV-137	>1,000
PIB	0.87 ± 0.18	BTA-1	1.28 ± 0.46
GE-067 (3'-F-PIB)	0.74 ± 0.38	AZD2184	1.70 ± 0.54
BF-170	428 ± 57	IMPY	1.29 ± 0.46
Thioflavin T	>1,000	FDDNP	172 ± 18
IMSB	>1,000	K-114	>1,000
SB-13	3.18 ± 1.04	CG	>1,000

^{*} More details in Appendix 2

The structural interaction of these compounds with amyloid plaques is still uncertain but some recent studies with $\text{A}\beta_{1-40}$ and $\text{A}\beta_{1-42}$ hypothesize that the hydrophobic aromatic rings composing the target compounds are positioned within the “channel” that is formed by the side-chains in the cross- β structure (**Figure 1.17**). The long axis of the molecule is parallel to the long axis of the fibril, allowing the π - π interactions and in some cases reflecting the increase of

fluorescence of the chromophore (Thioflavine T).¹³¹

Another hypothesis for the negatively charged Congo Red (CR) argues that the β -sheet structure implies that β -strands are packed side by side with a repetitive occurrence of a positively charged N-terminus. This nicely fits with the binding of a CR molecule that has one negative charge at each end, matching every fifth positive N-terminus. In the modelled A β hairpin the distance between K16 and K28 is about 20-25 Å, similar to the distance between the two sulfonate (SO_3^-) groups in Congo red.^{132,133}

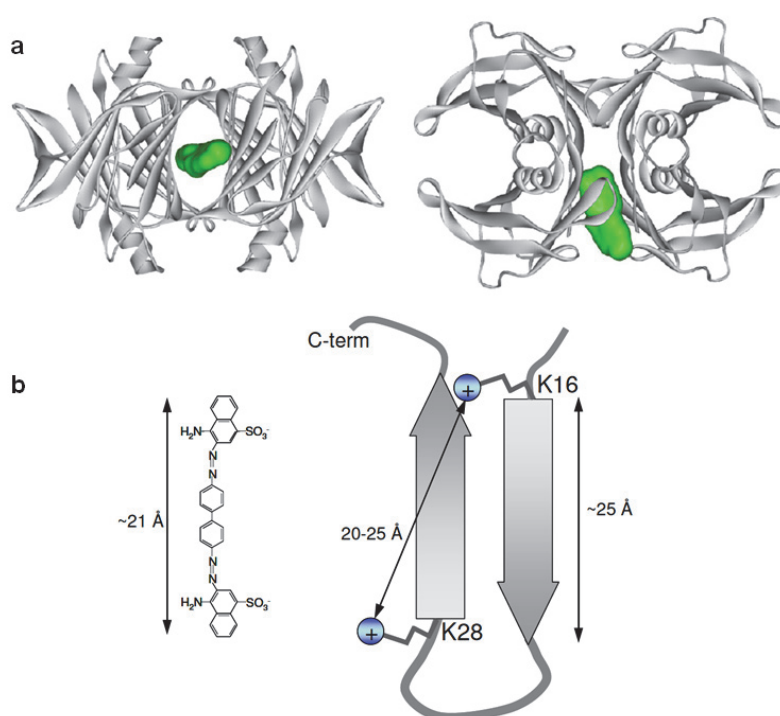


Figure 1.17. β -hairpin model of potential complementary interaction between (a) an A β fibril and Thioflavine T (benzothiazole)¹³¹ and (b) A β peptide and Congo red¹³².

Attempts have been also made to develop $^{99\text{m}}\text{Tc}$ -labelled A β SPECT imaging probes which, given the easier accessibility of $^{99\text{m}}\text{Tc}$ as compared to the cyclotron-based ^{18}F , could provide a more convenient and cost-effective approach to the detection of AD. Recently, small, neutral $^{99\text{m}}\text{Tc}$ -probes have been reported based on derivatives of biphenyl, benzothiazole aniline, chalcone, flavone, or pyridyl benzofurane. Some of them showed reasonable brain uptake and affinity towards

β -amyloid plaques (**Figure 1.18**).^{134–137}

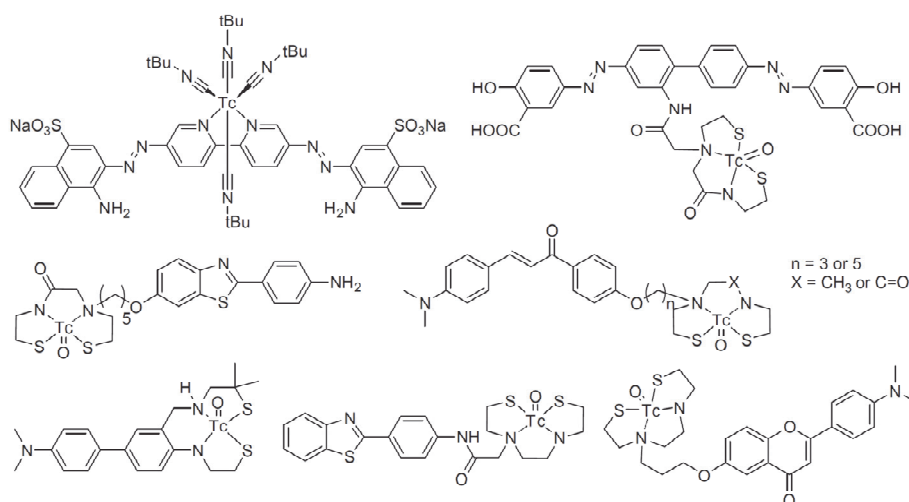


Figure 1.18. Structures of ^{99m}Tc -labeled amyloid imaging probes (image taken from the ref.¹³⁷).

1.5.3.2. MRI

In the absence of any contrast agent, the MR contrast in the amyloid plaques is associated to iron accumulation, which leads to hypointense spots in T_2 , T_2^* or susceptibility-weighted images.¹³⁸ The detection of plaques weakly loaded with iron is more challenging, and exogenous contrast agents become necessary.^{115,138} So far, the development of MRI contrast agents for the diagnosis of Alzheimer's disease has been rather modest. Poduslo et al. used CA-aided MRI to visualize AD plaques with GdDTPA conjugated to a putrescine-modified human $A\beta_{1-42}$ peptide able to cross the BBB and target individual amyloid deposits in the brain of AD transgenic mice. Given the large size of the probe, several days (weeks) were necessary to label the amyloid plaques in the transgenic mouse brain *in vivo*.¹³⁹ Yang et al. reported imaging studies with ultrasmall superparamagnetic iron oxide nanoparticles, chemically coupled with the $A\beta_{1-42}$ peptide to detect amyloid deposition. They applied intra-carotid mannitol treatment to enhance BBB permeability of the agent in transgenic mice.¹⁴⁰

Non-specific Gd-complexes like GdDTPA applied in intracerebroventricular injection protocols and in *ex vivo* MRI to stain Alzheimer brain tissues, are also able to increase the contrast of amyloid aggregates.^{113,141}

1.6. Outline of the Thesis

This thesis is the result of a multidisciplinary research work, with the goal to discover new contrast agents for the early diagnostics of Alzheimer disease with non-invasive *in vivo* imaging methods.

Chapter 2 gives a brief presentation of the imaging probe design by considering requirements for the choice of both the targeting unit and the imaging reporter moiety.

Chapter 3 describes all the synthetic work that gave rise to the various ligands investigated. The general synthesis is depicted for each ligand and a full characterization of the new molecules is presented.

The relaxometric physical-chemical characterization of the Gd^{3+} complexes with respect to their use as MRI probes is described in Chapter 4.

Chapter 5 deals with the determination of the affinity constants of our lanthanide complexes for amyloid peptides by using different techniques. We also try to answer the question if our complexes are able to detect and prevent aggregation of $A\beta$ peptides.

Finally, Chapter 6 concludes the work with the *ex vivo* and *in vivo* studies with AD human brain slices and mice, respectively. This Chapter answers also another key question: “Can our complexes be used for AD brain delivery and specific/selective targeting of amyloid plaques?”

CHAPTER 2

*“Objectives of the
Thesis and Probe
Design”*

Today, clinical medicine crucially lacks imaging techniques to diagnose Alzheimer's disease at an early stage. The main reason is that no specific imaging probes, in particular probes adapted to multimodal approaches, are available to visualize amyloid plaques *in vivo*.

For multimodal applications, metal-based imaging agents are particularly interesting. Metal ions provide suitable probes for various imaging modalities (PET, SPECT, MRI, optical imaging). By the appropriate choice of a chelating agent, one can complex, with the same ligand, different metal ions that possess properties for these imaging modalities.

In this context, our objective was to design, synthesize and investigate novel ligands with capability of (i) efficiently complexing different metal ions adapted to different imaging modalities, including Gd^{3+} for MRI, $^{111}In^{3+}$ for SPECT or $^{68}Ga^{3+}$ for PET, (ii) efficiently labelling $A\beta$ plaques *via* specific binding, and (iii) delivering the complexes across the blood-brain-barrier.

A molecular imaging probe must contain at least one targeting moiety and one reporter group. For the targeting moiety, the benzothiazole function (**Figure 2.1**) was selected among the list of compounds able to bind $A\beta$ plaques (see eg. **Figure 1.15**). This selection was based on two priority criteria, the binding affinities for amyloid plaques, defined by K_d or K_i values¹⁴², and the hydrophobicity evaluated by the $\log P_{Oct/H_2O}$ values. From **Table 1.4** in Chapter 1, one can conclude that the inhibition constant, K_i , of the Pittsburgh compound B (PiB) is among the lowest of all compounds known to bind amyloid deposits, implying very strong affinity.

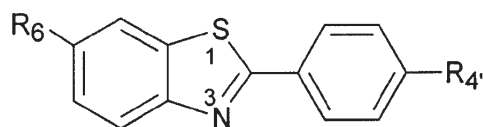


Figure 2.1. Structure of 6-substituted benzothiazole aniline (BTA) derivatives.

The probes should efficiently cross the Blood Brain Barrier (BBB). The Blood Brain Barrier permeability of compounds depends on various parameters: 1) molecular weight (MW); 2) number of possible hydrogen bonds formed by a chemical structure; 3) plasma pharmacokinetics.¹⁴³

Lipid mediated free diffusion is favoured for compounds with MW below 400Da. Therefore, low MW compounds cross the BBB more efficiently with rates that seem to correlate inversely with the square root of their MW,¹⁴⁴ at least for compounds under 600 Da. The H-bonding capacity of a compound can be estimated by the following rules: 4 H-bonds for each terminal amide group, 3 H-bonds for each internal amide, primary amino group or carboxyl group, 2 H-bonds for each hydroxyl group, 1 H-bond for each ether or carbonyl group and finally add the total H-bonds formed between drug and the solvent (water).¹⁰³ The total number of H-bonding capacity should not be higher than 8. This H-bonding counting is usually substituted by the octanol/water partition coefficient, $\log P_{\text{oct/water}}$, that reflects the hydrophobicity (lipophilicity) of a compound in water and which should be as close as possible to 2. This optimal value of 2 corresponds to a pronounced hydrophobic (lipophilic) behaviour of the compounds which make them able to permeate the BBB by free diffusion.¹⁰²

The design of a multimodal probe to be used with techniques such as MRI, PET and SPECT should also include a stable and efficient reporter group. Here we exploit the rich physical properties of trivalent metal cations, such as lanthanides (Ln^{3+}) particularly Gd^{3+} as MRI contrast agent, as well as In^{3+} and Ga^{3+} , with radioisotopes adequate for SPECT (^{111}In) and PET (^{68}Ga). Thus, our reporter group should include a chelating moiety capable of forming very stable complexes with those trivalent metal ions. Tetraaza macrocycles with four (DOTA) or three (DO3A) acetate arms form thermodynamically stable and kinetically inert complexes with trivalent metal ions (Ln^{3+} , In^{3+} , Ga^{3+}).¹⁴⁵⁻¹⁴⁷

Since these macrocyclic metal complexes are very hydrophilic, the choice of the targeting moiety is particularly important as it should substantially increase the overall hydrophobicity of the probe.¹⁰²

Table 2.1 shows that changes in the terminal amine at position 4' (R_4') or in the aromatic benzyl position 6 (R_6) in BTA derivatives induce important

changes in the partition coefficient ($\log P$) and in the affinity to A β_{1-40} amyloid deposits. The introduction of the methoxy group in the R₆ position of the benzothiazol always led to a simultaneous optimization of $\log P$ and K_i (see also **Appendix 2**).

Table 2.1. Lipophilicity ($\log P_{C18}$) and A β_{1-40} binding affinities (K_i) of 6-substituted BTA analogues.^{148,149}

R ₆ ^a	log P _{C18} R ₄ ^a			K _i (nM) R ₄ ^a		
	NH ₂	NHCH ₃	N(CH ₃) ₂	NH ₂	NHCH ₃	N(CH ₃) ₂
H	2.0	2.7 (2.7) ^b	3.4	37	11	4.0
CH ₃	2.4	3.1 (3.4) ^b	3.8	9.5	10	64
OCH ₃	1.9	2.6 (2.7) ^b	3.3	7.0	4.9	1.9
OH	0.7	1.2 (1.3) ^b	2.0	46	4.3	4.4
CN	1.8	2.5	3.2	64	8.6	11
Br	2.9	3.6	4.4	7.2	1.7	2.9

^a R₆ and R₄ refer to substituent positions as shown in **Figure 2.1**.

^b The numbers in parentheses are $\log P_{oct/water}$ values determined by conventional octanol-buffer partitioning.

With respect to BBB permeability in normal mice, Mathis et al.¹⁴⁸ reported that BTA derivatives enter easily the brain. Derivatives with certain R₆ or R₄ modifications (R₆, OCH₃, H, OH, CN; R₄, NH₂, NHCH₃, N(CH₃)₂) had better permeation than others. It is worth noting from **Table 2.2** that the introduction of the *methoxy group* in position 6 (R₆) leads to a reasonable brain uptake for 2 min and 30 min, measured as % of the normalized injected dose per gram (%ID-Kg/g), for any of the modifications presented in R₄ (primary amine, NH₂, secondary amine, NHCH₃; tertiary amine, N(CH₃)₂).

Table 2.2. Mouse brain entry and clearance of 6-substituted BTA analogues¹⁴⁸

R ₆	%ID·kg/g in brain at 2 min R _{4'}			%ID·kg/g in brain at 30 min R _{4'}			ratio of 2 min/30 min R _{4'}		
	NH ₂	NHCH ₃	N(CH ₃) ₂	NH ₂	NHCH ₃	N(CH ₃) ₂	NH ₂	NHCH ₃	N(CH ₃) ₂
H	–	0.43	0.19	–	0.057	0.078	–	7.6	2.5
CH ₃	–	0.22	0.078	–	0.083	0.15	–	2.7	0.52
OCH ₃	0.32	0.33	0.16	0.084	0.10	0.14	3.8	3.2	1.1
OH	–	0.21	0.32	–	0.018	0.10	–	12	3.0
CN	–	0.32	0.24	–	0.063	0.097	–	5.0	2.5
Br	–	0.12	0.054	–	0.12	0.11	–	1.0	0.49

With these considerations in mind, we have conjugated a BTA derivative, previously proved to possess optimized A β binding properties, to the metal chelating unit DO3A-monoamide (Figure 2.2). In our ligand design, the formation of neutral complexes with trivalent metal ions as well as a short linkage between the metal binding and the amyloid-recognition sites were essential elements to facilitate BBB permeability.

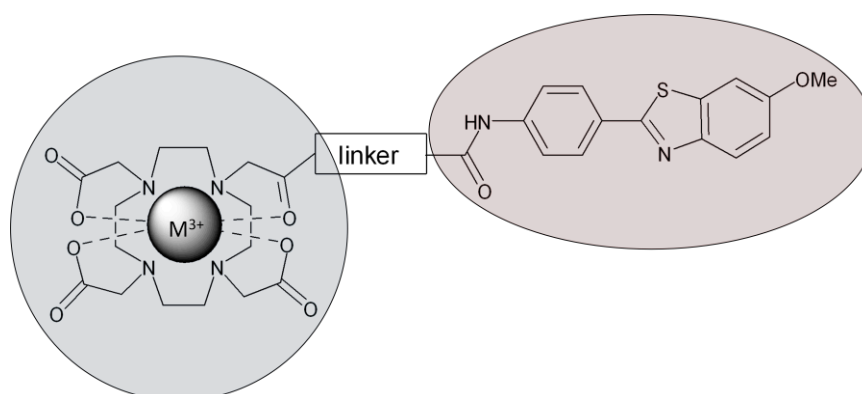


Figure 2.2. General structure of a trivalent metal complex of DO3A-BTA derivatives.

The R_{4'} linking position to the BTA structure includes an amide function and allows the introduction of different spacers linking the two moieties. With the introduction of different linkers, the hydrophobic properties and flexibility of the ligand can be changed in order to optimize the target binding properties and BBB permeation of the probe. The three ligands synthesized in the DO3A-BTA family are presented in Figure 2.3.

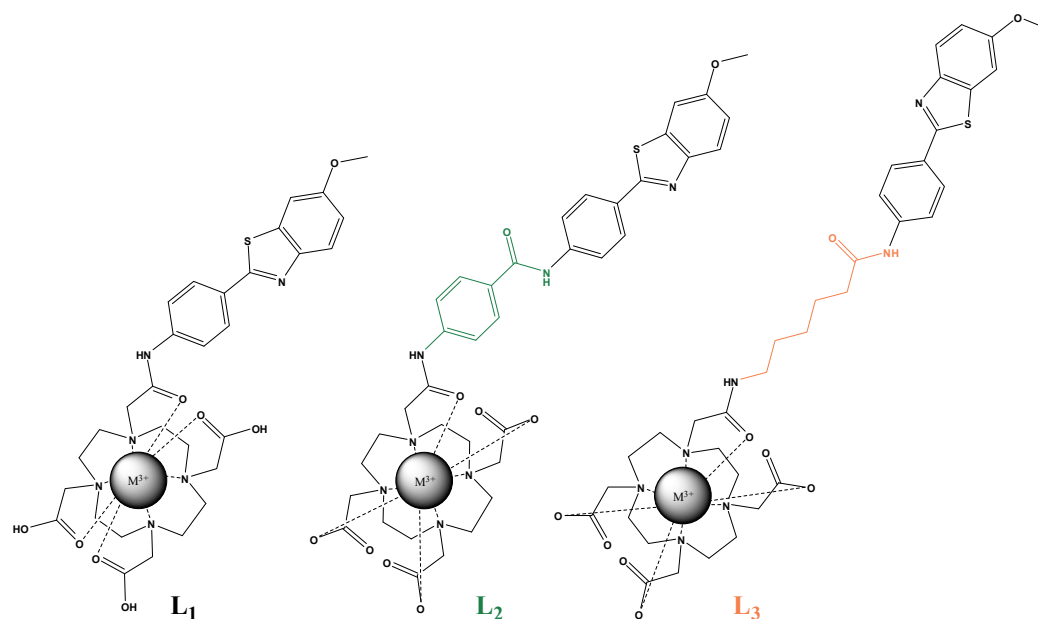


Figure 2.3. Structural representation of L₁, L₂ and L₃ coordinated to a metal, forming the complex M³⁺-L_x (x = 1,2,3)

The success of the organic synthesis (detailed in Chapter 3) and the structural flexibility of the probes led us to propose another two different structures. The first one uses a DOTA moiety substituted at the C_α atom of one methylene carboxylate arm (**Figure 2.4, A**), with the purpose of increasing the stability of the metal complexes, changing their total charge and avoiding the presence of an amide oxygen coordinating to Gd³⁺, which negatively affects its water exchange. In the other one, the chelating structure is a monoamine-monoamide (MAMA) moiety adapted to ^{99m}Tc labeling for SPECT (**Figure 2.4, B**). ^{99m}Tc-complexes with MAMA structures have been reported to present good brain uptake.^{19,150,151}

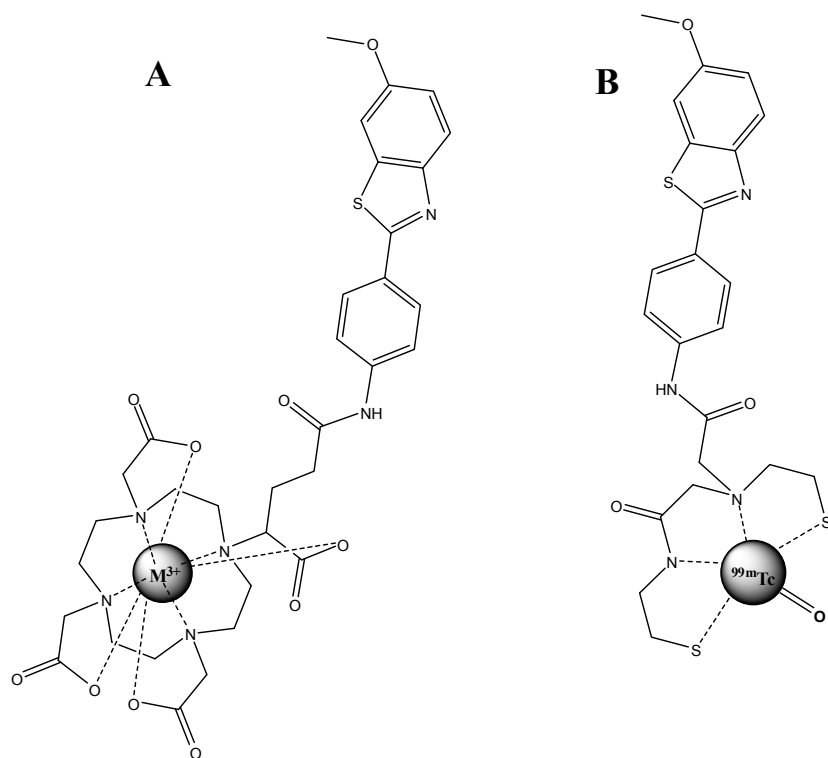


Figure 2.4. Structures of **A)** M^{3+} -DOTA-PiB (L_4) based probes and **B)** ^{99m}Tc -MAMA-PiB (L_5) based probes.^{145,151}

CHAPTER 3

*“Organic Synthesis of
the Ligands”*

3.1. Synthesis of the DO3A-BTA derivatives

This chapter is dedicated to the description of the synthesis and structural design of the new DO3A-BTA derivative ligands obtained in this work. The reasons that led us to choose the 4'-methylaminophenyl-benzothiazole targeting moiety, the tetraaza DO3A, DOTA and MAMA chelating structures (**See Abbreviation section**), the introduction of an amide function in the R₄ terminal position and the addition of the methoxy function in the 6 position of the benzothiazol group (R₆) have been explained in Chapter 2.

The structures of the three DO3A derivative ligands are described in **Figure 3.1**. The first ligand, **L**₁, has a short acetamide linker between the targeting and chelating moieties. The second ligand **L**₂, with a 4-acetamidobenzamide linker, was designed to increase its lipophilicity and rigidity and also to determine whether the BBB crossing capacity was altered or not. Ligand **L**₃ has a longer aliphatic 6-acetamidohexanamide spacer to confer flexibility to the structure, increase the lipophilic behaviour and contains one extra amide function, such as **L**₂. All these three ligands were conceived with the purpose of forming non-charged complexes with trivalent positive metal ions (M³⁺).

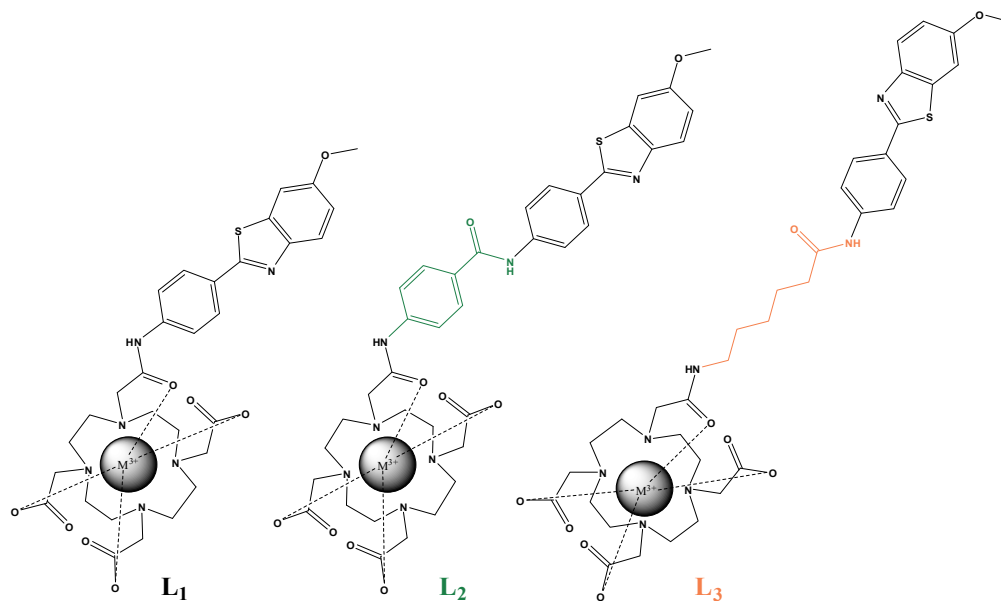


Figure 3.1. Structural representation of ligands L_1 , L_2 and L_3 coordinated to a metal ion, forming the complexes $M^{3+}-L_x$ ($x = 1, 2, 3$)

3.2. Synthesis of the BTA moiety, 4-(6-methoxybenzol[d]thiazol-2-yl)aniline

The synthesis of the BTA targeting moiety was done according to the work of Mathis et al.^{130,148,152}

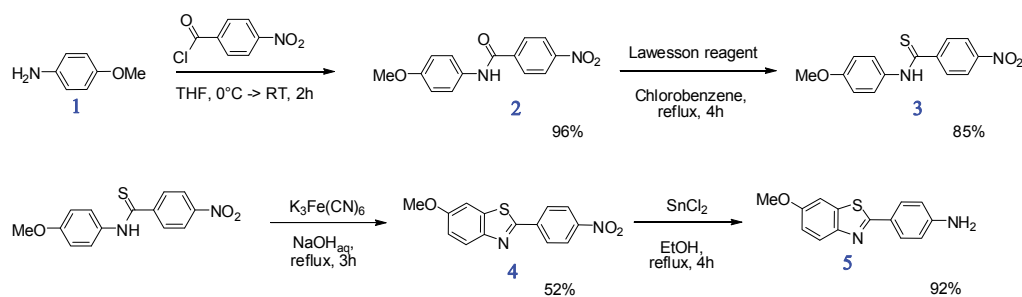


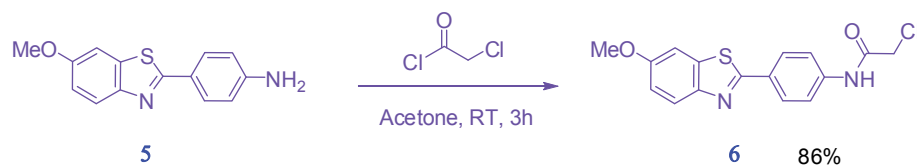
Figure 3.2. Synthetic route used to prepare the BTA targeting moiety 4-(6-methoxybenzol[d]thiazol-2-yl)aniline.

The general strategy for the BTA synthesis is outlined in **Figure 3.2**. Firstly, we have performed the amide formation by the acylation of 4-methoxyaniline (**1**) with 4-nitrobenzoyl chloride to form the product **2** with a very high yield (96 %). Subsequently, compound **2** was made to react with half equivalents of Lawesson's reagent and the thiation occurred with a good yield to obtain the corresponding thioamide **3**. The following reaction was the cyclization of the compound **3** in the *-ortho* position of the *methoxyphenyl* ring to form the 6-methoxy-2-(4-nitrophenyl)benzo[d]thiazole, **4**.¹⁵³ This Jacobson's cyclisation¹⁵⁴ is an oxidative reaction to form benzothiazol derivatives using *potassium ferricyanide* as oxidant with yields varying from 20-55%.¹⁵³ We tried other methods reported to have higher yields using DDQ-Promoted cyclization of thioformanilides.¹⁵⁵ However, the result was not better, directing us again to the Jacobson's cyclisation that is the most widely used.

In the final step of this pathway, compound **4** was reacted with *stannous chloride* to reduce the *nitrophenyl* group, to obtain, with a remarkably high yield, the envisaged benzothiazol derivative **5** (4-(6-methoxybenzo[d]thiazol-2-yl)aniline), containing a free terminal primary amine function.

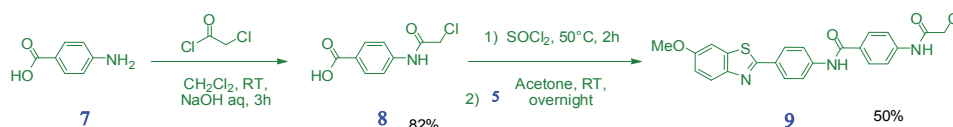
3.2.1. Synthesis of the BTA *chloroacetamide* reaction intermediates

The next step of our strategy was to synthesize the BTA chloroacetamide intermediates. For each final compound, a different procedure was used.



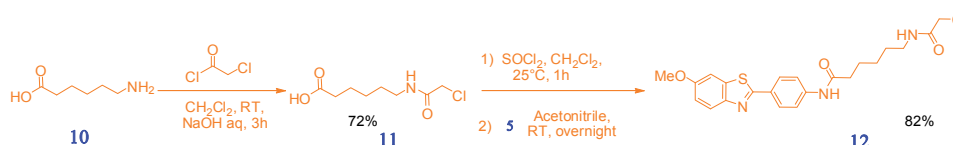
Scheme 3.1

Scheme 3.1 describes the introduction of the smaller acetamide linker into the BTA moiety (**5**) in order to obtain ligand **L**₁. For this step, we performed an acylation of compound **5** with *chloroacetyl chloride* in acetone. The available primary amine from the *aniline* moiety undergoes a fast reaction with the *chloroacetyl* group forming product **6** with a good yield, after recrystallization.



Scheme 3.2

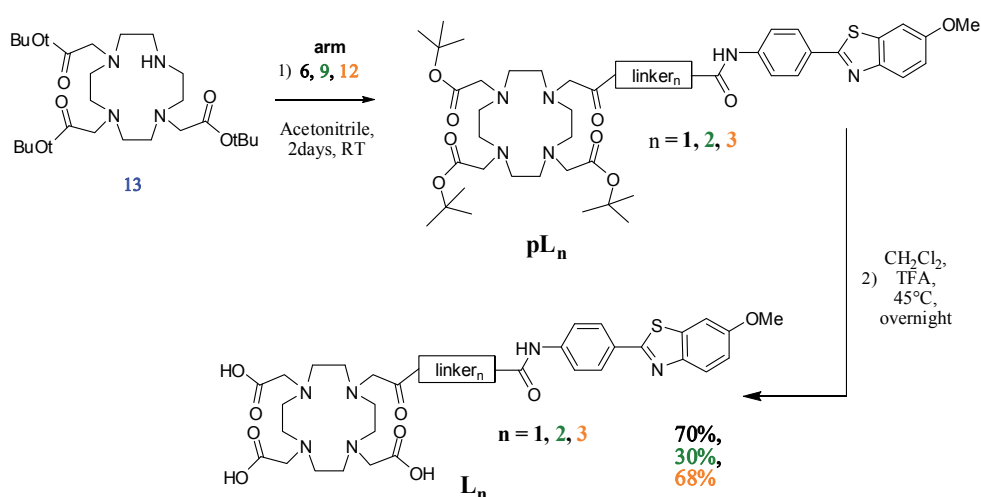
The strategy to obtain the *4-acetamidobenzamide* intermediate towards the second final product **L**₂ (**Scheme 3.2**), started by the functionalization of **7** by adding, *via* an amide formation, a halogenated function, necessary for the alkylation of the BTA derivative on the macrocycle. For that task, the reagent **7** (*4-aminobenzoic acid*) reacted with *chloroacetyl chloride* under Schotten-Baumann conditions,^{156,157} obtaining the corresponding amide **8**. Compound **8** was then activated by chlorination with *thionyl chloride* (SOCl₂). These two reactions were done in this order to prevent the reaction of the chlorinated product on itself. Consequently, the *4-(2-chloroacetamido)benzoyl chloride* was introduced in a fast reaction with compound **5** using acetone as solvent, to achieve the condensation and obtain the final intermediate **9** (*4-2-chloroacetamido)-N-(4-(6-methoxybenzothiazol-2-yl)phenyl)benzamide*).



Scheme 3.3

The intermediate for the synthesis of the third ligand **L₃** was obtained as represented in **Scheme 3.3** using a strategy similar to that in **Scheme 3.2**. The preparation of the longer **L₃** linker *6-acetoamidohexanamide* required the acylation of compound **10** *aminohexanoic acid* with chloroacetyl chloride in a reaction with *dichloromethane* under Schotten-Baumann conditions. The intermediate product **11** (*6-(2-chloroacetoamido)hexanoic acid*) obtained was reacted with SOCl_2 to achieve the chlorination of the carboxylic acid in very mild conditions (CH_2Cl_2 , 25°C) and to minimize side reactions (cyclization) that was observed when trying to perform the same reaction with (*4-(2-chloroacetoamido)butanoic acid*). The very reactive *2-chloro-6-acetoamidohexanamide chloride* **11** obtained before was reacted with compound **5** with the primary free amine available and enabled the condensation to obtain compound **12** (*6-(2-chloroactetamido)-N-(4-(6-methoxybenzol[d]thiazol-2-yl)phenyl)hexanamide*) with high yields.

3.2.2. Synthesis of DO3A-BTA derivatives, **L₁**, **L₂**, **L₃**.



Scheme 3.4

The last step of this first synthetic approach to obtain an imaging probe with the targeting moiety attached to the reporter structure is depicted in **Scheme 3.4**. The final ligands **L₁**, **L₂** and **L₃** were obtained by the monoalkylation of the functionalized compound **13**, *tri-tert-butyl-DO3A*, with compounds **6**, **9** and **12**. Compound **13** was commercially available, and the synthesis started from this functionalized macrocyclic building block.¹⁵⁸ In our hands, the reaction proceeded in acetonitrile at room temperature and for 48h. The acid sensitive *tert-butyl* protecting groups were then removed with trifluoroacetic acid (TFA) and the final ligands with the free carboxylic acid moieties were obtained with global yields over the two last steps of: $L_1 = 70\%$; $L_2 = 30\%$; $L_3 = 68\%$.

3.3.Synthesis of the DOTAGA-BTA derivative.

The strategy of the route for the synthesis of a DOTAGA-BTA (DOTAGA = 4-(4,7,10-tris(2-(*tert*-butoxy)-2-oxoethyl)-1,4,7,10-tetraazacyclododecan-1-yl)pentanoic acid) derivative (**Figure 3.4**) will be discussed in this section. As addressed in Chapter 2, the metal complexes of a tetracarboxylate DOTA derivative ligand have an increased thermodynamic stability and kinetic inertness as compared to DO3A-monoamide analogues. The additional charged coordinating arm can also render the final product more hydrophilic when forming complexes with trivalent metal ions, as the final complex is negatively charged (-1 charge).

The synthetic procedure used two different methodologies. The next section will detail them, which share the same objective in obtaining the intermediary product DOTAGA.

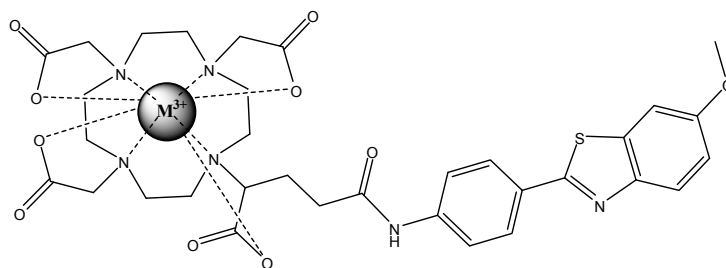
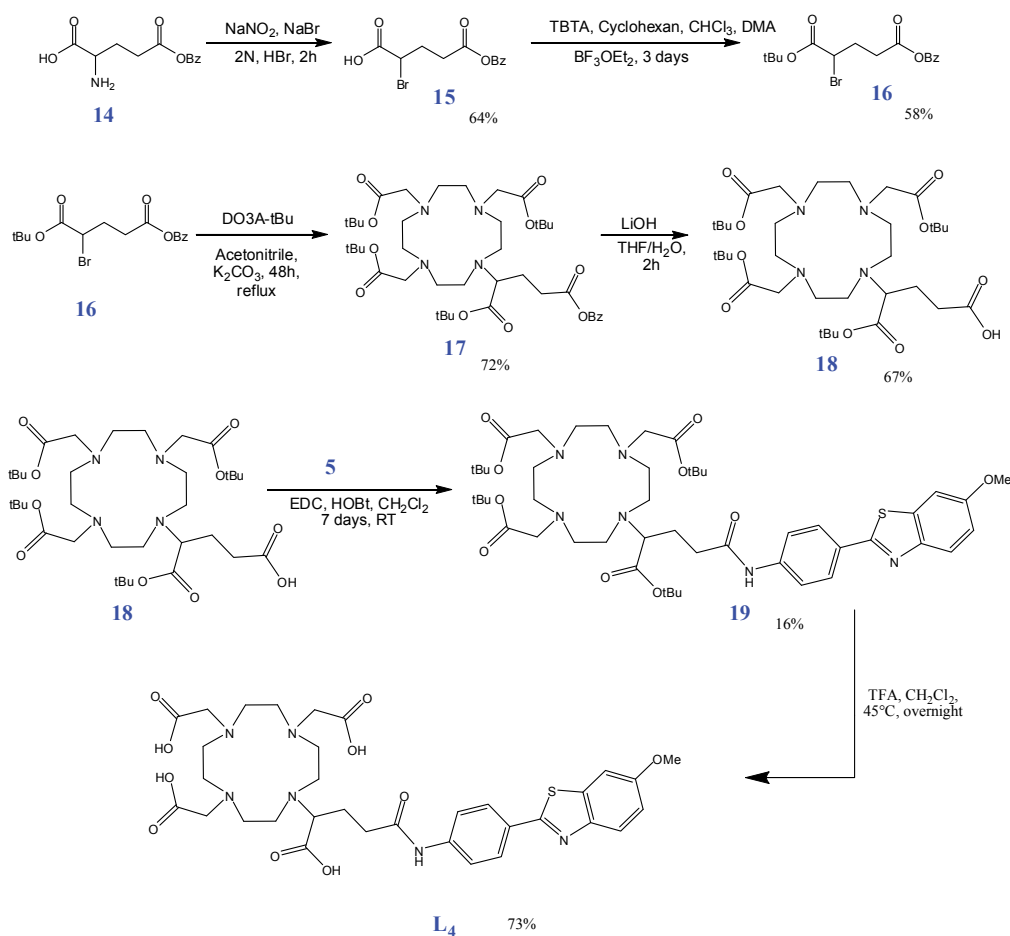


Figure 3.4. Structural representation of ligand **L₄** coordinated to a metal ion, forming the neutral complex $M^{3+}\text{-L}_4$.

3.3.1. Synthesis of the DOTAGA-BTA derivative, **L₄**

The first step (**Scheme 3.5**) starts with compound **14** *2-amino-5-(benzoyloxy)-5-oxopentanoic acid* using an analogous method to that of Eisenwiener to obtain several functional DOTA derivatives including DOTAGA.¹⁵⁹ It includes the synthesis of an orthogonally protected *bromo-alkyl-dicarboxylic acid diester* for the monoalkylation of cyclen or *tris-tert-butyl-DO3A*. The product **15** was protected by *tert*-butylation of the available carboxylic acid, aided by *tert*-butyl-trichloroacetimidate (TBTA) as reagent to obtain **16** *benzoic 4-bromo-5-(tert-butoxy)-5-oxopentanoic anhydride*. The alkylation reaction of *tris-tert-butyl-DO3A* **13** with compound **16** proceeded for 48H in acetonitrile and in the presence potassium carbonate. The benzoxy protection from compound **17** was removed by a saponification in a mixture THF/ water 1/1 (v/v) and with *lithium hydroxide* as a base. This step was obtained with a yield of 67% giving compound **18**, the *tris-tert-butyl-DOTAGA*.

Linking the BTA derivative **5** to the *tris-tert-butyl-DOTAGA* **18** was achieved in the presence of coupling reagents EDC, HOBt in CH_2Cl_2 for 48H. The *tris-tert-butyl-DOTAGA-BTA* derivative **19** obtained in the precedent step was deprotected in acidic conditions with TFA and the final product **L₄** was purified with low yields due to the low reactivity of aromatic primary amine.



Scheme 3.5

The overall yield of the two last steps of L_4 synthesis was around 12%, devoid of the effect of lateral π -sink orbitals from aromatic groups. The lone pair on the nitrogen touches the delocalized ring electrons and becomes delocalized with them. Delocalization of those electrons makes the molecules more stable and thus disrupting the delocalization costs energy, reason why nucleophilic character of compound 5 is quite weak.¹⁶⁰ So, we have tried another strategy with a more activated intermediate to obtain L_4 . This strategy (**Scheme 3.6**), published very recently by Bernhard *et al.*, uses the DOTAGA-anhydride (2,2',2''-(10-(2,6-dioxotetrahydro-2H-pyran-3-yl)-1,4,7,10-tetraazacyclododecane-1,4,7-triyl)triacetic acid) that is commercially available or can be synthesized directly

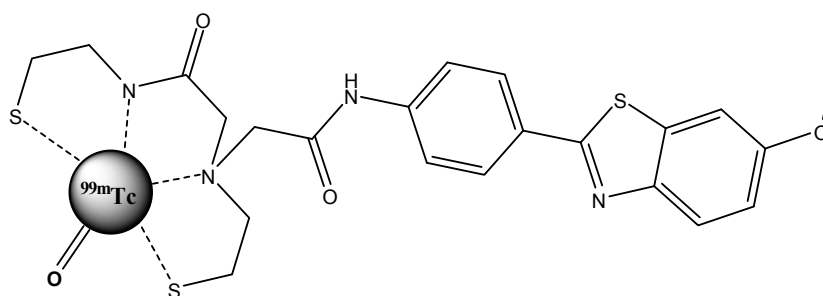
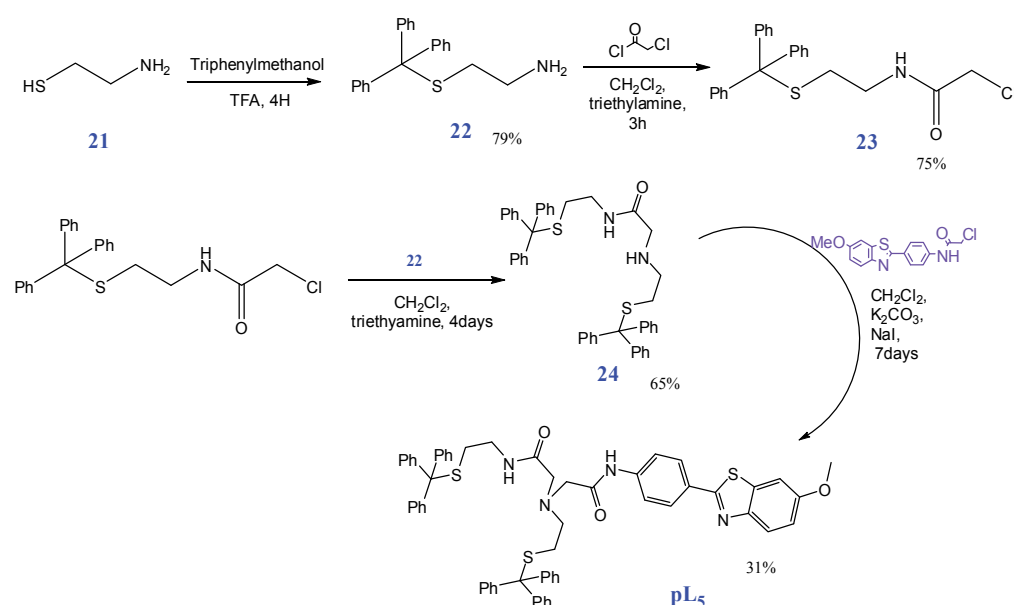


Figure 3.5. Structural representation of ligand **L₅** coordinated to $^{99\text{m}}\text{Tc}$, forming the neutral complex TcO-L_5 .¹⁶³



Scheme 3.7

2-aminoethanethiol **21** was firstly protected with a *trityl* group by the aid of TFA and *triphenylmethanol*. The protection was quick and after 2 hours the compound **22** *S*-triphenylmethyl-1-aminoethanethiol was obtained. Compound **23** was then obtained by chemical alkylation of compound **22** with chloroacetyl chloride in smooth conditions. The protected MAMA structure **24** was obtained in high yield by the reaction of compound **22**, having a primary amine available, with the *2*-chloroacetamide group of **23**.

The last step, also represented in **Scheme 3.7**, was successfully performed

by reacting compound **6** 2-chloro-N-(4-(6-methoxybenzol[d]thiazol-2-yl)phenyl)acetamide (Section 1.2) with **24**. The alkylation of the secondary amine from the bis-Trityl-MAMA was slow and after 2 weeks the protected product **pL₅** was obtained with 31% yield. To obtain the neutral complex TcO-L₅, the removal of the thiol protecting trityl groups is usually done with trifluoroacetic acid and triisomethylsilane in an inert solvent. However, some reported work alerts of the formation of several side products (mono-S-trityl, di-S-trityl, inter and intra-disulfide bonds), therefore deprotection and complexation in aqueous medium using heating in the presence of hydrochloric acid will be used.¹³⁴

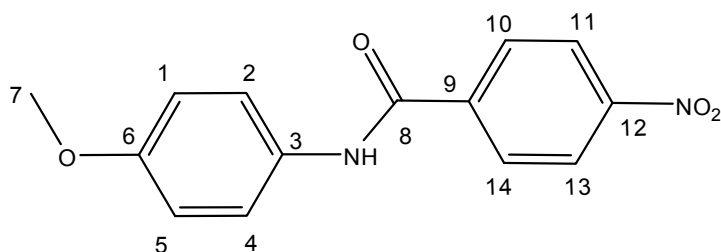
3.5.Experimental

3.5.1. Materials and methods

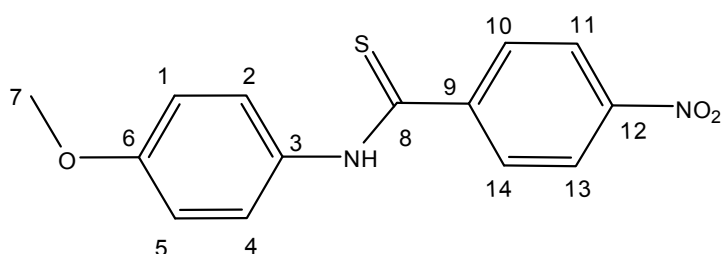
Chemicals were purchased from Sigma-Aldrich, Alfa Aesar and Chematech (DO3A-tBut₃) and used without further purification. Analytical grade solvents were used and were not further purified unless specified.

Reactions were monitored by TLC on Kieselgel 60 F254 (Merck) on aluminium support, with detection by examination under UV light (254 nm), by adsorption of iodine vapour, by spraying with ninhydrin and by complex coloration with Gragendorff solutions. Ion exchange chromatography was performed on Dowex 1X2-OH- resin and polar affinity chromatography with silica gel (Sigma Aldrich). ¹H and ¹³C NMR spectra were run on a Bruker Avance-500 (11.7 T) spectrometer, operating at 500.132 and 125.769 MHz, for ¹H and ¹³C, respectively. Chemical shifts (δ) are given in ppm relative to the CDCl₃ solvent (¹H, δ 7.27; ¹³C 77.36) as internal standard. For ¹H and ¹³C NMR spectra recorded in D₂O, chemical shifts (δ) are given in ppm, respectively, relative to TSP as internal reference (¹H, δ 0.0) and tert-butanol as external reference (¹³C, CH₃ δ 30.29). Mass spectrometry was performed at the Centre de Biophysique Moléculaire du CNRS in Orléans, France.

3.5.2. Synthesis of the Benzothiazol moiety

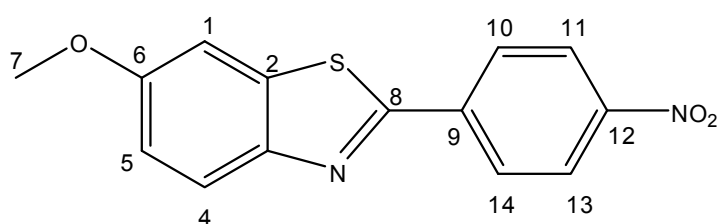


N-(4'-methoxyphenyl)-4-nitrobenzamide (2). To a solution of 60 ml of p-anisidine (3.08 g, 25 mmol) and dry triethylamine (3.48 ml, 25 mmol) in freshly distilled THF, was added dropwise at 0°C, 30 ml of a solution of 4-nitrobenzoyl chloride (3.03 ml, 25 mmol) in distilled THF over 20 minutes. The mixture was stirred 1h at 0°C then 1h at room temperature. The white precipitate was filtered and the solution was concentrated under vacuum to 30 ml. Then 50 ml of water was added and the solution was allowed to stand overnight at 4 °C overnight. The yellow-green precipitate was filtered and dry under vacuum to give 6.53 g of compound **2** (96 %). (¹H NMR (CDCl₃, 25°C, 500 MHz): δ (ppm) 3.75 (s, 3H, -OCH₃), 6.95 (d, ³J = 9Hz, 2H, *H*-1,5), 7.67 (d, ³J = 8.35Hz, 2H, *H*-2,4), 8.17 (d, ³J = 8.75 Hz, 2H, *H*-11,13), 8.36 (d, ³J = 8.75 Hz, 2H, *H*-10,14). ¹³C NMR (CDCl₃, 25°C, 500 MHz): δ (ppm) 55.173 (-OCH₃, *C*-7), 113.811 (*C*-6,5), 122.097 (*C*-11,13), 123.499 (*C*-10,11), 129.091 (*C*-2,4), 131.773 (*C*-3), 140.702 (*C*-9), 149,036 (*C*-12), 155.896 (*C*-6), 163.359 (*C*-8). HRMS (ESI): *m/z*: *ca*cd for C₁₄H₁₃N₂O₄: 273.08698, found 273.08697.

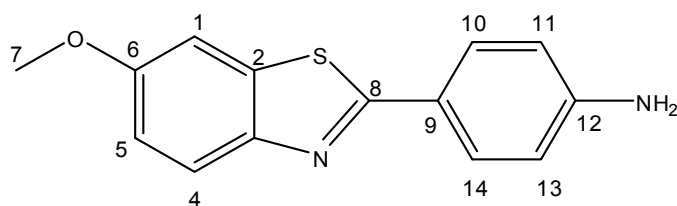


N-(4'-methoxyphenyl)-4-nitrothiobenzamide (3). Compound **2** (6 g, 22 mmol) was dissolved in 15 ml of chlorobenzene. Then, Lawesson's reagent (5.34 g, 13.2 mmol) was added to the solution and the mixture was refluxed 4h. After cooling, the solution was allowed to stand overnight at 0°C. The orange

precipitate was filtered and then dissolved with acetone to separate the residue of Lawesson's reagent. The solution was evaporated to dryness to give 5.40 g of the compound **3** (85 %). (^1H NMR (DMSO, 25°C, 500 MHz): δ (ppm) 3.37 (s, NH), 3.78 (s, 3H, -OCH₃), 7.02 (d, $^3\text{J} = 8.8\text{Hz}$, 2H, *H-11,13*), 7.76 (d, $^3\text{J} = 8.8\text{Hz}$, 2H, *H-10,14*), 7.99 (d, $^3\text{J} = 8.6\text{ Hz}$, 2H, *H-1,5*), 8.3 (d, $^3\text{J} = 8.6\text{ Hz}$, 2H, *H-2,4*). ^{13}C NMR (DMSO, 25°C, 500 MHz): δ (ppm) 55.313 (-O-CH₃, C-7), 113.692 (C-6,5), 123.281(C-11,12), 125.343 (C-10,14), 128.612 (C-2,4), 132.632 (C-3), 147.902 (C-9), 148.13 (C-12), 157.49 (C-6), 194.1 (C-8). HRMS (ESI): m/z: cacd for C₁₄H₁₃N₂O₃S : 289.06414 , found 289.06421.

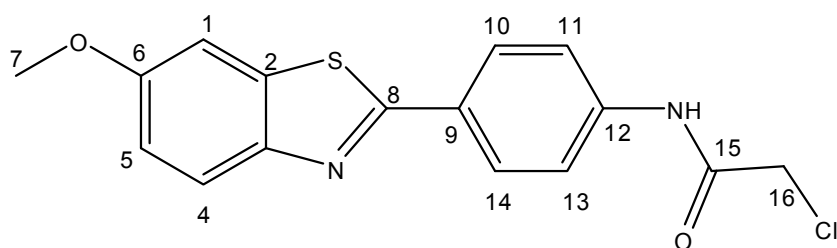


2-(4'-nitrophenyl)-6-methoxybenzothiazol (4). Compound **3** (5 g, 17.3 mmol) was wetted with 3ml of ethanol and then 15 ml of 10% aqueous NaOH was added. The mixture was diluted with water to provide a final suspension of 5% aqueous NaOH. The mixture was slowly added over 45 minutes into a refluxed solution of potassium hexacyanoferrate(III) (22.8 g, 69.4 mmol). Then the mixture was refluxed 3h. The brown precipitate was filtered and dried under vacuum and 100 ml of a mixture of dichloromethane-methanol (75/25 v/v) was added. The solid was filtered off and the solvent was evaporated. Then a 100 ml of a mixture of chloroform-methanol (20/80 v/v) was added to the residue and the brown-yellow precipitate was filtered to give 2.56 g of compound **4** (52 %). (^1H NMR (CDCl₃, 25°C, 500 MHz): δ (ppm) 3.93 (s, 3H, -OCH₃), 7.16 (dd, 1H, $^3\text{J} = 9.55\text{ Hz}$, $^4\text{J} = 2.4\text{ Hz}$, *H-5*), 7.4 (s, 1H, *H-1*), 8.02 (d, $^3\text{J} = 8.95\text{ Hz}$, 1H, *H-4*), 8.22 (d, $^3\text{J} = 8.75\text{ Hz}$, 2H, *H-11,13*), 8.35 (d, $^3\text{J} = 8.21\text{ Hz}$, 2H, *H-10,14*). ^{13}C NMR (CDCl₃, 25°C, 500 MHz): δ (ppm) 55.173 (-OCH₃, C-7), 104.209 (C-1), 116.803 (C-5), 124.487 (C-11,13), 124.695 (C-4), 127.991 (C-11,14), 137.267 (C-2), 139.562 (C-3), 148.862 (C-12), 148.928 (C-9), 158.774 (C-6), 162.75 (C-8). HRMS (ESI): m/z: cacd for C₁₄H₁₁N₂O₃S: 287.04849, found 287.04854.



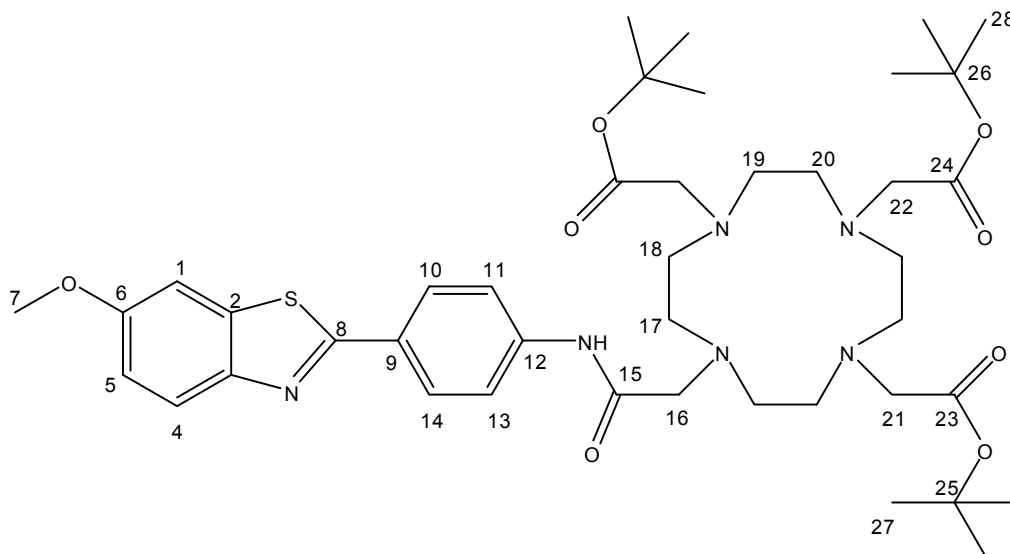
2-(4'-aminophenyl)-6-methoxybenzothiazol (5). To a solution of **4** (2.3 g, 8 mmol) in 120 ml of ethanol was added Sn(II) chloride dihydrate (5.87 g, 48.2 mmol) and the mixture was refluxed for 4 h. The ethanol was evaporated and the residue was dissolved in ethyl-acetate. The resulting solution was washed 3 times with an aqueous solution of 1M of NaOH and the organic phase was collected and washed 2 times with 25 ml of water. The organic phase was collected, dried over MgSO₄ and the solvent was evaporated. The crude product was purified by flash chromatography with dichloromethane-ethyl acetate (8/1). 1.89 g of compound **5** (92 %) was obtained. ¹H NMR (CDCl₃, 25°C, 500 MHz): δ (ppm) 3.88 (s, 3H, -OCH₃), 3.98 (s, NH), 6.73 (d, ³J = 8.5 Hz, 2H, *H-11,13*), 7.05 (dd, 1H, ³J = 9 Hz, ⁴J = 2.45 Hz, *H-5*), 7.323 (s, ³J = 2.35 Hz, 1H, *H-1*), 7.848 (d, ³J = 8.5 Hz, 2H, *H-10,14*), 7.873 (d, ³J = 9 Hz, 1H, *H-4*). HRMS (ESI): m/z: calcd for C₁₄H₁₃N₂OS : 257.07431, found 257.07442.

3.5.3. Synthesis of L₁



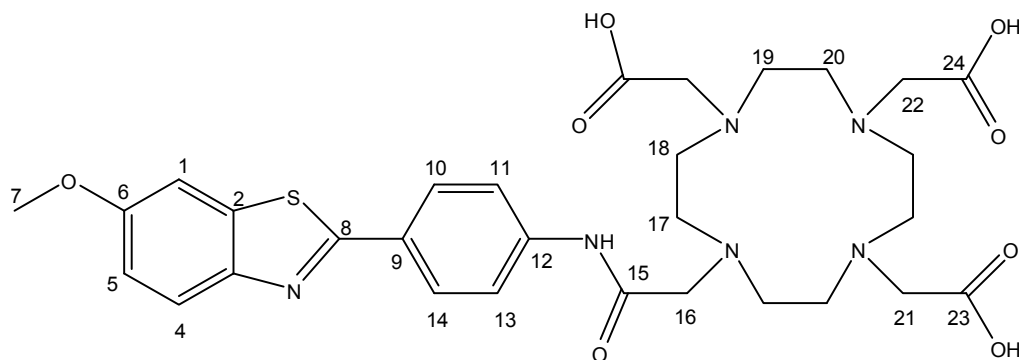
2-(4'-chloroacetamide-phenyl)-6-methoxybenzothiazol (6). To a solution of **5** (1.5 g, 5.9 mmol) in 45 ml of dry acetone was added potassium carbonate (2.42 g, 17.6 mmol) and a solution of chloroacetyl chloride (0.56 ml, 7.0 mmol) in 15 ml of dry acetonitrile. The mixture was stirred 2h. The potassium carbonate was filtered and washed with dichloromethane, and then solvents were evaporated. The crude product was recrystallized in a small amount of acetonitrile to give 1.65 g of compound **6** (86 %). ¹H NMR (CDCl₃, 25°C, 500 MHz): δ (ppm) 3.9 (s, 3H, -OCH₃, *H-7*), 4.41 (s, 2H, *H-16*), 7.12 (m, 1H, *H-5*), 7.34 (s, 1H, *H-1*),

7.73 (d, $^3J = 7.1$ Hz, 2H, *H-11,13*), 7.86 (d, $^3J = 7.5$ Hz, 1H, *H-4*), 7.88 (d, $^3J = 7.1$ Hz, 2H, *H-10,14*), 8.36 (s, NH).



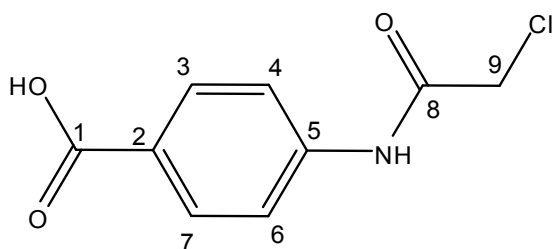
2-(4'-chloroacetamide-phenyl)-6-methoxybenzothiazol-*t*Bu₃DO3A

(**pL₁**). To a solution of DO3A-*t*Bu₃ (500 mg, 0.97 mmol) in 20 ml of dry acetonitrile was added potassium carbonate (552 mg, 4 mmol), and a solution of **6** (226 mg, 0.68 mmol) in 15 ml of dry acetonitrile. The reaction was stirred for 48 h at room temperature. The solid was filtered off and the solvent was evaporated. The crude product was purified by flash chromatography with dichloromethane-ethyl acetate (9/4). 692 mg of product **pL₁** was obtained as yellow oil (88%). ¹H NMR (CDCl₃, 25°C, 500 MHz): δ (ppm) 1.38 (bs, 18H, -*t*But, *H-27*), 1.49 (bs, 9H, -*t*But, *H-28*), 2.74 (bd, 4H, *H-17,18*), 2.93 (bs, 4H, *H-19,20*), 3.14 (s, 4H, *H-21*), 3.28 (m, 2H, *H-22*), 3.43 (s, 2H, *H-16*), 4.26 (bs, 4H), 3.9 (s, 3H, -OCH₃, *H-7*), 7.06 (bd, 1H, *H-5*), 7.34 (bs, 1H, *H-1*), 7.91 (d, 1H, *H-4*), 7.98 (bs, 4H, *H-9,13,10,9*). ¹³C NMR (CDCl₃, 25°C, 500 MHz): δ (ppm) 27.807 (*C-27*), 27.934 (*C-28*), 51.423 (*C-19,20*), 51.670 (*C-17,18*), 54.258 (*C-22*), 55.308 (*C-7*), 56.52 (*C-21*), 58.975 (*C-16*), 80.517 (*C-26*), 80.606 (*C-25*), 103.766 (*C-1*), 115.159 (*C-5*), 119.252 (*C-11,13*), 122.884 (*C-4*), 127.529 (*C-10,14*), 128.387 (*C-9*), 135.809 (*C-2*), 140.631 (*C-12*), 148.222 (*C-3*), 157.204 (*C-6*), 164.942 (*C-15*), 169.923 (*C-8*), 169.999 (*C-23*), 170.6 (*C-24*).



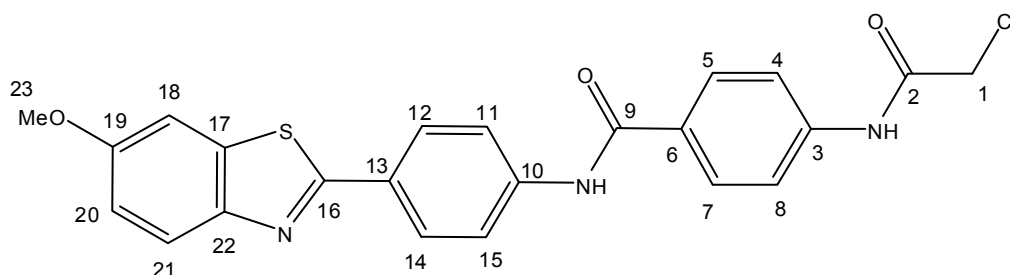
2-(4'-chloroacetamide-phenyl)-6-methoxybenzothiazol-DO3A (L_1). The compound pL_1 (657 mg, 0.81 mmol) was dissolved in 20 ml of a mixture of trifluoroacetic acid and dry dichloromethane (1:1) and heated at 45°C overnight. The solvents were evaporated and the crude product was dried under vacuum. The crude product was dissolved in a small amount of absolute ethanol and then diethyl ether was added and the mixture was allowed to stand overnight at -5°C. 351 mg of yellowish crystals were filtered and dried under vacuum (79 %). 1H NMR (D_2O , 50°C, 500 MHz): δ (ppm) 3.616 (bs, 8H, $H-17-18$), 3.82 (s, 8H, $H-19,20$), 3.9 (s, 3H, $-OCH_3$, $H-7$), 4.120 ($H-16$), 4.23 (s, 2H, $H-22$), 4.26 (bs, 4H, $H-21$) 7.14 (bd, 2H, $H-11,13$), 7.79 (bq, 4H, $H-10,14,1,4$), 7.9 (d, 1H, $H-5$). ^{13}C NMR (D_2O , 50°C, 500 MHz): δ (ppm) 49.699 ($C-17,18$), 49.833 ($C-19,20$), 51.521 ($C-21$), 54.73 ($C-22$), 55.900 ($C-16$), 56.401 ($-O-CH_3$, $C-7$), 105.06 ($C-1$), 116.304 ($C-5$), 120.715 ($C-11,13$), 123.146 ($C-4$), 128.182 ($C-10,14$), 128.702 ($C-9$), 136.024 ($C-2$), 140.595 ($C-12$), 147.710 ($C-3$), 157.811 ($C-6$), 166.559 ($C-15$), 155.304 ($C-8$), 170.866 ($C-23$), 173.399 ($C-24$). HRMS (ESI): m/z : *calcd* for $C_{30}H_{39}N_6O_8S$: 643.25446, *found* 643.25429.

3.5.4. Synthesis of L_2



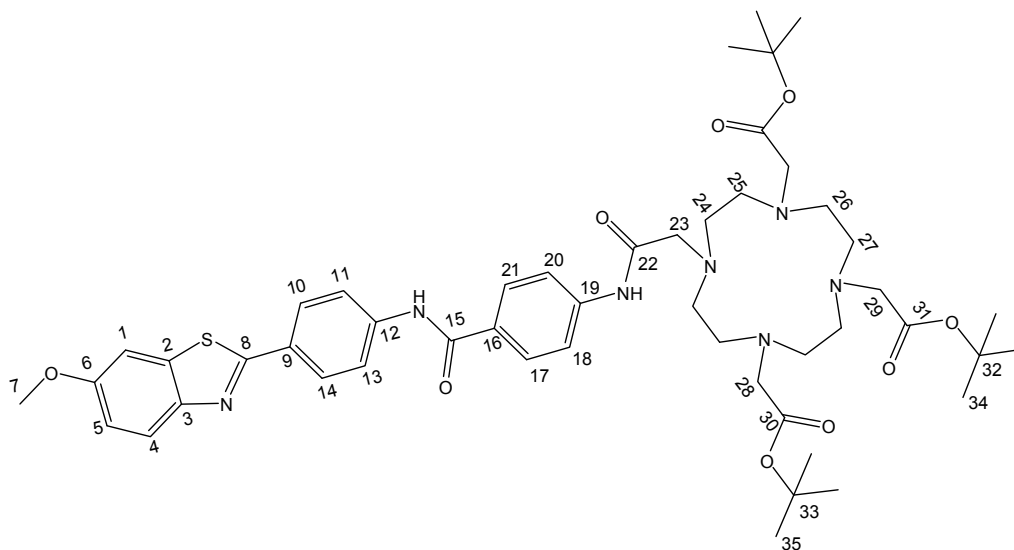
4-(2-chloroacetamido)benzoic acid (8).

A biphasic reaction containing **7** (1.2 g, 8.8 mmol) in 45 ml of CH₂Cl₂ and an aqueous 0.1M NaOH solution was performed adding a solution of chloroacetyl chloride (0.9 ml, 11.2 mmol) in 15 ml of CH₂Cl₂. The mixture was stirred 3h at room temperature and the aqueous phase was acidified at pH ~ 2 with an aqueous solution of 0.2M HCl. The organic phase was extracted by various (~6) washing processes with CH₂Cl₂, dried over MgSO₄ and the solvent was evaporated. The crude product was dissolved in a small amount of acetone and diethyl ether was added afterwards. Stand overnight at -5°C for recrystallisation and pale yellowish crystals were filtered to give 1.56 g of compound **8** (82 %). ¹H NMR (CDCl₃, 25°C, 500MHz): δ (ppm) 4.294 (s, 2H, , *H*-9), 4.41 (s, 2H, *H*-16), 7.705 (d, *J* = 8.5 Hz, 1H, *H*-4, 6), 7.905 (d, *J* = 8.5 Hz, 1H, *H*-3, 7), 10.660 (s, -OH). ¹³C NMR (CDCl₃, 25°C, 500 MHz): δ (ppm) 43.948 (*C*-9), 119.04 (*C*-4, 6), 130.830 (*C*-3, 7), 142.868 (*C*-2), 165.519 (*C*-8), 167.293 (*C*-1).

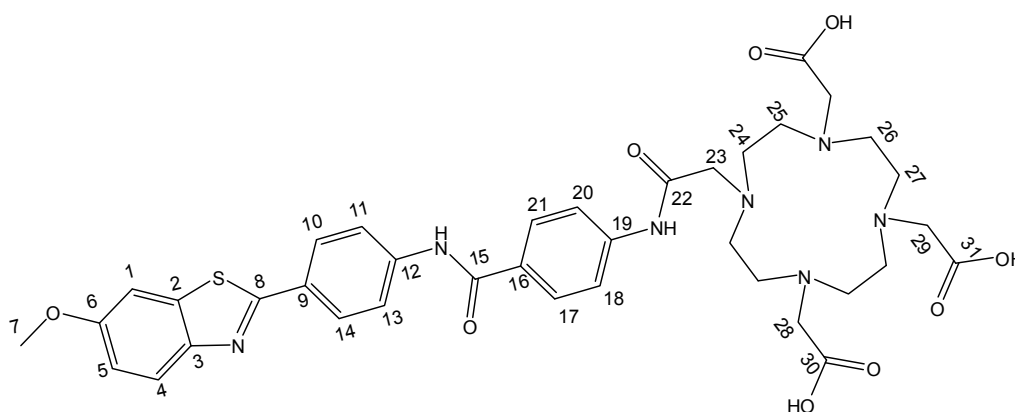


4-(2-chloroacetamido)-N-(4-(6-methoxybenzothiazol[d]thiazol-2-yl)phenyl)benzamide (9). A solution of **8** (1.2 g, 5.6 mmol) was solubilised in SOCl₂ for 2h at 50°C. The SOCl₂ was evaporated under vacuum, heating at 40°C and the crude product (1.2g, 5.2 mmol) was introduced in a 45 ml acetone solution containing **5** (1.2 g, 4.7 mmol) with potassium carbonate (2.14 g, 15.6 mmol) and the mixture was stirred overnight. The solid was filtered and washed with acetone, and then solvents were evaporated. The crude product was dissolved in a small amount of acetonitrile and the precipitate obtained was filtered to give 1.05 g of compound **9** (50 %). ¹H NMR (DMSO, 25°C, 500 MHz): δ (ppm) 3.855 (s, 3H, *H*-23), 4.315 (s, 2H, *H*-1), 7.123 (d, *J* = 6.5 Hz, 1H, *H*-20), 7.7 – 8.13 (m, 10H, *H*-18, 21, 5, 4, 2, 8, 12, 11, 14, 15), 10.438 (s, NH), 10.615 (s, NH). ¹³C NMR (DMSO, 25°C, 500 MHz): δ (ppm) 43.6 (*C*-1), 55.75 (*C*-23), 104.926 (*C*-18), 115.79 (*C*-18), 118.62 (*C*-11, 15), 119.076 (*C*-20), 120.386 (*C*-4, 8), 123.145 (*C*-21), 127.457 (*C*-12, 14), 128.086 (*C*-13), 128.891 (*C*-5, 7), 129.55 (*C*-6),

131.89 (C-17), 135.83 (C-10), 141.631 (C-3), 141.752 (C-22), 148.098 (C-19), 157.366 (C-9), 164.395 (C-2), 165.073 (C-16).

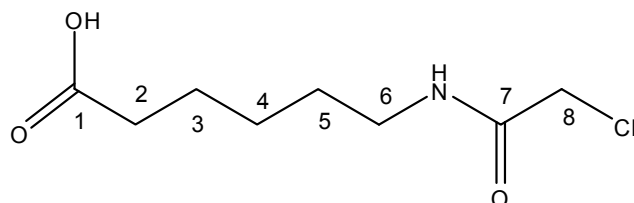


6-methoxybenzo[d]thiazol-2-yl)phenyl)carbamoyl)phenyl)amino)-2-oxoethyl)-tri-*tert*-Bu₃DO3A (pL₂). To a solution of DO3A-*t*Bu₃ **13** (300 mg, 0.58 mmol) with potassium carbonate (226 mg, 2 mmol) in 20 ml of dry acetonitrile, was added a solution of **9** (316 mg, 0.7 mmol) in 15 ml of dry acetonitrile at room temperature. The reaction was stirred for 48 h at room temperature and followed by TLC. The solid was filtered off and the solvent was evaporated. The crude product was purified by flash chromatography with dichloromethane-ethyl acetate (9/2). 200 mg of product pL₂ was obtained as orange oil (38%). ¹H NMR (CDCl₃, 25°C, 500 MHz): δ (ppm) 1.415 (t, 27H, -OtBut, *H*-33,34), 2.8-3.44 (bs, 18H, *H*-25, 24, 26, 27, 23), 3.84 (s, 3H, *H*-7), 7.015-8.072 (m, 11H, *H*-1, 5, 4, 10, 14, 11, 13, 21, 17, 20, 18), 10.159 (s, NH), 11.193 (s, NH). ¹³C NMR (CDCl₃, 25°C, 500 MHz): δ (ppm) 27.870 (C-34, 35), 42.263 (C-24, 25, 26, 27), 45.432 (C-29, 28), 67.26 (C-23), 81.988 (C-32), 82.132 (C-33), 104.130 (C-1), 115.400 (C-5), 119.378 (C-11, 13), 120.754 (C-20, 18), 123.305 (C-4), 124.659 (C-12), 127.672 (C-10, 14), 128.440 (C-16), 128.754 (C-21, 17), 130.845 (C-2), 136.245 (C-9), 141.720 (C-19), 142.382 (C-3), 148.705 (C-6), 157.492 (C-8), 164.623 (C-15), 165.530 (C-22), 166.112 (C-30), 171.372 (C-31).



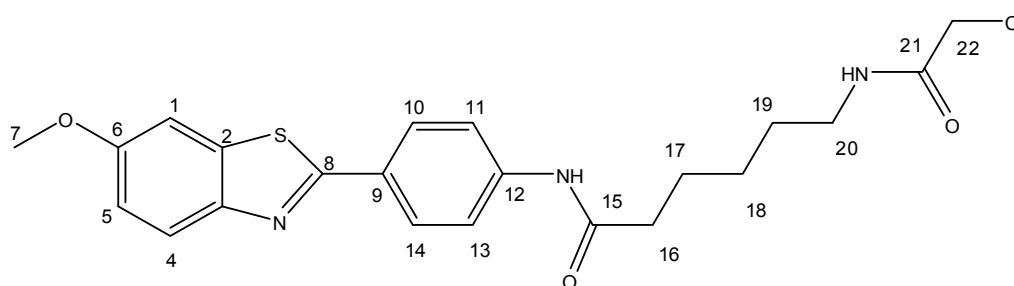
6-methoxybenzo[d]thiazol-2-yl)phenyl)carbamoyl)phenyl)amino)-2-oxoethyl)-DO3A (L₂**). The compound **pL₂** (200 mg, 0.22 mmol) was dissolved in a mixture of trifluoroacetic acid and dry dichloromethane (1:1) and heated at 45°C overnight. The solvents were evaporated and the crude product was dried under vacuum. The crude product was dissolved in a small amount of absolute ethanol and then diethyl ether was added and the mixture was allowed to stand overnight at -5°C. 130 mg of yellowish crystals were filtered and dried under vacuum (78 %). ¹H NMR (D₂O, 50°C, 500 MHz): δ (ppm) 2.75 (bs, 8H, *H*-22, 28, 29), 3.472 (bs, 16H, *H*-25, 24, 26, 27), 3.95 (s, 3H, *H*-7), 7.44 – 8.1 (m, 11H, *H*-1, 4, 5, 10, 14, 11, 13, 21, 17, 20, 18). HRMS (ESI): *m/z*: *calc*d for C₃₆H₄₉N₇O₉S: 761.284, found 761.244.**

3.5.5. Synthesis of **L₃**

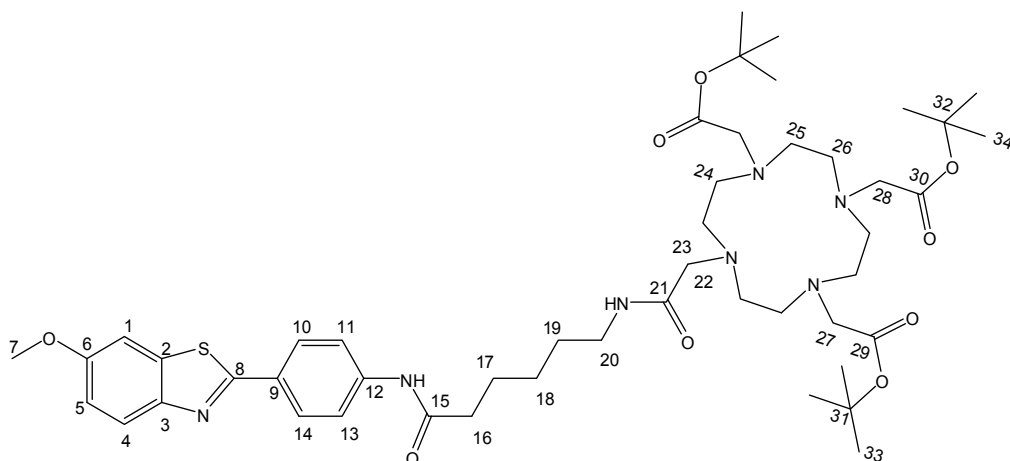


6-(2-chloroacetamido)hexanoic acid (11). To a biphasic mixture containing **10** (1.5 g, 11.4 mmol) in 45 ml of CH₂Cl₂ and an aqueous of 0.1M NaOH, a solution of chloroacetyl chloride (1.05 ml, 13.08 mmol) in 15 ml of

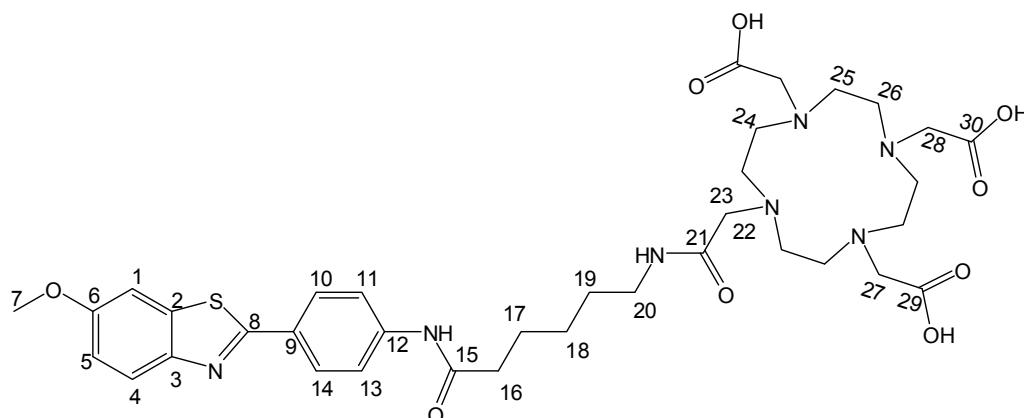
CH₂Cl₂ was added. The mixture was stirred 3h at room temperature and the aqueous phase was acidified at pH ~ 2 with an aqueous solution of 0.2M HCl. After extraction with CH₂Cl₂, the solvents were evaporated. The organic phase was extracted by various washing processes with CH₂Cl₂, dried over MgSO₄ and the solvent was evaporated. The crude product was dissolved in a small amount of acetone and diethyl ether was added afterwards. Stand overnight at -5°C for recrystallisation and bright yellow crystals were filtered to give 1.7 g of compound **11** (72 %). ¹H NMR (CDCl₃, 25°C, 500MHz): δ (ppm) 1.873 (m, 2H, , *H*-3), 2.384 (t, 2H, *H*-2), 3.353 (q, 2H, *H*-4), 4.032 (s, 2H, *H*-6), 6.984 (s, 1H, *H*-6), 10.928 (s, -OH). ¹³C NMR (CDCl₃, 25°C, 500 MHz): δ (ppm) 24.399 (*C*-3), 31.499 (*C*-2), 39.582 (*C*-4), 42.678 (*C*-6), 167.173 (*C*-5), 177.431 (*C*-1).



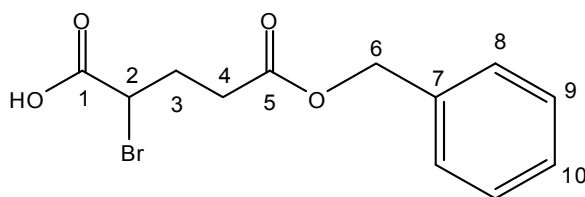
6-(2-chloroacetamido)-N-(4-(6-methoxybenzothiazol)hexanamide (12). A solution of **10** (1.2 g, 5.6 mmol) was solubilised in SOCl₂ for 1h at 25°C. The SOCl₂ was evaporated under vacuum at 25°C, solubilised in chloroform and extracted with a solution of NaOH aqueous (pH~9). The crude chlorinated product (1.2g, 5.2 mmol) was introduced in a 45 ml acetonitrile solution containing **5** (1.2 g, 4.7 mmol) with potassium carbonate (2.14 g, 15.6 mmol) and the mixture was stirred overnight at room temperature. The solid was filtered and washed with acetonitrile, and then solvents were evaporated. The crude product was dissolved in a small amount of acetonitrile and the precipitate obtained was filtered to give 2.04 g of compound **12** (82 %). ¹H NMR (CDCl₃, 25°C, 500 MHz): δ (ppm) 1.30 (t, 2H, *H*-18), 1.45 (t, 2H, *H*-19), 1.60 (t, 2H, *H*-17), 2.34 (t, 2H, *H*-16), 3.1 (m, 2H, *H*-20), 3.85 (s, 3H, -OCH₃, *H*-7), 4.40 (s, 2H, *H*-22), 7.11 (d, J = 8.0 Hz, 1H, *H*-5), 7.68 (s, 1H, *H*-1), 7.76 (d, J = 7.5 Hz, 2H, *H*-11,13), 7.89 (d, J = 7.5 Hz, 1H, *H*-4), 7.96 (d, J = 8 Hz, 2H, *H*-10,14), 8.20 (s, NH), 10.18 (s, NH).



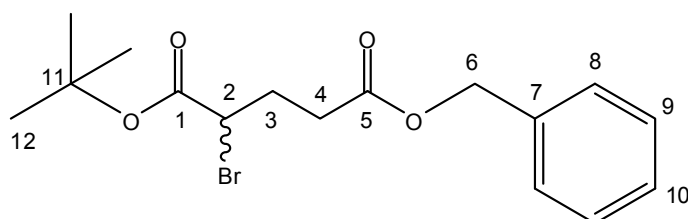
6-methoxybenzo[d]thiazol-2-yl)phenyl)amino)6-oxohexyl)amino)-2-oxoethyl)-tri-*t*Bu₃DO3A (pL₃). To a solution of DO3A-*t*Bu₃ (600 mg, 1.16 mmol) with potassium carbonate (552 mg, 4 mmol) in 20 ml of dry acetonitrile, was added a solution of **12 (400 mg, 0.89 mmol) in 15 ml of dry acetonitrile. The reaction was stirred for 48 h at room temperature and followed by TLC. The solid was filtered off and the solvent was evaporated. The crude product was purified by flash chromatography with dichloromethane-ethyl acetate (9/4). 750 mg of product **pL₃** was obtained as yellow oil (93%). ¹H NMR (CDCl₃, 25°C, 500 MHz): δ (ppm) 1.25 (t, 27H, -OtBut, *H*-33,34), 1.46 (bs, 2H, *H*-18), 1.60 (bs, 4H, *H*-19, 17), 2.43 (bs, 2H, *H*-15), 2.67 (s, 16H, *H*-25, 26, 23, 24), 2.74 (s, 8H, *H*-22, 27, 27', 28), 3.06 (bs, 2H, *H*-22), 3.7 (s, 3H, -OCH₃, *H*-7), 6.84 (d, *J* = 9.0, 1H, *H*-5), 7.10 (bs, 1H, *H*-1), 7.67 (d, *J* = 8.5, 1H, *H*-4), 7.77 (d, *J* = 8.5 Hz, 2H, *H*-11,13), 7.89 (d, *J* = 8.5 Hz, 2H, *H*-14,10), 8.26 (s, NH), 10.18 (s, NH). ¹³C NMR (CDCl₃, 25°C, 500 MHz): δ (ppm) 25.025 (*C*-18), 25.566 (*C*-17), 27.750 (*C*-34), 27.861 (*C*-33), 27.943 (*C*-22), 28.139 (*C*-19), 37.077 (*C*-16), 38.393 (*C*-20), 55.425 (*C*-25, 26), 55.632 (*C*-27, 28), 55.788 (*C*-24,23), 56.146 (*C*-7), 81.705 (*C*-32), 81.758 (*C*-31), 104.243 (*C*-1), 115.289 (*C*-5), 119.978 (*C*-11,13), 123.164 (*C*-4), 127.483 (*C*-10,14), 127.951 (*C*-9), 136.122 (*C*-2), 142.415 (*C*-12), 148.711 (*C*-3), 157.475 (*C*-6), 165.673 (*C*-21), 171.623 (*C*-8), 172.332 (*C*-29,30), 173.51 (*C*-15).**



-methoxybenzo[d]thiazol-2-yl)phenyl)amino)6-oxohexyl)amino)-2-oxoethyl)-DO3A (L₃). The compound **pL₃** (750 mg, 0.81 mmol) was dissolved in a mixture of trifluoroacetic acid and dry dichloromethane (1:1) and heated at 45°C overnight. The solvents were evaporated and the crude product was dried under vacuum. The crude product was dissolved in a small amount of CH₂Cl₂, and then acetone was added to the mixture and stand overnight at -5°C for recrystallisation. 450 mg of yellowish crystals were filtered and dried under vacuum (73 %). ¹H NMR (D₂O, 50°C, 500 MHz): δ (ppm) 1.71 (ms, 2H, *H*-18), 1.91 (bs, 2H, *H*-19), 1.98 (bs, 2H, *H*-17), 2.61 (s, 2H, *H*-16), 2.67 (s, 2H, *H*-20), 3.6 (bs, 12H, *H*-25, 26, 24), 3.70 (s, 2H, *H*-22), 3.74 (s, 3H, -OCH₃, *H*-7), 3.89 (s, 4H, *H*-25, 26), 4.10 (s, 5H, *H*-24, 23), 4.26 (s, 4H, *H*-27), 4.31 (s, 2H, *H*-28), 6.98 (s, 1H, *H*-1), 7.17 (s, 1H, *H*-4), 7.59 (s, 4H, *H*-10,14,11,13), 7.87 (d, 1H, *H*-5). ¹³C NMR (D₂O, 50°C, 500 MHz): δ (ppm) 25.39 (*C*-17), 26.619 (*C*-18), 28.784 (*C*-19), 37.279 (*C*-16), 40.135 (*C*-20), 49.9 (*C*-23,24), 51.33 (*C*-25, 26), 54.481 (*C*-28), 55.38 (*C*-22), 55.9 (-O-CH₃, *C*-7), 56.229 (*C*-27), 104.835 (*C*-1), 116.52 (*C*-5), 120.63 (*C*-11,13), 122.632 (*C*-4), 127.255 (*C*-9), 127.97 (*C*-10,14), 135.317 (*C*-2), 141.23 (*C*-12), 146.258 (*C*-3), 157.919 (*C*-6), 162.99 (*C*-21), 163.276 (*C*-8), 166.543 (*C*-15), 172.556 (*C*-30), 174.842 (*C*-29). HRMS (ESI): *m/z*: *cacd* for C₃₆H₄₉N₇O₉S: 755.331, found 755.265.

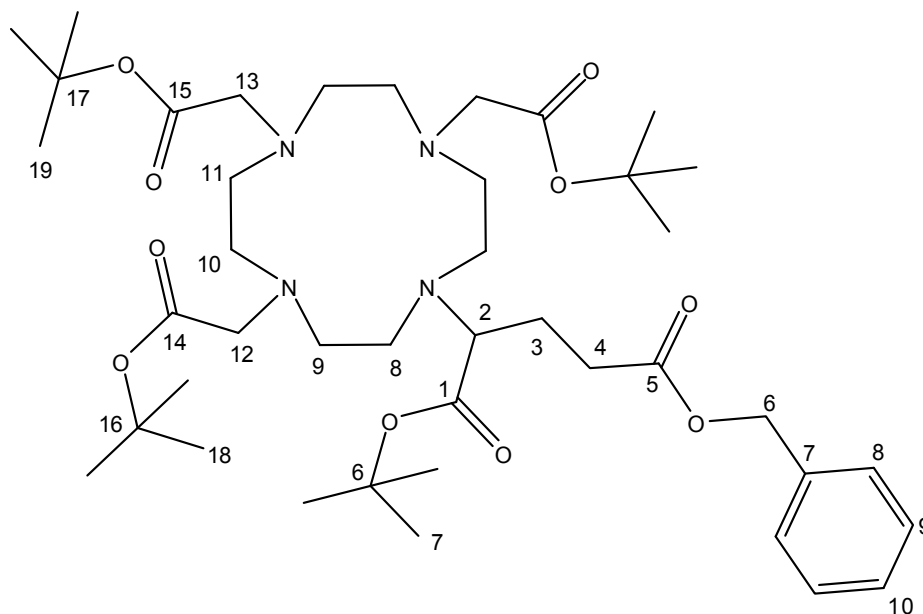
3.5.6. Synthesis of L₄

5-(benzyloxy)-2-bromo-5-oxopentanoic acid (15). To a solution of **14** L-Glutamic acid γ -benzyl ester (2 g, 8.43 mmol), 3.03g of NaBr (29.7 mmol) in 20 ml of aqueous 1N HBr were added in cold (0°C), NaNO₂ (1.06g, 17.6 mmol) and stirred for 2 hours. After that, 750 μ L of concentrated H₂SO₄ were added to the reaction and the water phase was extracted with diethyl ether 4 times. The organic phase was washed with brine, dried with Na₂SO₄ and the solvents evaporated in vacuum. The concentrated product gave 1.62 g of compound **15** (64 %). ¹H NMR (CDCl₃, 25°C, 500 MHz): δ (ppm) 2.429 (dm, 2H, *H*-3), 2.609 (m, 2H, *H*-4), 4.435 (q, 1H, *H*-2), 5.172 (s, 2H, *H*-6), 7.36 (m, 1H, *H*-10), 7.4 (s, 2H, *H*-8, 9), 9.369 (s, -OH). ¹³C NMR (CDCl₃, 25°C, 500 MHz): δ (ppm) 29.547 (*C*-3), 31.595 (*C*-4), 44.448 (*C*-2), 66.884 (*C*-6), 128.356 (*C*-10), 128.489 (*C*-8), 128.708 (*C*-9), 135.572 (*C*-7), 172.359 (*C*-1), 174.068 (*C*-5).

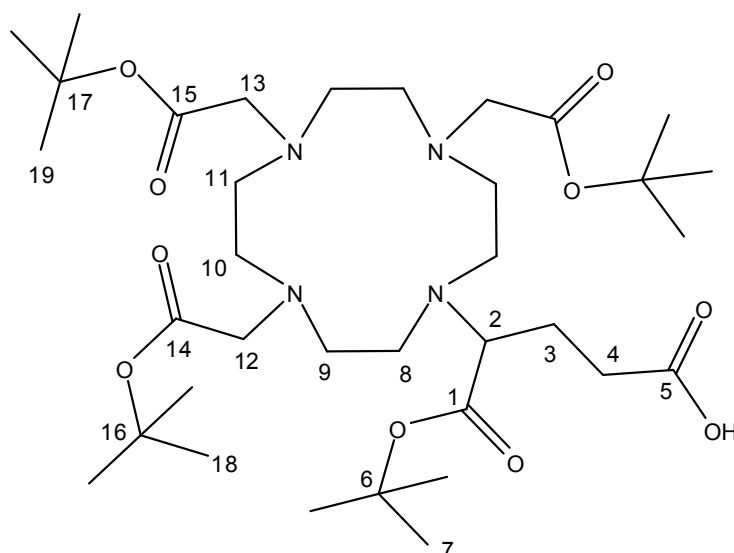


5-benzyl 1-tert-butyl 2-bromopentanedioate (16). To a solution of **15** (1.2 g, 3.9 mmol) in 20mL CHCl₃ a solution of 1.50mL (8.2 mmol) TBTA (tert-butyltrichloroacetimidate) in 20mL cyclohexane was added dropwise over 20 min. Then 3mL of dimethylacetamide (DMA) followed by 200 ml boron trifluoride ethyl etherate as catalyst. The reaction mixture was stirred for 3 days at room temperature. The mixture was concentrated and the remaining DMA phase was extracted three times with 30mL hexane. The hexane phase was evaporated and the residue chromatographed over silica gel 60 (CH₂Cl₂:EtOAc 9:1) affording 0.8 g (58%) of a colorless liquid. ¹H NMR (CDCl₃, 25°C, 500 MHz): δ (ppm) 1.445 (s, 9H, *H*-12), 2.295 (dm, 2H, *H*-3), 2.5 (m, 2H, *H*-4), 4.23 (q, 1H, *H*-2), 5.086 (s,

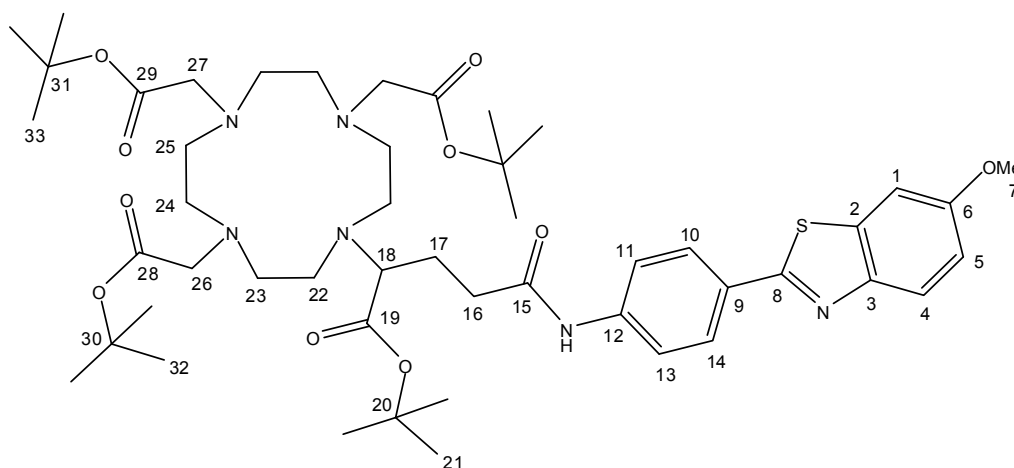
2H, *H-6*), 7.262 (m, 1H, *H-10*), 7.281 (s, 2H, *H-8, 9*). ^{13}C NMR (CDCl_3 , 25°C , 500 MHz): δ (ppm) 27.425 (*C-12*), 29.481 (*C-3*), 31.267 (*C-4*), 46.393 (*C-2*), 66.087 (*C-6*), 82.042 (*C-11*), 127.940 (*C-10*), 127.995 (*C-9*), 128.298 (*C-8*), 135.612 (*C-7*), 167.879 (*C-1*), 171.447 (*C-5*).



Tris-tert-butoxy-DOTAGA-5-benzyloxy-1-tert-butoxy (17). To a solution of **13** tri-tert-butyl-DO3A (0.518 g, 1.06 mmol) with 700mg of potassium carbonate in 45 ml of dry acetonitrile was added a solution of **16** (0.43g, 1.3 mmol) in 15 ml of dry acetonitrile and the mixture was stirred and refluxed over 48h. The solid was filtered and washed with dichloromethane, and then solvents were evaporated. The crude product was purified by column chromatography (silica gel 60; CH_2Cl_2 :EtOH 9:1 followed by EtOH: NH_3 95:5) 0.6 g of yellow oil **17** (72 %). ^1H NMR (CDCl_3 , 25°C , 500 MHz): δ (ppm) 1.418 (s, 36H, *H-12, 23, 24*), 1.885 (ds, 2H, *H-3*), 2.57 (m, 16H, *H-13, 14, 15, 16*), 3.205 (m, 7H, *H-17, 18, 2*), 5.125 (td, 2H, *H-6*), 7.312 (bs, 5H, *H-8, 9, 10*). ^{13}C NMR (CDCl_3 , 25°C , 500 MHz): δ (ppm) 25.148 (*C-3*), 28.330 (*C-23, 24, 12*), 30.771 (*C-4*), 49.703 (*C-13*), 52.196 (*C-16*), 52.388 (*C-15*), 52.679 (*C-14*), 56.083 (*C-18*), 56.319 (*C-17*), 63.745 (*C-6*), 66.147 (*C-2*), 80.660 (*C-11*), 80.687 (*C-21*), 80.895 (*C-22*), 128.216 (*C-10*), 128.328 (*C-9*), 128.606 (*C-8*), 136.245 (*C-7*), 171.073 (*C-19*), 171.228(*C-20*), 172.435 (*C-1*), 173.675 (*C-5*).

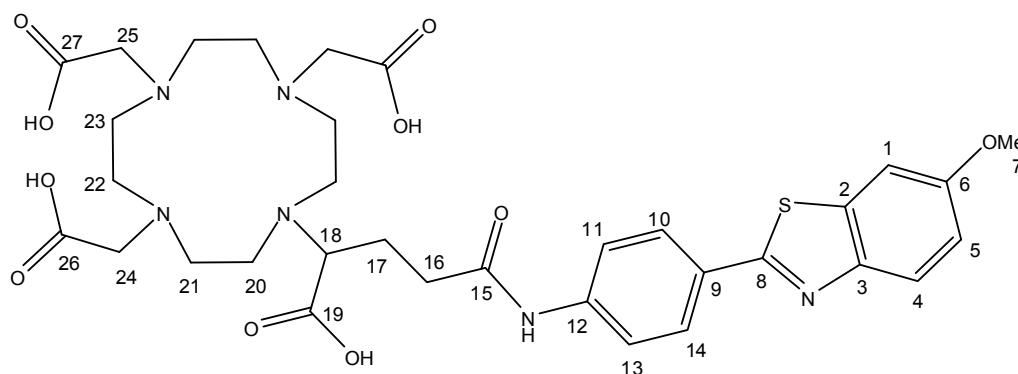


Tris-tert-butoxy-DOTAGA-1-tert-butoxy (18). To a solution of **17** (0.6 g, 0.76mmol) in 15 ml of THF was added LiOH (75mg, 3.04mmol) in 15 ml of water and the mixture was stirred 3h. The THF was evaporated and the solution was acidified at pH ~ 3 with 1N HCl. The product was extracted from the aqueous solution with chloroform for three times. The organic phase was dried with Na₂SO₄, filtered and then solvents were evaporated to get 0.36 g of compound **18** (67 %). ¹H NMR (CDCl₃, 25°C, 500 MHz): δ (ppm) 1.86 (d, 2H, *H*-4), 1.39 (s, 36H, *H*-7, 18, 19), 2.372 (ds, 2H, *H*-3), 2.904 (m, 16H, *H*-8, 9, 10, 11), 3.369 (s, 2H, , *H*-13), 3.419 (bs, 3H, *H*-12, 2), 7.902 (s, -OH). ¹³C NMR (CDCl₃, 25°C, 500 MHz): δ (ppm) 24.849 (*C*-3), 27.901 (*C*-18, 19, 7), 32.503 (*C*-4), 48.440 (*C*-8), 50.684 (*C*-11), 51.721 (*C*-10), 52.104 (*C*-9), 55.532 (*C*-13), 55.582 (*C*-12), 63.413 (*C*-7), 81.059 (*C*-6), 81.193 (*C*-16), 81.581 (*C*-17), 169.518 (*C*-14), 171.430 (*C*-15), 172.428 (*C*-1), 176.298 (*C*-5).

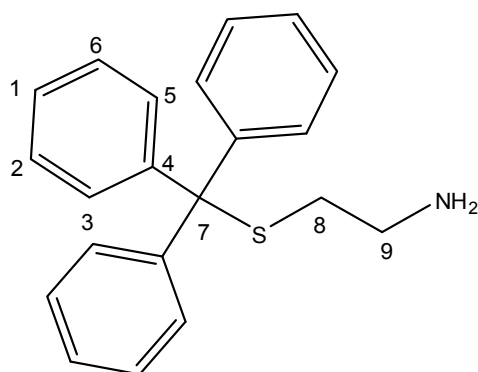


Tris-tert-butoxy-DOTAGA-1-tert-butoxy-6-methoxy-benzothiazol (19). A solution of the amine **5** BTA derivative (0.18g, 0.70mmol) in CH_2Cl_2 (45 mL) is added to an ice-cooled solution with compound **18** (0.41g, 0.58mmol) containing HOBT (2.0 equiv) in CH_2Cl_2 . EDC (1.50 equiv) is added to the mixture, which is then stirred at room temperature for 7 days, followed by TLC (it was still not completed). The reaction mixture is diluted with dichloromethane and washed with brine, dried with MgSO_4 , and filtered. The crude product was purified by column chromatography (silica gel 60; CH_2Cl_2 :EtOAc 8:2 followed by EtOAc:MeOH 95:5) and 0.3g of product **19** was obtained with a yield of 16%.

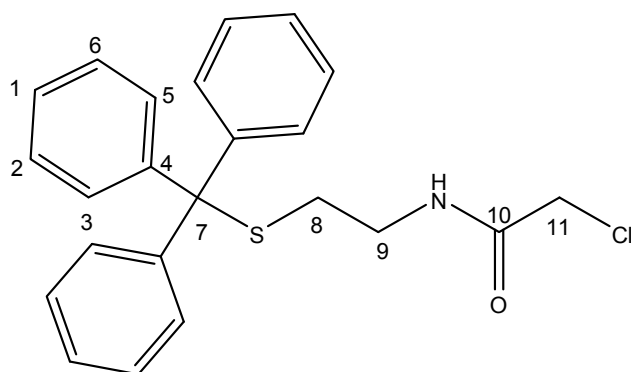
^1H NMR (CDCl_3 , 25°C , 500 MHz): δ (ppm) 1.375 (bs, 36H, *H*-21, 32, 33), 1.856 (bs, 2H, *H*-16), 2.113 (bs, 2H, *H*-17), 2.53 (ms, 8H, *H*-25, 24), 2.78 (s, 8H, *H*-23, 22), 3.133 (bs, 6H, *H*-26, 27), 3.175 (s, 1H, *H*-18), 3.78 (s, 3H, $-\text{OCH}_3$, *H*-7), 6.973 (d, $J = 9.0$, 1H, *H*-5), 7.247 (bs, 1H, *H*-1), 7.746 (d, $J = 8.5$, 1H, *H*-4), 7.812 (d, $J = 8.5$ Hz, 2H, *H*-11,13), 7.89 (d, $J = 8.5$ Hz, 2H, *H*-14,10). ^{13}C NMR (CDCl_3 , 25°C , 500 MHz): δ (ppm) 24.872 (*C*-17), 28.195 (*C*-21, 32, 33), 33.119 (*C*-16), 49.329 (*C*-22), 52.532 (*C*-23), 52.774 (*C*-25), 53.253 (*C*-24), 55.724 (*C*-7), 56.768 (*C*-26), 57.037 (*C*-27), 62.383 (*C*-18), 80.807 (*C*-31), 80.902 (*C*-30), 80.986 (*C*-20), 104.182 (*C*-1), 115.408 (*C*-5), 119.648 (*C*-11,13), 123.170 (*C*-4), 127.670 (*C*-10,14), 128.598 (*C*-9), 136.190 (*C*-2), 142.412 (*C*-12), 148.701 (*C*-3), 157.554 (*C*-6), 165.337 (*C*-21), 171.112 (*C*-19), 171.324 (*C*-8), 172.304 (*C*-28), 172.489 (*C*-15).



DOTAGA-6-methoxy-benzothiazol (L₄). a) The compound **19** (0.3g, 0.32mmol) was dissolved in a mixture of trifluoroacetic acid and dry dichloromethane (1:1) and heated at 45°C overnight. The solvents were evaporated and the crude product was dried under vacuum. The crude product was dissolved in a small amount of absolute ethanol and then dimethyl ether was added and the mixture was allowed to stand overnight at -5°C. 450 mg of yellowish crystals were filtered and dried under vacuum (73 %). b) A solution of DOTAGA-anhydride **20** in DMF at 70°C was put into reaction with a solution of the **5** BTA derivative (1.2 equiv) in the presence of triethylamine (3 equiv). The mixture was heated 36h. After the evaporation of DMF, the crude solid was purified by reverse phase column chromatography on C18. After evaporation of acetonitrile, the aqueous solution was lyophilized to afford a pale yellow solid of **L₄** with 35% yield. ¹H NMR (D₂O, 50°C, 500 MHz): δ (ppm) 2.415 (ms, 2H, *H*-23), 2.732 (ms, 2H, *H*-22), 3.024 (bs, 4H, *H*-20,21), 3.335 (dd, 2H, *H*-16), 3.614 (t, 2H, *H*-17), 3.8 (ms, 4H, *H*-25, 24), 3.929 (s, 4H, -OCH₃, *H*-18), , 7.58 (d, 2H, *H*-11,13), 7.935 (s, 1H, *H*-1), 8.0 (s, 1H, *H*-4), 8.243 (ds, 1H, *H*-5), 8.31 (ds, 2H, *H*-14,10). HRMS (ESI): *m/z*: *ca*cd for C₃₆H₄₉N₇O₉S: 714.79, found 714.276.

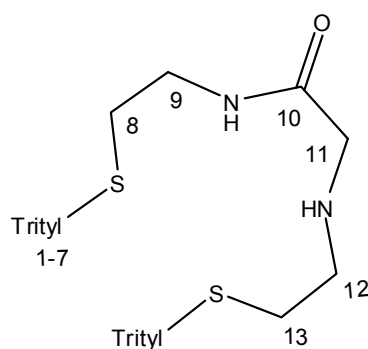
3.5.7. Synthesis of L₅

S-triphenylmethyl-1-aminoethanethiol (22). Triphenylmethanol (3.40 g, 14 mmol) and 2-aminoethanethiol hydrochloride (175 g, 1.1 equiv.) were stirred in pure trifluoroacetic acid (100 mL) for 4 h at room temperature. After evaporation of TFA, the residual oil was dissolved in DCM and the pH was raised to 9 by dropwise addition of 1 M sodium bicarbonate. Elimination of DCM under reduced pressure led to the formation of a white precipitate which was isolated by filtration to give **22**. The product was recrystallized with 100mL of diethyl ether at -25°C. (5.13 g, 79%); ¹H NMR (CDCl₃, 25°C, 500 MHz): δ (ppm) 2.27 (t, 2H, *J* = 6.5Hz, *H*-8), 2.6 (t, 2H, *J* = 7Hz, *H*-9), 7.44–7.19 (m, 15H, (*H*-1, 2, 3, 5, 6)*x*3), 7.79 (s, 2H, -NH₂). ¹³C NMR (CDCl₃, 25°C, 500 MHz): δ (ppm) 31,751 (*C*-8), 38.013 (*C*-9), 66.885 (*C*-7), 126.567 (*C*-1), 127.463 (*C*-3, 5), 127.739 (*C*-2, 6), 143.608 (*C*-4).

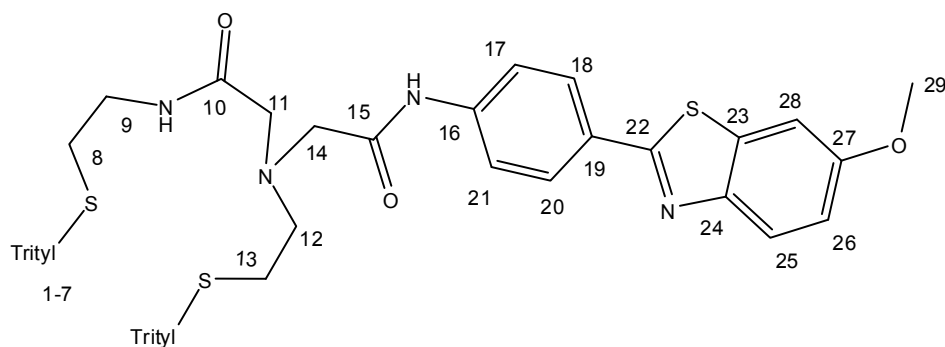


BrAc-S-trityl-cysteamine (23). Compound **22** (2.5g, 7.8mmol) and chloroacetylchloride (1.3g, 11.7mmol) were stirred in 80 mL anhydrous dichloromethane, and 3ml of triethylamine (3ml, 21.3mmol), for 3hours at room temperature. The reaction was followed by TLC (dichloromethane). The final

solution was washed with an aqueous solution of sodium bicarbonate and the organic layer taken. The organic phase dehydrated and concentrated by Na_2SO_4 . Evaporation of the dichloromethane under reduced pressure gave the final product **23** (2.3g, 75%). ^1H NMR (CDCl_3 , 25°C , 500 MHz): δ (ppm) 2.45 (t, 2H, $J=6.5\text{Hz}$, $H-8$), 3.16 (q, 2H, $J=6\text{Hz}$, $H-9$), 3.99 (s, 2H, $H-11$), 6.685 (s, 1H, -, NH), 7.32–7.22 (m, 15H, ($H-1$, 2, 3, 5, 6) $\times 3$), 7.79 (s, 2H, $-\text{NH}_2$). ^{13}C NMR (CDCl_3 , 25°C , 500 MHz): δ (ppm) 31,714 ($C-8$), 38.388 ($C-9$), 42.561 ($C-11$), 66.95 ($C-7$), 126.867 ($C-1$), 128.016 ($C-3$, 5), 129.531 ($C-2$, 6), 144.537 ($C-4$), 165.650 ($C-10$).



Tris S-trityl-N₂S₂ (24). Compound **23** (2g, 5.05mmol) and compound **22** (2.58g, 8.05mmol) were stirred in 80 mL anhydrous dichloromethane, and 3ml of triethylamine (3ml, 21.3mmol), and then the solution was heated under reflux for four days. After cooling down, the product was extracted with CH_2Cl_2 and an aqueous solution of sodium bicarbonate. The organic layer was taken and dehydrated by Na_2SO_4 . The solvents were evaporated and the crude product was purified by column chromatography on silica gel (CH_2Cl_2 :EtOAc 8:3) to give compound **24** (2.2 g, 65%). ^1H NMR (CDCl_3 , 25°C , 500 MHz): δ (ppm) 2.39 (m, 4H, $H-8$, 13), 2.48 (t, 2H, $J=6\text{Hz}$, $H-12$), 3.099 (s, 2H, $H-11$), 3.121 (q, 2H, $J=6\text{Hz}$, $H-9$), 7.44–7.21 (m, 15H, ($H-1$, 2, 3, 5, 6) $\times 3$). ^{13}C NMR (CDCl_3 , 25°C , 500 MHz): δ (ppm) 31,634 ($C-13$), 31,956 ($C-8$), 37.290 ($C-12$), 47.897 ($C-9$), 51.401 ($C-11$), 66.289 and 66.320 ($C-7$, 7'), 126.305 and 126.320 ($C-1$, 1'), 127.510 ($C-3$, 5), 129.121 ($C-2$, 6), 144.275 ($C-4$), 170.878 ($C-10$).



N-(4-(6-methoxybenzo[d]thiazol-2-yl)phenyl)-2-((2-oxo-2-((2-(tritylthio)ethyl) amino)ethyl)(2-(tritylthio)ethyl)acetamide (**pL₅**). To a 100 mL CH₂Cl₂ solution containing 0.558 g (0.822 mmol) of **24** and 0.383 g (1.15 mmol) of compound **6** were added 0.31 g (2.24 mmol) K₂CO₃ and 0.130 g (0.87 mmol) of NaI and the reaction mixture was brought to reflux. After 7 days, reflux was ceased and the reaction mixture was concentrated to a dark red residue which was taken up in 100 mL CH₂Cl₂ and washed with NaHCO₃(aq) and brine, dried over MgSO₄ and concentrated. Flash chromatography on silica gel (CH₂Cl₂:EtOAc 9:1) yielded 0.25 g (31%) of product as a pale orange foam solid. ¹H NMR (CDCl₃, 25°C, 500 MHz): δ (ppm) 2.43 (m, 4H, *H*-8, 13), 2.47 (t, 2H, *J* = 6Hz, *H*-12), 3.036 (q, 2H, *J*=6Hz, *H*-9), 3.175 (s, 2H, *H*-11), 3.9 (s, 3H, *H*-29), 6.390 (t, 1H, *J* = 6Hz, *H*-26), 7.111 (d, 1H, *J* = 6Hz, *H*-25), 7.45–7.21 (m, 15H, (*H*-1, 2, 3, 5, 6)x3), 7.665 (d, 2H, *J* = 6Hz, *H*-21, 17), 7.771 (d, 2H, *J* = 6Hz, *H*-18, 20), 7.97 (d, 1H, *J* = 9Hz, *H*-28), 9.603 (s, 1H, -NH). ¹³C NMR (CDCl₃, 25°C, 500 MHz): δ (ppm) 29.855 (*C*-13), 31.544 (*C*-8), 37.577 (*C*-12), 53.725 (*C*-9), 55.356 (*C*-29), 57.079 (*C*-11), 59.450 (*C*-14), 66.598 and 67.119 (*C*-7, 7'), 103.807 (*C*-28), 115.026 (*C*-26), 118.923 (*C*-17, 21), 123.053 (*C*-25), 126.302 (*C*-19), 126.553 (*C*-1), 127.523 (*C*-18,20), 127.632 (*C*-2,6) 128.748 (*C*-3, 5), 129.121 (*C*-2, 6), 135.826 (*C*-23), 139.439 (*C*-16), 144.017 (*C*-4), 148.341(*C*-24), 157.196 (*C*-27), 164.719 (*C*-15), 168.027 (*C*-22), 169.016 (*C*-10).

CHAPTER 4

*”Physical-Chemical
Characterization of
Gd-DO3A-PiB
Derivatives ”*

4.1. Introduction

Magnetic Resonance Imaging (MRI) offers non-invasive mapping of structure and function with excellent spatial resolution. MR images can be enhanced by improving the contrast with paramagnetic contrast agents (CAs), ideally with specific and selective delivery. Given the high electron spin and slow electronic relaxation of the Gd^{3+} ion, Gd^{3+} complexes are the most widely used MRI contrast materials, ensuring positive contrast (Chapter 1 section 1.3).¹⁶⁴ The efficacy of a contrast agent is measured by its relaxivity defined as the paramagnetic enhancement of the water proton relaxation rate normalized to 1 mM concentration of Gd^{3+} .¹⁶⁴ The overall relaxivity of a CA is the sum of the relaxivities originating from the inner and outer sphere terms, the two contributions being comparable for small molecular weight agents.¹⁶⁵ The inner sphere relaxivity term is determined by the microscopic parameters of the Gd^{3+} complex, the most important being the hydration number (q), the rotational correlation time (τ_R), the water exchange rate (k_{ex}) and the electron spin relaxation times.

The values of τ_R and k_{ex} of the Gd^{3+} complex can be tuned by appropriate ligand design. The maximum relaxivities predicted by the Solomon–Bloembergen–Morgan (SBM) theory can only be attained by chelates displaying simultaneous optimization of k_{ex} , and τ_R , implying also that the molecular constructs/assemblies are rigid enough.¹⁶⁶

As discussed in Chapter 1 (section 1.5 d), so far, the development of MRI contrast agents for the diagnosis of Alzheimer's disease has been modest and limited to two approaches: 1) a GdDTPA probe conjugated to a putrescine-modified human $A\beta_{1-42}$ peptide¹³⁹, and 2) ultrasmall superparamagnetic iron oxide nanoparticles, chemically coupled with the $A\beta_{1-42}$ peptide.¹⁴⁰ In addition, non-specific, clinical contrast agents have been also tested for their utility in the detection of amyloid plaques.^{113,141} T_2^* -weighted MR images without any contrast agent can be also recorded by taking advantage of the paramagnetism of highly iron loaded amyloid plaques.¹⁶⁷

To the best of our knowledge, the Gd^{3+} complexes of ligands $\text{L}_1\text{-L}_3$ are the first small molecular weight, potential MRI contrast agents bearing a specific unit that allows targeting towards amyloid plaques. In Chapter 4, we describe the most important physical-chemical parameters that characterize these complexes with respect to their use as MRI probes for $\text{A}\beta$ amyloid detection. These studies include the determination of the water/octanol partition coefficients characterizing the lipophilicity of the complexes, the determination of the parameters influencing their relaxivity, as well as a relaxometric assessment of their micellization in aqueous solution and their binding to serum albumin and to the $\text{A}\beta_{1-40}$ amyloid peptide.

4.2. Experimental

4.2.1. Sample Preparation

GdL_x , ($x = 1,2,3$) complexes were prepared by mixing GdCl_3 solutions and ligand L_x , ($x = 1,2,3$) in equimolar quantities and the pH of the solution was adjusted to 7 by adding aqueous NaOH (0.1 mM). The solution was allowed to react for 24 hours at 60°C by regularly controlling the pH. The absence of free metal was checked in each sample by using the xylenol orange test.¹⁶⁸ In the relaxometric HSA binding studies, we used 0.6 mM HSA (4%) solutions. For the $\text{A}\beta_{1-40}$ binding studies, the peptide was added directly from the bottle to an equimolar solution of GdL_x , ($x = 1,3$) complex (200 μM) in 0.05 M HEPES buffer at pH 7 and the sample was sonicated. Milli-Q water was always used to avoid metal contamination. The sample containing the reconstituted peptide was used immediately to avoid degradation in solution.

4.2.2. Determination of the Octanol-Water Partition Coefficient

The partition coefficient was determined as a ratio of compound concentration in the octanol phase to the amount of compound in the aqueous phase (Equation (1)). The logarithm of the partition coefficient is referred to as the log P value.

$$\text{Partition Coefficient (P)} = \frac{[\text{Solute}]_{\text{Octanol Phase}}}{[\text{Solute}]_{\text{Aqueous Phase}}} \quad (1)$$

The “shake flask” method was used for the determination of log P.¹⁶⁹ Water saturated with octanol and octanol saturated with water were used in the experiments. The benzothiazol ring absorbs strongly at approximately 330 nm thus the partition was quantified using UV spectrophotometry on a Perkin-Elmer Lambda 19 UV/VIS Spectrophotometer.¹⁷⁰ For each phase, the maximum wavelength (λ_{max}) was verified. A 1:1 volume ratio was used for the partitioning of the solution with GdL_x, (x = 1,2,3). In a 2mL Eppendorf, 0.5ml of a 100 μ M solution of GdL_x, (x = 1,2,3) was added to 0.5ml of the saturated phase of 1-octanol. 30 mins of centrifugation were taken for each sample. GdL_x, (x = 1,2,3) concentrations were determined in each phase using standard curves.

4.2.3. ¹H NMRD measurements

Proton NMRD (nuclear magnetic relaxation dispersion) profiles were recorded on a Stellar SMARtracer Fast Field Cycling NMR relaxometer (0.01-10 MHz) and a Bruker WP80 NMR electromagnet (20, 40, 60 and 80 MHz) adapted to variable field measurements and controlled by a SMARtracer PC-NMR console. The temperature was monitored by a VTC91 temperature control unit and maintained by a gas flow. The temperature was determined by previous calibration with a Pt resistance temperature probe. The longitudinal relaxation rates ($1/T_1$)

were determined in water. Measurements were performed at 25 and 37 °C.

4.2.4. ^{17}O NMR experiments

Variable-temperature ^{17}O NMR measurements were performed on a Bruker Avance-500 (11.7 T) spectrometer and a BVT-3000 temperature control unit were used to stabilize the temperature, measured by a substitution technique. The samples were sealed in glass spheres that fitted into 10 mm o.d. NMR tubes, to eliminate susceptibility corrections to the chemical shifts.^{165,171} Longitudinal relaxation rates $1/T_1$ were obtained by the inversion recovery method and transverse relaxation rates $1/T_2$ by the Carr-Purcell-Meiboom-Gill spin-echo technique. As an external reference, acidified water of pH 3.4 was used.

4.2.5. HSA affinity constants determination for $\text{GdL}_{1,3}$

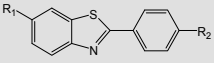
HSA (defatted, from SigmaAldrich, $\leq 0.01\%$ fatty acids and $\leq 1\%$ globulins) affinity constants were assessed by Proton Relaxation Enhancement (PRE) measurements. The proton relaxation rates at increasing concentrations of the protein and of the metal chelate were measured using a Bruker WP80 NMR electromagnet adapted to variable field measurements and controlled by a SMARtracer PC-NMR console (40 MHz, 310 K). Constant concentrations of $\text{GdL}_{1,3}$ (0.1 mM) for the E-titration and 0.6 mM HSA for the M-titration were used.

4.3. Results and discussion

4.3.1. Lipophilicity determined by the partition coefficient

A contrast agent designed to detect amyloid plaques in the brain has to pass the blood brain barrier. The BBB permeability of a compound is related to its i) lipophilicity, often expressed by the water/octanol partition coefficient, $\log P_{\text{oct/water}}$, ii) molecular weight (MW), and iii) plasma pharmacokinetics.¹⁴³ Low MW, amphiphilic molecules are expected to have the best BBB permeability. Typically, compounds with $\log P_{\text{oct/water}} \sim 2$ have optimal BBB penetration. We have determined the $\log P$ values for all the three GdL_x complexes (x = 1,2,3). The $\log P_{\text{oct/water}}$ values obtained are -0.15, 0.32 and 0.03 for GdL₁, GdL₂, and GdL₃, respectively. As expected, these are lower than those for the highly lipophilic PiB itself or for other phenylbenzothiazole derivatives (**Table 4.1**).^{130,143,150}

Table 4.1. Molecular weight (MW) and lipophilicity ($\log P_{\text{Oct/H}_2\text{O}}$) of phenylbenzothiazole (BTA) derivatives

	$\log P_{\text{Oct/H}_2\text{O}}$	MW	Ref.
Thioflavin T	0.57	319	149
R ₁ =CH ₃ , R ₂ =NH ₂	2.6	240	148,149
R ₁ = CH ₃ , R ₂ = NHCH ₃	2.6	254	149
R ₁ = OCH ₃ , R ₂ = NH ₂	1.9	256	149
R ₁ = OH, R ₂ = NHCH ₃ (PiB)	1.23	256	150
R ₁ = OH, R ₂ = ReO-TEEDA	1.21	602	150
R ₁ = OCH ₃ , R ₂ = ReO-TEEDA	2.52	616	150
^{99m} TcO-BAT-Bp-1	0.68	559	135
^{99m} TcO-BAT-Bp-2	1.35	573	135
^{99m} TcO-BAT-Bp-3	2.09	587	135
GdL ₁	-0.15	842	This work
GdL ₂	0.32	918	This work
GdL ₃	0.03	912	This work

However, the $\log P_{\text{oct/water}}$ values are similar to those reported for neutral In(DTPA-bisamide) complexes bearing two hydrophobic chains,¹⁷² and much higher than $\log P_{\text{oct/water}}$ for the double-charged In(DTPA)²⁻ chelate (-2.86). Some Re and Tc complexes have also relatively high, close to optimal $\log P_{\text{oct/water}}$ values and correspondingly, they had interesting BBB passage *in vivo*.¹³⁵ These complexes are structurally very different from those of Gd³⁺. The Gd³⁺ ion is much larger and needs considerably more chelating units in order to form stable and inert complexes, therefore it is not possible to create stable lanthanide complexes as compact as those of Tc or Re. Moreover, the chemical nature of lanthanide ions requires strongly ionic coordinating functions. These factors all contribute to an increased hydrophilic character of the chelates. The addition of bulky lipophilic groups could increase the overall lipophilicity of the complex; however, it would also increase the molecular weight, which disfavours BBB permeability. Indeed, low MW compounds cross the BBB more efficiently with rates that seem to correlate inversely with the square root of their MW,¹⁴⁴ at least for compounds under 600 Da. The molecular weights of the GdL_x complexes are MW = 842, 918, 912 Da, respectively, for x = 1,2,3, above the optimal values. We should note, however, that peptide analogues with a MW over 1000 Da were shown to cross the BBB.^{173,174} From **Table 4.1**, we can note also that neutral complexes with rhenium were reported to have optimal properties, including the blood brain barrier crossing and selective binding to amyloid plaques.¹⁵⁰

4.3.2. Relaxometric measurements

4.3.2.1. Micellar aggregation

Nuclear Magnetic Relaxation Dispersion (NMRD) profiles reflect the magnetic field dependency of the proton relaxivity (r_1) and are commonly used to characterize MRI contrast agents. The NMRD curves of the GdL_x chelates recorded at 0.2 mM (L₁, L₃) and 0.1 mM (L₂) concentrations are characteristic of a small-molecular weight complex (**Figure 4.2**).

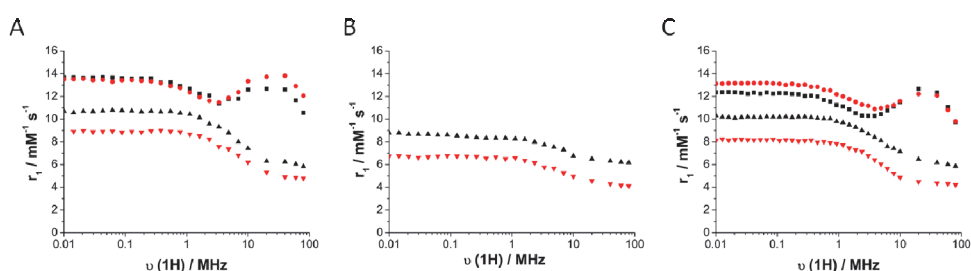


Figure 4.2. ^1H NMRD profiles of **A)** GdL₁, **B)** GdL₂ and **C)** GdL₃ at 0.2 mM (GdL₁ and GdL₃) or 0.1 mM (GdL₃) (\blacktriangledown , \blacktriangle) and at 5 mM (\blacksquare , \bullet) at 25°C (black) and 37° (red) (0.05M HEPES; pH 7.4).

Even at these low concentrations, the GdL_x complexes present relatively high relaxivities when compared to clinical contrast agents (see **Table 1.2** from Chapter 1); the r_1 values are 6.30 mM⁻¹s⁻¹, 6.48 mM⁻¹s⁻¹ and 6.46 mM⁻¹s⁻¹, respectively, for $x = 1,2,3$ at 20MHz, 25°C.^{39,166} These higher r_1 values are the consequence of the slower rotation of the complexes, resulting from the presence of the bulky PiB moiety with respect to the commercial agents.

Upon increasing the concentration to 5 mM, the NMRD profiles change considerably, and correspond to slowly tumbling systems presenting a typical high field peak around 30 MHz proton Larmor frequency (**Figure 4.2, A and C**). The maximum solubility of GdL₂ is very low (0.133 mM, as determined by bulk magnetic susceptibility shift ^1H NMR measurements),¹⁷⁵ which does not allow observing this state. In the case of GdL₁ and GdL₃, the slowly tumbling systems correspond to micellar aggregates, as it has been previously observed for different amphiphilic Gd³⁺ complexes.^{164,176,177}

We have determined the critical micellar concentrations (cmc) for both GdL₁ and GdL₃ complexes by relaxometric measurements according to previous reports.¹⁷⁷ For this, the paramagnetic relaxation rates, R_1 , have been plotted vs. the Gd³⁺ concentration at 40 MHz, a magnetic field where the effect of slower rotation is the most pronounced (**Figure 4.3**).¹⁷⁷

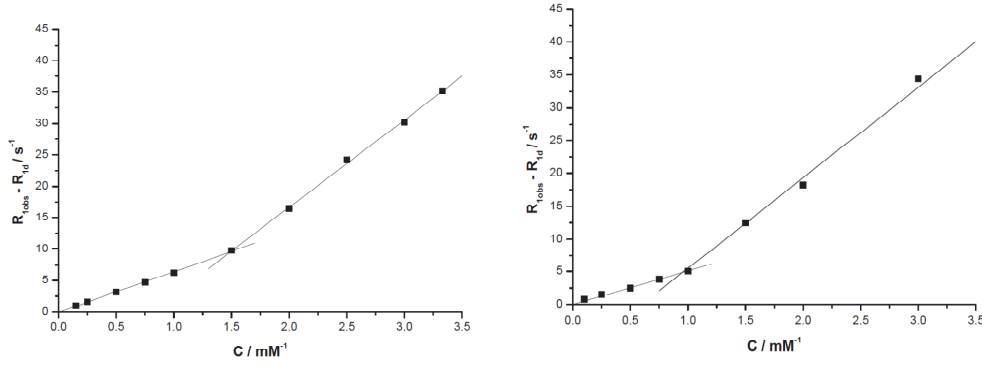


Figure 4.3. Water ¹H longitudinal relaxation rates as a function of GdL₁ (right) and GdL₃ (left) concentration at 40 MHz and 25 °C.

At concentrations below the cmc no aggregates form, and under these conditions, only the monomeric chelate contributes to the paramagnetic ¹H relaxation rate measured in the solution, which is given by Equation (2). Here R_d^1 is the diamagnetic contribution to the longitudinal relaxation rate (the relaxation rate of pure water), $r_1^{n.a}$ represents the relaxivity of the free, non aggregated Gd^{3+} chelate ($mM^{-1}s^{-1}$), and C_{Gd} is the analytical Gd^{3+} concentration.

$$R_1^{obs} - R_1^d = r_1^{n.a} \times C_{Gd} \quad (2)$$

At concentrations above the cmc, the measured relaxation rate is the sum of two contributions, one due to the chelate as monomer (free surfactant) present at a concentration given by the cmc, and the other due to the aggregated form (micelles). The water ¹H relaxation rate measured for the paramagnetic solution can be then expressed as in Equation (2), in which r_1^a is the relaxivity of the micellar (aggregated) form.

$$R_1^{obs} - R_1^d = (r_1^{n.a} - r_1^a) \times cmc + r_1^a \times C_{Gd} \quad (3)$$

The cmc is determined from the plot of the paramagnetic relaxation rates versus the Gd^{3+} concentration by a simultaneous least-squares fit of the two straight lines obtained (Fig. S1). The slopes of these two lines define $r_1^{n.a}$ and r_1^a ,

below and above the cmc, respectively. The values obtained were $r_1^{\text{na}} = 6.4 \text{ mM}^{-1}\text{s}^{-1}$ and $r_1^{\text{a}} = 13.9 \text{ mM}^{-1}\text{s}^{-1}$ for GdL_1 , and $r_1^{\text{na}} = 6.1 \text{ mM}^{-1}\text{s}^{-1}$ and $r_1^{\text{a}} = 13.8 \text{ mM}^{-1}\text{s}^{-1}$ for GdL_3 (25°C, 40 MHz). The cmc was found to be: $\text{cmc}_{\text{GdL}_1} = 1.49 \pm 0.02 \text{ mM}$ and $\text{cmc}_{\text{GdL}_3} = 1.00 \pm 0.02 \text{ mM}$ (**Table 4.2**), which, in a comparison to previously studied, larger hydrocarbon chained amphiphilic Gd^{3+} complexes, as shown in **Table 4.2**, fall into ranges expected for the compounds comprising between twelve to fourteen-carbon lipophilic tails.

Table 4.2. Parameters obtained from the ^1H relaxivity study for $[\text{GdL}_1(\text{H}_2\text{O})]$ and $[\text{GdL}_3(\text{H}_2\text{O})]$ at 40 MHz and at 25°C, compared with other micellar systems from the literature.

Gd-complex	r_1^{na} ($\text{mM}^{-1}\text{s}^{-1}$)	r_1^{a} ($\text{mM}^{-1}\text{s}^{-1}$)	cmc (mM)
$[\text{GdL}_1(\text{H}_2\text{O})]$	6.4 ± 0.1	13.9 ± 0.2	1.49 ± 0.02
$[\text{GdL}_2(\text{H}_2\text{O})]$	-	-	-
$[\text{GdL}_3(\text{H}_2\text{O})]$	6.1 ± 0.2	13.8 ± 0.4	1.00 ± 0.02
$[\text{GdDOTAC}_{10}(\text{H}_2\text{O})]^{-\text{a,b}}$	5.3	10.8	7.20
$[\text{GdDOTAC}_{12}(\text{H}_2\text{O})]^{-\text{a,b}}$	5.5	17.9	4.45
$[\text{GdDOTAC}_{14}(\text{H}_2\text{O})]^{-\text{a,b}}$	5.4	22.0	0.87
$[\text{GdDOTASAC}_{18}(\text{H}_2\text{O})]^{-\text{a,b}}$	10.5	17.0	0.06

^a parameters obtained at 60MHz and 25°C

^b from ref. ¹⁷⁷

4.3.3. ^{17}O NMR and NMRD measurements

The magnetic-field dependence of the proton longitudinal relaxation of complexes GdL_{1-3} were recorded as a series of ^1H NMRD profiles at 25°C and 37 °C over the frequency range 0.01 to 100 MHz and at concentrations below and above the cmc, except for GdL_2 , for which low solubility prevented working in the aggregated state (**Figure 4.2, B**). The features of the NMRD curve are influenced by the water exchange rate, electron relaxation parameters and rotational correlation times. Due to the high number of parameters affecting relaxivity, their determination exclusively from the NMRD curves can lead to false results. Therefore, NMRD measurements are usually combined with ^{17}O NMR

spectroscopy. By performing variable temperature ^{17}O T_2 measurements, it is possible to accurately determine the water exchange rate. The rotational correlation time can be assessed by performing variable temperature ^{17}O T_1 measurements. On the other hand, variable temperature measurements of the chemical shift difference between bulk and bound water ($\Delta\omega_r$), give an indication of the q value. A reliable determination of the parameters common to ^1H NMRD and ^{17}O NMR is often performed through the simultaneous least-squares fitting of all the data obtained. Nevertheless, given the different concentrations typically used in NMRD and ^{17}O NMR measurements, such a simultaneous fit is not possible when concentration-dependent phenomena, such as micellar aggregation occur in the system.

Therefore, in order to assess the parameters describing water exchange and rotational dynamics on GdL_3 , we have performed a variable temperature ^{17}O NMR study on its aqueous solution. The low water solubility of the two other Gd^{3+} complexes does not allow for ^{17}O NMR measurements which require typically concentrations above 10 mM in order to obtain reliable data. **Figure 4.4** shows the measured temperature dependency of the reduced ^{17}O chemical shifts ($\Delta\omega_r$), transverse ($1/T_{2r}$) and longitudinal ($1/T_{1r}$) relaxation rates. For GdL_3 , the transverse ^{17}O relaxation rates, $1/T_{2r}$, increase with decreasing temperatures above 0°C , indicating here that this complex is in the fast exchange regime. At lower temperatures, the transverse relaxation rates turn into a slow exchange regime. The reduced chemical shifts are in accordance with this trend.

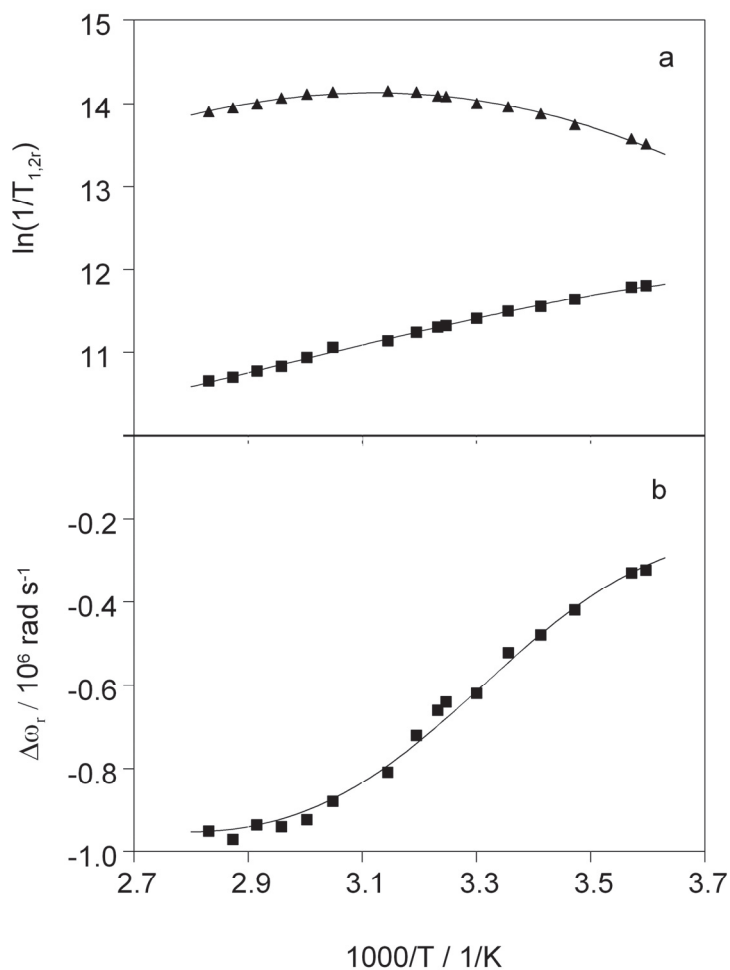


Figure 4.4. Temperature dependence of the logarithms of the reduced longitudinal (a, ■) and transverse (a, ▲) ^{17}O relaxation rates and reduced chemical shifts (b, ■) of $[\text{GdL}_3]$ in aqueous solution ($B = 11.7 \text{ T}$, $c = 10.28\text{mM}$).

In the slow exchange regime, the reduced transverse relaxation rates are directly determined by the water exchange rate. In the fast exchange regime, on the other hand, the reduced transverse relaxation rate is defined by the transverse relaxation rate of the bound water oxygen (Equation (4)), $1/T_{2m}$, which is in turn influenced by the water exchange rate, k_{ex} , the longitudinal electronic relaxation rate, $1/T_{1e}$, and the scalar coupling constant, A/\hbar (see **Appendix 1**).

$$\frac{1}{\tau_{1r}} = \frac{1}{T_{1m}} + \frac{1}{T_m}, \quad i=1,2 \quad (4)$$

The reduced ^{17}O chemical shifts are determined by A/\hbar . Transverse ^{17}O relaxation is governed by the scalar relaxation mechanism, thus contains no information on the rotational motion of the system. In contrast to $1/T_{2r}$, the longitudinal ^{17}O relaxation rates, $1/T_{1r}$, are determined by dipole-dipole and quadrupolar relaxation mechanisms, both related to rotation. The dipolar term depends on the Gd^{3+} -water oxygen distance, r_{GdO} , while the quadrupolar term is influenced by the quadrupolar coupling constant, $\chi(1+\eta^2/3)^{1/2}$ (Equations (A9-A11), **Appendix 1**).

Since the ^{17}O NMR and the NMRD data have been obtained at different concentrations where the aggregation state of the GdL_3 complex is different, their simultaneous analysis is not possible. For the NMRD data, we have analyzed the curves both below and above the cmc (except for GdL_2 ; **Figures 4.5-4.9**). The analysis of the experimental ^{17}O NMR and the NMRD data was performed separately according to the traditional Solomon-Bloembergen-Morgan theory.^{164,165} The theoretical equations used in the data analysis are shown in the **Appendix 1**. All parameters obtained from the fits are given in **Tables 4.3** and **4.4**.

Table 4.3. Best fit parameters obtained for $[\text{GdL}_3(\text{H}_2\text{O})]$ from the analysis of ^{17}O NMR

Parameters	$[\text{GdL}_3(\text{H}_2\text{O})]$	$[\text{GdDOTA}(\text{H}_2\text{O})]^{-166}$	$[\text{GdDTPA}(\text{H}_2\text{O})]^{-166}$
k_{ex}^{298} [10^6 s^{-1}]	2.8 ± 0.4	4.1	3.3
ΔH^\ddagger [kJ/mol]	32.0 ± 1.0	49.8	51.6
ΔS^\ddagger [J/molK]	14 ± 4	48.5	53.0
E_R [kJ/mol]	14.2 ± 0.2	16.1	17.3
τ_{RO}^{298} [ps]	601 ± 10	77	58
E_V [kJ/mol]	<u>1.0</u>	<u>1.0</u>	1.6
τ_V^{298} [ps]	8.4 ± 1	11	25.1
Δ^2 [10^{20} s^{-2}]	0.28 ± 0.01	0.16	0.46
A/\hbar [MHz]	-3.7 ± 0.2	-3.7	-3.8

^a The underlined values have been fixed in the fitting

In the fitting procedure of the ^{17}O NMR data, r_{GdO} has been fixed to 2.50 \AA , based

on available crystal structures and recent electron spin-echo envelope modulation (ESEEM) results.¹⁷⁸ The quadrupolar coupling constant, $\chi(1+\eta^2/3)^{1/2}$, has been set to the value for pure water, 7.58 MHz.¹⁶⁴ The following parameters have been adjusted: the water exchange rate, k_{ex}^{298} , the activation entropy, ΔS^\ddagger , the activation enthalpy for water exchange, ΔH^\ddagger , the scalar coupling constant, A/\hbar , the rotational correlation time (τ_{R}^{298}) and its activation energy, E_{R} , and the parameters characterizing the electron spin relaxation, such as the correlation time for the modulation of the zero-field-splitting, τ_{v}^{298} , and its activation energy, E_{v} , and the mean-square zero-field-splitting energy, Δ^2 . The empirical constant describing the outer sphere contribution to the ^{17}O chemical shift, C_{os} , was also fitted and gave a reasonable value (0.18).¹⁶⁶ E_{v} was fixed to 1 kJ/mol, otherwise small negative values were obtained. One inner sphere water molecule has been supposed for GdL_3 , based on analogy to structurally similar systems.¹⁶⁴ For GdL_3 , partially in the fast water exchange regime, the reduced chemical shifts and, consequently the scalar coupling constant calculated, give a direct indication of the hydration state of the complexes. The chemical shifts and thus the scalar coupling constant clearly evidence one inner sphere water molecule.

In the fitting of the NMRD data in the monomer state, we have fixed the r_{GdH} distance to 3.10 Å and the closest approach of the bulk water protons to the Gd^{3+} , a_{GdH} to 3.65 Å.³⁹ The diffusion constant has been fixed to $26 \times 10^{-10} \text{ m}^2/\text{s}$ and its activation energy to 16 kJ/mol. The hydration number was 1 and the water exchange rate and the water exchange enthalpy were also fixed for all three complexes to the values obtained in the ^{17}O NMR study for GdL_3 .

The proton relaxation rates measured above the cmc represent the sum of the relaxivity contribution of the monomer complex, present at a concentration equal to the cmc, and the relaxivity contribution of the aggregated state. Therefore, in order to calculate the relaxivity of the aggregated form, the relaxivity contribution of the monomer has been subtracted from the relaxation rates measured above cmc. The relaxivities calculated in this way for the micellar form have been fitted to the Solomon-Bloembergen-Morgan theory by including the Lipari-Szabo treatment for the description of the rotational motion. In this approach, two kinds of motion are assumed to modulate the interaction causing

the relaxation, namely a rapid, local motion which lies in the extreme narrowing limit and a slower, global motion. We calculate therefore τ_g , the correlation time for the global motion (common to the whole micelle), and τ_l , the correlation time for the fast local motion, which is specific for the individual relaxation axis, and thus related to the motion of the individual Gd^{3+} chelate units. The generalized order parameter, S^2 , is a model-independent measure of the degree of spatial restriction of the local motion, with $S^2 = 0$ if the internal motion is isotropic, $S^2 = 1$ if the motion is completely restricted. In the fit of the micellar form, we used only the relaxivities above 4 MHz, where the validity of the SBM theory for slowly rotating systems is respected. We have fixed the r_{GdH} distance to 3.10 Å and the closest approach of the bulk water protons to the Gd^{3+} , a_{GdH} to 3.65 Å. The diffusion constant has been fixed to $26 \times 10^{-10} \text{ m}^2/\text{s}$ and its activation energy to 16 kJ/mol. The hydration number was 1 and the water exchange rate and the water exchange enthalpy were fixed for GdL_3 to the values obtained in the ^{17}O NMR study (**Figure 4.4 and Table 4.3**). The GdL_1 complex in its micellar form presents an unusual temperature dependency: the relaxivities at 37 °C are higher than those at 25 °C. This shows that the slow water exchange rate is a limiting factor for this complex, in contrast to GdL_3 . Indeed, the temperature dependency of the proton relaxivities for GdL_1 could not be fitted with a k_{ex}^{298} value fixed to that of GdL_3 ; a reasonable fit could only be obtained when smaller values were considered. We obtained an acceptable fit for $k_{\text{ex}}^{298} = 1.0 \times 10^6 \text{ s}^{-1}$, a value about one third of that determined for GdL_3 by ^{17}O NMR (**Figures 4.8, 4.9 and Table 4.5**).

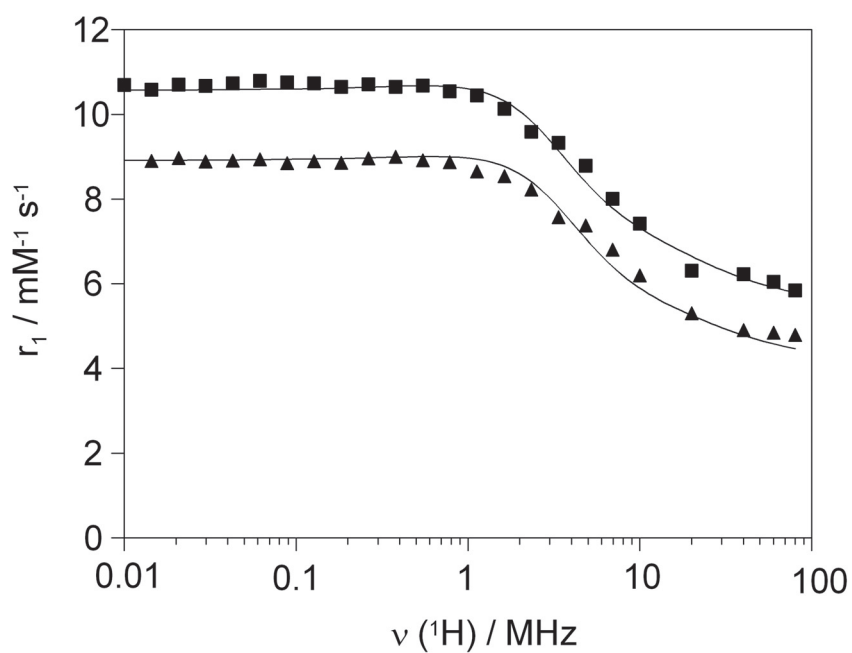


Figure 4.5. NMRD profiles of GdL₁ at 25°C (■) and 37°C (▲) at 0.2 mM concentration. The solid line corresponds to the fit as explained in the text.

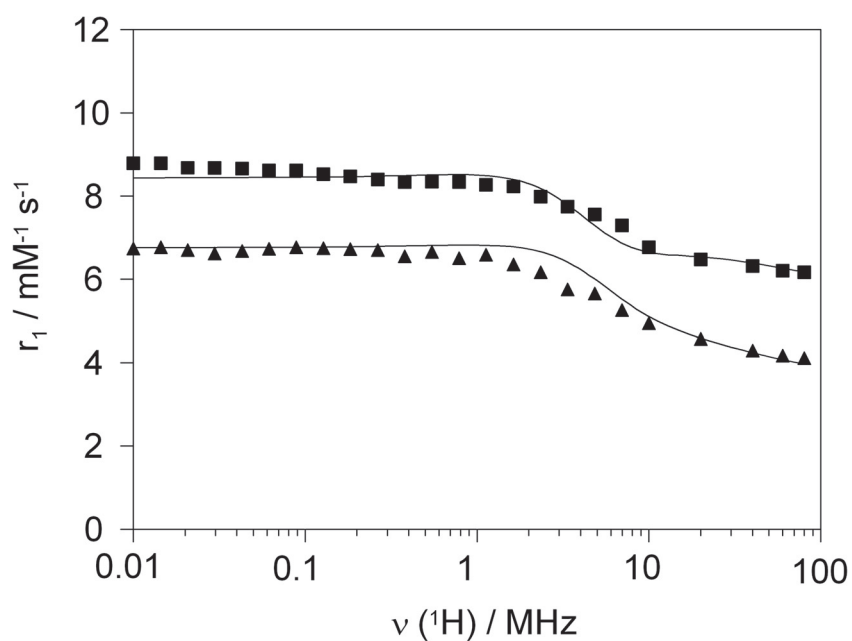


Figure 4.6. NMRD profiles of GdL₂ at 25°C (■) and 37°C (▲) at 0.1 mM concentration. The solid line corresponds to the fit as explained in the text.

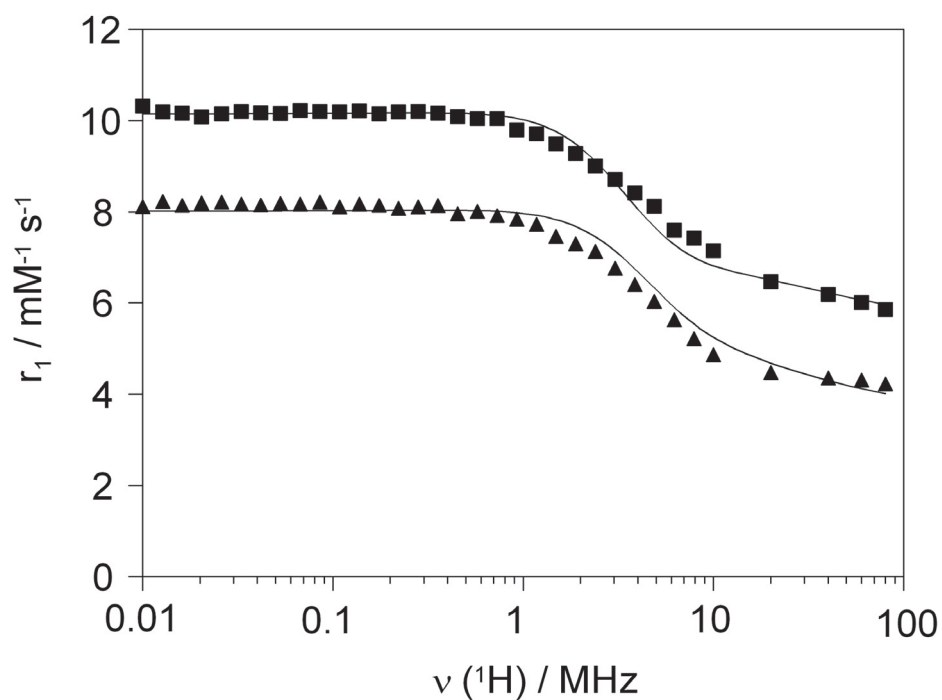


Figure 4.7. NMRD profiles of GdL_3 at 25°C (■) and 37°C (▲) at 0.2 mM concentration. The solid line corresponds to the fit as explained in the text.

Table 4.4. Best fit parameters obtained for the monomer $[\text{GdL}_{1,2,3}(\text{H}_2\text{O})]$ complexes from the analysis of NMRD data below cmc

Parameters	$[\text{GdL}_1(\text{H}_2\text{O})]$	$[\text{GdL}_2(\text{H}_2\text{O})]$	$[\text{GdL}_3(\text{H}_2\text{O})]$
$k_{\text{ex}}^{298} [10^6 \text{ s}^{-1}]$	<u>2.8</u>	<u>2.8</u>	<u>2.8</u>
$\Delta H^\ddagger [\text{kJ/mol}]$	<u>32.0</u>	<u>32.0</u>	<u>32.0</u>
$E_R [\text{kJ/mol}]$	18.2 ± 0.2	37.2 ± 0.2	32.3 ± 0.8
$\tau_{\text{RH}}^{298} [\text{ps}]$	130 ± 10	150 ± 10	141 ± 11
$E_V [\text{kJ/mol}]$	<u>1.0</u>	<u>1.0</u>	<u>1.0</u>
$\tau_V^{298} [\text{ps}]$	50 ± 5	27 ± 3	25 ± 3
$\Delta^2 [10^{20} \text{ s}^{-2}]$	0.11 ± 0.01	0.40 ± 0.01	0.26 ± 0.02

4.3.3.1. Water exchange rate

The water exchange rate has been directly determined from the ^{17}O T_2 data for GdL_3 . The value, $k_{\text{ex}}^{298} = 2.8 \times 10^6 \text{s}^{-1}$, is in good agreement with water exchange rates reported for similar, DO3A-monoamide derivative Gd^{3+} complexes.¹⁶⁴ According to the empirical rule that has been observed on a large number of amide derivative complexes of DOTA or DTPA, the water exchange is decreased to about one half / one third by the replacement of each carboxylate by an amide function (**Tables 4.3 and 4.4**).¹⁶⁴ An amide group is coordinated less strongly towards the lanthanide ion than a carboxylate, which is exhibited by smaller stability constants of the amide complexes compared to carboxylates in solution, and by longer Gd-amide oxygen distances in the solid state, when compared to Gd-carboxylate oxygen distances. As a consequence, the inner sphere is less crowded in amide than in carboxylate complexes.¹⁶⁴ In dissociatively activated water exchange processes the steric crowding is of primary importance, i.e, a less tightly coordinating ligand pushes less the water molecule to leave, and thus disfavours the dissociative activation step leading to a lower water exchange rate.

4.3.3.2. Rotational dynamics

The rotational dynamics is directly assessed here for both the monomer species and the aggregated state by the NMRD measurements. The rotational correlation time calculated from the ^{17}O T_1 data is an effective value, since it has contributions from both the monomer and the aggregated state, which cannot be separated. In addition, one cannot use the Lipari-Szabo treatment to analyse the ^{17}O NMR data, since they have been acquired only at one magnetic field which does not allow for separating local and global motions. Nevertheless, the τ_{RO}^{298} calculated from ^{17}O T_1 data clearly show slow rotational motion, 601 ps for GdL_3 at 10 mM concentration vs 77 ps for the monomer GdDOTA (**Table 4.3**). On the other hand, the NMRD of the aggregated form could be analysed in terms of global and local rotation and these values characterize directly the micellar state. The rotational correlation times obtained from the NMRD curves for the $\text{GdL}_{1,2,3}$ monomers are in accordance with their larger size with respect to GdDOTA for

instance. The small variations between the three systems are also coherent with the increasing size of the side chain and its flexibility. Indeed, the smallest τ_{RH}^{298} is determined for GdL₁ having the shortest linker between the DO3A and the PiB unit. GdL₃ has the longest linker; however, it is more flexible with the C5 alkyl chain than the benzene derivative L₂ which has therefore the highest τ_{RH}^{298} value. As expected, these are also in accordance with the relaxivities measured at high field.

For the micellar state (Figures 4.8, 4.9 and Table 4.5), the global rotational correlation times are in the range of a few nanoseconds (7.9 and 5.5 ns for GdL₁ and GdL₃, respectively), while the local rotational correlation times are very short (55 and 32 ps for GdL₁ and GdL₃, respectively).¹⁷⁷ The generalized order parameter, S^2 , has also very low values implying a large flexibility of the system.¹⁷⁷ In overall, the slightly higher global and local rotational correlation times and S^2 value obtained for GdL₁ explain its higher relaxivity at intermediate fields (20-60 MHz) with respect to GdL₃.

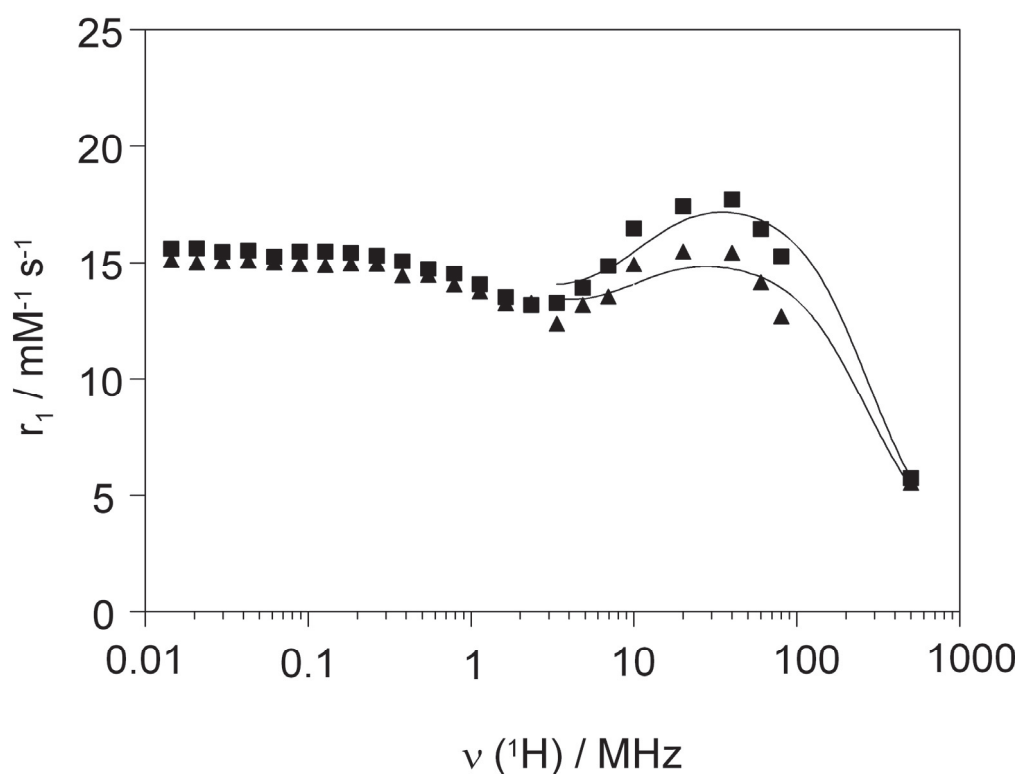


Figure 4.8. NMRD profiles of the micellar form of GdL₁ at 25°C (▲) and 37°C (■). The solid lines correspond to the fit as explained in the text.

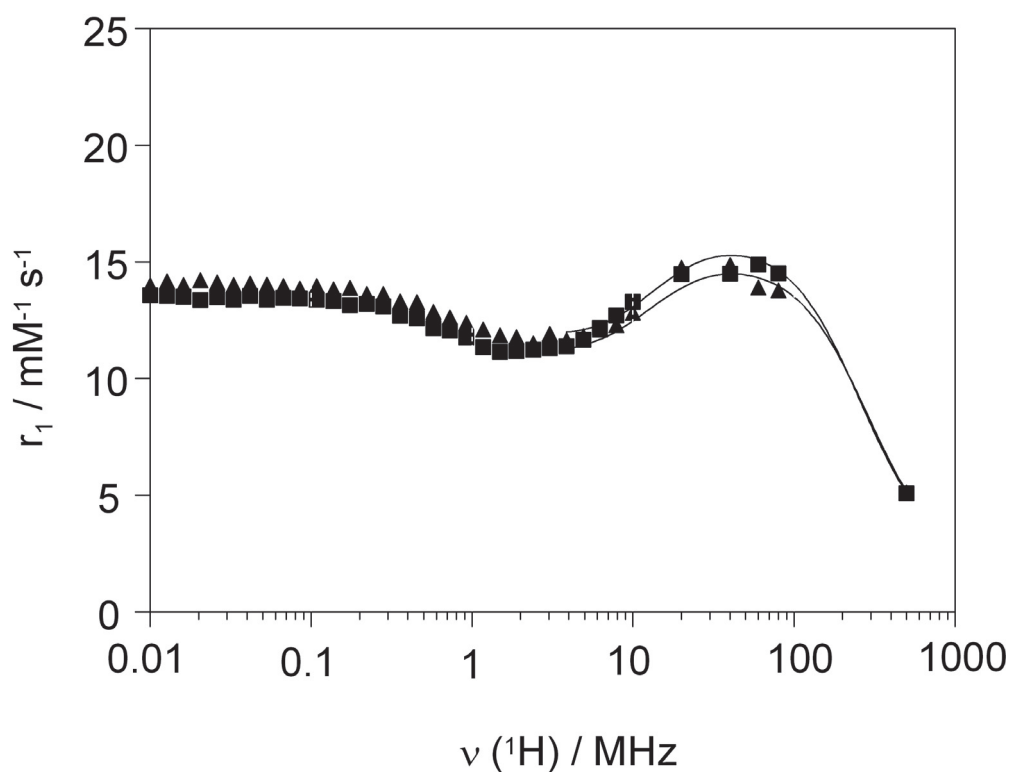


Figure 4.9. NMRD profiles of the micellar form of GdL₃ at 25°C (▲) and 37°C (■). The solid lines correspond to the fit as explained in the text.

Table 4.5. Best fit parameters obtained for the micellar [GdL_{1,3}(H₂O)] complexes from the analysis of NMRD data above the cmc, after subtraction of the monomer relaxivities

Parameters	[GdL ₁ (H ₂ O)]	[GdL ₃ (H ₂ O)]
k_{ex}^{298} [10^6 s^{-1}]	1.0±0.1	<u>2.8</u>
ΔH^\ddagger [kJ/mol]	30.0±0.2	<u>32.0</u>
E_1 [kJ/mol]	16±0.2	16±0.2
τ_{H}^{298} [ps]	55±3	32±3
E_g [kJ/mol]	16±0.2	16±0.2
τ_{gH}^{298} [ns]	7.9±0.8	5.5±0.5
S^2	0.17±0.03	0.11±0.03
E_V [kJ/mol]	<u>1.0</u>	<u>1.0</u>
τ_V^{298} [ps]	20±5	20±5
Δ^2 [10^{19} s^{-2}]	0.13±0.01	0.19±0.01

4.3.4. Relaxometric assessment of the interaction of the complexes with Human Serum Albumin (HSA) and $A\beta_{1-40}$ peptide

Upon binding of the monomeric form of GdL_x , ($x = 1,2,3$) to $A\beta$ plaques, higher relaxivity is expected, in particular at intermediate fields, since the complex becomes immobilized. Indeed, in the presence of the amyloid peptide $A\beta_{1-40}$ ($c_{Gd} = c_{A\beta_{1-40}} = 0.2$ mM), the relaxivity of $GdL_{1,3}$ increases considerably at magnetic fields where the effect of slower rotation is most pronounced (80% increase at 40 MHz). GdL_1 and GdL_3 interact with serum albumin as well, causing a remarkable increase of relaxivity at intermediate fields (**Figure 4.10**). Data suggest that albumin binding leads to a prolonged life-time of the agent in the blood pool that, given the slower elimination from the body, can be useful for a MRI probe, even though unfavourable for nuclear imaging probes due to longer radiation exposure and higher non specific signal. Strong HSA binding can be also detrimental for the BBB permeability of the agent.¹⁴³

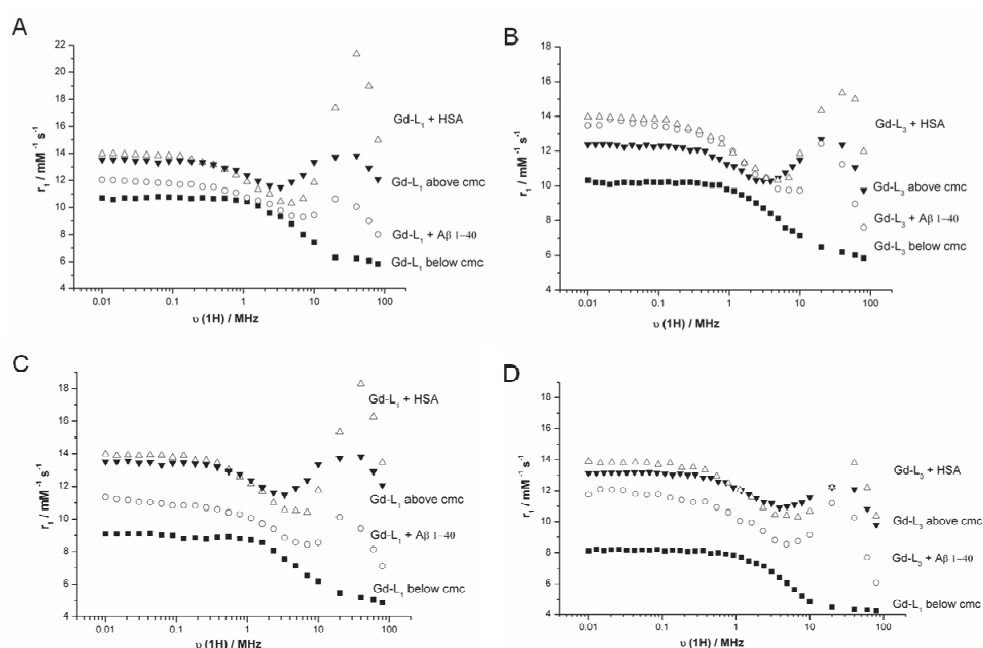


Figure 4.10. 1H NMRD profiles of (A,C) GdL_1 and (B,D) GdL_3 at: 0.2mM (■), 5 mM (▼), 0.2mM in the presence of 0.2mM $A\beta_{1-40}$ (○) 0.2mM in the presence of 0.2mM HSA (Δ) (0.05M HEPES; pH 7.4, T = 298 K (A,B) and 310 K (C,D)).

The binding affinities for GdL₁ and GdL₃ to HSA have been assessed by Proton Relaxation Enhancement (PRE) measurements commonly used to determine affinity constants of Gd³⁺ complexes to HSA. The PRE method is a non-separative technique in which the binding parameters can be obtained by exploiting the differences in the NMR water solvent relaxation rates between the bound and the unbound substrates. Since the relaxation rate is markedly increased in the presence of a paramagnetic substrate interacting with the protein, this method is perfectly tailored to investigate the binding of paramagnetic metal chelates. It consists of measuring the proton relaxation rates at increasing concentrations of the protein and of the metal chelate (**Figures 4.11**). Assuming that there is one binding site in HSA ($n = 1$), a binding constant K_A of $709 \pm 89 \text{ M}^{-1}$ and a relaxivity of the non-covalently bound complex (r_1^c) of $55.5 \pm 8.6 \text{ s}^{-1} \text{ mM}^{-1}$ were obtained for GdL₁ and K_A of $250 \pm 18 \text{ M}^{-1}$; $r_1^c = 77 \pm 5.3 \text{ s}^{-1} \text{ mM}^{-1}$ for for GdL₃, at 310K, 40MHz using Equation (5) (**Table 4.6**).^{45,164}

The PRE technique is not applicable to PiB and we have not found any literature data concerning the binding of PiB to HSA.

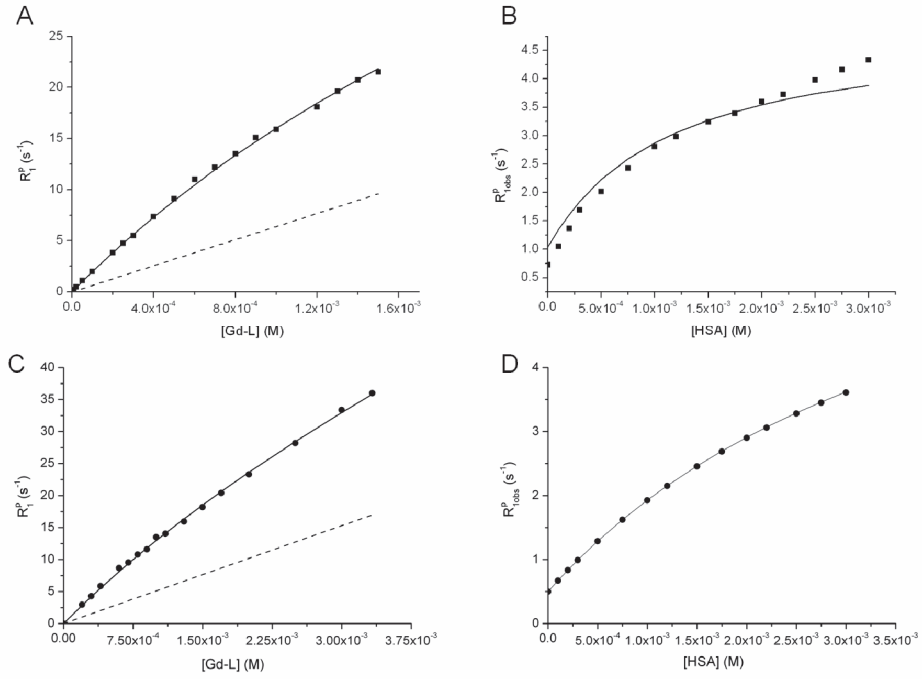


Figure 4.11. Proton Relaxation Enhancement data to assess HSA binding: M-titration obtained for GdL₁ (A) and GdL₃ (C) at 0.6 mM HSA concentration (40 MHz, 37°C, pH 7.4); E-titration data obtained for GdL₁ (B) and GdL₃ (D) at 0.1 mM GdL concentration (40 MHz, 37°C, pH 7.4).

$$R_1^{pobs} = 10^3 \times \left\{ \left(r_1^f \cdot c_1 \right) + \frac{1}{2} \left(r_1^c - r_1^f \right) \times \left(n \cdot c_{HSA} + c_1 + k_A^{-1} - \sqrt{\left(n \cdot c_{HSA} + c_1 + k_A^{-1} \right)^2 - 4 \cdot n \cdot c_{HSA} \cdot C_1} \right) \right\} \quad (5)$$

Table 4.6. Results of the fittings of the relaxometric titrations of [GdL₁(H₂O)] and [GdL₃(H₂O)] with HSA (at 40 MHz) according to Equation (5). Comparison with data for other complexes at 310 K from the literature is shown.

Complex	$K_A/10^3 \text{ M}^{-1}$	n	$r_1^c / \text{s}^{-1} \text{mM}^{-1}$	$r_1^f / \text{s}^{-1} \text{mM}^{-1}$	Ref.
[GdL ₁ (H ₂ O)]	0.71 ± 0.09	1	55 ± 8.6	5.3 ± 0.2	This work
[GdL ₃ (H ₂ O)]	0.25 ± 0.02	1	77 ± 5.3	4.9 ± 0.1	This work
[GdBOPTA(H ₂ O)] ²⁻	1.5	1	42.9	5.2	179
[GdMS-325(H ₂ O)] ²⁻	6.1	1	48.9	5.6	179
[GdBz-DTTA(H ₂ O) ₂] ⁻	0.71	1	45.5	7.1	45

4.4. Conclusion

In conclusion, we have studied the physico-chemical properties of novel amyloid targeted Gd³⁺-complexes. The GdL_x, (x = 1,2,3) complexes have an amphiphilic behavior as shown by their water/octanol partition coefficients and form micelles at higher concentrations in solution. The critical micellar concentrations have been obtained by relaxometric measurements. The parameters that influence water proton relaxivity, including the water exchange rate and the rotational correlation times have been determined in an ¹⁷O NMR study for GdL₃. All three complexes have been characterized by their NMRD curves.

GdL_x, (x = 1,2,3) are capable of binding the amyloid peptide Aβ₁₋₄₀ and HSA. The binding, results in elevated relaxivity of the Gd³⁺ analogue due to reduced rotational motion which will lead to an increased positive contrast in T₁-weighted images upon binding to senile plaques associated with AD and HSA in the human blood. The binding affinity for GdL₁ and GdL₃ to HSA has been assessed by Proton Relaxation Enhancement (PRE) and confirms the effective but not strong interaction, with K_A values varying from 250-701 M⁻¹.

CHAPTER 5

*”In Vitro Interactions
and Beta-Amyloid Self-
Assembly with Ln-
DO3A-PiB Derivatives ”*

5.1. Introduction

The amyloid cascade hypothesis is currently the most accepted cause for the development of Alzheimer's disease (AD).⁸⁵ One of the neuropathological findings in the brain of AD patients is the formation of extracellular senile plaques containing A β -amyloid peptides.¹⁸⁰ These are 39-42 residue peptides cleaved by processing of the amyloid- β precursor protein (APP),⁸⁵ and their self-assembly, interactions with other molecules, stabilization and toxicity of their aggregates have been the subject of many studies for imaging and therapeutical applications.¹⁸¹ In the monomeric form, these peptides interchange easily their conformation, leading to β -strand oligomers, toxic aggregates¹⁸² and finally to highly ordered fibril structures.¹⁸³ Oligomerization and/or fibrillization of these peptides can be modulated by the presence of small organic molecules¹⁸⁴ and amphiphilic detergent-like molecules, such as Congo red,¹³³ SDS¹⁸⁵ and lacmoid.¹⁸⁶ Disruption of the self-assembly of A β peptides by small organic molecules that can solubilize the toxic oligomeric aggregates is an important process that has been explored to obtain AD therapeutics,^{184,187} but its mechanism of action is not yet understood for most of these compounds.

Early *in vivo* visualization of the amyloid plaques is a critical issue in AD clinical diagnostics, which is also important for monitoring new therapies. Significant advances have been made in the field of nuclear imaging, in particular in Positron Emission Tomography (PET). Small organic compounds such as derivatives of thioflavin T, benzoxazoles and stilbenes, have high binding affinities for the A β aggregates and led to the development of amyloid-labelling nuclear imaging PET probes^{128,129,149,188} in particular ¹¹C -and ¹⁸F-labelled derivatives of stilbene¹²⁸ and the Pittsburgh compound-B (PiB).^{129,149} Small, neutral, more easily available ^{99m}Tc-labelled A β Single Photon Emission

Computed Tomography (SPECT) probes have also been reported based on derivatives of biphenyl,¹³⁶ benzothiazole aniline,¹³⁴ Pittsburgh compound-B (PiB),¹⁸⁹ chalcone,¹⁹⁰ flavone,¹⁹¹ or pyridyl benzofurane.¹³⁵ In all these targeted imaging probes, the radiolabel is either part of the organic molecular targeting moiety (¹¹C or ¹⁸F) or is a metal center (^{99m}Tc) chelated by a ligand moiety which is coupled through a spacer to the organic targeting moiety.

Our family of multimodal imaging agents consists of a PiB derivative conjugated through different spacer groups to the metal chelating unit DO3A-monoamide, which is capable of efficiently complexing metal ions adapted to different imaging modalities, including Gd³⁺ as Magnetic Resonance Imaging (MRI) contrast agents (CAs), ¹¹¹In³⁺ for SPECT or ⁶⁸Ga³⁺ for PET, and of labelling A β plaques *via* specific binding (see ref. ¹⁹² and Chapter 4). The structures of the Ln³⁺ complexes of two of these DO3A-PiB derivatives, L₁ and L₃, are shown in Chapter 2, **Figure 2.3**. In this chapter we describe studies of the interaction of the complexes, LnL₁ and LnL₃, with the A β ₁₋₄₀ peptide in the aggregated or monomeric form using a series of biophysical techniques. These include studying their affinity and mode of binding by Surface Plasmon Resonance (SPR) and Saturation Transfer Difference (STD) NMR, as well as the assessment of their effect on the secondary structure and aggregation process by Circular Dichroism (CD), ThT Fluorescence, Dynamic Light Scattering (DLS) and Transmission Emission Microscopy (TEM). Finally, their mode of interaction with the ¹⁵N-labeled A β ₁₋₄₀ peptide monomer was studied at the atomic level using ¹H-¹⁵N Heteronuclear Single Quantum Coherence (HSQC) NMR. We show in this study that the two complexes interact weakly with the A β ₁₋₄₀ peptide monomer, but do not affect its self-association in the same way, by inhibiting or promoting the formation of amyloid fibrils. These studies also give important clues to improve the targeted specificity and affinity of this type of multimodal imaging probes.

5.2. Experimental

5.2.1. Materials and sample preparation

The ligands L_1 and L_3 and their Ln^{3+} complexes were synthesized as described in Chapters 3 and 4. The ^{15}N -labeled and unlabeled $A\beta_{1-40}$ peptides for the NMR, CD and DLS experiments were purchased from AlexoTech (Umeå, Sweden). Deuterium oxide (99.9%) was obtained from Cambridge Isotope Labs, UK. As the NMR chemical shift reference, sodium 2,2-dimethyl-2-silapentane-sulfonate (DSS; obtained from Stohler Isotope Labs, USA) was employed at a final concentration of 50 μ M.

The $A\beta_{1-40}$ peptides were stored in solid form at -20 °C and warmed up to room temperature before use. They were dissolved in 10 mM NaOH to a final concentration of 1-2 mg/ml followed by 1 min of sonication. $H_2O/{}^2H_2O$ was then added to give a solution of half the final volume. Finally 20 mM sodium phosphate buffer was added to obtain the final volume and the pH was adjusted to 7.4 by adding small amounts of NaH_2PO_4 and Na_2HPO_4 . Throughout the whole sample preparation the peptides and solvents were kept on ice.

5.2.2. Surface Plasmon Resonance

Real time binding studies of the Ln^{3+} complexes to immobilized $A\beta_{1-40}$ by SPR spectroscopy were performed using a Biacore 3000 instrument (Biacore Life Sciences/GE Healthcare, Uppsala, Sweden) equipped with four flow cells on a sensor chip. Series S Sensor Chips CM5, *N*-hydroxysuccinimide (NHS), *N*-ethyl-*N'*-[(dimethylamino)propyl]-carbodiimide (EDC) and ethanolamine HCl, as well as sampling vials and caps, were obtained from Biacore. $A\beta_{1-40}$ was dissolved in deionized water to a concentration of 1 mg/mL and small aliquots were frozen until use. HEPES buffered saline (HBS-EP) buffer containing 0.01 mol/L HEPES, pH 7.4, 0.15 mol/L NaCl, 3 mmol/L EDTA, and 0.005% of surfactant P20 was used as assay running buffer and also for sample preparation. The immobilization protocol of $A\beta_{1-40}$ to the CM5 chip followed standard amine coupling conditions.¹⁹³ The carboxymethyl dextran matrix in the sensor chip was activated

by injection of a 1:1 mixture of EDC and NHS (70 μL , 200 mM EDC, 50 mM NHS) to allow the subsequent covalent cross linking of the injected peptide through primary amine groups forming amide bonds. The $\text{A}\beta_{1-40}$ solution was then injected into the activated flow cell (0.5 mg/mL peptide in sodium acetate buffer). Unreacted NHS esters were capped with ethanolamine (70 μL , 1 M, pH 8.5) to afford a surface that gave a final change in resonance units (RU) of 4100.^{193,194} Since 1000 RU determined by SPR corresponds to 1.0 pg/mm^2 of bound ligand, the total immobilized mass of $\text{A}\beta_{1-40}$ under these conditions was approx. 4.1 pg/mm^2 .

All binding data were collected with the biosensor instrument thermostated to 25°C. To maximize the contact time, the flow rate employed for all steps was 5 $\mu\text{L}/\text{min}$. 70 μL of 2 mM solutions of the LaL_1 and LaL_3 complexes in running buffer were injected for association (contact time 400 sec). Dissociation was followed in the same buffer for 350 sec. After each run, the sensor chip was regenerated with the regeneration buffer (100 mM glycine-HCl in 10 mM Tris buffer (pH 9), contact time 240 sec) and washed with running buffer for 5-10 min before the next injection. All buffers were filtered through 0.22 mm nylon filters (Millipore, USA) prior to use. The injection system was rinsed to change buffers when necessary.

A Biacore 3000 control software (version 4.1) provided by Biacore Life Sciences/GE Healthcare was used to record and analyse the time changing of the RUs (sensograms) and plot the binding curves. The control data were subtracted from the raw data obtained from the flow cell with immobilized $\text{A}\beta_{1-40}$. The response at equilibrium was then plotted versus concentration. The binding plots were fitted to a simple 1:1 Langmuir binding isotherm to obtain the dissociation equilibrium constant (K_D) using the Biacore 3000 program.

5.2.3. Nuclear Magnetic Resonance

The NMR spectra for the protein-based high resolution binding studies were recorded using pulse sequences in Bruker Topspin 2.1 on Bruker AV-600 operating at 600.13 MHz (^1H), equipped with a cryoprobe and z-gradients. ^1H - ^{15}N HSQC¹⁹⁵ spectra were recorded at 5, 15 and 25 °C on the 600 MHz

spectrometer using 8 scans and 1024 complex points per increment and 256 increments in the ^{15}N dimension. ^1H - ^{13}C HSQC spectra were also recorded at 5 °C on the Bruker AV-600 spectrometer using 320 to 400 scans and 1024 complex points per increment and 80 to 96 increments in the ^{13}C dimension.

Typically, 0.10 mg of ^{15}N -labeled $\text{A}\beta_{1-40}$ was dissolved in 0.20 mL of aqueous buffer consisting of 10 mM K_2HPO_4 and KH_2PO_4 (pH 7.2) and 90 % milliQ H_2O and 10 % $^2\text{H}_2\text{O}$. La^{3+} -complexes were titrated into this sample containing 50 μM ^{15}N - $\text{A}\beta_{1-40}$ in 10 mM potassium phosphate buffer, pH 7.2, with 10% $^2\text{H}_2\text{O}$ to give a final molar ratio of La^{3+} -complex to $\text{A}\beta_{1-40}$ of 4:1. Most measurements were made in a 5mm Shigemi tube. Solvent suppression was performed with a 3-9-19 WATERGATE module for 1D ^1H spectra¹⁹⁶ and no solvent suppression for the 2D HSQC experiments.

Since DSS is known to bind to $\text{A}\beta_{1-40}$ ¹⁹⁷ and can form ternary complexes with $\text{A}\beta$ and other ligands¹⁹⁸, it was not added to the samples containing $\text{A}\beta_{1-40}$. Instead, the ^1H chemical shift reference of DSS was measured in the same buffer in a separate NMR tube, at 5, 15 and 25°C. The ^{13}C and ^{15}N chemical shift reference values were set by multiplying the experimental ^1H shift reference by the gyromagnetic ratio of these nuclei relative to that of ^1H .¹⁹⁸

The data were processed using Bruker Topspin 2.1 and analyzed in Sparky 3.114 (T. D. Goddard and D. G. Kneller, SPARKY 3, University of California, San Francisco, USA. <http://www.cgt.ucsf.edu/home/sparky>). The weighted average of ^1H and ^{15}N chemical shift differences was calculated as follows¹⁹⁹:

$$[\Delta\delta(^1\text{H})^2 + (\Delta\delta(^{15}\text{N})/5)^2]^{1/2} \quad (1)$$

The chemical shift changes and relative intensities were evaluated only for cross-peaks with a sufficient signal-to-noise ratio. At high temperature the intensity and chemical shifts for Q15/M35 and V24/I31 were not evaluated due to cross-peak overlap.

STD NMR spectra^{200,201} were measured on a Varian VNMRS 600 (14.09 T, 600.14 MHz) NMR spectrometer using a 3 mm z-pulse field gradient (PFG) inverse probe. The $\text{A}\beta_{1-40}$ peptide was incubated for 7 days at room temperature in

20 mM sodium phosphate buffer adjusted to pH 7.4 to promote aggregation. The final samples for STD NMR contained 100 μM unlabeled $\text{A}\beta_{1-40}$ peptide in the absence and presence of 1 mM La^{3+} -complexes (molar ratio of La^{3+} -complex to $\text{A}\beta_{1-40}$ of 10:1) in 10 mM sodium phosphate buffer prepared using D_2O (99.9%), pH 7.4, taking into account the deuterium isotopic effect.²⁰² Solvent suppression was performed using the Double Pulse Field Gradient Spin Echo (DPFGSE) sequence²⁰³

Since in this NMR system the STD NMR spectra are acquired directly from phase cycling, the ^1H 1D NMR spectra were used as off-resonance references in order to calculate the STD amplification factor.²⁰¹ All STD spectra were acquired using the same parameters: equal spectrometer gain value, 10k complex points and 12 ppm spectral width and 512 scans per transient. A selective Gaussian saturation pulse was applied at the peptide resonances. The saturation time varied from 0 to 2.5 seconds²⁰⁴. The on-resonance saturation was applied at 0.50 ppm (methyl region), while the off-resonance frequency was set to 30 ppm. On- and off- resonance experiments were recorded in an interleaved fashion. A previously calibrated spin-lock filter ($T_{1\rho}$) was used to remove the peptide resonances.

All spectra were analyzed using Mestre Nova Software v5.3.1-4825. In order to compare the reference spectra with the STD NMR spectra, the different number of acquisitions was normalized according to equation (2),

$$\text{Rel. STD \%} = \frac{I_{\text{STD}} \times 2 \times \text{scans}_{\text{reference}}}{I_0 \times \text{scans}_{\text{STD}}} \quad (2)$$

where I_{STD} is the peak intensity of the STD NMR spectra, I_0 is the intensity of the peaks in the ^1H reference spectra. Then, the peak intensities were normalized to the amplification factor STD (A_{STD}), equation (3),

$$A_{\text{STD}} = \text{Rel. STD \%} \times \text{Lig. Exc.} \quad (3)$$

where the ligand L (= LaL_x) excess, $\text{Lig. Exc} = [\text{L}]_0/[\text{P}]_0$ ($\text{P} = \text{A}\beta_{1-40}$).

The A_{STD} value is thus dependent on the fraction of bound $A\beta_{1-40}$ at the ligand excess. However, the direct evaluation of K_D values from the variation of A_{STD} values upon increasing $[\text{LaL}_x]$ in a ligand - protein titration is not correct because it depends on a series of experimental parameters, such as the saturation time (t_{sat}). Thus we used in this work a published protocol,²⁰⁴ where the A_{STD} values extrapolated to zero saturation time, $(A_{\text{STD}})_0$, were used instead. The A_{STD} values for each LaL_x proton at increasing t_{sat} were obtained at a given $[\text{LaL}_x]$ and the corresponding $(A_{\text{STD}})_0$ value were calculated by fitting the data to eq. (4)

$$(A_{\text{STD}})(t_{\text{sat}}) = A_{\text{STD}(\text{max})} [1 - \exp(-k_{\text{sat}} t_{\text{sat}})] \quad (4)$$

where $A_{\text{STD}(\text{max})}$ is the maximum A_{STD} value achievable for that proton at very long t_{sat} , and k_{sat} is its saturation rate constant. After the final fit, the initial slope $(A_{\text{STD}})_0$ was easily obtained by the product $A_{\text{STD}(\text{max})} k_{\text{sat}}$. The $(A_{\text{STD}})_0$ values calculated at every increasing $[\text{LaL}_x]$ along the titration were plotted as a function of $[\text{LaL}_x]$, and the resulting isotherm of initial slopes was mathematically fitted to a Langmuir equation for a 1:1 binding model ($n=1$) to obtain the K_D value for interaction of LaL_x with the aggregated form of $A\beta_{1-40}$ in aqueous solution at 25 °C.

For the determination of K_D values using STD NMR, the saturation times used to obtain the STD buildup curves were 1, 2, 3, 4 and 5 seconds. The number of scans for each experiment was typically 1024.

5.2.4. Circular Dichroism

The far-UV CD spectra were acquired on a Jasco J-810 CD spectropolarimeter equipped with a Jasco PTC-423S temperature control system. Measurements were performed at 3, 25°C and 37 °C using a cell with a 1 mm optical path length. The spectral region was recorded from 190 to 260 nm with a step size of 0.5 and a bandwidth of 1 nm. Data were collected with a time of 0.5 s per point, the spectra were averaged over 10 scans, and the buffer contribution was corrected. The samples contained 40 μM $A\beta_{1-40}$ peptide in 10 mM sodium phosphate buffer, pH

7.4 and 0 – 400 μM Gd^{3+} -complexes (corresponding to 0:1 to 10:1 molar ratio of Gd^{3+} -complexes to $\text{A}\beta_{1-40}$). The samples used for the time dependence experiments at low temperature were stored on ice or at 3 °C during the investigation. For the time dependence measurements at 25°C and 37 °C, the samples were kept in a Cole-Parmer Eppendorf heater at these temperatures throughout the incubation time.

5.2.5. Aggregation assays using ThT Fluorescence

Samples of Thioflavin-T and of Gd^{3+} -complexes GdL_1 and GdL_3 in the absence and presence of 20 μM $\text{A}\beta_{1-40}$ (in 10 mM sodium phosphate buffer, pH 7.4) were excited at 440 nm and 323 nm, respectively, and the fluorescence emission spectra were measured at 450nm — 700nm and 330nm — 650nm range, respectively, with a FluoroMax-2 fluorometer (Jobin Yvon – Spex, Instruments S.A, Inc.). The fluorescence of samples containing 20 μM ThT and 30 μM $\text{A}\beta_{1-40}$ peptide were also monitored as a function of time.

5.2.6. Dynamic Light Scattering

DLS was measured using a Malvern Zetasizer Nano Range apparatus. The samples contained 40 μM $\text{A}\beta_{1-40}$ in 10 mM sodium phosphate buffer, pH 7.4 in the absence and in the presence of 40, 80 and 160 μM of Gd^{3+} -complexes. The measurements were carried out at 25 °C and the scattered light was detected at an angle of 150°.

5.2.7. Transmission Electron Microscopy

Samples of 10 μL volume of aggregated $\text{A}\beta_{1-40}$ peptide solution (20days time evolution solutions from CD studies at 37°C and pH 7.4) were deposited on Formvar/ Cu^{2+} grids and left for 2 min. The grids were washed twice with distilled filtered water. In order to stain the amyloid fibrils negatively, 10 μL

aliquots of uranyl acetate 2% (w/v) were deposited on the grid and left for 2 min before drying in air. Grids were stored at room temperature until examination in a Philips CM100 TEM microscope, operating at 80 keV.

5.3. Results and Discussion

5.3.1. Binding of LnL₁ and LnL₃ to A β ₁₋₄₀

Affinity constants of small molecules interacting with Abeta amyloid peptides have been determined using different techniques.²⁰⁵ Amongst these, we have chosen to use for the present work two techniques with different sensitivity and time resolution: SPR^{193,194,206,207} and ¹H STD NMR measurements.^{200,204,208}

Binding targets like A β ₁₋₄₀ that are prone to aggregation in solution present specific data interpretation problems in binding assays if the aggregation state of the binding target varies during the experiment. Also, it may be difficult to achieve the reproducibility of the aggregation state between experiments may become difficult. Both of these problems can be avoided by immobilization of A β ₁₋₄₀ either in the disaggregated form or as an aggregate. The immobilization protocol used in the present work leads to immobilized A β ₁₋₄₀ in the aggregated form,²⁰⁹ which is the state at which the SPR binding data presented here refer to.

Figure 5.1 shows the SPR sensograms obtained from the binding of LaL₁ and LaL₃ complexes to immobilized aggregated A β ₁₋₄₀ and the corresponding binding plots. The fitting of these SPR plots to a simple 1:1 Langmuir binding isotherm gave K_D values of 169.6 (\pm 21.0) μ M for LaL₁ binding and 66.6 (\pm 8.0) μ M for LaL₃ binding.

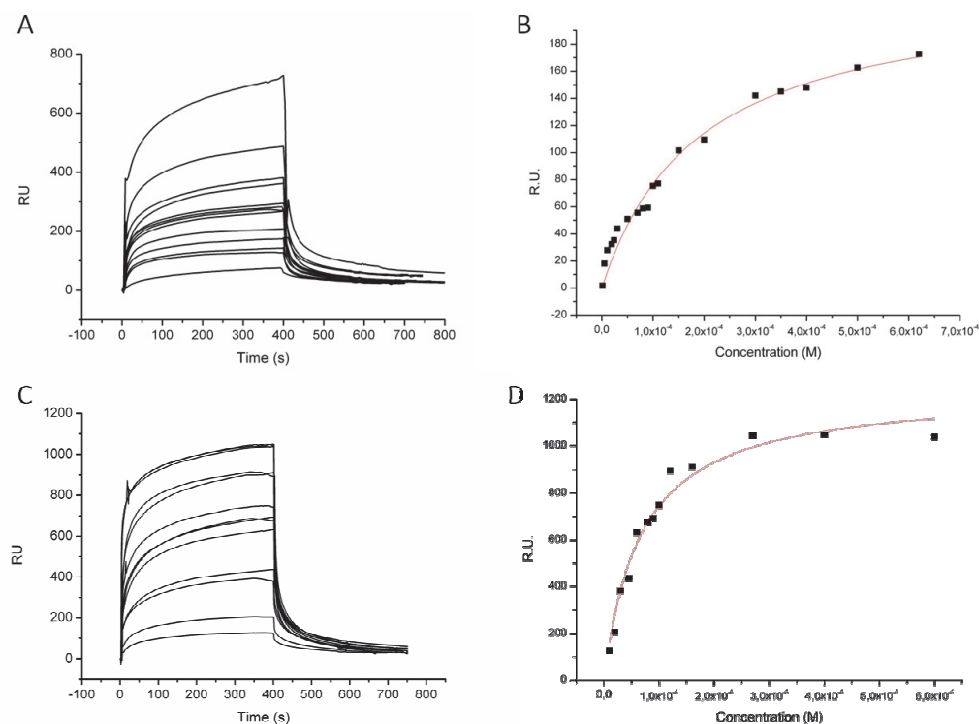


Figure 5.1. Surface Plasmon Resonance sensograms (A, C) and binding plots fitted as Langmuir isotherm functions ($n = 1$) (B, D) for (A, B) LaL₁ and (C, D) LaL₃.

The direct evaluation of K_D values from the variation of A_{STD} upon increasing $[LaL_x]$ in a simple STD NMR titration is not feasible due to the complex dependence of STD intensities on a number of experimental parameters, namely the saturation time (t_{sat}), the LaL_x residence time in the complex with $A\beta_{1-40}$ and the intensity of the signal, which affect the accumulation of saturation in the free LaL_x by processes related to fast $A\beta_{1-40} - LaL_x$ rebinding and longitudinal relaxation of the LaL_x protons.²⁰⁴ In this work we thus followed the published protocol to avoid these limitations in the determination of K_D values, by analysing the binding curve using A_{STD} values at the limit of zero saturation time, when no LaL_x rebinding or relaxation occurs.²⁰⁴ Following the procedure described in the Experimental section, **Figure 5.2** illustrates the experimental saturation time dependence of A_{STD} values (methoxy protons, 9-CH₃) for increasing LaL_x concentrations and the corresponding fitting to Equation (4) to obtain the $(A_{STD})_0$ values. **Figure 5.3** shows the corresponding binding plots of $(A_{STD})_0$ versus $[LaL_x]$

and their fits to obtain the K_D values for interaction of LaL_x with the aggregated form of $\text{A}\beta_{1-40}$ in aqueous solution.

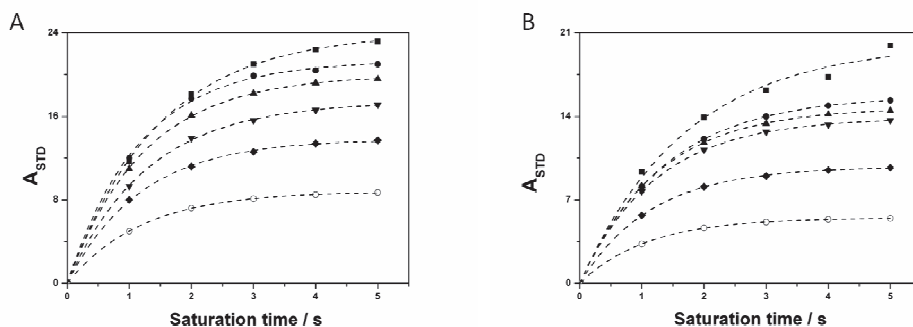


Figure 5.2. Dependence of the experimental A_{STD} values for methoxy protons (9- CH_3) on the saturation time at increasing LaL_x concentrations for (A) LaL_1 (\blacksquare – 600 μM ; \bullet – 500 μM ; \blacktriangle – 400 μM ; \blacktriangledown – 300 μM ; \blacklozenge – 200 μM ; \circ – 100 μM) and (B) LaL_3 (\blacksquare – 500 μM ; \bullet – 400 μM ; \blacktriangle – 300 μM ; \blacktriangledown – 200 μM ; \blacklozenge – 100 μM ; \circ – 50 μM) and their fits to obtain $(A_{\text{STD}})_0$ values (100 μM $\text{A}\beta_{1-40}$, 25 $^\circ\text{C}$, pH 7.2).

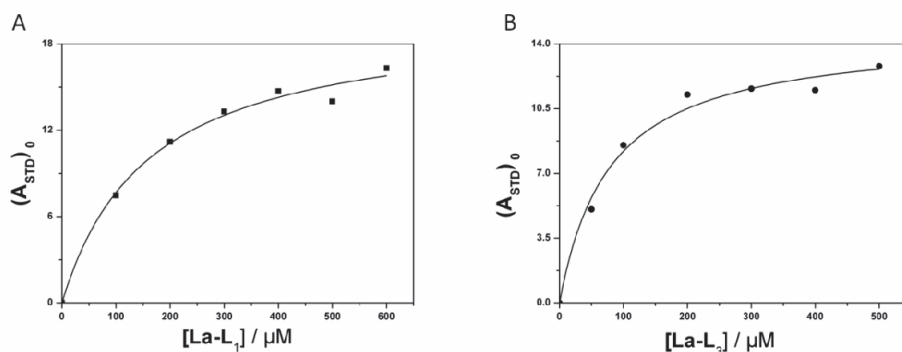


Figure 5.3. Binding STD plots, showing $(A_{\text{STD}})_0$ versus $[\text{LaL}_x]$ and their fits to obtain the K_D values for interaction of LaL_x with $\text{A}\beta_{1-40}$, (A) LaL_1 and (B) LaL_3 (100 μM $\text{A}\beta_{1-40}$, 25 $^\circ\text{C}$, pH 7.2).

The STD binding curves for LaL_1 and LaL_3 are hyperbolic and give a $K_D = 160.7 (\pm 29.0) \mu\text{M}$ and $K_D = 78.3 (\pm 14.1) \mu\text{M}$, respectively. These values are in good agreement with the corresponding values obtained by SPR for LaL_1 and

LaL₃ ($K_D = 169.6 (\pm 21.0) \mu\text{M}$; $K_D = 66.6 (\pm 8.0) \mu\text{M}$, respectively). The small differences of the values obtained might result from the possible differences of the aggregated forms of the A β_{1-40} peptide obtained in solution and in the immobilized state (**Figure 5.3**). The combined data show that, despite different techniques used, the K_D values for the binding of the two LaL_x complexes to the aggregated form(s) of A β_{1-40} are of the same order of magnitude (~ 67 - $170 \mu\text{M}$).

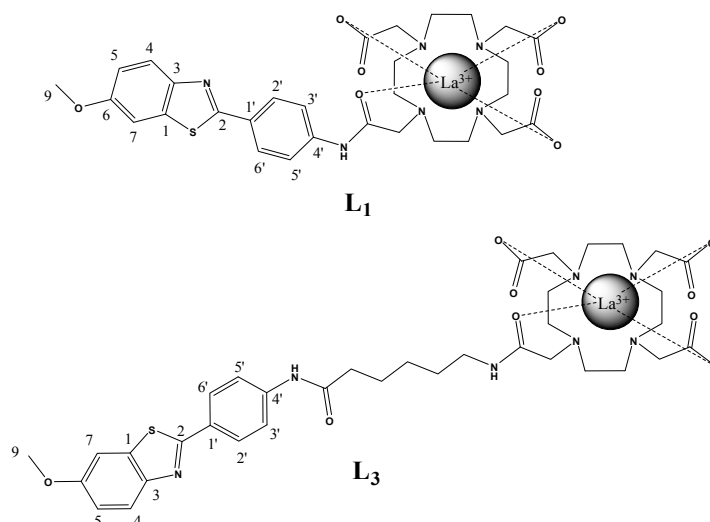
These K_D values are compared in **Table 5.1** with the affinities of various small molecules and proteins to immobilized A β_{1-40} obtained by different techniques. The affinities of these complexes to A β_{1-40} aggregates are two orders of magnitude lower than for the positively charged ThT, and five orders of magnitude lower than for neutral ThT analogues such as PiB.^{148,210} Apolipoprotein E (ApoE3) and the monoclonal antibody 6E10 also show very high (four to five orders of magnitude higher) affinities to A β_{1-40} aggregates.^{194,209}

Table 5.1. Binding affinities of various small molecules and proteins to A β_{1-40} obtained by using different techniques.

Molecule	A β_{1-40} aggregation state	K_D (μM)	Technique	Reference
LaL ₁	Aggregated	169.6 ± 21.0	SPR	This work
LaL ₁	Aggregated	160.7 ± 29.0	STD NMR	This work
LaL ₃	Aggregated	66.6 ± 8.0	SPR	This work
LaL ₃	Aggregated	147.9 ± 43.8	STD NMR	This work
ThT	Aggregated	2	Fluorescence	210
[¹¹ C]-ThT	Aggregated	0.580^a	¹¹ C radioactivity competition	148
[¹¹ C]-PiB	Aggregated	0.0047	¹¹ C radioactivity	148
ApoE3	Aggregated	0.010 ± 0.05	SPR	193
6E10	Aggregated	0.0014	SPR	209
6E10	Monomeric	0.0223	SPR	209

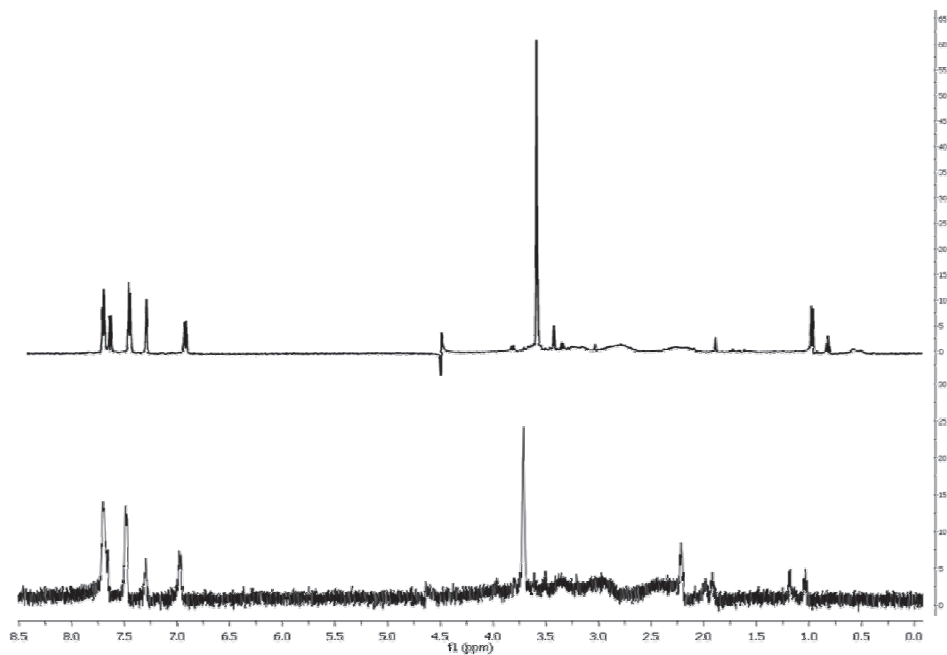
^a Inhibition constant (K_i); see Appendix 3

^1H STD NMR was used to perform the proton group epitope mapping (GEM) of our complexes (**Appendix 2**), defining the ligand region responsible for binding to the $\text{A}\beta_{1-40}$ peptide. **Figure 5.4** shows the proton NMR reference spectra of 0.5 mM LaL_1 and LaL_3 in the presence of 80 μM $\text{A}\beta_{1-40}$ assigned according to the numbering scheme shown in **Scheme 5.1**, and the corresponding STD spectra. The group epitope mapping was obtained by calculating the A_{STD} values for all PiB moiety protons and their relative STD (to 9- CH_3) (**Figure 5.5** and **Table 5.2**). The protons interacting with $\text{A}\beta_{1-40}$ are in both cases mainly those from the benzothiazole ring and the attached methoxy group. However, some important differences in the GEM between the two La^{3+} complexes are observed. The overall A_{STD} percentages are higher for the LaL_3 complex than for LaL_1 , while the absolute A_{STD} value for the methoxy group decreases by 13% in LaL_3 when compared to LaL_1 . Weak non-specific interactions are present in the STD spectrum of LaL_1 involving the macrocyclic ring protons, as well as stronger interactions can be seen for LaL_3 involving the aliphatic C_6 linker (**Figure 5.5**). These interactions, as well as the different linking spacer flexibility and length could explain the slightly higher affinity observed for complex LaL_3 .



Scheme 5.1. Chemical structures and numbering scheme of the PiB moiety of the ligands in the LaL_1 (top) and LaL_3 (bottom) complexes.

A



B

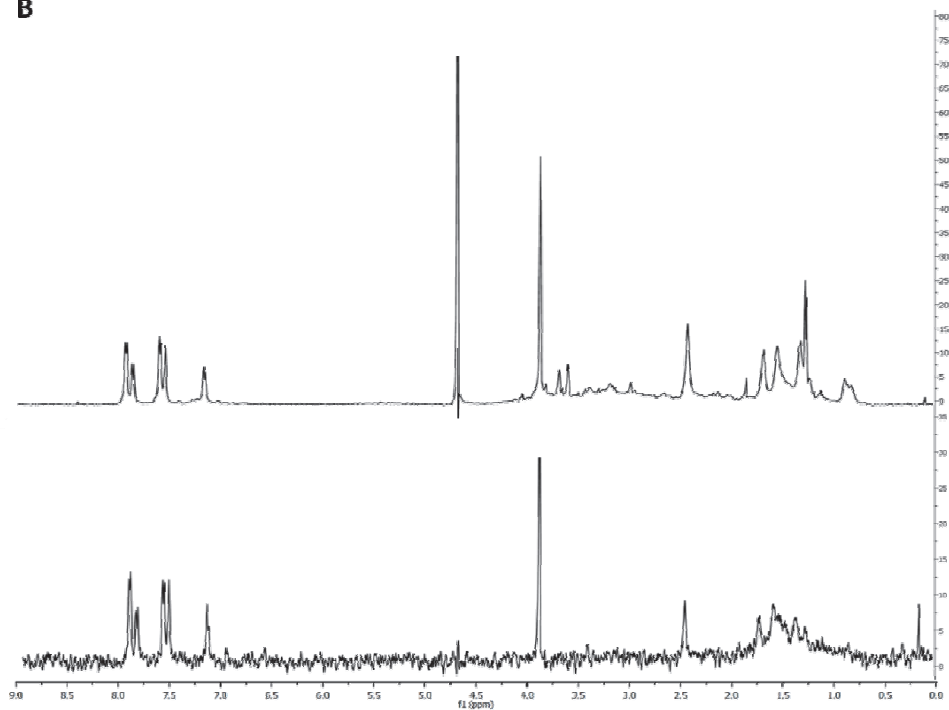


Figure 5.4. ^1H DPGSE reference NMR spectra of (A, bottom) 0.5 mM LaL₁ and (B, bottom) LaL₃ and corresponding ^1H STD NMR spectra for LaL₁ (A, top) and LaL₃ (B, top) in the presence of 80 mM A β_{1-40} (600 MHz, 25 °C, pH 7.2, saturation time 3 sec).

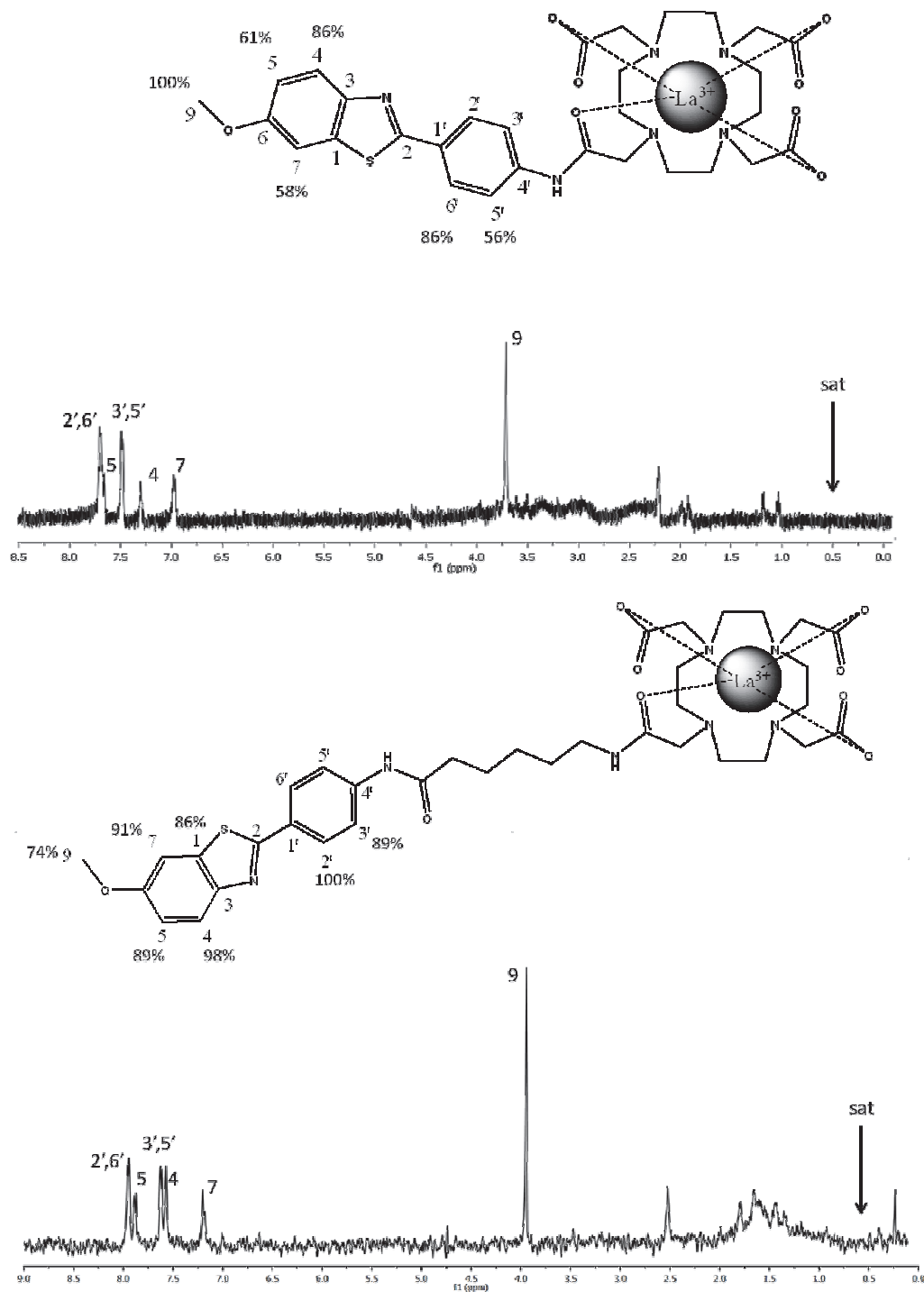


Figure 5.5. ^1H STD NMR spectra for LaL_1 (top) and LaL_3 (bottom) in the presence of 80 mM $\text{A}\beta_{1-40}$ and respective GEM (600 MHz, 25 °C, pH 7.2).

Table 5.2. STD amplification factor (A_{STD}) and relative STD (to the proton with the largest) for 500 μM LaL₁ and LaL₃ in the presence of 80 μM A β_{1-40}

Proton	LaL ₁		LaL ₃	
	A_{STD}	Relative STD (%)	A_{STD}	Relative STD (%)
9	17.3	100	18.5	74
5	10.6	61	16.8	98
4	10.2	59	16.5	89
7	10.0	58	16.5	89
2',6'	14.9	86	18.1	100
3',5'	9.7	56	13.7	91

Protein based NMR was also used to monitor the binding of the Ln³⁺ complexes to A β_{1-40} and to identify the peptide regions involved in the interaction. Previous studies have shown that ¹⁵N-¹H HSQC spectra constitute a sensitive probe of backbone conformational changes that can result from ligand binding to A β_{1-40} ^{133,186,211,212}. To test for possible interactions with the Ln³⁺ complexes, we followed changes in the ¹H-¹⁵N-HSQC spectra of ¹⁵N-A β_{1-40} at 5 °C in 10 mM K₂HPO₄ buffer, pH 7 upon the addition of aliquots of the diamagnetic La³⁺ complexes prepared in the same buffer. These initial experiments were carried out at low temperatures (5 °C) to minimize NMR signal loss due to amide hydrogen exchange with water and the effects resulting from peptide self-association.

An expansion of the ¹⁵N-¹H HSQC spectrum of ¹⁵N-labeled A β_{1-40} alone is shown in **Figure 5.6**. Peaks due to the side chain H₂N moieties of Gln 15 and Asn 27, and the peak arising from Arg 5's HNe are not shown. All the backbone HN groups appear in this spectrum, except for those belonging to D1, A2, H6 and H12, which are predicted to quickly exchange their hydrogen with solvent²¹³. The absence of these peaks can therefore be attributed to solvent exchange broadening. This spectrum is very similar to A β_{1-40} spectra recorded under similar conditions,^{186,214,215} except for our observation of the H13 signal which was not seen before.^{186,215} The peak assignments correspond to previous reports.²¹⁶

The A β_{1-40} peptide has the following sequence: DAEFR₅HDSGY₁₀EVHHQ₁₅KLVFF₂₀AEDVG₂₅ SNKGA₃₀IIGLM₃₅VGGVV₄₀.

Analysis of its ^1H and ^{15}N shifts and relaxation rates R_1 and R_2 revealed that the $\text{A}\beta_{1-40}$ monomer in aqueous solution at low temperature is chiefly disordered (random coil) with two regions with β -strand propensity (residues 16-24 and 31-36), two regions with propensity to adopt a poly-proline type II helix (PII-helix, a left-handed 3_1 -helix) (residues 1-4 and 11-15) and two unstructured regions with higher mobility (residues 5-10 and 25-30) connecting those structural elements. The monomer slowly trends towards the formation of oligomers and amyloid fibrils.²¹⁵

Upon titration with the LaL_1 complex, significant chemical shift changes, defined as $\Delta\delta > 0.01$ ppm for ^1H and > 0.1 ppm for ^{15}N ppm, were detected for the backbone NH crosspeaks of R5, S8, V12, K16 and L17 (**Figure 5.6**). In addition, the side chain $\text{HN}\epsilon$ of R5 shifts significantly and the backbone HNs of H13 and Q15 become invisible. These residues belong to a stretch of residues with contains most of the positively charged residues in $\text{A}\beta_{1-40}$. These changes are visible at $\text{A}\beta_{1-40}$ and LaL_1 concentrations as low as 100 μM and 50 μM , respectively, which suggest that their association constant is 10^4 M^{-1} or higher. Regarding the other backbone NH signals and the peaks arising from the side chains of Q15 and N27, no significant changes were observed in their chemical shifts, while the NH signals of residues Y10 and V12 are significantly broadened (**Figures 5.6 and 5.7**).

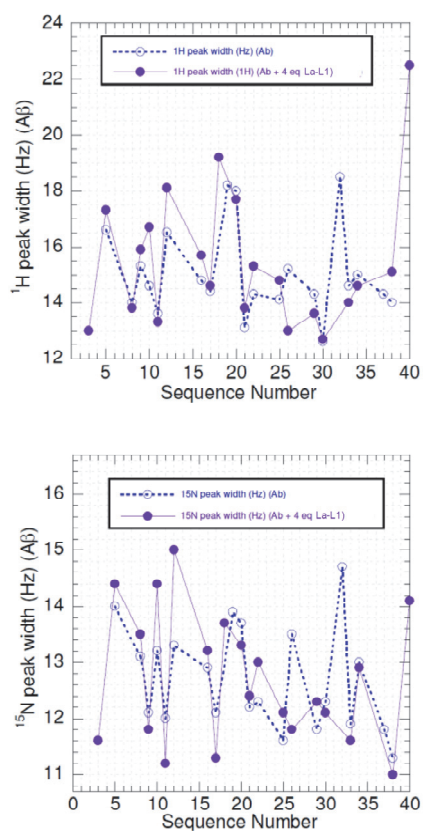


Figure 5.7. ^1H and ^{15}N line widths from the 5.0 $^\circ\text{C}$ ^1H - ^{15}N -HSQC cross-peaks of A β_{1-40} alone (\circ blue) or in the presence of a four-fold molar excess of LaL $_1$ (\bullet purple).

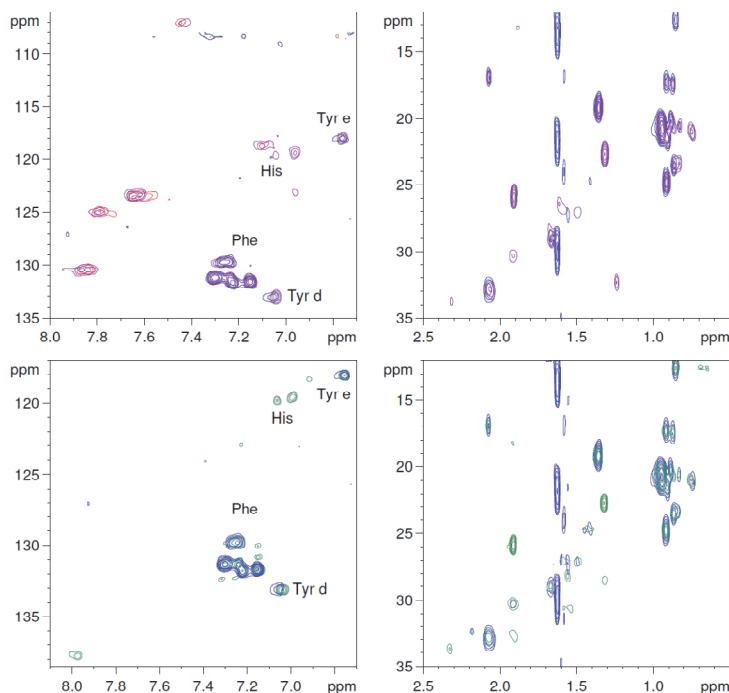


Figure 5.8. ^1H - ^{13}C HSQC spectra of 100 μM $\text{A}\beta_{1-40}$ recorded at 5.0 $^\circ\text{C}$ in 10 mM K_2HPO_4 buffer (pH 7) alone (blue) or in the presence of a four-fold molar excess of LaL_1 (purple, top panels) or LaL_3 (green, lower panels). The spectrum of LaL_1 alone is shown in red in the top left panel. These spectra were recorded on a Bruker AV-600 spectrometer operating at 600 MHz (^1H) and equipped with a cryoprobe. Aromatic and aliphatic regions are shown in the left and right panels, respectively.

The temperature dependence of ^1H and ^{15}N chemical shifts ($\Delta\delta/\Delta T$) and linewidths is quite sensitive to protein conformation²¹⁷. Therefore, as a further test for interactions between $\text{A}\beta_{1-40}$ and LaL_3 , we recorded ^1H - ^{15}N -HSQC spectra of ^{15}N -labeled $\text{A}\beta_{1-40}$ alone or in the presence of a four-fold excess of LaL_3 between 5.0 and 25 $^\circ\text{C}$. Generally, the proton resonances are shifted upfield, compared to the random-coil values.²¹⁸ The temperature-induced changes in peptide average conformation induce small upfield shifts in the $\text{A}\beta_{1-40}$ NH protons, which have some sequence specificity. Dependencies of ^1H shifts on temperature which are lower than -0.006 ppm per K (marked by the line in the upper panel of **Figure 5.9** top), corresponding to residues E3, Y10, E22, S26 and A30, have been interpreted as evidence of some folding propensity (PPII helix, β -sheet structures) at low

temperature.²¹⁵ However, our data are consistent other papers which have generally found that monomeric A β is chiefly random coil, specially at room temperature.^{214,216} The amide ^{15}N resonances also generally shift upfield with increasing temperature (Figure **Figure 5.7** bottom). $\Delta\delta^1\text{H} / \Delta T$ values are sensitive to changes in structure²¹⁹ and the residues with the smallest shift changes (E3-E11, O15, A21-E22, S26-A30, L34 and G38) are in general agreement with those observed for the ^1H shifts, indicating that La^{3+} -complex binding to the monomer does not induce significant changes in the backbone structure of the A β monomer.²¹⁵ We found that the temperature dependence of the chemical of A β_{1-40} are hardly affected by the presence of LaL_3 (**Figure 5.9**), which strongly suggests that LaL_3 binding does not significantly change the backbone conformational ensemble of monomeric A β_{1-40} .

The ^1H and ^{15}N linewidths of A β_{1-40} are hardly affected by the presence of a four-fold molar excess of LaL_3 (**Figure 5.10** top).

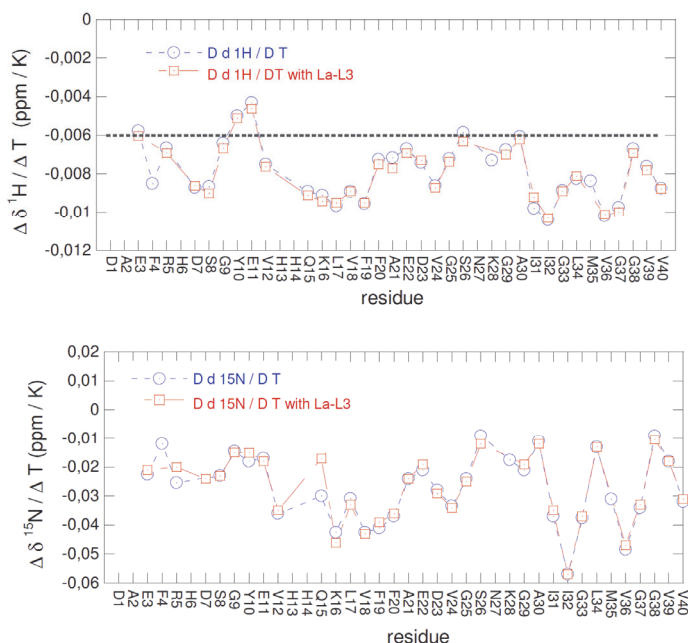


Figure 5.9. Temperature dependence of the ^1H (top) and ^{15}N (bottom) chemical shifts of A β_{1-40} alone (blue) and A β_{1-40} with a four-fold molar excess of LaL_3 (red).

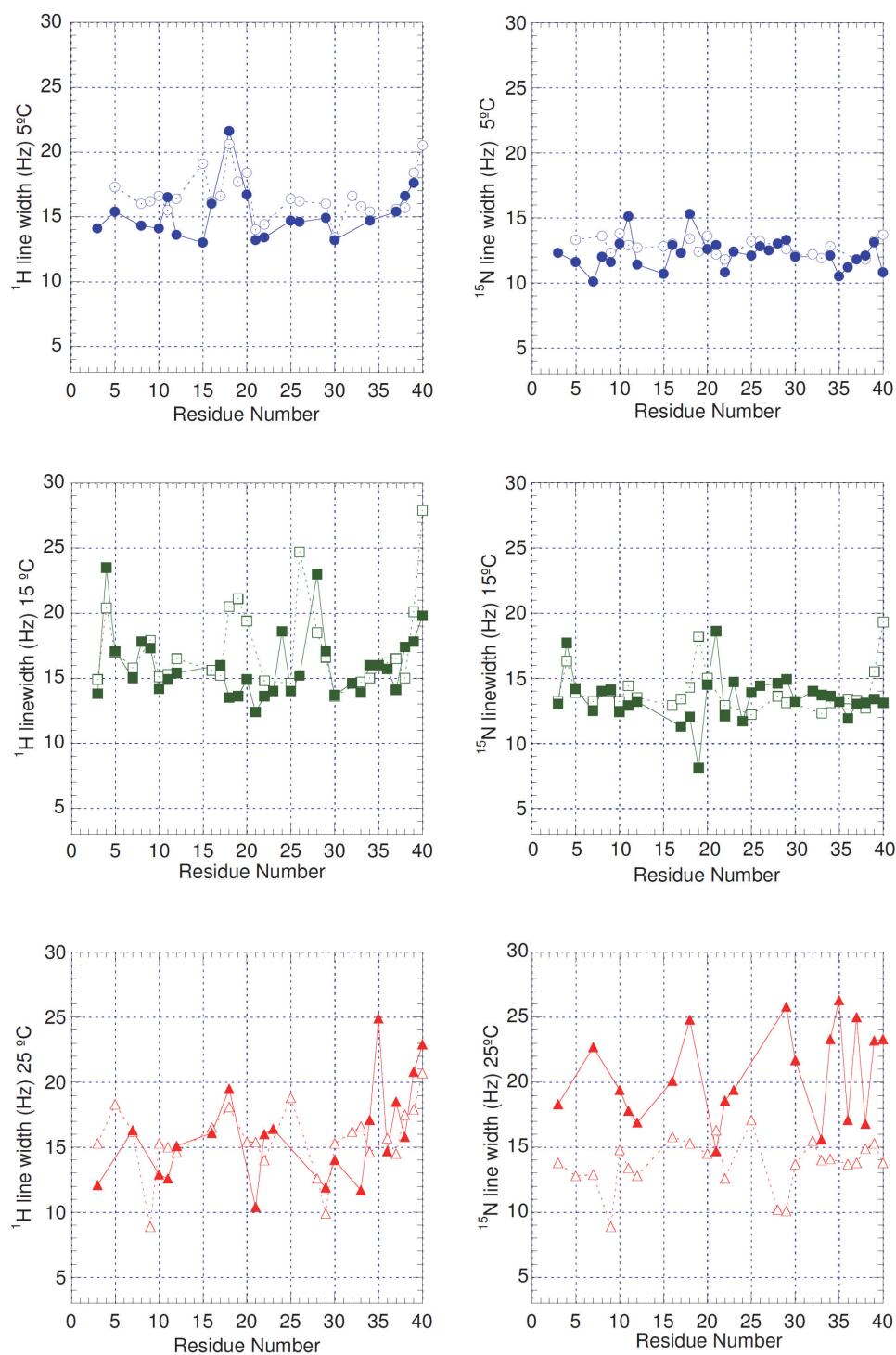


Figure 5.10. Temperature dependence of the ^1H (left) and ^{15}N (right) line widths from the ^1H - ^{15}N -HSQC cross-peaks of $\text{A}\beta_{1-40}$ alone (open symbols) and $\text{A}\beta_{1-40}$ with a four-fold molar excess of LaL_3 (full symbols) at 5.0 (top), 15 (middle) and 25 (bottom) °C.

In conclusion, a relatively specific interaction of $A\beta_{1-40}$ with LaL_1 is detectable by 1H - ^{15}N -HSQC NMR involving mainly the hydrophilic R5-L17 peptide region with a high concentration of charged residues, which includes the unstructured R5-Y10 region, the PII-helix prone E11-Q15 region, as well as K16 and L17 at the beginning of the first β -strand prone region. The interaction of monomeric $A\beta_{1-40}$ with LaL_3 is scarcely detectable by NMR. In any case, there is no evidence of significant formation of small peptide aggregates in the short time interval of those experiments. These results are in sharp contrast with the concentration-dependent decreases of cross-peak intensities throughout the whole $A\beta_{1-40}$ 1H - ^{15}N -HSQC spectrum observed upon addition of low concentrations of detergent-like molecules such as SDS (or LiDS)²¹² and Congo red¹³³ or hydrophobic molecules like lacmoid,¹⁸⁶ while their chemical shifts undergo only minor changes, which have been interpreted as evidence of formation of small heterogeneous peptide aggregates in intermediate exchange in the NMR time scale.

5.3.2. Effect of binding of Ln^{3+} complexes on the secondary structure of $A\beta_{1-40}$

The NMR data described above provide no clear evidence of any changes of secondary structure upon binding of LnL_x complexes to $A\beta_{1-40}$. Therefore we used far UV CD spectroscopy to assess the secondary structural changes of $A\beta_{1-40}$ upon LnL_x binding and how this affects the kinetics of $A\beta_{1-40}$ aggregation in solution.^{133,186,212,220}

In CD measurements of proteins the bands corresponding to the $n \rightarrow \pi^*$ (~220 nm) and $\pi \rightarrow \pi^*$ (~190 nm) electronic transitions involving the amide groups are very sensitive to secondary structural changes, and can be used to study them.^{221,222} The α -helical secondary structure is represented by a curve with an intense positive maximum residual molar ellipticity at 193 nm and two negative minima at 208 and 222 nm, respectively. The β -sheet structure is recognized as a curve with a positive maximum at 195 nm and a weak negative minimum at 215

nm. The random coil structure is characterized by a strong negative minimum at 197 nm. Other less common structures are beta turns I and II, with positive maximum at 195 and 205 nm, respectively, and negative minima at 205 and 223 nm, respectively. Another structure, which is common for small peptides with random coil propensity, such as A β ₁₂₋₂₈, is the left-handed polyproline II (PPII) helix, also known as 3₁ helix, characterized by a strong negative minimum at 197 nm and a weak positive band at 220 nm.^{223,224}

We started by performing CD experiments for free A β ₁₋₄₀ as a function of time at 3 °C, 25°C and 37°C. **(Figure 5.11)** At 3 °C, the initial CD spectra of free monomeric A β ₁₋₄₀ showed a predominant random coil contribution (minimum at 197 nm) with a significant contribution from the PPII helix (small maximum at 220 nm), in agreement with the literature,²²⁵ which estimated a PPII content of 43 % at 0 °C.²²³ The CD spectrum at 5 °C did not change for 5 days, but after 20 days the intensity of the whole spectrum decreased, perhaps due to light scattering from formation of larger particles. At 25 °C, and especially at 37°C, the initial CD spectrum corresponds more closely to a random coil conformation, with a marked decrease of the PPII contribution. This is in agreement with a previous study, which estimated the PPII content as 43 % at 37 °C.²²⁵ At these higher temperatures, the CD spectrum evolves more rapidly with time. At 25 °C, it starts to evolve after 24 hours, showing increasing contributions first from α -helix and later from β -sheet structures. At 37 °C, this evolution starts earlier (after 2 hours) and is more marked, as the α -helix is clearly predominant at 52 hours, and the β -sheet structure becomes predominant after 20 days.

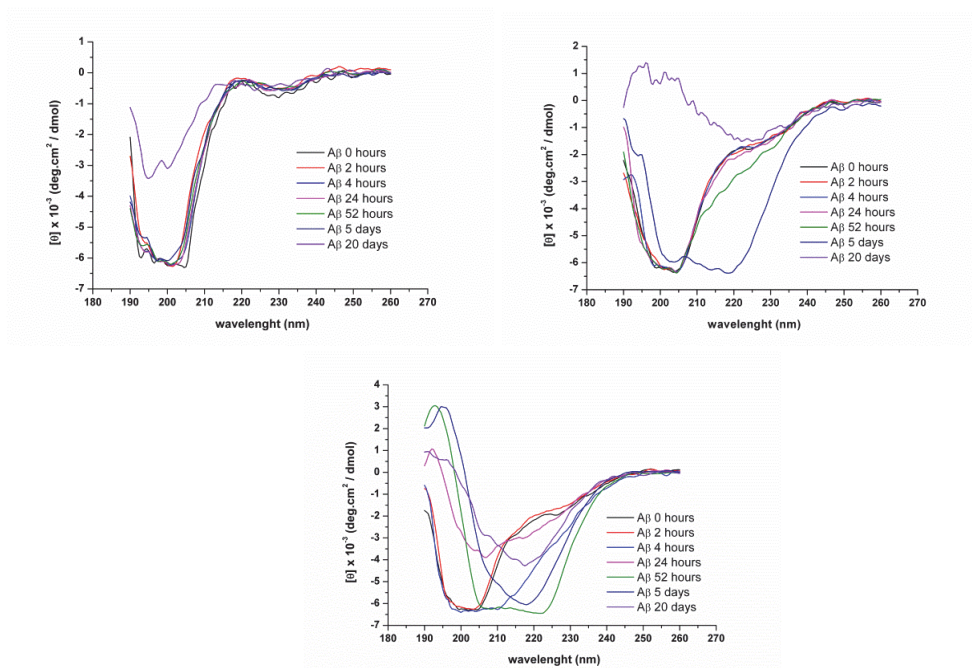


Figure 5.11. Time evolution of far-UV CD spectra of 40 μM $\text{A}\beta_{1-40}$ in 10 mM sodium phosphate buffer (pH = 7.3) at 3°C (up-left), 25°C (up-right) and 37°C (center-bottom).

The time evolution of the CD spectra of $\text{A}\beta_{1-40}$ was also investigated in the presence of increasing concentrations of the complexes GdL_1 and GdL_3 . The following experimental conditions were used: temperature - 3°C, 25°C and 37°C; GdL_x concentration - 0, 40, 80, 160, and 400 μM ; and time evolved - 0, 2, 4, 24, 48 hours, 5, 20 days. The solution pH was kept constant at 7.3 using 10 mM phosphate buffer. The data obtained in the presence of increasing concentrations of GdL_1 and GdL_3 are illustrated at time zero (**Figure 5.12**) and after 20 days (**Figure 5.13**).

The addition of increasing concentrations of the Gd^{3+} complexes induced, at time zero and at 5 °C up to a 1:4 molar excess, no changes in the positive peak at 220 nm corresponding to the PII helix region, and small amplitude decreases in the 190-205 nm region, indicating that some subtle structural changes might occur. However, no ordered α -helix and beta sheet structures become present upon binding of the complexes in these conditions. At higher temperatures the PII helix is not present at all complex concentrations and for a 1:10 equivalent excess, the disappearance of the PII helix conformation and a very small increase of ordered

α -helix and beta sheet structures could be detected (Figure 5.12). The lower intensity and resolution of the CD spectra observed for the solutions containing 400 μM Gd-complexes (1:10 molar ratio) could be related to light scattering effects possibly due to formation of aggregates involving the $\text{A}\beta_{1-40}$ peptide and/or the GdL_x complexes.^{133,186}

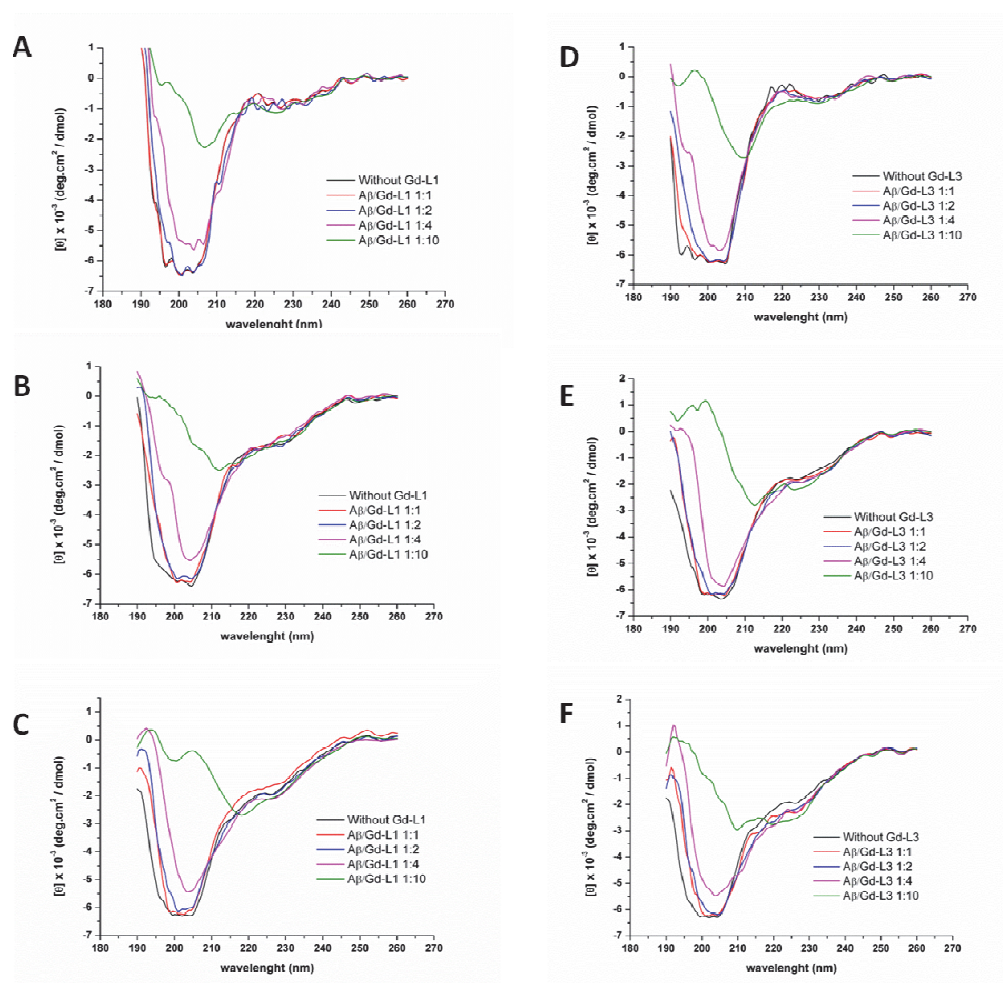


Figure 5.12. Far-UV CD spectra of 40 μM $\text{A}\beta_{1-40}$ in 10 mM sodium phosphate buffer (pH = 7.3) at time = 0 hours, in the presence of increasing concentrations of GdL_1 (left block: A,B,C) and GdL_3 (right block: D,E,F) at 3°C (A,D), 25°C (B,E) and 37°C (C,F).

We only observed clear changes to ordered α -helix and β -sheet structures for times longer than 2 hours and at the higher temperatures, 25 and 37 °C. Comparing the data at 20 days in the presence of the complexes, suggests that, at

37°C, GdL₁ preferentially induced formation of α -helix structure at lower peptide-to-complex ratios and of β -sheet structures at higher ratios, while GdL₃ stabilizes the α -helix relative to the β -sheet at all ratios. This is in contrast with the evolution after 20 days of the peptide in the absence of the complexes, where both at 25 and 37 °C the β -sheet structure predominates relative to the α -helix (**Figure 5.13**).

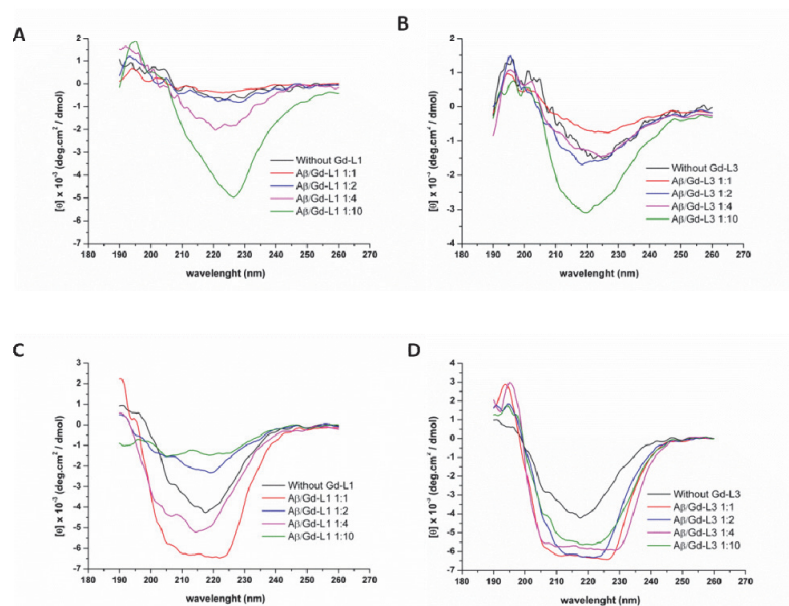


Figure 5.13. Far-UV CD spectra of 40 μ M A β ₁₋₄₀ in 10 mM sodium phosphate buffer (pH = 7.3) at time = 20 days, in the presence of increasing concentrations of GdL₁ (left block: A,C) and GdL₃ (right block: B,D) at 25°C (A,B) and 37°C (C,D).

The effect of these complexes on the secondary structure of A β ₁₋₄₀ is quite different from what has been observed for other additives at short times, such as the detergent molecules SDS and LiDS at concentrations below and above their cmc,²¹² Congo Red (CR)¹³³ and lacmoid.¹⁸⁶ At 20 °C, SDS and LiDS have been shown to induce a structural change from predominant random coil to β -sheet structure at concentrations below their cmc, and to α -helix above their cmc.²¹² On the other hand, CR promotes β -sheet formation by stabilizing the formation of a β -hairpin in the monomeric peptide through a strong specific electrostatic interaction of the positively charged side-chains of two lysine residues (K16 and

K28) with the two negatively charged sulfonate groups of CR,¹³³ while lacmoid binds more weakly and less specifically to exposed hydrophobic residues of the peptide monomer form, with no major effect on its secondary structure.¹⁸⁶ Thus, our complexes have a short-term effect on the secondary structure of A β ₁₋₄₀ closer to that of lacmoid, but its long-term observed effects, promoting both β -sheet and α -helical structures are the first reported studies of this kind.

5.3.3. Studies of the aggregation of A β ₁₋₄₀ by Thioflavin T fluorescence, dynamic light scattering and transmission electron microscopy

The effect of the GdL₁ and GdL₃ complexes on the aggregation process of A β ₁₋₄₀ was studied by three different techniques: Thioflavin T (Th T) fluorescence, DLS and TEM.

The well known fluorescence test for A β amyloid formation using the reporting dye ThT is based on the rapid association of Th T with aggregated fibrils of A β peptides, giving rise to a new excitation (ex) (absorption) maximum at 450 nm and enhanced emission (em) at 482 nm, as opposed to the 325 nm (ex) and 445 nm (em) of the free dye.²¹⁰ This change is dependent on the aggregated state, as monomeric and dimeric peptides, do not bind, but aggregated peptides do, eg. A β ₁₋₄₀ binds Th T with a K_D of 2 μ M.²¹⁰ **Figure 5.14 A** shows that this test worked in our hands and that A β ₁₋₄₀ is fully aggregated in the conditions used (30 μ M, 25 °C, pH 7.4) at 3 hours after sample preparation, as shown by the kinetic trace in **Figure 5.14 B**.

Many studies have been reported on the effect of additives on the kinetics of A β ₁₋₄₀ aggregation monitored by ThT fluorescence, finding that some promote the aggregation and others inhibit it.^{133,186,210,211,226,227} However, this technique was not applied for our studies on the effect of the GdL₁ and GdL₃ complexes on the kinetics of A β ₁₋₄₀ aggregation, because the fluorescence intensity of the free complexes was very high, with a maximum at ~430 nm, resulting from the PiB moiety²²⁸ which only slightly increased in the presence of aggregated (10days) A β ₁₋₄₀ (**Figure 5.15**).

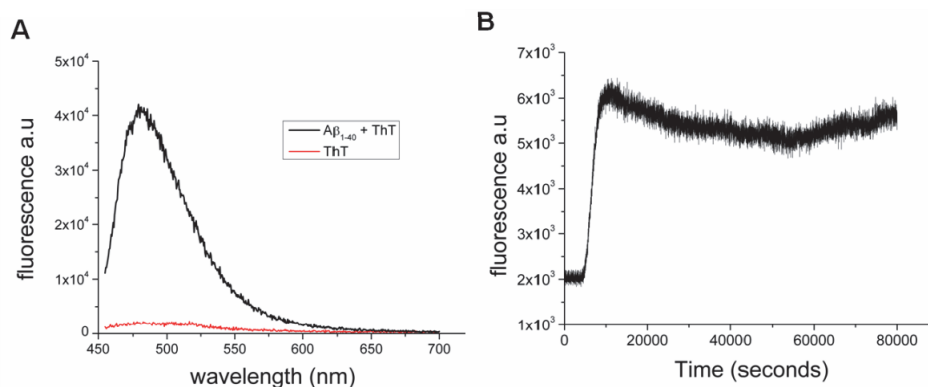


Figure 5.14. (A) Fluorescence spectra of 20 μM ThT alone (red line) and in the presence of 30 μM $\text{A}\beta_{1-40}$ (in 10 mM sodium phosphate buffer, pH 7.4) at 3 hours after dissolution (B) Kinetic traces of $\text{A}\beta_{1-40}$ fibril formation at 25 $^{\circ}\text{C}$ monitored by ThT fluorescence (20 μM) in a solution containing 30 μM $\text{A}\beta_{1-40}$. Samples were excited at 440 nm and the fluorescence emission was measured at 480 nm.

This effect would cause a strong background interference with the monitoring of the Th T fluorescence enhancement. Such an interference between ThT and another amyloid binding dye has been observed before, for example in the case of CR.^{133,226} Competition experiments with CR showed that the ThT fluorescence in the presence of $\text{A}\beta_{1-42}$ fibrils is partially suppressed in the presence of CR, which was interpreted as either fluorescence quenching or displacement of ThT from the fibrils.²²⁶ For these reasons, we did not pursue in this work the Th T fluorescence competition experiment with our complexes in the presence of aggregated $\text{A}\beta_{1-40}$.

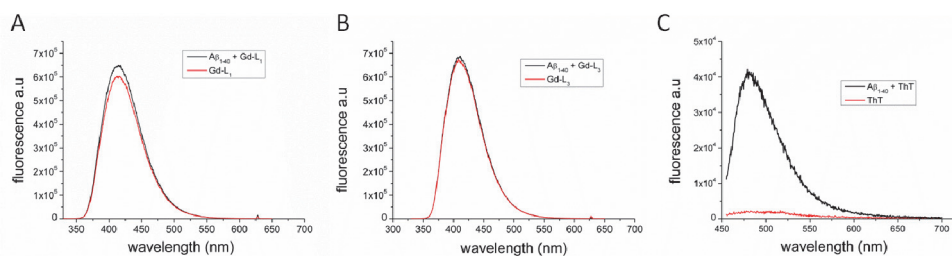


Figure 5.15. Emission spectra of (A) 20 μM GdL_1 , (B) 20 μM GdL_3 and (C) 20 μM Th T in the absence and presence of 20 μM $\text{A}\beta_{1-40}$ ($t = 0$) in 10 mM sodium phosphate buffer, pH 7.4). Th T and the Gd^{3+} -complexes were excited at 440 nm and 323 nm, respectively, and the fluorescence emission spectra were measured at 450nm — 700nm and 330nm — 650nm range, respectively.

Therefore, DLS was used to monitor the fibrillar evolution of $\text{A}\beta_{1-40}$ with time (up to 10 days) and concentration (40, 80 and 160 μM) of complexes at 25°C. **Figure 5.13** shows only a small DLS intensity (counts per second) increase with time for the $\text{A}\beta_{1-40}$ control solution. The solutions containing $\text{A}\beta_{1-40}$ and the Gd^{3+} complexes showed different time evolutions: a large increase with time of the DLS intensity for the $\text{A}\beta_{1-40}$ solutions in the presence of GdL_1 and a small decrease in the presence of the GdL_3 complexes. The hydrodynamic profiles obtained for the same DLS experiments exhibited small particles (hydrodynamic radius $R_H \sim 10\text{-}20$ nm size) for the solutions containing the GdL_3 complexes, while the $\text{A}\beta_{1-40}$ solutions in the absence and presence of GdL_1 had large particles ($R_H \sim 240\text{-}250$ nm) (**Figure 5.14**). DLS autocorrelation functions also showed a shift toward shorter correlation times as the concentration of GdL_3 increased (data not shown). These findings could be related to a promotion of β -amyloid aggregation by GdL_1 and an inhibitory effect of GdL_3 . Such effects have been observed before for CR and low concentrations of SDS,¹⁸⁵ and lacmoid,¹⁸⁶ respectively.

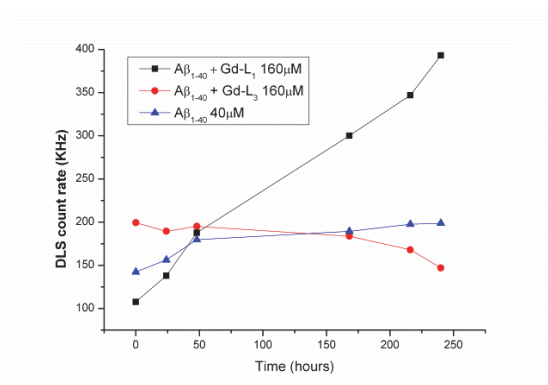


Figure 5.16. Light scattering intensity as function of time for samples containing 40 μM A β_{1-40} (blue), 160 μM GdL₁ (black) and 160 μM GdL₃ (red).

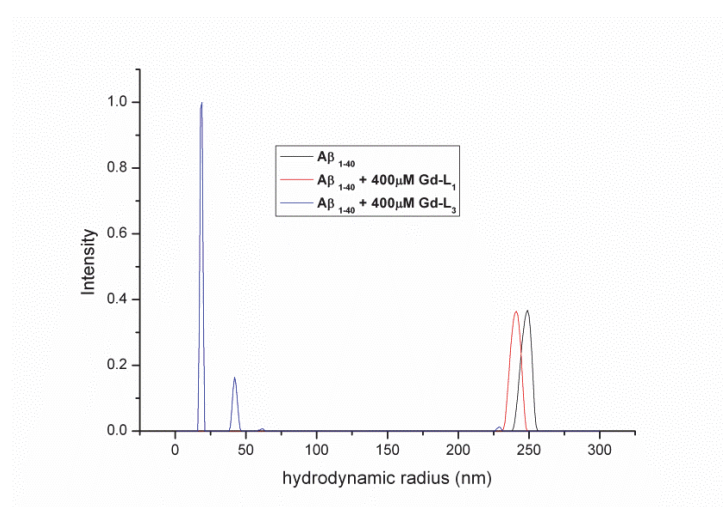


Figure 5.17. Particle size (given by hydrodynamic radius R_H) distributions determined using the regularization algorithm of the Malvern software: 40 μM A β_{1-40} alone (black) and in the presence of 160 μM GdL₁ (red) or 160 μM GdL₃ (blue) at 10 days.

TEM images were also obtained to evaluate the influence of the two Gd³⁺ complexes on A β_{1-40} amyloid fibril formation and morphology. We have recorded TEM images of A β_{1-40} in the absence and in the presence of increasing concentration equivalents of the complexes (1:0, 1:1 and 1:4) (**Figure 5.17**). The images clearly show that after 20 days of incubation A β_{1-40} presented: organized amyloid fibrils when alone; disorganized structured aggregates and fibrils, in the presence of GdL₁; and reduced amyloid fibrils, in the presence of GdL₃ (mainly seen at 1:1 equivalent concentration of 40 μM). TEM images also showed the

presence of small fibrils of 34-86 nm in both samples containing GdL₁ and GdL₃ (see **Figure 5.14**, magnetizations at 100 nm). These studies confirm that GdL₃ could induce an inhibitory effect on β -amyloid aggregation, similar to that observed in the presence of lacmoid,¹⁸⁶ while the effect of GdL₁ is more akin to that observed in the presence of CR, which on TEM images show an increased presence of fibrillar peptide aggregates.¹³³

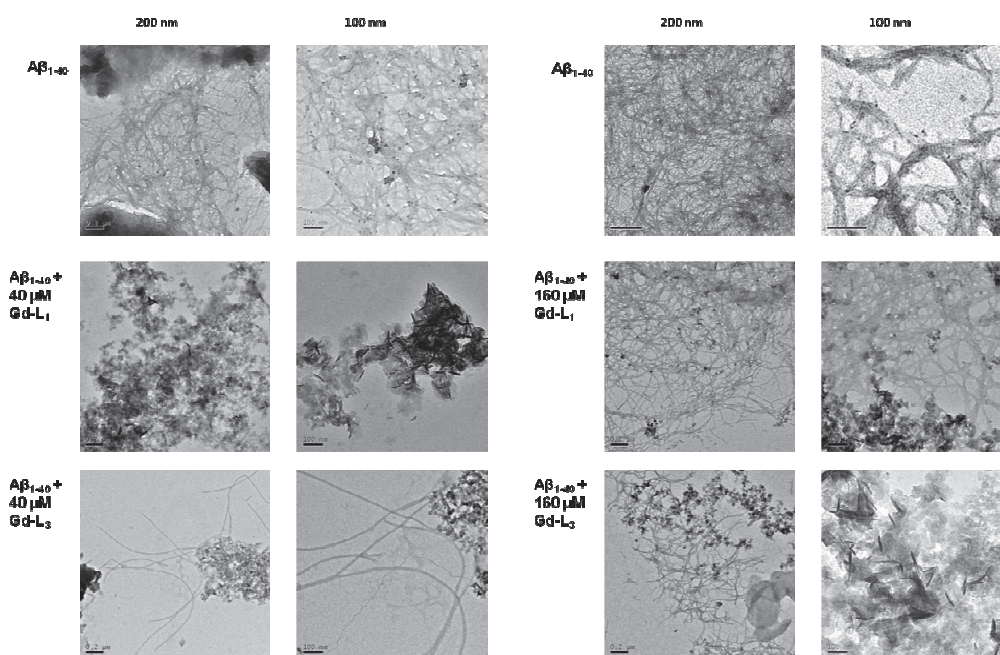


Figure 5.18. TEM images after 20 days incubation of 40 μ M A β ₁₋₄₀ alone (first row), 40 μ M A β ₁₋₄₀ / 160 μ M GdL₁ (second row) and 40 μ M A β ₁₋₄₀ / 160 μ M GdL₃ (third row). Left and right images of each block group represent different magnifications.

5.4. Conclusions

In the present work we found that the stable neutral complexes of lanthanide ions with two new synthetic DO3A-PiB derivatives, L₁ and L₃, interact with both monomeric and aggregated A β ₁₋₄₀ in aqueous solution. A slight modification of the L₁ ligand by introduction of an aliphatic C₆ chain spacer between the chelating DO3A macrocycle and the targeting PiB (Pittsburgh

compound B) moiety turns out to change not just the strength of the interaction (as measured by the dissociation constants, K_D), but also the stability of the aggregated structures. The affinity values of LaL₁ and LaL₃ to immobilized A β ₁₋₄₀ (measured by SPR) and of LaL₃ to are two orders of magnitude lower than for the positively charged ThT, and five orders of magnitude lower than for neutral ThT analogues such as PiB.^{148,210} The group epitope mapping (GEM) for LaL₁ and LaL₃, obtained by STD NMR,²⁰⁴ shows in both cases that the complexes interact with immobilized A β ₁₋₄₀ mainly through the benzothiazole ring and the attached methoxy group. However, some important differences are observed which could explain the slightly higher affinity observed for the LaL₃ complex. The increased absolute A_{STD} values for the PiB moiety suggesting an increased interaction with the peptide aggregate surface and a contribution from non-specific interactions involving the flexible aliphatic C₆ linker suggests an optimization on the binding properties in this complex. Although both La³⁺ complexes interact with the aggregated A β ₁₋₄₀,¹⁹³ the short distance between the two moieties (chelating and targeting) in GdL₁ perturbs its effective interaction with the peptide.¹⁵⁰

These findings take special relevance when we relate them with the A β ₁₋₄₀ aggregation kinetics data presented in this work. Are our neutral complexes able to inhibit A β ₁₋₄₀ amyloid fibril formation in water solutions or do they promote it? Our Circular Dichroism (CD), Dynamic Light Scattering (DLS) and TEM studies at different temperatures, complex-peptide ratios and times, suggest that the natural fibril formation is inhibited by GdL₃ and slightly promoted by GdL₁. The formation of β -sheet structure is linked to A β ₁₋₄₀ self-assembly in solution, while polyproline PII and specially α -helical structures are related to the inhibition of large amyloid assemblies.^{212,230,231} Our extensive CD studies showed that, while at 3 °C the random coil and polyproline PII conformational mixture present in the free A β ₁₋₄₀ peptide did not significantly change in the presence of the complexes, at 25 and 37 °C the PII conformation disappeared immediately and ordered α -helical and β -sheet structures were formed more rapidly even in the absence of the complexes. The presence of these complexes promoted the earlier formation of these ordered structures, depending on their concentration: the α -helical structure dominated in the presence of GdL₃ at all concentrations, while GdL₁ promoted the formation of β -sheet structures at higher concentrations.

DLS data supported the inhibition of A β ₁₋₄₀ aggregation by GdL₃, indicating the formation of particles with reduced hydrodynamic radius for the A β ₁₋₄₀ solutions in the presence of the GdL₃, with autocorrelation functions shifted toward shorter correlation times. The TEM images also confirmed that the addition of GdL₃ to A β ₁₋₄₀ fibrils induced the dissociation of large A β aggregates. Thioflavin-T fluorescence kinetics profiles confirmed the slow fibrillation process of A β ₁₋₄₀ but the effect of the complexes in this process was not studied by this technique, due to the interference of the two dyes used.

The mechanisms by which monomeric soluble A β ₁₋₄₀ converts into large self-assembled aggregates or fibrils are extremely relevant for the elucidation of the origins of Alzheimer's disease.^{85,89} A favored aggregation mechanism for A β ₁₋₄₀ involves an initial formation, from the disordered monomer, of an antiparallel β -hairpin involving association of the two β -strands (K16-V24 and I31-V36) with an interior hydrophobic core, followed by formation of soluble oligomers by hydrophobic stacking of β -hairpins and by a concerted conformational transition to a fibril containing parallel β -sheets. The specific stabilization of this β -hairpin monomeric intermediate by the affibody protein Z_{A β 3} dimer was found to inhibit amyloid formation.²¹¹ However, the effect of non-specific small molecule modulators of A β peptide self-assembly through structural changes involving less specific hydrophobic or electrostatic interactions is a more controversial issue.^{232,233} An hydrophobic aromatic molecule like lacmoid inhibits the aggregation process A β ₁₋₄₀ by binding to the exposed hydrophobic surfaces of the peptide, favoring its monomer state.¹⁸⁶ CR stabilizes the β -hairpin intermediate by specific interaction with two positively charged lysine residues, K16 and K28, thus promoting fibril formation.¹³³ The dual effect of surfactants like SDS or LiDS on the aggregation process, favoring it at low concentrations (below cmc) and inhibiting above the cmc, depends on how they modulate the hydrophobic attraction between the peptide monomers as well as their conformational preferences. Such an example is given by SDS, where at low concentrations, the individual surfactant molecules promote the β -hairpin structure,²¹² while at high concentration the micelles present incorporate the peptide monomer by promoting the formation of two α -helical structures separated by a flexible loop, one in the Q15-G25 region with an amphipatic surface stabilized by the micellar surface and

the second in the I31-V36 region with an hydrophobic surface buried in the micelle core.¹⁸⁵

Our two neutral complexes have quite high cmc values and different hydrophobicities: GdL₁ (cmc = 1.49 mM, log P = - 0.15) and GdL₃ (cmc = 1.0 mM, log P = 0.03) (see **Chapter 4**). The present study was carried out at concentrations much below those cmc values, thus only monomers are present, and the most hydrophobic monomer, GdL₃, stabilizes the α -helical peptide structure and has the better protective effect against peptide aggregation.

The explanation for this observation is present in the interaction of the individual complex molecules with the binding domains of the A β ₁₋₄₀ monomer.^{234,235} This was investigated by protein-based ¹H-¹⁵N-HSQC NMR of the ¹⁵N-labeled peptide. In the case of the LaL₁ complex, ¹H-¹⁵N-HSQC spectra provide evidence suggesting that the complex binds to an hydrophilic segment of A β ₁₋₄₀ with a high concentration of charged residues that spans residues R5 - L17. The lack of alterations in the ¹H-¹³C-HSQC spectra leads us to advance that the binding A β and LaL₁ does not involve their nonpolar moieties.

Evidence for binding to A β ₁₋₄₀ monomer is more scarce in the case of LaL₃, contrasting to some reported works with lacmoid and Cu²⁺ binding to A β in which ¹H-¹⁵N-HSQC NMR signals specifically broaden greatly and disappear,^{186,216} leading us to conclude that the binding of LaL₃ to monomeric A β ₁₋₄₀ (the form chiefly detected by liquid state NMR spectroscopy) has a K_D of 3 x10⁻⁴ M or weaker. The main difference between the two ligands is the presence of a rather long aliphatic linker in LaL₃. This leads us to suggest that the proximity of the hydrophilic lanthanide cage to the PiB moiety of the complex could be a factor in the stronger binding of the LaL₁ ligand to monomeric A β . Moreover, the increased flexibility of the aliphatic C₆ chain in LaL₃ gave rise to: higher hydrophobic nature, stronger affinity constants to the aggregate, weaker molecular constraints and increased inter/intra molecular disorder.

Our results strongly suggest that LaL₃ and probably LaL₁ will not interact with monomeric A β at normal, physiologically relevant concentrations of the peptide. This is important for two reasons. First, A β ₁₋₄₀ has been reported to protect the brain against bacterial infection as at low (μ M) concentrations as it is a potent bacteriostatic²³⁶, and therefore the weak to insignificant binding of these

lanthanide complexes will not interfere with the $A\beta_{1-40}$'s normal beneficial activity. Second, it can be predicted that the relatively weak binding of the corresponding Gd^{3+} complexes to monomeric $A\beta_{1-40}$, which is normally present, will reduce background and enhance the signal contrast when these MRI probes bind to $A\beta_{1-40}$ amyloid fibrils and plaques.

Taken together, our findings prove a principle to guide the scientific community on the discovery of optimized small molecules able to: target specifically aggregated amyloid $A\beta$, improve their hydrophobic nature, inhibit $A\beta$ toxic self-assemblies and evince a therapeutic effect.

CHAPTER 6

*"In Vivo Studies of M^{3+} -
DO3A-PiB Derivatives"*

6.1. Introduction

This Chapter reports the results of the experiments undertaken to answer the key question that will determine the success of the prepared compounds in their *in vivo* applications: have the trivalent metal complexes $M^{3+}L_x$, $x=1,2,3$ the capability to cross *in vivo* the Blood Brain Barrier (BBB) and specifically target amyloid plaques, despite the adverse *in vitro* data described in the previous Chapters 4 and 5 (molecular weight, $\log P_{\text{Oct/water}}$, weaker affinity to $A\beta$ peptides)?

Several advances in PET (and also SPECT) technology contributed extensively to *in vivo* imaging studies of small animals.^{237–239} So far, the attempts to use MRI to obtain molecular images able to non-invasively detect amyloid plaques have met only limited success, as only few studies have been reported to achieve this goal, as discussed in Chapter 1 (**Section 1.5 d**).^{139,140} Transgenic mice, possessing specific mutations (APP/PS1-21) which develop $A\beta$ deposits, tangles and synaptic dysfunction, thus mimicking the human AD pathology, have been shown to be useful models for *in vivo* imaging of AD onset.^{240–242} However, the translation from preclinical to clinical $A\beta$ imaging remains a challenge with the current transgenic models of AD. Indeed, some of the imaging probes, including PiB derivatives, give negative results in preclinical models while they are useful in humans. This is due to the difference in composition, structure and compaction of $A\beta$ peptides between human and rodent amyloid plaques.^{243–245}

The development of diagnostic agents for early *in vivo* visualization of the amyloid plaques is an important challenge in molecular imaging today, and it would also be important for monitoring new therapies of AD. Small organic compounds, such as derivatives of thioflavin T, benzoxazoles, stilbenes and oxazines, have high binding affinities for the $A\beta$ aggregates and some of them pass the BBB. They inspired the development of amyloid-labelling nuclear imaging probes.^{126,128,129,149,188,246} ^{11}C - and ^{18}F -labelled derivatives of stilbene¹²⁸ and Pittsburgh compound-B (PiB)^{129,149} are some of these examples making their way into the clinics.^{128,129,188} Attempts have been also made to develop neutral

^{99m}Tc -labelled $\text{A}\beta$ SPECT probes which, given the easier accessibility of ^{99m}Tc as compared to ^{18}F , could provide a more convenient approach to the detection of AD (see Chapter 1, section 1.5.4. b).^{134–137}

In this study, we explored the binding selectivity of amphiphilic $\text{M}^{3+}\text{-L}_1$ complexes to amyloid plaques via *ex vivo* assays with AD human and Tg APP_{swe}, PSEN1dE9 mice brain slices, as well as the *in vivo* biodistribution of the radioactive $^{111}\text{In}^{3+}\text{-L}_1$ complex as SPECT tracer in normal Swiss mice which informs about the brain uptake of the injected dose per gram (ID/g) of the radioactive complex.

6.2. Experimental

6.2.1. *Ex vivo* human immunostaining studies

6.2.1.1. Cases

AD patients had been enrolled in a brain donation program of the Brain Bank “GIE NeuroCEB” run by a consortium of Patients Associations (including France Alzheimer Association) and declared to the Ministry of Research and Universities, as requested by French Law. An explicit consent had been signed by the patient himself, or by the next of kin, in the name of the patient, in accordance with the French Bioethical Laws. The project had been approved by the ad hoc committee of the Brain Bank. At the time of death, the corpse was transported to the mortuary of a University Hospital belonging to the NeuroCEB network and the brain was removed. One hemisphere randomly left or right, was fixed in buffered 4% formaldehyde for the neuropathological diagnosis of AD. The other hemisphere was immediately sliced. Samples from the superior temporal gyrus (Brodmann area 22), around 4 cm³ in volume, were mounted on a cork piece with Cryomount embedding medium and dipped in isopentane cooled by liquid nitrogen. The samples were kept in a deep freezer at -80°C .

6.2.2. Diagnosis

Multiple samples from the formalin-fixed hemisphere, including the hippocampus and isocortical area Brodmann 22, were embedded in paraffin and cut at 5 μm of thickness. The sections were stained with hematoxylin-eosin and immunostained with anti-A β (6F/3D clone; Dako, Trappes France) and anti-tau (polyclonal rabbit anti-tau antibody; Dako; Trappes code number A 0024). The lesions were staged according to Braak and Braak.²⁴⁷ The density of the SPs was evaluated according to the CERAD protocol.²⁴⁸ The diagnosis criteria of the NIA-Reagan Institute were used.²⁴⁹ Care was taken to select cases with a high number of mature SPs containing an amyloid central core of A β peptide. One sporadic case at Braak stage VI with “frequent” SPs and NIA-Reagan “high probability” was finally chosen.

6.2.3. Samples for staining

Ten micrometer thick brain sections from the temporal cortex of the AD subject (determined as previously described) were obtained from the frozen block with a Leica CM 3050 S cryostat. They were mounted on “Superfrost Plus” slides (Thermo Scientific) and stored at -80°C until immunostaining or staining with PiB and EuL₁.

6.2.4. Senile plaques staining

Post-mortem frozen samples of temporal cortex of three Alzheimer Disease (AD) subjects (Braak stage VI: numerous focal, diffuse, subpial deposits as well as amyloid angiopathy) were studied.

The frozen 10 μm thick brain sections were thawed for few minutes at room temperature and fixed for 10 min in 100% acetone (Prolabo), then washed three times for 5 min with PBS (Sigma). Afterward, the samples were incubated in a 200 μl solution of PiB or EuL₁, at a concentration of 1mM in PBS during 90 min. The samples were washed in PBS and mounted using a fluorescent mounting medium (Dako). All preparations were performed at room temperature. An epifluorescent microscope (Olympus BX50) was used for the examination of the tissue. Images were collected in violet filter with a photometrix camera using Metaview software.

6.2.5. Immunofluorescent labeling of senile plaques²⁵⁰

A method for reliably staining the senile plaques (SPs) on the brain tissue was needed to confirm the positive staining of PIB or EuL₁ derivative by co-localization. In this case, after acetone fixing and PBS washing the sections were incubated for 4h in a 200 µl solution of 6F/3D antibody (Dako). The samples were washed 3 times with PBS and incubated for another 2 h with the secondary antibody bearing the chromogen red CY3. Following the immunostaining, the samples were further washed 3 times in PBS before incubation with PIB or EuL₁, the same concentration as previously used, for 90 min. The co-localization was examined by epifluorescent microscopy using either green or violet filter of the same zone. The analysis of images was performed with Photoshop 7.0 and the colocalization was confirmed by superposing the images corresponding to the green filter - representing the immunostaining of senile plaques and the violet filter –corresponding to the staining by PIB and EuL₁.

6.2.6. Animal studies

Animal experiment procedures were performed in strict accordance with the directives of the European Union (86/609/EEC) and validated by the Regional Ethics Committee (approval number: 0310-02). APP/PS1-21 (line 21) and corresponding (C57Bl6) control mice were used and also adult male Swiss mice. APP/PS1-21 mice coexpress human APP carrying the K670N/M671L “Swedish” double mutation and hPS1 L166P with a 3-fold overexpression of human APP over endogenous mouse APP. Mice express the transgene under the control of a neuron-specific mThy-1 promoter element and generated on a C57Bl6 background (Radde et al., 2006). C57Bl6 mice, that do not display amyloid plaques, were used as controls. Animals were housed at constant temperature (22 °C) and humidity (50%) with a 12-hour/12-hour light/dark cycle and had access to water and laboratory chow *ad libitum*.

6.2.7. *In vitro* autoradiography

The *in vitro* autoradiography was recorded on Tg APP^{swe}, PSEN1^{dE9} mice brain sections. Frozen brains from Tg and control mice were cut into 20-mm sections. The sections were incubated with ¹¹¹InL₁ in 40% ethanol at a concentration of 1 μM for 1 h. Non-specific binding was defined by adding 500 μM of “cold” AV-45 (a reference ligand for Aβ). The sections were then dipped in saturated Li₂CO₃ in 40% ethanol (2-min wash twice) and washed with 40% ethanol (2-min wash once), followed by rinsing with water for 30 s. After drying, the sections were exposed to Kodax Biomax MRI film for 2 days. After the film was developed, the images were digitized.

6.2.8. Radiolabeling

The DO3A-PiB precursor in isotonic ammonium acetate pH 7.0 buffer was treated with a solution of ¹¹¹InCl₃ (specific activity 15.38 TBq/mg, PerkinElmer, Boston, USA), in order to obtain 1:1 ¹¹¹In³⁺ complexes (with 10% precursor excess). Complexation was performed by heating the mixture at 100°C for 30 min. The efficiency of radiolabeling with ¹¹¹In³⁺ was controlled by thin layer chromatography (ITLC-SG / MeOH:H₂O:NH₄OH (2:4:0.1) system), indicating that a >96% radiochemical purity of the complex was achieved (**Figure 6.5**). The *in vitro* stability of the complex was evaluated and the complex remained stable with a degradation rate of 2% up to 22h after radiolabeling.

6.2.9. *In vivo* biodistribution in mice

Studies were carried out on adult male Swiss mice that had no amyloid deposits in their brain (Centre d'élevage René Janvier, Le Genest-Saint-Isle, France), weighing 36±1 g, in compliance with the French legislation on animal experimentation and European directives. Animals were housed in a temperature (23±0.5°C)- and humidity (43%±8%)-controlled environment under a 12-h light–dark cycle with food and water available *ad libitum*. A saline solution of ¹¹¹InL₁ (2 – 2.5 MBq/100 μL) was intravenously injected through the penis vein. The mice

were euthanized by decapitation at 2 (n=6), or 30 min (n=4) after radioligand injection, and organ samples, including cortex, cerebellum, heart, liver, lung, and kidney were quickly removed and weighed. The radioactivity was measured with an automated γ -counter (Cobra Quantum Packard), and the percentage injected dose per gram of wet tissue (% ID/g) was calculated by comparison to a diluted standard solution derived from the initial injected solution.

6.3. Results and Discussion

We have tested the capability of the imaging agent to bind amyloid aggregates on post-mortem human brain tissue of AD patients by using the Eu^{3+} analogue EuL_1 . The staining with EuL_1 revealed the presence of various amyloid deposits. The distribution pattern and intensity of the senile plaques were similar for PiB or Thioflavin-S and EuL_1 (**Figures 6.1 and 6.2**). Nevertheless, EuL_1 seems to have lower affinity for neurofibrillary tangles, being thus more specific to $\text{A}\beta$ deposits than its PiB precursor (**Figure 6.3**). In order to confirm that PiB and EuL_1 labelling is specific for the amyloid deposits, we performed a double fluorescence staining experiment using the routinely employed 6F3D antibody. **Figure 6.4** shows the labelling of a senile plaque with both the 6F3D antibody and PiB or EuL_1 . The staining of PiB and EuL_1 is strong in the focal deposits while the surrounding crown is slightly less positive, probably due to its partially fibrillar morphology. Some of the less intense $\text{A}\beta$ positive structures were not labelled by PiB or EuL_1 .

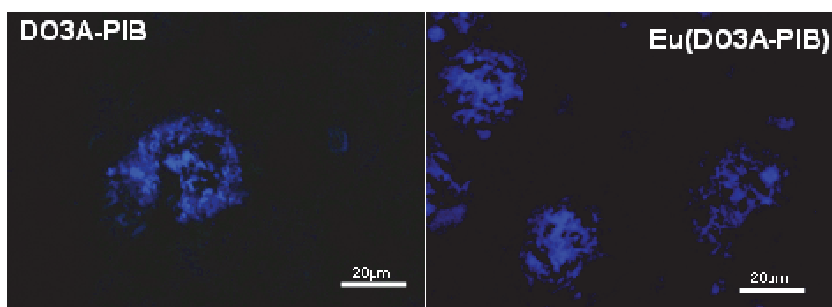


Figure 6.1. Micrographs illustrating the staining of amyloid deposits by L_1 and EuL_1 , on post-mortem AD brain tissue.

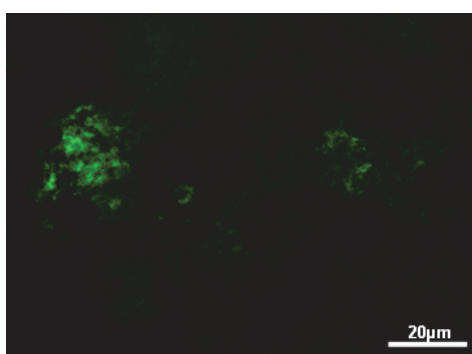


Figure 6.2: Micrograph illustrating the staining of amyloid deposits by Thioflavin-S, on post-mortem AD brain tissue.

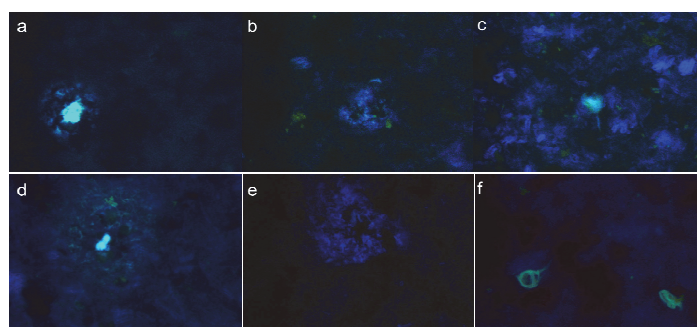


Figure 6.3. Positive staining of an Alzheimer tissue with PiB (a, b, c) and EuL_1 (d, e, f). Senile plaques (left), diffuse deposits (middle), and neurofibrillary tangles (right) are put into evidence by the PiB and EuL_1 staining.

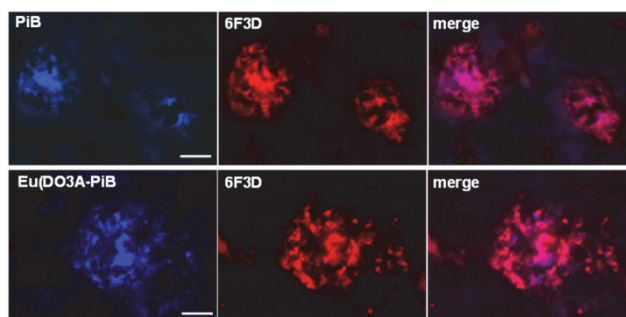


Figure 6.4. Micrographs illustrating the co-localisation of PiB or EuL₁ and 6F3D-antibody labelling of amyloid deposits of post-mortem human brain tissue of an AD patient: the colocalization is confirmed by the magenta color in the “merge” images; scale bar = 20 μ m.

In order to evaluate the penetration of our complexes across the BBB, we have performed *in vivo* biodistribution experiments with the ¹¹¹In-analogue in adult male Swiss mice which had no amyloid deposits in their brain. The radiolabelling of the ligand has been carried out in isotonic ammonium acetate at pH 7.0, by adding a solution of ¹¹¹InCl₃ (specific activity 15.38 TBq/mg), in order to obtain 1:1 ¹¹¹In³⁺ complexes (with 10% ligand excess). Complexation was achieved by heating the mixture at 100°C for 30 min. The efficiency of radiolabelling with ¹¹¹In³⁺ was controlled by thin layer chromatography, indicating >96% radiochemical purity of the complex (**Figure 6.5**, details in Experimental). The *in vitro* stability of the complex was evaluated and the complex remained stable with only 2% degradation at 22h after radiolabelling. The *in vivo* biodistribution of ¹¹¹InL₁ in Swiss male mice at 2 and 30 mins after tracer injection is presented in **Table 6.1**. Kidney displayed the highest uptake of activity of all organs, suggesting a urinary elimination of the activity. The distribution data showed that the radioactive signal was also elevated in lungs 2 min after tracer injection (11.42 \pm 0.77 %ID/g tissue), then decreased at the 30 min time point. This transient high lung uptake reflects the large blood volume of this blood-rich content organ. In the brain, the % ID/g in the cortex and cerebellum at 2 mins was 0.36 and 0.5, while at 30 mins it was 0.11 and 0.21, respectively. The clearance measured by the ratio of % ID/g values at 2 min and 30 min is 3.3, a value

comparable to that determined for PiB.¹⁴⁸ ^{99m}Tc-based β -amyloid tracers were reported to have a similar or higher brain uptake (0.1-1.4 % ID/g at 2 mins and 0.1-1.08 % ID/g at 30 mins, post injection).^{134-136,190,191} Given the considerably (~50 %) higher molecular weight of ¹¹¹InL₁, the brain % ID/g values determined are quite remarkable. They are also similar to the cerebral biodistribution of some SPECT radioligands, including PE2I^{251,252} and CLINDE^{253,254}, developed for molecular imaging of the dopaminergic system and neuroinflammation in the brain, respectively. Therefore, the BBB crossing of ¹¹¹InL₁ might be sufficient for nuclear imaging of amyloid deposits in relevant rodent transgenic models overexpressing A β aggregates, even though the *in vitro* autoradiograms of frozen mice Tg APP_{swe}, PSEN1_{dE9} brain sections labeled with ¹¹¹InL₁ were inconclusive, as reported from Klunk et al. for PiB labeled with ¹¹C (**Figure 6.6**).²⁴⁴ Similar to Klunk et al., we hypothesize that different structural rearrangements, composition and compaction of A β peptides between human and rodent amyloid plaques, as well as the weaker affinity constants and different aqueous solution concentrations of the metal complex used for the fluorescent immunohistochemistry and radioactive autoradiography, are responsible for those opposite results.

BBB permeability sufficient for MRI detection with the Gd³⁺ analogue will be certainly difficult to attain. However, such an MRI contrast agent specifically binding to amyloid deposits can be still useful in small animal studies where the opening of the BBB with mannitol or ultrasound is feasible. In small animal studies, the high resolution of MRI with respect to nuclear techniques is particularly important. These agents can also bring more specificity and complement the use of non-specific Gd-complexes like GdDTPA applied in intracerebroventricular injection protocols or can be useful in *ex vivo* MRI to stain Alzheimer brain tissues.¹¹³

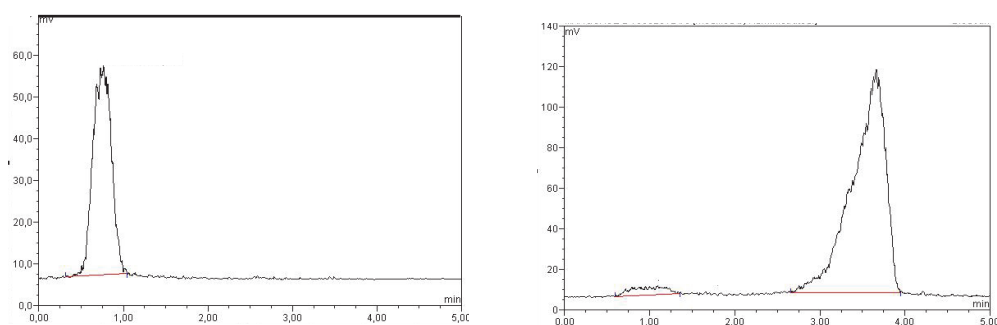


Figure 6.5. Thin layer chromatograph obtained for free Indium = $^{111}\text{InCl}_3$ used for radiolabeling of L_1 (left) and after complexation with L_1 (right), in the system ITLC-SG / MeOH:H₂O:NH₄OH (2:4:0.1). Free indium has a $R_f = 0$, whereas $^{111}\text{In}L_1$ migrates with a $R_f \approx 0.7$ in this system. The radiochemical purity was $> 96\%$. The x axis is in minutes.

Table 6.1. Distribution of $^{111}\text{In}L_1$ in Swiss mice 2 min and 30 min after tracer injection. The data represent the mean \pm SD percent injected dose per gram (% ID/g, n = 4).

% ID/g	2 min	30min
Kidney	12.53 \pm 1.07	4.23 \pm 0.42
Cerebellum	0.50 \pm 0.07	0.21 \pm 0.02
Cortex	0.36 \pm 0.03	0.11 \pm 0.01
Heart	7.36 \pm 0.18	1.51 \pm 0.21
Liver	4.90 \pm 0.12	7.65 \pm 1.59
Blood	14.59 \pm 0.23	4.23 \pm 0.45
Lung	11.42 \pm 0.77	1.44 \pm 0.14

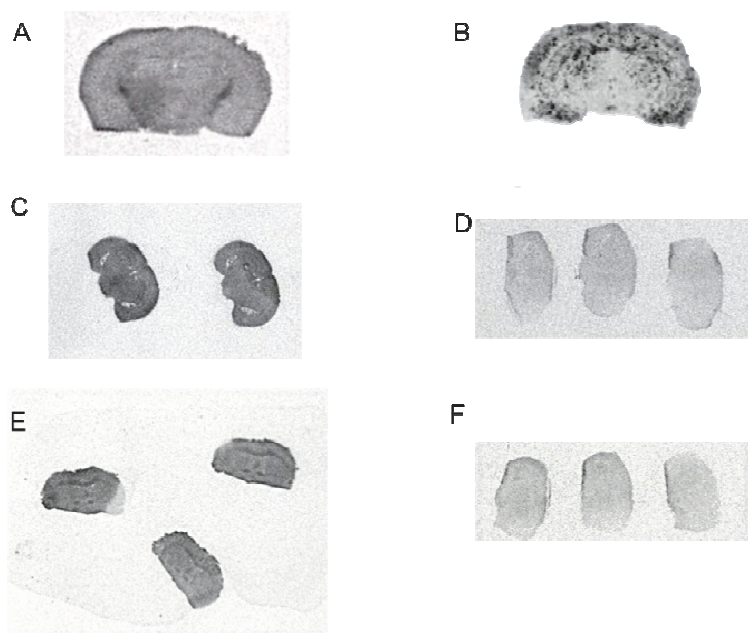


Figure 6.6. *In vitro* autoradiograms of frozen mice Tg APP^{swe}, PSEN1dE9 brain sections labeled with (A) $^{111}\text{InL}_1$ and (B) $^{18}\text{F-AV-45}$. (C and D) represent the same autoradiograms in the presence of cold AV-45 and (C and D) non specific binding with wild type mice not presenting A β deposits.

In conclusion, the amphiphilic, non-charged, trivalent $\text{Eu}^{3+}\text{-L}_1$ complexes show affinity for amyloid deposits in post-mortem human tissue, revealing its selectivity for human amyloid plaques like the reported benzothiazol neutral derivatives, but not for Tg APP^{swe}, PSEN1dE9 brain sections labeled with $^{111}\text{InL}_1$. The biodistribution experiments in normal mice with $^{111}\text{In}^{3+}\text{-L}_1$ proved moderate brain uptake, similar to the values for $^{99\text{m}}\text{Tc}$ -based amyloid tracers. Given their similar charge and the fact that the binding interaction mainly involves the PiB moiety, similar selectivity and biodistribution profiles can be expected for the Eu^{3+} and In^{3+} analogues as well.

*Conclusions
and
Perspectives*

The work presented in this thesis focused on the development of multimodal probes for the detection of A β amyloid plaques in Alzheimer's disease (AD) using molecular imaging techniques.

In recent years, multimodality imaging has emerged as a novel concept that combines simultaneously or successively two or more imaging methodologies to provide complementary information in biological studies and medical diagnostics. Magnetic Resonance Imaging (MRI) is endowed with excellent resolution, while nuclear imaging techniques offer detection of the probes with remarkable sensitivity.

Our objective was to create a new class of ligands capable of forming thermodynamically stable and kinetically inert complexes with several trivalent metal ions in particular with lanthanides. The complexes formed are expected to 1) have amphiphilic behaviour and high relaxivities (for the Gd³⁺ analogues) in aqueous solution, 2) bind to aggregated A β peptides and amyloid deposits, 3) act as amyloid aggregation "protectors", 4) permeate the Blood Brain Barrier.

To achieve this, different tetraaza macrocyclic (DO3A, DOTA) and MAMA chelating structures were conjugated to a 4'-methylaminophenyl-benzothiazole targeting moiety via different linkers and the ligands were characterized. According to their chelating structures, these ligands include DO3A derivatives (L₁, L₂, L₃), one DOTA derivative (L₄), a MAMA derivative (L₅). Indeed, DO3A and DOTA derivatives are well known to form very stable complexes with lanthanide (Ln³⁺) and other trivalent metal ions (M³⁺), while MAMA derivatives are commonly used for complexation of the reduction products of ^{99m}TcO₄⁻ in Nuclear Medicine for application in SPECT brain imaging.

The Gd³⁺-complexes have been evaluated with respect to their potential use as contrast agents in T₁-weighted MRI (Chapter 4). This included the assessment of their logP_{oct/water} coefficients (logP_{oct/water} = -0.15-0.32), their critical

micellar concentration (cmc) by relaxometry, their relaxometric properties in the absence and in the presence of A β ₁₋₄₀ and Human Serum Albumin (HSA), their affinity constants characterizing HSA binding assessed by paramagnetic relaxation enhancement (PRE) measurements ($K_{A,GdL1} = 709 \pm 89 \text{ M}^{-1}$; $K_{A,GdL3} = 250 \pm 18 \text{ M}^{-1}$), as well as a complete ¹⁷O NMR and ¹H NMRD study of the GdL₃ complex. These *in vitro* studies suggest that our Gd³⁺-complexes show promising characteristics to be used as MRI contrast agents for A β amyloid detection in AD.

We have also investigated the *in vitro* interaction of our Ln³⁺ complexes with A β ₁₋₄₀ in solution using different experimental techniques, such as Surface Plasmon Resonance (SPR), Saturation Transfer Difference NMR (¹H STD NMR), Circular Dichroism, Thioflavin-T fluorescence, 2D HSQC NMR, Dynamic Light Scattering and TEM images (Chapter 5). The neutral Ln³⁺ complexes of the two DO3A-PiB derivatives, L₁ and L₃, interact with moderate affinity to an aggregated form A β and weakly to the monomeric A β ₁₋₄₀ in aqueous solution. A modification of the L₁ ligand by introduction of an aliphatic C₆ chain spacer between the chelating DO3A macrocycle and the targeting PiB moiety changes the strength of the interaction (as measured by the dissociation constants, K_D), as well as the stability of the aggregated structures. We also found that the most hydrophobic monomer, GdL₃, stabilizes the α -helical peptide structure and has the better protective effect against peptide aggregation.

Our results also suggest that LaL₃ and probably LaL₁ will not interact with monomeric A β at normal, physiologically relevant concentrations of the peptide. This is important for two reasons. First, A β ₁₋₄₀ has been reported to protect the brain against bacterial infection as at low (μM) concentrations as it is a potent bacteriostatic, and therefore the weak to insignificant binding of these lanthanide complexes will not interfere with the A β ₁₋₄₀'s normal beneficial activity. Second, it can be predicted that the relatively weak binding of the corresponding Gd³⁺ complexes to monomeric A β ₁₋₄₀, which is normally present, will reduce background and enhance the signal contrast when these MRI probes bind to A β ₁₋₄₀ amyloid fibrils and plaques.

Taken together, these findings can contribute to the design of optimized small molecules able to specifically target aggregated amyloid A β by improving their hydrophobic nature, to inhibit A β toxic self-assemblies and to evince a

therapeutic effect.

We have investigated the capability of our neutral complexes to bind amyloid deposits *ex vivo* and *in vivo*. *Ex vivo* studies with post-mortem AD human brain slices confirm the selective binding of our EuL₁ complexes to human A β amyloid deposits. The *in vivo* biodistribution studies of the SPECT tracer formed by labelling ligand L₁ with the radioactive γ -emitter Indium³⁺ (InL₁) in normal Swiss mice show that they are able to permeate the Blood Brain Barrier, giving permeation values of 0.36/0.11 %ID/g of the InL₁ complex at 2/30 min post injection.

Alzheimer's disease is a major concern of the 21st century and the economic burden is considerable. The development of novel diagnostic probes for early *in vivo* visualisation of the amyloid plaques associated to Alzheimer's disease remains an important issue. Early diagnosis would allow treatment that slows disease progression and also determine the response to therapeutic drugs.

In the future, specific efforts should concentrate on the delivery of the diagnostic probes via the BBB and on the development of multimodal approaches. Therapeutics could be directly coupled to these probes in order to explore theragnostic routes.

The conclusions of this thesis as well as the future results to be obtained with the ligands L₄ and L₅ not yet investigated, contribute to understand the role of hydrophobicity, ligand flexibility, charge and size on the *in vitro* and *in vivo* behaviour of this kind of imaging probes. This will provide important clues to an optimized design of imaging probes for AD.

APPENDIX 1: Analysis of NMRD and ^{17}O NMR data

NMRD and ^{17}O NMR data have been analysed within the framework of Solomon-Bloembergen-Morgan theory.

^{17}O NMR spectroscopy

From the measured ^{17}O NMR relaxation rates and angular frequencies of the paramagnetic solutions, $1/T_1$, $1/T_2$ and ω , and of the acidified water reference, $1/T_{1A}$, $1/T_{2A}$ and ω_A , one can calculate the reduced relaxation rates and chemical shifts, $1/T_{2r}$ and $\Delta\omega_r$, which may be written as in Equations (A1)-(A3), where, $1/T_{1m}$, $1/T_{2m}$ is the relaxation rate of the bound water and $\Delta\omega_m$ is the chemical shift difference between bound and bulk water, τ_m is the mean residence time or the inverse of the water exchange rate k_{ex} and P_m is the mole fraction of the bound water.^{255,256}

$$\frac{1}{T_{1r}} = \frac{1}{P_m} \left[\frac{1}{T_1} - \frac{1}{T_{1A}} \right] = \frac{1}{T_{1m} + \tau_m} + \frac{1}{T_{1os}} \quad (\text{A1})$$

$$\frac{1}{T_{2r}} = \frac{1}{P_m} \left[\frac{1}{T_2} - \frac{1}{T_{2A}} \right] = \frac{1}{\tau_m} \frac{T_{2m}^{-2} + \tau_m^{-1} T_{2m}^{-1} + \Delta\omega_m^2}{(\tau_m^{-1} + T_{2m}^{-1})^2 + \Delta\omega_m^2} + \frac{1}{T_{2os}} \quad (\text{A2})$$

$$\Delta\omega_r = \frac{1}{P_m} (\omega - \omega_A) = \frac{\Delta\omega_m}{(1 + \tau_m T_{2m}^{-1})^2 + \tau_m^2 \Delta\omega_m^2} + \Delta\omega_{os} \quad (\text{A3})$$

The outer sphere contributions to the ^{17}O relaxation rates $1/T_{1os}$ and $1/T_{2os}$ can be neglected according to previous studies.²⁵⁷ Therefore, Equations (A1-A2) can be further simplified into Equations (A4) and (A5):

$$\frac{1}{T_{1r}} = \frac{1}{T_{1m} + \tau_m} \quad (\text{A4})$$

$$\frac{1}{T_{2r}} = \frac{1}{T_{2m} + \tau_m} \quad (\text{A5})$$

The exchange rate is supposed to obey the Eyring equation. In equation (A6) ΔS^\ddagger and ΔH^\ddagger are the entropy and enthalpy of activation for the water exchange process, and k_{ex}^{298} is the exchange rate at 298.15 K.

$$\frac{1}{\tau_m} = k_{\text{ex}} = \frac{k_B T}{h} \exp\left\{\frac{\Delta S^\ddagger}{R} - \frac{\Delta H^\ddagger}{RT}\right\} = \frac{k_{\text{ex}}^{298} T}{298.15} \exp\left\{\frac{\Delta H^\ddagger}{R} \left(\frac{1}{298.15} - \frac{1}{T}\right)\right\} \quad (\text{A6})$$

In the transverse relaxation, the scalar contribution, $1/T_{2\text{sc}}$, is the most important [Equation (A7)]. $1/\tau_{s1}$ is the sum of the exchange rate constant and the electron spin relaxation rate [Equation (A8)].

$$\frac{1}{T_{2m}} \cong \frac{1}{T_{2\text{sc}}} = \frac{S(S+1)}{3} \left(\frac{A}{\hbar}\right)^2 \left(\tau_{s1} + \frac{\tau_{s2}}{1 + \omega_S^2 \tau_{s2}^2}\right) \quad (\text{A7})$$

$$\frac{1}{\tau_{s1}} = \frac{1}{\tau_m} + \frac{1}{T_{1e}} \quad (\text{A8})$$

The ^{17}O longitudinal relaxation rates in Gd^{3+} solutions are the sum of the contributions of the dipole-dipole (dd) and quadrupolar (q) mechanisms as expressed by Equations (A11-A13) for non-extreme narrowing conditions, where γ_S is the electron and γ_I is the nuclear gyromagnetic ratio ($\gamma_S = 1.76 \times 10^{11} \text{ rad s}^{-1} \text{ T}^{-1}$, $\gamma_I = -3.626 \times 10^7 \text{ rad s}^{-1} \text{ T}^{-1}$), r_{GdO} is the effective distance between the electron charge and the ^{17}O nucleus, I is the nuclear spin (5/2 for ^{17}O), χ is the quadrupolar coupling constant and η is an asymmetry parameter :

$$\frac{1}{T_{lm}} = \frac{I}{T_{ldd}} + \frac{I}{T_{lq}} \quad (\text{A9})$$

with:

$$\frac{1}{T_{ldd}} = \frac{2}{15} \left(\frac{\mu_0}{4\pi} \right)^2 \frac{\hbar^2 \gamma_I^2 \gamma_S^2}{r_{GdO}^6} S(S+1) \times [3J(\omega_I; \tau_{d1}) + 7J(\omega_S; \tau_{d2})] \quad (\text{A10})$$

$$\frac{1}{T_{lq}} = \frac{3\pi^2}{10} \frac{2I+3}{I^2(2I-1)} \chi^2 (1 + \eta^2 / 3) \times [0.2J_1(\omega_I) + 0.8J_2(\omega_I)] \quad (\text{A11})$$

In Equation (A3) the chemical shift of the bound water molecule, $\Delta\omega_m$, depends on the hyperfine interaction between the Gd^{3+} electron spin and the ^{17}O nucleus and is directly proportional to the scalar coupling constant, $\frac{A}{\hbar}$, as expressed in Equation (A12).²⁵⁸

$$\Delta\omega_m = \frac{g_L \mu_B S(S+1) B}{3k_B T} \frac{A}{\hbar} \quad (\text{A12})$$

The isotopic Landé g factor is equal to 2.0 for the Gd^{3+} , B represents the magnetic field, and k_B is the Boltzmann constant.

The outer-sphere contribution to the chemical shift is assumed to be linearly related to $\Delta\omega_m$ by a constant C_{os} [Equation (A13)].²⁵⁹

$$\Delta\omega_{os} = C_{os} \Delta\omega_m \quad (\text{A13})$$

NMRD

The measured longitudinal proton relaxation rate, $R_1^{obs} = 1/T_1^{obs}$, is the sum of a paramagnetic and a diamagnetic contribution as expressed in Equation (A14), where r_l is the proton relaxivity:

$$R_1^{obs} = R_1^d + R_1^p = R_1^d + r_l [Gd^{3+}] \quad (A14)$$

The relaxivity can be divided into an inner and an outer sphere term as follows:

$$r_l = r_{lis} + r_{los} \quad (A15)$$

The inner sphere term is given in Equation (A16), where q is the number of inner sphere water molecules.²⁶⁰

$$r_{lis} = \frac{l}{1000} \times \frac{q}{55.55} \times \frac{l}{T_{lm}^H + \tau_m} \quad (A16)$$

The longitudinal relaxation rate of inner sphere protons, $1/T_{lm}^H$ is expressed by Equation (A11), where r_{GdH} is the effective distance between the electron charge and the 1H nucleus, ω_l is the proton resonance frequency and ω_S is the Larmor frequency of the Gd^{3+} electron spin.

$$\frac{1}{T_{lm}^H} = \frac{2}{15} \left(\frac{\mu_0}{4\pi} \right)^2 \frac{\hbar^2 \gamma_I^2 \gamma_S^2}{r_{GdH}^6} S(S+1) \times [3J(\omega_l; \tau_{d1}) + 7J(\omega_S; \tau_{d2})] \quad (A17)$$

$$\frac{1}{\tau_{di}} = \frac{1}{\tau_m} + \frac{1}{\tau_{RH}} + \frac{1}{T_{ie}} \quad \text{for } i=1,2 \quad (A18)$$

where τ_{RH} is the rotational correlation time of the Gd-H_{water} vector.

For small molecular weight chelates (fast rotation), the spectral density function is expressed as in Equation (A19).

$$J(\omega; \tau) = \left(\frac{\tau}{1 + \omega^2 \tau^2} \right) \quad (\text{A19})$$

For slowly rotating species, the spectral density functions are described the Lipari-Szabo approach.²⁶¹ In this model we distinguish two statistically independent motions; a rapid local motion with a correlation time τ_l and a slower global motion with a correlation time τ_g . Supposing the global molecular reorientation is isotropic, the relevant spectral density functions are expressed as in Equations (A20-A24), where the general order parameter S^2 describes the degree of spatial restriction of the local motion. If the local motion is isotropic, $S^2 = 0$; if the rotational dynamics is only governed by the global motion, $S^2 = 1$.

$$J(\omega_I; \tau_{d1}) = \left(\frac{S^2 \tau_{d1g}}{1 + \omega_I^2 \tau_{d1g}^2} + \frac{(1 - S^2) \tau_{d1}}{1 + \omega_I^2 \tau_{d1}^2} \right) \quad (\text{A20})$$

$$J(\omega_S; \tau_{d2}) = \left(\frac{S^2 \tau_{d2g}}{1 + \omega_S^2 \tau_{d2g}^2} + \frac{(1 - S^2) \tau_{d2}}{1 + \omega_S^2 \tau_{d2}^2} \right) \quad (\text{A21})$$

$$\frac{1}{\tau_{dig}} = \frac{1}{\tau_m} + \frac{1}{\tau_g} + \frac{1}{T_{ie}} \quad i = 1, 2 \quad (\text{A22})$$

$$\frac{1}{\tau} = \frac{1}{\tau_g} + \frac{1}{\tau_l} \quad (\text{A23})$$

$$J_i(\omega_i) = \left(\frac{S^2 \tau_g}{1 + i^2 \omega_i^2 \tau_g^2} + \frac{(1 - S^2) \tau}{1 + i^2 \omega_i^2 \tau^2} \right) \quad i = 1, 2 \quad (\text{A24})$$

The rotational correlation time, τ_{RH} is assumed to have simple exponential temperature dependence with an E_R activation energy as given in Equation (A25).

$$\tau_{RO} = \tau_{RO}^{298} \exp \left[\frac{E_R}{R} \left(\frac{1}{T} - \frac{1}{298.15} \right) \right] \quad (\text{A25})$$

The outer-sphere contribution can be described by Equations (A26 and A27) where N_A is the Avogadro constant, and J_{os} is its associated spectral density function as given by Equation (A15).^{262,263}

$$r_{1os} = \frac{32 N_A \pi}{405} \left(\frac{\mu_0}{4\pi} \right)^2 \frac{\hbar^2 \gamma_S^2 \gamma_I^2}{a_{GdH} D_{GdH}} S(S+1) [3J_{os}(\omega_1, T_{1e}) + 7J_{os}(\omega_S, T_{2e})] \quad (\text{A26})$$

$$J_{os}(\omega, T_{je}) = \text{Re} \left[\frac{1 + 14 \left(i\omega \tau_{GdH} + \frac{\tau_{GdH}}{T_{je}} \right)^{1/2}}{1 + \left(i\omega \tau_{GdH} + \frac{\tau_{GdH}}{T_{je}} \right)^{1/2} + 49 \left(i\omega \tau_{GdH} + \frac{\tau_{GdH}}{T_{je}} \right) + 19 \left(i\omega \tau_{GdH} + \frac{\tau_{GdH}}{T_{je}} \right)^{3/2}} \right] \quad (\text{A27})$$

$j=1,2$

The longitudinal and transverse electronic relaxation rates, $1/T_{1e}$ and $1/T_{2e}$ are expressed by Equation (A28 and A29), where τ_v is the electronic correlation time for the modulation of the zero-field-splitting interaction, E_v the corresponding activation energy and Δ^2 is the mean square zero-field-splitting energy. We assumed a simple exponential dependence of τ_v versus $1/T$ as written in Equation (A30).

$$\left(\frac{1}{T_{1e}} \right)^{ZFS} = \frac{1}{25} \Delta^2 \tau_v \{ 4S(S+1) - 3 \} \left(\frac{1}{1 + \omega_S^2 \tau_v^2} + \frac{4}{1 + 4\omega_S^2 \tau_v^2} \right) \quad (\text{A28})$$

$$\left(\frac{1}{T_{2e}} \right)^{ZFS} = \Delta^2 \tau_v \left(\frac{5.26}{1 + 0.372\omega_S^2 \tau_v^2} + \frac{7.18}{1 + 1.24\omega_S^2 \tau_v^2} \right) \quad (\text{A29})$$

$$\tau_v = \tau_v^{298} \exp \left[\frac{E_v}{R} \left(\frac{1}{T} - \frac{1}{298.15} \right) \right] \quad (\text{A30})$$

The diffusion coefficient for the diffusion of a water proton away from a Gd^{3+} complex, D_{GdH} , is assumed to obey an exponential law versus the inverse of the temperature, with activation energy E_{DGdH} , as given in Equation (A31). D_{GdH}^{298} is the diffusion coefficient at 298.15K.

$$D_{GdH} = D_{GdH}^{298} \exp\left\{\frac{E_{GdH}}{R} \left(\frac{1}{298.15} - \frac{1}{T}\right)\right\} \quad (\text{A31})$$

APPENDIX 2: Saturation Transfer Difference (STD) NMR

STD NMR is commonly used to characterise the binding in ligand–receptor complexes.^{200,201}

In this method, selective irradiation of the protein NMR spectrum results in saturation of the protein signals and of any ligand protons interacting with the protein. Subtraction of this spectrum from the one collected in non-saturated protein and ligand conditions gives the saturation transfer difference spectrum, in which only protein-interacting protons are visible and the epitope is mapped by analysing the signal intensities of these protons in the STD spectrum.²⁰⁰

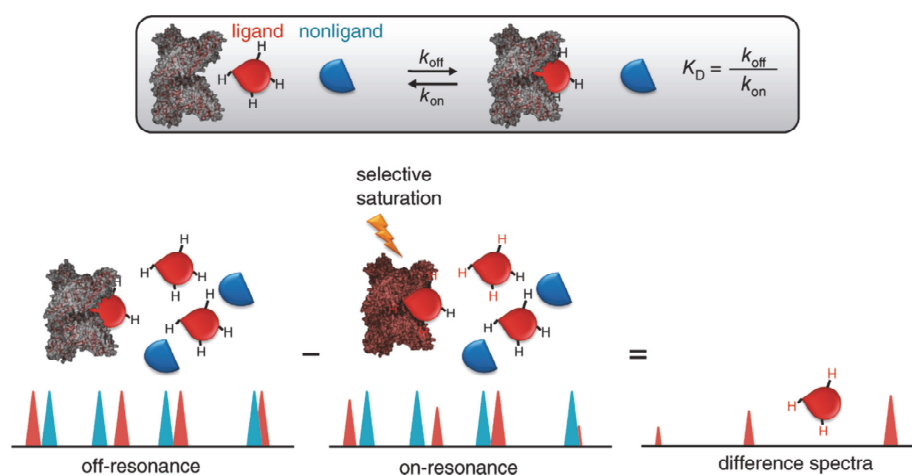


Figure S1. Scheme of the STD-NMR experiment. The exchange between free and bound ligand allows intermolecular transfer of magnetization from the receptor to the bound small molecule.²⁰⁸

Looking at **Figure S1**, the difference spectra is obtained from the difference between the *off-resonance* (*r.f.* pulse set far away from the system resonances) reference spectrum and the *on-resonance* spectrum under the same conditions. The *off-resonance* experiment yields a spectrum identical to the *on-resonance* except that the resonance intensities (I_0 , both ligand and receptor) are not affected by saturation. Therefore the difference spectrum, or the STD spectrum ($I_{\text{STD}} = I_0 - I_{\text{SAT}}$) yields only those resonances that experienced saturation in the *on-resonance* experiment, the receptor resonances and the ones from the binding ligands. Generally the intensity of the detected STD-NMR signal depends on the efficiency of the receptor-to-ligand saturation transfer²⁶⁴ and also on the

number of ligand molecules in solution that received saturation from the receptor (excess 10 to 100 fold). Normally, for a determinate system the ligand-to-protein ratio and the saturation time have to be selected according to the expected K_D .

The STD-NMR experiment has some limitations, for high-affinity ligands (k_{off} rates in the range of 0.1-0.01 s⁻¹), the saturation cannot be transferred effectively to solution resulting in no observable STD effect. On the other hand, when binding is very weak, the probability of the ligand being in the receptor site becomes very low resulting in weak STD signals. The saturation transfer takes place only to molecules bound to the protein with a rate that depends on the protein mobility, ligand/protein complex lifetime, and geometry. Some knowledge and understanding of the relative timescales of several important events is crucial for setting-up a successful STD NMR experiment and to understand its limitations. The binding of the ligand to the receptor can be characterized by an *off* (k_{off}) and an *on* rate (k_{on}), and the corresponding thermodynamic equilibrium dissociation constant, K_D , given by equation (A31):

$$K_D = k_{off} / k_{on} \quad (\text{A31})$$

Normally it is considered that k_{on} is diffusion controlled, this means that when the receptor and ligand find each other in solution they will form a complex, being the lifetime of the complex ($1/k_{off}$) controlled by the k_{off} rate. For a successful STD NMR experiment it is desirable that the exchange between free and bound ligand is fast enough to allow the build-up of a population of saturated ligand in solution. For that reason k_{off} should be large enough to allow this amplification to occur, but not so high that does not allow the ligand to remain in the binding site time enough to receive the saturation from the receptor. If one assumes a diffusion limited k_{on} rate, then it has been shown that the upper limit for K_D in a STD experiment will be controlled by the minimum residence time needed for saturation transfer, leading to a maximum K_D of 10⁻³ M.²⁶⁵

Before indicating the lower limit of K_D for the STD experiment, we have to consider the kinetics of another important NMR process; the rate at which the magnetization relaxes back to equilibrium. This rate is small for a small molecule and large for a large molecule.²⁶⁶ When the small ligand is bound to the large receptor it behaves as part of the receptor and therefore its relaxation rate is much

faster than in the free-state. As a consequence, the ligand has to dissociate faster than the magnetization relaxation rate, otherwise relaxation occurs and the magnetization is lost. This represents a problem for tight binding ligands and sets a maximum residence time for the ligand in the binding site of the receptor, determined by the relaxation rate of the large receptor. As before, assuming a diffusion limited k_{on} rate the lower limit for the K_D , for normal STD experiments, was determined to be 10^{-8} M. The K_D range of the STD NMR experiment is then between $10^{-8} < K_D < 10^{-3}$ M.

APPENDIX 3 : Competitive Binding Data

Competitive binding experiments measure the binding of a single concentration of labeled ligand in the presence of various concentrations of unlabeled ligand (**Figure S2**).²⁶⁷

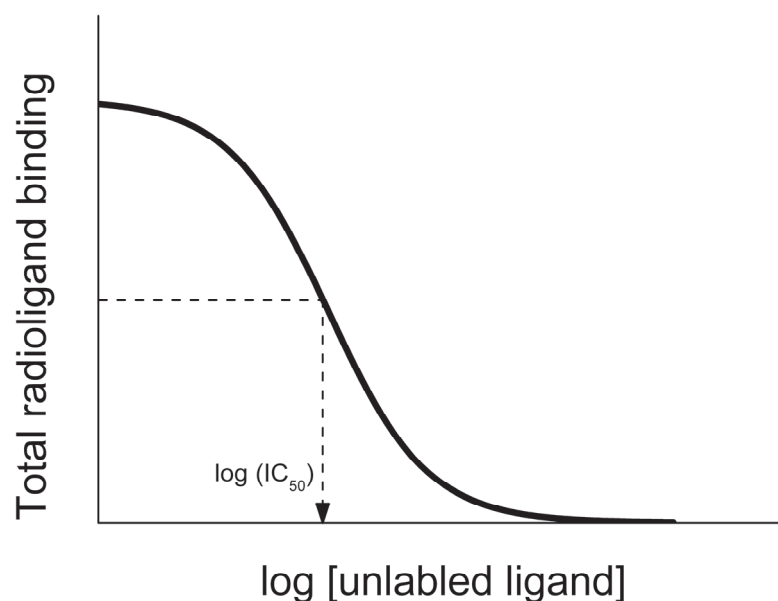


Figure S2. Competitive binding curve

The top of the curve is a plateau at a value equal to radioligand binding in the absence of the competing unlabeled drug. The bottom of the curve is a plateau equal to nonspecific binding. The concentration of unlabeled drug that produces radioligand binding half way between the upper and lower plateaus is called the IC₅₀ (inhibitory concentration 50%) or EC₅₀ (effective concentration 50%).

If the radioligand and competitor both bind reversibly to a single binding site, binding at equilibrium follows this equation.

$$F(x) = Y_{Bottom} + \frac{(Y_{Top} - Y_{Bottom})}{1 + 10^{x - \log IC_{50}}} \quad (A32)$$

The K_i is an equilibrium dissociation constant of the enzyme-inhibitor complex, or the reciprocal of the binding affinity of the inhibitor to the enzyme. It is determined indirectly by measuring the competition of the unlabeled ligand with a known radioligand. The K_i can be calculated once the IC_{50} and the thermodynamic dissociation constant, K_D , for a known substrate, S , are determined by Cheng and Prusoff's equations¹⁴² involving one competitor.

$$K_i = \frac{IC_{50}}{1 + \frac{[S]}{K_D}} \quad (A33)$$

REFERENCES

- (1) Weissleder, R.; Mahmood, U. *Radiology* **2001**, *219*, 316–333.
- (2) Becquerel, H. *J. Phys. Theor. Appl.* **1897**, *6*, 681–688.
- (3) Curie, M.; Debiere, A.; Eve, A. S.; Geiger, H.; Hahn, O.; Lind, S. C.; Meyer, S.; Rutherford, E.; Schweidler, E. *J. Am. Chem. Soc.* **1931**, *53*, 2437–2450.
- (4) Berlinguet, L.; Bégin, N.; Babineau, L. M. *Biochem. Cell Biol.* **1962**, *40*, 1111–1114.
- (5) Yonekura, Y.; Nishizawa, S.; Mukai, T.; Fujita, T.; Fukuyama, H.; Ishikawa, M.; Kikuchi, H.; Konishi, J.; Andersen, A. R.; Lassen, N. A. *J. Cereb. Blood Flow Metab.* **1988**, *8*, S82–S89.
- (6) Langen, K.-J.; Herzog, H.; Kuwert, T.; Roosen, N.; Rota, E.; Kiwit, J. C. W.; Bock, W. J.; Feinendegen, L. E. *J. Cereb. Blood Flow Metab.* **1988**, *8*, S90–S94.
- (7) Joliot, F.; Curie, I. *Nature* **1934**, *133*, 201–202.
- (8) Baskin, J. M.; Prescher, J. A.; Laughlin, S. T.; Agard, N. J.; Chang, P. V.; Miller, I. A.; Lo, A.; Codelli, J. A.; Bertozzi, C. R. *PNAS* **2007**, *104*, 16793–16797.
- (9) Moorhouse, A. D.; Moses, J. E. *ChemMedChem* **2008**, *3*, 715–723.
- (10) McBride, W. J.; Sharkey, R. M.; Karacay, H.; D'Souza, C. A.; Rossi, E. A.; Laverman, P.; Chang, C.-H.; Boerman, O. C.; Goldenberg, D. M. *J Nucl Med* **2009**, *50*, 991–998.
- (11) Deng, H.; Tang, X.; Wang, H.; Tang, G.; Wen, F.; Shi, X.; Yi, C.; Wu, K.; Meng, Q. *J Nucl Med* **2011**, *52*, 287–293.
- (12) Helms, M. W.; Brandt, B. H.; Contag, C. H. In *Contributions to Microbiology*; Dittmar, T.; Zaenker, K. S.; Schmidt, A., Eds.; KARGER: Basel, 2006; pp. 209–231.
- (13) Scheffel, U.; Dannals, R. F.; Cline, E. J.; Ricaurte, G. A.; Carroll, F. I.; Abraham, P.; Lewin, A. H.; Kuhar, M. J. *Synapse* **1992**, *11*, 134–139.
- (14) Zhen, W.; Han, H.; Anguiano, M.; Lemere, C. A.; Cho, C.-G.; Lansbury, P. T. *J. Med. Chem.* **1999**, *42*, 2805–2815.
- (15) A, A.-D.; Ms, G.; Ga, D.; Y, Z.-P.; Ss, Z.; Rm, B.; M, L.; Ds, C.; Pb, H.; Jl, N.; Rb, I. *J Nucl Med* **1996**, *37*, 1129–1133.
- (16) Kung, M.-P.; Hou, C.; Oya, S.; Mu, M.; Acton, P. D.; Kung, H. F. *Eur J Nucl Med* **1999**, *26*, 844–853.
- (17) Kung, H. F.; Ohmomo, Y.; Kung, M.-P. *Semin. Nucl. Med.* **1990**, *20*, 290–302.
- (18) Saha, G. B.; MacIntyre, W. J.; Go, R. T. *Semin. Nucl. Med.* **1994**, *24*, 324–349.
- (19) Moretti, J.-L.; Defier, G.; Cinotti, L.; Cesaro, P.; Degos, J.-D.; Vigneron, N.; Ducassou, D.; Holman, B. L. *Eur J Nucl Med* **1990**, *16*, 17–22.
- (20) Lecomte, R. *AIP Conference Proceedings* **2007**, *958*, 115–122.
- (21) Anderson, P. *Expert Opin Pharmacother* **2006**, *7*, 1475–1486.
- (22) Pirotte, B.; Goldman, S.; Massager, N.; David, P.; Wikler, D.; Vandesteene, A.; Salmon, I.; Brotchi, J.; Levivier, M. *J Nucl Med* **2004**, *45*, 1293–1298.
- (23) T, H.; N, K.; N, S.; T, K. *J Nucl Med* **1997**, *38*, 842–847.
- (24) Nordberg, A. *Lancet Neurol.* **2004**, *3*, 519–527.
- (25) Morrish, P. K.; Sawle, G. V.; Brooks, D. J. *Brain* **1996**, *119*, 585–591.
- (26) Ioannides, A. *The Neuroscientist* **2006**, *12*, 524–544.
- (27) Jeeves, M. A. *Mind fields: reflections on the science of mind and brain*; Baker Books: Grand Rapids, Mich., 1994.
- (28) Bloch, F. *Phys. Rev.* **1946**, *70*, 460–474.
- (29) Purcell, E. M.; Torrey, H. C.; Pound, R. V. *Phys. Rev.* **1946**, *69*, 37–38.

- (30) Lauterbur, P. C. *Nature* **1973**, *242*, 190–191.
- (31) Damadian, R. *Science* **1971**, *171*, 1151–1153.
- (32) Damadian, R.; Zaner, K.; Hor, D.; DiMaio, T. *Proc Natl Acad Sci U S A* **1974**, *71*, 1471–1473.
- (33) Hoboken, N. J. *Encyclopedia of Magnetic Resonance*; Wiley and Sons, 1996.
- (34) Liew, A.; Yan, H. *Curr. Med. Imaging Rev.* **2006**, *2*, 91–103.
- (35) Bandettini, P. A.; Jesmanowicz, A.; Wong, E. C.; Hyde, J. S. *Magn. Reson. Med.* **1993**, *30*, 161–173.
- (36) Pujol, A.; Graus, F.; Peri, J.; Mercader, J. M.; Rimola, A. *Neurology* **1991**, *41*, 1526–1526.
- (37) Ba, W.; Dl, M.; Ja, F.; Aj, D.; Jt, S.; R, C.; Th, S.; P, C.; Ae, C. *Surgery* **1989**, *105*, 180–187.
- (38) Lauffer, R. B. *Chem. Rev.* **1987**, *87*, 901–927.
- (39) Caravan, P.; Ellison, J. J.; McMurry, T. J.; Lauffer, R. B. *Chem. Rev.* **1999**, *99*, 2293–2352.
- (40) Reilly, R. F. *Clin J Am Soc Nephrol* **2008**, *3*, 747–751.
- (41) Wiginton, C. D.; Kelly, B.; Oto, A.; Jesse, M.; Aristimuno, P.; Ernst, R.; Chaljub, G. *Am. J. Roentgenol.* **2008**, *190*, 1060–1068.
- (42) Bhave, G.; Lewis, J. B.; Chang, S. S. *J. Urol.* **2008**, *180*, 830–835.
- (43) Yantasee, W.; Fryxell, G. E.; Porter, G. A.; Pattamakomsan, K.; Sukwarotwat, V.; Chouyyok, W.; Koonsiripaiboon, V.; Xu, J.; Raymond, K. N. *Nanomedicine* **2010**, *6*, 1–8.
- (44) Baranyai, Z.; Pálkás, Z.; Uggeri, F.; Maiocchi, A.; Aime, S.; Brücher, E. *Chem. Eur. J.* **2012**, *18*, 16426–16435.
- (45) Silverio, S.; Torres, S.; Martins, A. F.; Martins, J. A.; Andre, J. P.; Helm, L.; Prata, M. I. M.; Santos, A. C.; Geraldés, C. F. G. C. *Dalton Trans.* **2009**, 4656–4670.
- (46) Research, C. for D. E. and Postmarket Drug Safety Information for Patients and Providers - Information on Gadolinium-Based Contrast Agents
<http://www.fda.gov/Drugs/DrugSafety/PostmarketDrugSafetyInformationforPatientsandProviders/ucm142882.htm> (accessed Jan 29, 2013).
- (47) Wang, X.; Jin, T.; Comblin, V.; Lopez-Mut, A.; Merciny, E.; Desreux, J. F. *Inorg. Chem.* **1992**, *31*, 1095–1099.
- (48) Aime, S.; Botta, M.; Panero, M.; Grandi, M.; Uggeri, F. *Magn. Reson. Chem.* **1991**, *29*, 923–927.
- (49) Martell, A. E.; Smith, R. M. *Critical Stability Constants: Inorganic Complexes*; Plenum Press, 1976.
- (50) Kumar, K.; Chang, C. A.; Francesconi, L. C.; Dischino, D. D.; Malley, M. F.; Gougoutas, J. Z.; Tweedle, M. F. *Inorg. Chem.* **1994**, *33*, 3567–3575.
- (51) Cacheris, W. P.; Quay, S. C.; Rocklage, S. M. *Magn Reson Imaging* **1990**, *8*, 467–481.
- (52) Shukla, R.; Fernandez, M.; Pillai, R. K.; Ranganathan, R.; Ratsep, P. C.; Zhang, X.; Tweedle, M. F. *Magn Reson Med* **1996**, *35*, 928–931.
- (53) Tóth, É.; Király, R.; Platzek, J.; Radüchel, B.; Brücher, E. *Inorganica Chim. Acta* **1996**, *249*, 191–199.
- (54) Vogler, H.; Platzek, J.; Schuhmann-Giampieri, G.; Frenzel, T.; Weinmann, H.-J.; Radüchel, B.; Press, W.-R. *Eur. J. Radiol.* **1995**, *21*, 1–10.
- (55) Aime, S.; Calabi, L.; Cavallotti, C.; Gianolio, E.; Giovenzana, G. B.; Losi, P.; Maiocchi, A.; Palmisano, G.; Sisti, M. *Inorg Chem* **2004**, *43*, 7588–7590.
- (56) Datta, A.; Raymond, K. N. *Acc. Chem. Res.* **2009**, *42*, 938–947.
- (57) Silvério, S.; Torres, S.; Martins, A. F.; Martins, J. A.; André, J. P.; Helm, L.; Prata,

- M. I. M.; Santos, A. C.; Geraldles, C. F. G. C. *Dalton Trans.* **2009**, 4656.
- (58) Morawski, A. M.; Lanza, G. A.; Wickline, S. A. *Curr. Opin. Biotechnol.* **2005**, *16*, 89–92.
- (59) Caravan, P. *Acc. Chem. Res.* **2009**, *42*, 851–862.
- (60) Werner, E. J.; Datta, A.; Jocher, C. J.; Raymond, K. N. *Angew. Chem. Int. Ed. Engl.* **2008**, *47*, 8568–8580.
- (61) Livramento, J. B.; Toth, E.; Sour, A.; Borel, A.; Merbach, A. E.; Ruloff, R. *Angew. Chem. Int. Ed. Engl.* **2005**, *44*, 1480–1484.
- (62) Zhang; Wu; Sherry *Angew. Chem. Int. Ed. Engl.* **1999**, *38*, 3192–3194.
- (63) Hanaoka, K.; Kikuchi, K.; Terai, T.; Komatsu, T.; Nagano, T. *Chemistry* **2008**, *14*, 987–995.
- (64) Li, W.; Fraser, S. E.; Meade, T. J. *J. Am. Chem. Soc.* **1999**, *121*, 1413–1414.
- (65) Hanaoka, K.; Kikuchi, K.; Urano, Y.; Narazaki, M.; Yokawa, T.; Sakamoto, S.; Yamaguchi, K.; Nagano, T. *Chem. Biol.* **2002**, *9*, 1027–1032.
- (66) Bertini, I.; Turano, P.; Vila, A. J. *Chem. Rev.* **1993**, *93*, 2833–2932.
- (67) Johnson, A.; Everett, G. W. *J. Am. Chem. Soc.* **1972**, *94*, 1419–1425.
- (68) Jaffer, F. A.; Kim, D.-E.; Quinti, L.; Tung, C.-H.; Aikawa, E.; Pande, A. N.; Kohler, R. H.; Shi, G.-P.; Libby, P.; Weissleder, R. *Circulation* **2007**, *115*, 2292–2298.
- (69) Schellenberger, E. A.; Högemann, D.; Josephson, L.; Weissleder, R. *Acad Radiol* **2002**, *9 Suppl 2*, S310–311.
- (70) Yeh, T.-C.; Zhang, W.; Ildstad, S. T.; Ho, C. *Magn. Reson. Med.* **1995**, *33*, 200–208.
- (71) Na, H. B.; Song, I. C.; Hyeon, T. *Adv. Mater.* **2009**, *21*, 2133–2148.
- (72) Choi, J. H.; Nguyen, F. T.; Barone, P. W.; Heller, D. A.; Moll, A. E.; Patel, D.; Boppart, S. A.; Strano, M. S. *Nano Lett.* **2007**, *7*, 861–867.
- (73) Pereira, G. A.; Ananias, D.; Rocha, J.; Amaral, V. S.; Muller, R. N.; Elst, L. V.; Tóth, É.; Peters, J. A.; Geraldles, C. F. G. C. *J. Mater. Chem.* **2005**, *15*, 3832–3837.
- (74) Pereira, G. A.; Peters, J. A.; Almeida Paz, F. A.; Rocha, J.; Geraldles, C. F. G. C. *Inorg. Chem.* **2010**, *49*, 2969–2974.
- (75) Frullano, L.; Meade, T. J. *J. Biol. Inorg. Chem.* **2007**, *12*, 939–949.
- (76) Lee, D.-E.; Koo, H.; Sun, I.-C.; Ryu, J. H.; Kim, K.; Kwon, I. C. *Chem Soc Rev* **2012**, *41*, 2656–2672.
- (77) Lin, X.; Xie, J.; Niu, G.; Zhang, F.; Gao, H.; Yang, M.; Quan, Q.; Aronova, M. A.; Zhang, G.; Lee, S.; Leapman, R.; Chen, X. *Nano Lett.* **2011**, *11*, 814–819.
- (78) Ritchie, K.; Lovestone, S. *Lancet* **2002**, *360*, 1759–1766.
- (79) Ferri, C. P.; Prince, M.; Brayne, C.; Brodaty, H.; Fratiglioni, L.; Ganguli, M.; Hall, K.; Hasegawa, K.; Hendrie, H.; Huang, Y.; Jorm, A.; Mathers, C.; Menezes, P. R.; Rimmer, E.; Sczufca, M. *Lancet* **2005**, *366*, 2112–2117.
- (80) Minati, L.; Jones, C. L.; Gray, M. A.; Medford, N.; Harrison, N. A.; Critchley, H. D. *Neuroreport* **2009**, *20*, 1344–1350.
- (81) Batsch, N.; Mittelman, M. Overcoming the stigma of dementia. *World Alzheimer Report 2012* **2012**, 1–75.
- (82) McKhann, G.; Drachman, D.; Folstein, M.; Katzman, R.; Price, D.; Stadlan, E. M. *Neurology* **1984**, *34*, 939–944.
- (83) Morra, J. H.; Tu, Z.; Apostolova, L. G.; Green, A. E.; Avedissian, C.; Madsen, S. K.; Parikshak, N.; Toga, A. W.; Jack, C. R., Jr; Schuff, N.; Weiner, M. W.; Thompson, P. M. *Neuroimage* **2009**, *45*, S3–15.
- (84) Selkoe, D. J. *Physiol. Rev.* **2001**, *81*, 741–766.
- (85) Hardy, J.; Selkoe, D. J. *Science* **2002**, *297*, 353–356.

- (86) Gatz, M.; Reynolds, C. A.; Finkel, D.; Pedersen, N. L.; Walters, E. *Behav Genet* **2010**, *40*, 768–775.
- (87) Gatz, M.; Pedersen, N. L.; Berg, S.; Johansson, B.; Johansson, K.; Mortimer, J. A.; Posner, S. F.; Viitanen, M.; Winblad, B.; Ahlbom, A. *J. Gerontol. A Biol. Sci. Med. Sci.* **1997**, *52*, M117–125.
- (88) Papassotiropoulos, A.; Stephan, D. A.; Huentelman, M. J.; Hoernkli, F. J.; Craig, D. W.; Pearson, J. V.; Huynh, K.-D.; Brunner, F.; Corneveaux, J.; Osborne, D.; Wollmer, M. A.; Aerni, A.; Coluccia, D.; Hänggi, J.; Mondadori, C. R. A.; Buchmann, A.; Reiman, E. M.; Caselli, R. J.; Henke, K.; Quervain, D. J.-F. de *Science* **2006**, *314*, 475–478.
- (89) Hardy, J. *J. Neurochem.* **2009**, *110*, 1129–1134.
- (90) Brouwers, N.; Slegers, K.; Engelborghs, S.; Maurer-Stroh, S.; Gijssels, I.; van der Zee, J.; Pickut, B. A.; Van den Broeck, M.; Mattheijssens, M.; Peeters, K.; Schymkowitz, J.; Rousseau, F.; Martin, J.-J.; Cruts, M.; De Deyn, P. P.; Van Broeckhoven, C. *Neurology* **2008**, *71*, 656–664.
- (91) Mahley, R. W.; Weisgraber, K. H.; Huang, Y. *Proc. Natl. Acad. Sci. U.S.A.* **2006**, *103*, 5644–5651.
- (92) Bertram, L.; Tanzi, R. E. *Nat. Rev. Neurosci.* **2008**, *9*, 768–778.
- (93) Cedazo-Minguez, A.; Cowburn, R. F. *J. Cell. Mol. Med.* **2001**, *5*, 254–266.
- (94) Castano, E. M.; Prelli, F.; Wisniewski, T.; Golabek, A.; Kumar, R. A.; Soto, C.; Frangione, B. *Biochem. J.* **1995**, *306*, 599–604.
- (95) Stefani, M.; Liguri, G. *Curr Alzheimer Res* **2009**, *6*, 15–29.
- (96) Jack, C. R., Jr; Knopman, D. S.; Jagust, W. J.; Shaw, L. M.; Aisen, P. S.; Weiner, M. W.; Petersen, R. C.; Trojanowski, J. Q. *Lancet Neurol.* **2010**, *9*, 119–128.
- (97) Crouch, P. J.; Tew, D. J.; Du, T.; Nguyen, D. N.; Caragounis, A.; Filiz, G.; Blake, R. E.; Trounce, I. A.; Soon, C. P. W.; Laughton, K.; Perez, K. A.; Li, Q.-X.; Cherny, R. A.; Masters, C. L.; Barnham, K. J.; White, A. R. *J. Neurochem.* **2009**, *108*, 1198–1207.
- (98) Li, M.; Chen, L.; Lee, D. H. S.; Yu, L.-C.; Zhang, Y. *Prog. Neurobiol.* **2007**, *83*, 131–139.
- (99) Haass, C.; Selkoe, D. J. *Nat. Rev. Mol. Cell Biol.* **2007**, *8*, 101–112.
- (100) Dam, D. V.; Deyn, P. P. D. *Nat. Rev. Drug Discov.* **2006**, *5*, 956–970.
- (101) Darghal, N.; Garnier-Suillerot, A.; Bouchemal, N.; Gras, G.; Geraldès, C. F. G. C.; Salerno, M. *J. Inorg. Biochem.* **2010**, *104*, 47–54.
- (102) *The Blood-Brain Barrier and Drug Delivery to the CNS*; Bradbury, M.; Begley, D.; Kreuter, J., Eds.; 1st ed.; CRC Press, 2000.
- (103) Pardridge, W. M. *Drug Discov. Today* **2007**, *12*, 54–61.
- (104) Fischer, H.; Gottschlich, R.; Seelig, A. *J. Membr. Biol.* **1998**, *165*, 201–211.
- (105) Pardridge, W. M. *J. Neurovirol.* **1999**, *5*, 556–569.
- (106) Horsfield, M. A.; Rocca, M. A.; Cercignani, M.; Filippi, M. *Magn. Reson. Imaging* **2000**, *18*, 139–142.
- (107) Balériaux, D.; Colosimo, C.; Rusalleda, J.; Korves, M.; Schneider, G.; Bohndorf, K.; Bongartz, G.; van Buchem, M. A.; Reiser, M.; Sartor, K.; Bourne, M. W.; Parizel, P. M.; Cherryman, G. R.; Salerio, I.; La Noce, A.; Pirovano, G.; Kirchin, M. A.; Spinazzi, A. *Neuroradiology* **2002**, *44*, 191–203.
- (108) Xu, S.; Jordan, E. K.; Brocke, S.; Bulte, J. W. M.; Quigley, L.; Tresser, N.; Ostuni, J. L.; Yang, Y.; McFarland, H. F.; Frank, J. A. *J. Neurosci. Res.* **1998**, *52*, 549–558.
- (109) Kim, D. K.; Zhang, Y.; Kehr, J.; Klason, T.; Bjelke, B.; Muhammed, M. *J. Magn. Magn. Mater.* **2001**, *225*, 256–261.

- (110) Pautler, R. G.; Koretsky, A. P. *Neuroimage* **2002**, *16*, 441–448.
- (111) Gumerlock, M. K.; Belshe, B. D.; Madsen, R.; Watts, C. *J Neuro-Oncol* **1992**, *12*, 33–46.
- (112) McDannold, N.; Vykhodtseva, N.; Raymond, S.; Jolesz, F. A.; Hynynen, K. *Ultrasound Med. Biol.* **2005**, *31*, 1527–1537.
- (113) Petiet, A.; Dhenain, M. *Curr. Med. Imaging Rev.* **2011**, *7*, 8–15.
- (114) Kapural, M.; Krizanac-Bengez, L.; Barnett, G.; Perl, J.; Masaryk, T.; Apollo, D.; Rasmussen, P.; Mayberg, M. ; Janigro, D. *Brain Res.* **2002**, *940*, 102–104.
- (115) Wadghiri, Y. Z.; Sigurdsson, E. M.; Sadowski, M.; Elliott, J. I.; Li, Y.; Scholtzova, H.; Tang, C. Y.; Aguinaldo, G.; Pappolla, M.; Duff, K.; Wisniewski, T.; Turnbull, D. H. *Magn. Reson. Med.* **2003**, *50*, 293–302.
- (116) Pardridge, W. M. *J. Cereb. Blood Flow Metab.* **2012**, *32*, 1959–1972.
- (117) Kusuhara, H.; Sugiyama, Y. *Drug Discov. Today* **2001**, *6*, 150–156.
- (118) Tamai, I.; Tsuji, A. *J Pharm Sci* **2000**, *89*, 1371–1388.
- (119) Darghal, N.; Garnier-Suillerot, A.; Salerno, M. *Biochem. Biophys. Res. Commun.* **2006**, *343*, 623–629.
- (120) Pardridge, W. M.; Kang, Y. S.; Buciak, J. L.; Yang, J. *Pharm. Res.* **1995**, *12*, 807–816.
- (121) Boado, R. J.; Zhang, Y.; Zhang, Y.; Xia, C.-F.; Wang, Y.; Pardridge, W. M. *Biotechnol. Bioeng.* **2008**, *99*, 475–484.
- (122) Sumbria, R. K.; Boado, R. J.; Pardridge, W. M. *Bioconjug. Chem.* **2012**.
- (123) Khachaturian ZS *Arch Neurol* **1985**, *42*, 1097–1105.
- (124) Klunk, W. E.; Wang, Y.; Huang, G.; Debnath, M. L.; Holt, D. P.; Mathis, C. A. *Life Sciences* **2001**, *69*, 1471–1484.
- (125) Choi, S. R.; Golding, G.; Zhuang, Z.; Zhang, W.; Lim, N.; Hefti, F.; Benedum, T. E.; Kilbourn, M. R.; Skovronsky, D.; Kung, H. F. *J. Nucl. Med.* **2009**, *50*, 1887–1894.
- (126) Nesterov, E. E.; Skoch, J.; Hyman, B. T.; Klunk, W. E.; Bacskai, B. J.; Swager, T. M. *Angew. Chem. Int. Ed. Engl.* **2005**, *44*, 5452–5456.
- (127) Bacskai, B. J.; Hickey, G. A.; Skoch, J.; Kajdasz, S. T.; Wang, Y.; Huang, G.; Mathis, C. A.; Klunk, W. E.; Hyman, B. T. *Proc Natl Acad Sci U S A* **2003**, *100*, 12462–12467.
- (128) Camus, V.; Payoux, P.; Barré, L.; Desgranges, B.; Voisin, T.; Tauber, C.; La Joie, R.; Tafani, M.; Hommet, C.; Chételat, G.; Mondon, K.; de La Sayette, V.; Cottier, J. P.; Beaufils, E.; Ribeiro, M. J.; Gissot, V.; Vierron, E.; Vercouillie, J.; Vellas, B.; Eustache, F.; Guilloteau, D. *Eur. J. Nucl. Med. Mol. Imaging* **2012**, *39*, 621–631.
- (129) Vandenberghe, R.; Van Laere, K.; Ivanoiu, A.; Salmon, E.; Bastin, C.; Triau, E.; Hasselbalch, S.; Law, I.; Andersen, A.; Korner, A.; Minthon, L.; Garraux, G.; Nelissen, N.; Bormans, G.; Buckley, C.; Owenius, R.; Thurfjell, L.; Farrar, G.; Brooks, D. J. *Ann. Neurol.* **2010**, *68*, 319–329.
- (130) Mathis, C. A.; Bacskai, B. J.; Kajdasz, S. T.; McLellan, M. E.; Frosch, M. P.; Hyman, B. T.; Holt, D. P.; Wang, Y.; Huang, G.-F.; Debnath, M. L.; Klunk, W. E. *Bioorg. Med. Chem. Lett.* **2002**, *12*, 295–298.
- (131) Groenning, M.; Olsen, L.; van de Weert, M.; Flink, J. M.; Frokjaer, S.; Jørgensen, F. S. *J Struct Biol.* **2007**, *158*, 358–369.
- (132) Hoyer, W.; Grönwall, C.; Jonsson, A.; Ståhl, S.; Härd, T. *Proc. Natl. Acad. Sci. U.S.A.* **2008**, *105*, 5099–5104.
- (133) Lendel, C.; Bolognesi, B.; Wahlström, A.; Dobson, C. M.; Gräslund, A. *Biochemistry* **2010**, *49*, 1358–1360.
- (134) Serdons, K.; Verduyckt, T.; Cleynhens, J.; Terwinghe, C.; Mortelmans, L.;

- Bormans, G.; Verbruggen, A. *Bioorg. Med. Chem. Lett.* **2007**, *17*, 6086–6090.
- (135) Cheng, Y.; Ono, M.; Kimura, H.; Ueda, M.; Saji, H. *J. Med. Chem.* **2012**, *55*, 2279–2286.
- (136) Zhuang, Z.-P.; Kung, M.-P.; Hou, C.; Ploessl, K.; Kung, H. F. *Nucl. Med. Biol.* **2005**, *32*, 171–184.
- (137) Cui, M.; Tang, R.; Li, Z.; Ren, H.; Liu, B. *Bioorg. Med. Chem. Lett.* **2011**, *21*, 1064–1068.
- (138) Jack, C. R., Jr; Garwood, M.; Wengenack, T. M.; Borowski, B.; Curran, G. L.; Lin, J.; Adriany, G.; Gröhn, O. H. J.; Grimm, R.; Poduslo, J. F. *Magn. Reson. Med.* **2004**, *52*, 1263–1271.
- (139) Poduslo, J. F.; Wengenack, T. M.; Curran, G. L.; Wisniewski, T.; Sigurdsson, E. M.; Macura, S. I.; Borowski, B. J.; Jack, C. R. *Neurobiol Dis.* **2002**, *11*, 315–329.
- (140) Yang, J.; Wadghiri, Y. Z.; Hoang, D. M.; Tsui, W.; Sun, Y.; Chung, E.; Li, Y.; Wang, A.; de Leon, M.; Wisniewski, T. *Neuroimage* **2011**, *55*, 1600–1609.
- (141) Petiet, A.; Santin, M.; Bertrand, A.; Wiggins, C. J.; Petit, F.; Houitte, D.; Hantraye, P.; Benavides, J.; Debeir, T.; Rooney, T.; Dhenain, M. *Neurobiol. Aging* **2011**.
- (142) Cheng, Y.; Prusoff, W. H. *Biochem. Pharmacol.* **1973**, *22*, 3099–3108.
- (143) Mensch, J.; Oyarzabal, J.; Mackie, C.; Augustijns, P. *J Pharm Sci* **2009**, *98*, 4429–4468.
- (144) Levin, V. A. *J. Med. Chem.* **1980**, *23*, 682–684.
- (145) Moi, M. K.; Meares, C. F.; DeNardo, S. J. *J. Am. Chem. Soc.* **1988**, *110*, 6266–6267.
- (146) Stetter, H.; Frank, W. *Angew. Chem. Int. Ed. Engl.* **1976**, *15*, 686–686.
- (147) Liu, S.; Pietryka, J.; Ellars, C. E.; Edwards, D. S. *Bioconjugate Chem.* **2002**, *13*, 902–913.
- (148) Mathis, C. A.; Wang, Y.; Holt, D. P.; Huang, G.-F.; Debnath, M. L.; Klunk, W. E. *J. Med. Chem.* **2003**, *46*, 2740–2754.
- (149) Mathis, C. A.; Bacskai, B. J.; Kajdasz, S. T.; McLellan, M. E.; Frosch, M. P.; Hyman, B. T.; Holt, D. P.; Wang, Y.; Huang, G.-F.; Debnath, M. L.; Klunk, W. E. *Bioorg. Med. Chem. Lett.* **2002**, *12*, 295–298.
- (150) Lin, K.-S.; Debnath, M. L.; Mathis, C. A.; Klunk, W. E. *Bioorg. Med. Chem. Lett.* **2009**, *19*, 2258–2262.
- (151) Chen, X.; Yu, P.; Zhang, L.; Liu, B. *Bioorg. Med. Chem. Lett.* **2008**, *18*, 1442–1445.
- (152) Wang, Y.; Klunk, W. E.; Huang, G.-F.; Debnath, M. L.; Holt, D. P.; Mathis, C. A. *J Mol Neurosci* **2002**, *19*, 11–16.
- (153) Thyagarajan, B. S. *Chem. Rev.* **1958**, *58*, 439–460.
- (154) Rawat, A. G. S. *J. Curr. Pharm. Res.* **2010**, *3*, 13–23.
- (155) Bose, D.; Idrees, M.; Srikanth, B. *Synthesis* **2007**, *2007*, 819–823.
- (156) Schotten, C. *Ber. Dtsch. Chem. Ges.* **1884**, *17*, 2544–2547.
- (157) Baumann, E. *Ber. Dtsch. Chem. Ges.* **1886**, *19*, 3218–3222.
- (158) Marom, H.; Miller, K.; Bechor-Bar, Y.; Tsarfaty, G.; Satchi-Fainaro, R.; Gozin, M. *J. Med. Chem.* **2010**, *53*, 6316–6325.
- (159) Eisenwiener, K. P.; Powell, P.; Mäcke, H. R. *Bioorg. Med. Chem. Lett.* **2000**, *10*, 2133–2135.
- (160) Vollhardt, K. P. C.; Schore, N. E. *Organic Chemistry*; W.H. Freeman, 1994.
- (161) Bernhard, C.; Moreau, M.; Lhenry, D.; Goze, C.; Boschetti, F.; Rousselin, Y.; Brunotte, F.; Denat, F. *Chem. Eur. J.* **2012**, *18*, 7834–7841.
- (162) Gale, E. M.; Simmonett, A. C.; Telser, J.; Schaefer, H. F.; Harrop, T. C. *Inorg. Chem.* **2011**, 9216–9218.

- (163) Walovitch, R. C.; Hill, T. C.; Garrity, S. T.; Cheesman, E. H.; Burgess, B. A.; O’Leary, D. H.; Watson, A. D.; Ganey, M. V.; Morgan, R. A.; Williams, S. J. *J. Nucl. Med.* **1989**, *30*, 1892–1901.
- (164) Merbach, A. E.; Tóth, É. *The Chemistry of Contrast Agents in Medical Magnetic Resonance Imaging*; John Wiley & Sons, 2001.
- (165) Solomon, I. *Phys. Rev.* **1955**, *99*, 559.
- (166) Powell, D. H.; Dhubhghaill, O. M. N.; Pubanz, D.; Helm, L.; Lebedev, Y. S.; Schlaepfer, W.; Merbach, A. E. *J. Am. Chem. Soc.* **1996**, *118*, 9333–9346.
- (167) Meadowcroft, M. D.; Connor, J. R.; Smith, M. B.; Yang, Q. X. *J. Magn. Reson. Imaging* **2009**, *29*, 997–1007.
- (168) Barge, A.; Cravotto, G.; Gianolio, E.; Fedeli, F. *Contrast Media Mol. Imaging* **2006**, *1*, 184–188.
- (169) Leo, A.; Hansch, C.; Elkins, D. *Chem. Rev.* **1971**, *71*, 525–616.
- (170) Anthony, J. L.; Maginn, E. J.; Brennecke, J. F. *J. Phys. Chem. B* **2001**, *105*, 10942–10949.
- (171) Hugli, A. D.; Helm, L.; Merbach, A. E. *Helv. Chim. Acta.* **1985**, *68*, 508–521.
- (172) Prata, M. I.; Santos, A. C.; Bligh, S. W.; Chowdhury, A. H.; Geraldès, C. F.; de Lima, J. J. *Nucl. Med. Biol.* **2000**, *27*, 605–610.
- (173) Bornebroek, M.; Verzijlbergen, J. F.; Haan, J.; Van Scheyen, E. J.; Verhoeff, N. P.; Pauwels, E. K.; Roos, R. A. *Nucl Med Commun* **1996**, *17*, 929–933.
- (174) Saito, Y.; Buciak, J.; Yang, J.; Pardridge, W. M. *Proc Natl Acad Sci U S A* **1995**, *92*, 10227–10231.
- (175) Corsi, D.; Platas-Iglesias, C.; van Bekkum, H.; Peters, J. .
- (176) Torres, S.; Martins, J. A.; André, J. P.; Geraldès, C. F. G. C.; Merbach, A. E.; Tóth, É. *Chem. Eur. J.* **2006**, *12*, 940–948.
- (177) Nicolle, G. M.; Toth, E.; Eisenwiener, K.-P.; Mäcke, H. R.; Merbach, A. E. *J. Biol. Inorg. Chem.* **2002**, *7*, 757–769.
- (178) Raitsimring, A. M.; Astashkin, A. V.; Baute, D.; Goldfarb, D.; Caravan, P. *J. Phys. Chem. A* **2004**, *108*, 7318–7323.
- (179) Henrotte, V.; Vander Elst, L.; Laurent, S.; Muller, R. N. *J Biol Inorg Chem* **2007**, *12*, 929–937.
- (180) Rauk, A. *Chem. Soc. Rev.* **2009**, *38*, 2698.
- (181) Ono, K.; Yamada, M. *J. Neurochem.* **2011**, *117*, 19–28.
- (182) Chiti, F.; Dobson, C. M. *Annu. Rev. Biochem.* **2006**, *75*, 333–366.
- (183) Montalto, M. C.; Farrar, G.; Hehir, C. T. *Ann. N. Y. Acad. Sci.* **2007**, *1097*, 239–258.
- (184) Dobson, C. M. *Science* **2004**, *304*, 1259–1262.
- (185) Jarvet, J.; Danielsson, J.; Damberg, P.; Oleszczuk, M.; Gräslund, A. *J. Biomol. NMR* **2007**, *39*, 63–72.
- (186) Abelein, A.; Bolognesi, B.; Dobson, C. M.; Gräslund, A.; Lendel, C. *Biochemistry* **2012**, *51*, 126–137.
- (187) Necula, M.; Kayed, R.; Milton, S.; Glabe, C. G. *J. Biol. Chem.* **2007**, *282*, 10311–10324.
- (188) Barthel, H.; Gertz, H.-J.; Dresel, S.; Peters, O.; Bartenstein, P.; Buerger, K.; Hiemeyer, F.; Wittmer-Rump, S. M.; Seibyl, J.; Reininger, C.; Sabri, O. *Lancet Neurol* **2011**, *10*, 424–435.
- (189) Cui, M.-C.; Li, Z.-J.; Tang, R.-K.; Liu, B.-L. *Bioorg. Med. Chem.* **2010**, *18*, 2777–2784.
- (190) Ono, M.; Ikeoka, R.; Watanabe, H.; Kimura, H.; Fuchigami, T.; Haratake, M.; Saji, H.; Nakayama, M. *ACS Chem. Neurosci.* **2010**, *1*, 598–607.

- (191) Ono, M.; Ikeoka, R.; Watanabe, H.; Kimura, H.; Fuchigami, T.; Haratake, M.; Saji, H.; Nakayama, M. *Bioorg. Med. Chem. Lett.* **2010**, *20*, 5743–5748.
- (192) Martins, A. F.; Morfin, J.-F.; Kubičková, A.; Kubiček, V.; Buron, F.; Suzenet, F.; Salerno, M.; Lazar, A. N.; Duyckaerts, C.; Arlicot, N.; Guilloteau, D.; Geraldès, C. F. G. C.; Tóth, É. *ACS Med. Chem. Lett.* **2013**, *5*, 436–440.
- (193) Shuvaev, V. V.; Siest, G. *FEBS Lett.* **1996**, *383*, 9–12.
- (194) Myszka, D. G.; Wood, S. J.; Biere, A. L. In *Methods in Enzymology*; Elsevier, 1999; Vol. 309, pp. 386–402.
- (195) Schleucher, J.; Schwendinger, M.; Sattler, M.; Schmidt, P.; Schedletsky, O.; Glaser, S. J.; Sørensen, O. W.; Griesinger, C. *J. Biomol. NMR* **1994**, *4*, 301–306.
- (196) Liu, M.; Mao, X.; Ye, C.; Huang, H.; Nicholson, J. K.; Lindon, J. C. *J. Magn. Reson.* **1998**, *132*, 125–129.
- (197) Laurents, D. V.; Gorman, P. M.; Guo, M.; Rico, M.; Chakrabarty, A.; Bruix, M. *J. Biol. Chem.* **2005**, *280*, 3675–3685.
- (198) Markley, J. L.; Bax, A.; Arata, Y.; Hilbers, C. W.; Kaptein, R.; Sykes, B. D.; Wright, P. E.; Wüthrich, K. *Eur. J. Biochem.* **1998**, *256*, 1–15.
- (199) Grzesiek, S.; Bax, A.; Clore, G. M.; Gronenborn, A. M.; Hu, J. S.; Kaufman, J.; Palmer, I.; Stahl, S. J.; Wingfield, P. T. *Nat. Struct. Biol.* **1996**, *3*, 340–345.
- (200) Mayer, M.; Meyer, B. *Angew. Chem. Int. Ed.* **1999**, *38*, 1784–1788.
- (201) Mayer, M.; Meyer, B. *J. Am. Chem. Soc.* **2001**, *123*, 6108–6117.
- (202) Glasoe, P. K.; Long, F. A. *J. Phys. Chem.* **1960**, *64*, 188–190.
- (203) Hwang, T. L.; Shaka, A. J. *J. Magn. Reson.* **1995**, *112*, 275–279.
- (204) Angulo, J.; Enríquez-Navas, P. M.; Nieto, P. M. *Chem. Eur. J.* **2010**, *16*, 7803–7812.
- (205) Ryan, T. M.; Friedhuber, A.; Lind, M.; Howlett, G. J.; Masters, C.; Roberts, B. R. *J. Biol. Chem.* **2012**, *287*, 16947–16954.
- (206) Cairo, C. W.; Strzelec, A.; Murphy, R. M.; Kiessling, L. L. *Biochemistry* **2002**, *41*, 8620–8629.
- (207) Bohrmann, B.; Adrian, M.; Dubochet, J.; Kuner, P.; Müller, F.; Huber, W.; Nordstedt, C.; Döbeli, H. *J. Struct. Biol.* **2000**, *130*, 232–246.
- (208) Viegas, A.; Manso, J.; Nobrega, F. L.; Cabrita, E. J. *J. Chem. Educ.* **2011**, *88*, 990–994.
- (209) Ramakrishnan, M.; Kandimalla, K. K.; Wengenack, T. M.; Howell, K. G.; Poduslo, J. F. *Biochemistry* **2009**, *48*, 10405–10415.
- (210) LeVine, H. *Protein Sci.* **1993**, *2*, 404–410.
- (211) Hoyer, W.; Grönwall, C.; Jonsson, A.; Ståhl, S.; Härd, T. *PNAS* **2008**, *105*, 5099–5104.
- (212) Wahlström, A.; Hugonin, L.; Perálvarez-Marín, A.; Jarvet, J.; Gräslund, A. *FEBS J.* **2008**, *275*, 5117–5128.
- (213) Bai, Y.; Milne, J. S.; Mayne, L.; Englander, S. W. *Proteins* **1993**, *17*, 75–86.
- (214) Hou, L.; Shao, H.; Zhang, Y.; Li, H.; Menon, N. K.; Neuhaus, E. B.; Brewer, J. M.; Byeon, I.-J. L.; Ray, D. G.; Vitek, M. P.; Iwashita, T.; Makula, R. A.; Przybyla, A. B.; Zagorski, M. G. *J. Am. Chem. Soc.* **2004**, *126*, 1992–2005.
- (215) Danielsson, J.; Andersson, A.; Jarvet, J.; Gräslund, A. *Magn. Reson. Chem.* **2006**, *44 Spec No*, S114–121.
- (216) Hou, L.; Zagorski, M. G. *J. Am. Chem. Soc.* **2006**, *128*, 9260–9261.
- (217) Baxter, N. J.; Williamson, M. P. *J. Biomol. NMR* **1997**, *9*, 359–369.
- (218) Wishart, D. S.; Sykes, B. D.; Richards, F. M. *J. Mol. Biol.* **1991**, *222*, 311–333.
- (219) Andersen, N. H.; Neidigh, J. W.; Harris, S. M.; Lee, G. M.; Liu, Z.; Tong, H. *J. Am. Chem. Soc.* **1997**, *119*, 8547–8561.

- (220) Chang, E. S.-H.; Liao, T.-Y.; Lim, T.-S.; Fann, W.; Chen, R. P.-Y. *J. Mol. Biol.* **2009**, *385*, 1257–1265.
- (221) Greenfield, N. J. *Anal. Biochem.* **1996**, *235*, 1–10.
- (222) Greenfield, N. J. *Nat. Protoc.* **2007**, *1*, 2876–2890.
- (223) Kelly, M. A.; Chellgren, B. W.; Rucker, A. L.; Troutman, J. M.; Fried, M. G.; Miller, A.-F.; Creamer, T. P. *Biochemistry* **2001**, *40*, 14376–14383.
- (224) Jarvet, J.; Damberg, P.; Danielsson, J.; Johansson, I.; Eriksson, L. E. G.; Gräslund, A. *FEBS Lett.* **2003**, *555*, 371–374.
- (225) Danielsson, J.; Jarvet, J.; Damberg, P.; Gräslund, A. *FEBS J.* **2005**, *272*, 3938–3949.
- (226) Buell, A. K.; Dobson, C. M.; Knowles, T. P. J.; Welland, M. E. *Biophys. J.* **2010**, *99*, 3492–3497.
- (227) Maezawa, I.; Hong, H.-S.; Liu, R.; Wu, C.-Y.; Cheng, R. H.; Kung, M.-P.; Kung, H. F.; Lam, K. S.; Oddo, S.; LaFerla, F. M.; Jin, L.-W. *J. Neurochem.* **2008**, *104*, 457–468.
- (228) Sharma, A. K.; Pavlova, S. T.; Kim, J.; Finkelstein, D.; Hawco, N. J.; Rath, N. P.; Kim, J.; Mirica, L. M. *J. Am. Chem. Soc.* **2012**, *134*, 6625–6636.
- (229) Petkova, A. T. *Science* **2005**, *307*, 262–265.
- (230) Fezoui, Y.; Teplow, D. B. *J. Biol. Chem.* **2002**, *277*, 36948–36954.
- (231) Nerelius, C.; Sandegren, A.; Sargsyan, H.; Raunak, R.; Leijonmarck, H.; Chatterjee, U.; Fisahn, A.; Imarisio, S.; Lomas, D. A.; Crowther, D. C.; Strömberg, R.; Johansson, J. *PNAS* **2009**, *106*, 9191–9196.
- (232) Chiti, F.; Stefani, M.; Taddei, N.; Ramponi, G.; Dobson, C. M. *Nature* **2003**, *424*, 805–808.
- (233) Kim, W.; Hecht, M. H. *PNAS* **2006**, *103*, 15824–15829.
- (234) Pawar, A. P.; DuBay, K. F.; Zurdo, J.; Chiti, F.; Vendruscolo, M.; Dobson, C. M. *J. Mol. Biol.* **2005**, *350*, 379–392.
- (235) Cecchini, M.; Curcio, R.; Pappalardo, M.; Melki, R.; Caflisch, A. *J. Mol. Biol.* **2006**, *357*, 1306–1321.
- (236) Soscia, S. J.; Kirby, J. E.; Washicosky, K. J.; Tucker, S. M.; Ingelsson, M.; Hyman, B.; Burton, M. A.; Goldstein, L. E.; Duong, S.; Tanzi, R. E.; Moir, R. D. *PLoS ONE* **2010**, *5*, e9505.
- (237) Chatziioannou, A. F. *Mol. Imaging Biol.* **2002**, *4*, 47–63.
- (238) Bao, Q.; Newport, D.; Chen, M.; Stout, D. B.; Chatziioannou, A. F. *J. Nucl. Med.* **2009**, *50*, 401–408.
- (239) De Kemp, R. A.; Epstein, F. H.; Catana, C.; Tsui, B. M. W.; Ritman, E. L. *J. Nucl. Med.* **2010**, *51 Suppl 1*, 18S–32S.
- (240) Games, D.; Adams, D.; Alessandrini, R.; Barbour, R.; Berthelette, P.; Blackwell, C.; Carr, T.; Clemens, J.; Donaldson, T.; Gillespie, F. *Nature* **1995**, *373*, 523–527.
- (241) Hsiao, K.; Chapman, P.; Nilsen, S.; Eckman, C.; Harigaya, Y.; Younkin, S.; Yang, F.; Cole, G. *Science* **1996**, *274*, 99–102.
- (242) Holcomb, L.; Gordon, M. N.; McGowan, E.; Yu, X.; Benkovic, S.; Jantzen, P.; Wright, K.; Saad, I.; Mueller, R.; Morgan, D.; Sanders, S.; Zehr, C.; O’Campo, K.; Hardy, J.; Prada, C. M.; Eckman, C.; Younkin, S.; Hsiao, K.; Duff, K. *Nat. Med.* **1998**, *4*, 97–100.
- (243) Teipel, S. J.; Buchert, R.; Thome, J.; Hampel, H.; Pahnke, J. *Prog. Neurobiol.* **2011**, *95*, 547–556.
- (244) Klunk, W. E.; Lopresti, B. J.; Ikonovic, M. D.; Lefterov, I. M.; Koldamova, R. P.; Abrahamson, E. E.; Debnath, M. L.; Holt, D. P.; Huang, G.; Shao, L.; DeKosky, S. T.; Price, J. C.; Mathis, C. A. *J. Neurosci.* **2005**, *25*, 10598–10606.

- (245) Kuntner, C.; Kesner, A. L.; Bauer, M.; Kremslehner, R.; Wanek, T.; Mandler, M.; Karch, R.; Stanek, J.; Wolf, T.; Müller, M.; Langer, O. *Mol Imaging Biol* **2009**, *11*, 236–240.
- (246) Hintersteiner, M.; Enz, A.; Frey, P.; Jatton, A.-L.; Kinzy, W.; Kneuer, R.; Neumann, U.; Rudin, M.; Staufienbiel, M.; Stoeckli, M.; Wiederhold, K.-H.; Gremlich, H.-U. *Nat Biotech* **2005**, *23*, 577–583.
- (247) Braak, H.; Braak, E. *Acta Neuropathol* **1991**, *82*, 239–259.
- (248) Mirra, S. S.; Heyman, A.; McKeel, D.; Sumi, S. M.; Crain, B. J.; Brownlee, L. M.; Vogel, F. S.; Hughes, J. P.; van Belle, G.; Berg, L. *Neurology* **1991**, *41*, 479–486.
- (249) *Neurobiol. Aging* **1997**, *18*, S1–2.
- (250) Panchal, M.; Loeper, J.; Cossec, J.-C.; Perruchini, C.; Lazar, A.; Pompon, D.; Duyckaerts, C. *J. Lipid Res.* **2010**, *51*, 598–605.
- (251) Emond, P.; Guilloteau, D.; Chalon, S. *CNS Neurosci Ther* **2008**, *14*, 47–64.
- (252) Guilloteau, D.; Emond, P.; Baulieu, J. L.; Garreau, L.; Frangin, Y.; Pourcelot, L.; Mauclaire, L.; Besnard, J. C.; Chalon, S. *Nucl. Med. Biol.* **1998**, *25*, 331–337.
- (253) Arlicot, N.; Katsifis, A.; Garreau, L.; Mattner, F.; Vergote, J.; Duval, S.; Kousignian, I.; Bodard, S.; Guilloteau, D.; Chalon, S. *Eur. J. Nucl. Med. Mol. Imaging* **2008**, *35*, 2203–2211.
- (254) Mattner, F.; Mardon, K.; Katsifis, A. *Eur. J. Nucl. Med. Mol. Imaging* **2008**, *35*, 779–789.
- (255) Swift, T. J.; Connick, R. E. *J. Chem. Phys.* **1962**, *37*, 307–320.
- (256) Zimmerman, J. R.; Brittin, W. E. *J. Phys. Chem.* **1957**, *61*, 1328–1333.
- (257) Micskei, K.; Helm, L.; Brucher, E.; Merbach, A. E. *Inorg. Chem.* **1993**, *32*, 3844–3850.
- (258) Brittain, H. G.; Desreux, J. F. *Inorg. Chem.* **1984**, *23*, 4459–4466.
- (259) Gonzalez, G.; Powell, D. H.; Tissieres, V.; Merbach, A. E. *J. Phys. Chem.* **98**, 53–59.
- (260) Luz, Z.; Meiboom, S. *J. Chem. Phys.* **1964**, *40*, 2686–2692.
- (261) Dunand, F. A.; Tóth, E.; Hollister, R.; Merbach, A. E. *J. Biol. Inorg. Chem.* **2001**, *6*, 247–255.
- (262) Freed, J. H. *J. Chem. Phys.* **1978**, *68*, 4034–4037.
- (263) Koenig, S. H.; Brown, R. D.; Spiller, M.; Chakrabarti, B.; Pande, A. *Biophys J* **1992**, *61*, 776–785.
- (264) Yan, J.; Kline, A. D.; Mo, H.; Shapiro, M. J.; Zartler, E. R. *J. Magn. Reson.* **2003**, *163*, 270–276.
- (265) Meyer, B.; Peters, T. *Angew. Chem. Int. Ed. Engl.* **2003**, *42*, 864–890.
- (266) Claridge, T. D. W. *High-Resolution NMR Techniques in Organic Chemistry*; 2nd ed.; Elsevier Science, 2008; Vol. 27.
- (267) Zettner, A.; Duly, P. E. *Clinical Chemistry* **1974**, *20*, 5–14.